



HAL
open science

Vaporization of water at subatmospheric pressure : Fundamentals of boiling phenomena and path towards the design of compact evaporators for sorption chillers

Florine Giraud

► **To cite this version:**

Florine Giraud. Vaporization of water at subatmospheric pressure : Fundamentals of boiling phenomena and path towards the design of compact evaporators for sorption chillers. Thermics [physics.class-ph]. INSA de Lyon, 2015. English. NNT : 2015ISAL0109 . tel-01368517

HAL Id: tel-01368517

<https://theses.hal.science/tel-01368517v1>

Submitted on 19 Sep 2016

HAL is a multi-disciplinary open access archive for the deposit and dissemination of scientific research documents, whether they are published or not. The documents may come from teaching and research institutions in France or abroad, or from public or private research centers.

L'archive ouverte pluridisciplinaire **HAL**, est destinée au dépôt et à la diffusion de documents scientifiques de niveau recherche, publiés ou non, émanant des établissements d'enseignement et de recherche français ou étrangers, des laboratoires publics ou privés.

THÈSE

Vaporization of water at subatmospheric pressure: fundamentals of boiling phenomena and path towards the design of compact evaporators for sorption chillers

présentée devant

L'INSTITUT NATIONAL DES SCIENCES APPLIQUÉES DE LYON

pour obtenir le grade de

Docteur

École Doctorale MEGA

(Mécanique, Énergétique, Génie Civil, Acoustique)

Spécialité : THERMIQUE ET ÉNERGÉTIQUE

par

Florine GIRAUD

(Ingénieur INSA)

Soutenue le 24 novembre 2015 devant la commission d'examen :

BONJOUR Jocelyn	Professeur (INSA de Lyon)	-	<i>Co-directeur de Thèse</i>
CLAUSSE Marc	Professeur (INSA de Lyon)	-	<i>Co-directeur de Thèse</i>
DI MARCO Paolo	Professeur (Università di Pisa)	-	<i>Président</i>
ROBINSON Anthony J.	Professeur (Trinity College Dublin)	-	<i>Rapporteur</i>
RULLIÈRE Romuald	Maître de Conférences (INSA de Lyon)	-	<i>Co-encadrant</i>
SCHNABEL Lena	Docteur (Fraunhofer ISE)	-	<i>Examineur</i>
STUTZ Benoit	Professeur (Université de Savoie)	-	<i>Rapporteur</i>
TOUBLANC Cyril	Maître de Conférences (Oniris Nantes)	-	<i>Co-encadrant</i>

Thèse préparée dans le cadre d'un partenariat entre le Centre d'Énergétique et de Thermique de Lyon (CETHIL - UMR5008 - INSA de Lyon) et le laboratoire de Chimie Moléculaire, Génie des Procédés Chimiques et Énergétiques (CMGPCE EA7341- CNAM Paris)

INSA Direction de la Recherche - Ecoles Doctorales – Quinquennal 2011-2015

SIGLE	ECOLE DOCTORALE	NOM ET COORDONNEES DU RESPONSABLE
CHIMIE	CHIMIE DE LYON http://www.edchimie-lyon.fr Sec : Renée EL MELHEM Bat Blaise Pascal 3 ^e etage 04 72 43 80 46 Insa : R. GOURDON secretariat@edchimie-lyon.fr	M. Jean Marc LANCELIN Université de Lyon – Collège Doctoral Bât ESCPE 43 bd du 11 novembre 1918 69622 VILLEURBANNE Cedex Tél : 04.72.43 13 95 directeur@edchimie-lyon.fr
E.E.A.	ELECTRONIQUE, ELECTROTECHNIQUE, AUTOMATIQUE http://edeea.ec-lyon.fr Sec : M.C. HAVGOUDOUKIAN Ecole-doctorale.eea@ec-lyon.fr	M. Gérard SCORLETTI Ecole Centrale de Lyon 36 avenue Guy de Collongue 69134 ECULLY Tél : 04.72.18 60.97 Fax : 04 78 43 37 17 Gerard.scorletti@ec-lyon.fr
E2M2	EVOLUTION, ECOSYSTEME, MICROBIOLOGIE, MODELISATION http://e2m2.universite-lyon.fr Sec : Safia AIT CHALAL Bat Atrium- UCB Lyon 1 04.72.44.83.62 Insa : S. REVERCHON Safia.ait-chalal@univ-lyon1.fr	M. Fabrice CORDEY Laboratoire de Géologie de Lyon Université Claude Bernard Lyon 1 Bât Géode – Bureau 225 43 bd du 11 novembre 1918 69622 VILLEURBANNE Cédex Tél : 04.72.44.83.74 Sylvie.reverchon-pescheux@insa-lyon.fr fabrice.cordey@univ-lyon1.fr
EDISS	INTERDISCIPLINAIRE SCIENCES-SANTE http://www.ediss-lyon.fr Sec : Safia AIT CHALAL Bat Atrium – UCB Lyon 1 04 72 44 83 62 Insa : Safia.ait-chalal@univ-lyon1.fr	Mme Emmanuelle CANET-SOULAS INSERM U1060, CarMeN lab, Univ. Lyon 1 Bâtiment IMBL 11 avenue Jean Capelle INSA de Lyon 696621 Villeurbanne Tél : 04.72.11.90.13 Emmanuelle.canet@univ-lyon1.fr
INFOMATHS	INFORMATIQUE ET MATHÉMATIQUES http://infomaths.univ-lyon1.fr Sec :Renée EL MELHEM Bat Blaise Pascal 3 ^e etage infomaths@univ-lyon1.fr	Mme Sylvie CALABRETTO LIRIS – INSA de Lyon Bat Blaise Pascal 7 avenue Jean Capelle 69622 VILLEURBANNE Cedex Tél : 04.72. 43. 80. 46 Fax 04 72 43 16 87 Sylvie.calabretto@insa-lyon.fr
Matériaux	MATERIAUX DE LYON http://ed34.universite-lyon.fr Sec : M. LABOUNE PM : 71.70 –Fax : 87.12 Bat. Direction 1 ^{er} et. Ed.materiaux@insa-lyon.fr	M. Jean-Yves BUFFIERE INSA de Lyon MATEIS Bâtiment Saint Exupéry 7 avenue Jean Capelle 69621 VILLEURBANNE Cedex Tél : 04.72.43 71.70 Fax 04 72 43 85 28 Ed.materiaux@insa-lyon.fr
MEGA	MECANIQUE, ENERGETIQUE, GENIE CIVIL, ACOUSTIQUE http://mega.universite-lyon.fr Sec : M. LABOUNE PM : 71.70 –Fax : 87.12 Bat. Direction 1 ^{er} et. mega@insa-lyon.fr	M. Philippe BOISSE INSA de Lyon Laboratoire LAMCOS Bâtiment Jacquard 25 bis avenue Jean Capelle 69621 VILLEURBANNE Cedex Tél : 04.72 .43.71.70 Fax : 04 72 43 72 37 Philippe.boisse@insa-lyon.fr
ScSo	ScSo* http://recherche.univ-lyon2.fr/scso/ Sec : Viviane POLSINELLI Brigitte DUBOIS Insa : J.Y. TOUSSAINT viviane.polsinelli@univ-lyon2.fr	

On se lasse de tout, sauf de comprendre.
Attribué à Virgile

Acknowledgement

This PhD Thesis has been supported financially by the French funding organization ANR (Agence Nationale de la Recherche) in the context of the project ECOSS (contract n°: ANR-11-SEED-0007-001) which is gratefully acknowledged.

This study has been carried out half of the time at the Centre d'Énergétique et de Thermique de Lyon (CETHIL UMR5008) National Institute of Applied Sciences (INSA de Lyon) and the other half of the time at the laboratory of Chimie Moléculaire, Génie des Procédés Chimiques et Énergétiques (CMGPCE EA7341), Conservatoire National des Arts et Métiers (CNAM Paris), under the direction of Prof. Jocelyn Bonjour, Prof. Marc Clause, Dr. Romuald Rullière and Dr. Cyril Toublanc. I thank these two laboratories for the opportunity to work in their premises.

I gratefully thank Jocelyn for his precious advice, rigor and support, Romuald for the everyday work together, his advices and support during all these years, Marc for his advice, direction and technologic discussions and Cyril for his implication and advice in experimental work. During these years, periods of discouragement occurred and I am very grateful for their everyday supports and advices. Thank you very much for everything.

I would like to thank Prof. Anthony J. Robinson from Trinity College and Prof. Benoît Stutz from Université de Savoie for being reviewers of this thesis and Prof. Paolo Di Marco from Università Di Pisa, and Dr. Lena Schnabel from Fraunhofer ISE for being examiners of this work.

I thank Lilian Durey for his scientific contribution to this work and Pierrick Vallon for designing and mounting the experimental setup at CNAM under the direction of Cyril.

I thank Florence and more generally all the administrative staff in CETHIL for your kindness, your help and your cheerfulness. I also thank the technicians and engineers of the two laboratories.

I thank my colleagues and all the office-mates I had during the PhD. Thank you very much for fun and time spent together. Particularly I thank Gabriel for his support and music, Pierrick for his help whenever I needed it, Alex and Paul for their cheerfulness, and Mehdi for our scientific discussions whereas it was only a matter of a closed valve.

Finally I thank my family, especially my mother, and my friend for their support and for taking my mind off things.

ABSTRACT

In order to be able to design properly low pressure evaporators for sorption chillers, knowledge on vaporization of the refrigerant under conditions that might occur in these evaporators is fundamental. Acquiring this knowledge could allow to minimize the size of the chillers and make this technology competitive with respect to usual vapor-compression refrigeration systems. However, few studies focus on this subject and there is a lack of knowledge about vaporization (boiling or evaporation) phenomena occurring in compact evaporator at low pressure. The aim of the present thesis is thus to go further into the understanding of these phenomena both from a fundamental point of view and from an applicative point of view. In that goal, two experimental test setups were designed and built.

The first experimental setup allows the observation of the water behavior at a pressure down to 0.8 kPa in pool boiling configuration. As the hydrostatic pressure is of the same order of magnitude as the vapor pressure, the boiling environment is highly subcooled. Varying the height of the liquid level and/or the vapor pressure allows to vary the local saturation pressure, the maximal subcooling degree and the subcooling gradient. This unusual environment has an influence on the bubble size and on the bubble growth: its influence is therefore analyzed. Boiling curves for pressures ranging from 0.8 kPa to 100 kPa were also plotted. Since significant fluctuations of the wall superheat in certain conditions of imposed heat flux were observed, these curves were plotted as the instantaneous heat fluxes vs. the instantaneous wall superheat for a given heat flux imposed at the heater. Then, in order to be closer to a plate-type heat exchanger configuration, water pool-boiling in vertical configuration first without and then with confinement was studied. Boiling curves for different vapor pressures and heights of the liquid level are plotted and compared with those obtained in horizontal configuration. Then, boiling curves for different channel thicknesses and for a pressure ranging from 1.2 kPa to 5 kPa were plotted and analyzed. As the pressure and the channel thickness decrease, the occurrence of a specific boiling regime already observed in horizontal orientation is observed. The influence of the onset of this specific regime on the heat transfer is shown. Experiments with high speed PIV were also conducted to highlight the influence of the wake-induced flow for very narrow channels. Results are presented and discussed. The significance of the Bond number, often used in study of boiling in confined space, is also discussed.

The second experimental setup allows the observation of the water vaporization inside a channel of a smooth plate-type heat exchanger (0.2 m width x 0.5 m height) in conditions that might occur in sorption chillers (working pressure ranging from 16 kPa to 0.85 kPa, secondary fluid temperature ranging from 10.9 to 23.1 °C, filling ratio ranging from 1/2 to 1/10 of the whole channel height). The methodology of the design of experiments was followed for a thickness of the channel equal to 2 mm and 4 mm in order to find conditions which yield the maximal cooling capacity under a given set of constraints. During these experiments three main flow regimes were observed and three different working areas were identified: a pool boiling area, a film evaporation area and a vapor area. It was shown that the major part of the cooling capacity achieved is obtained in the film evaporation area. In this part, the creation of a liquid film due to the splashing of droplets is observed. These droplets come from the breaks of the membrane of a previously formed large bubble of several centimeters in the pool boiling area, few centimeters above the free surface. The higher and thinner the liquid film created, the higher the cooling capacity achieved. Cooling capacities ranging from 0 to 503 W were measured and conditions to obtain the best cooling capacity were determined. Finally, an overall heat transfer coefficient is estimated and in order to provide some first tool or guidelines for the design of low pressure evaporators, reflexions based on dimensionless numbers are proposed.

Keywords: compact evaporators, subatmospheric pressure, experimentation, water vaporization, pool boiling, sorption chillers.

RÉSUMÉ

Afin d'optimiser la taille et le coût des évaporateurs basse pression utilisés dans les systèmes de climatisation à sorption, une bonne connaissance des phénomènes de vaporisation du fluide frigorigène tels qu'ils pourraient se produire dans ces évaporateurs est nécessaire. Acquérir cette connaissance est fondamental afin d'être en mesure de développer des machines à sorption pour le refroidissement d'air compétitives par rapport aux systèmes de climatisation actuellement commercialisés. Cependant très peu d'études portent sur ce sujet et il y a un sérieux manque de données concernant les phénomènes de vaporisation (ébullition et évaporation) qui pourraient se produire dans des évaporateurs compacts basse pression. Le but de cette étude est donc d'aller plus loin dans la compréhension de ces phénomènes aussi bien d'un point de vue très fondamental que d'un point de vue applicatif. Dans cette optique, deux bancs d'essais ont été réalisés.

Le premier banc d'essais permet d'étudier le comportement de l'eau dans une configuration d'ébullition en vase à une pression pouvant atteindre 0.8 kPa. À ces basses pressions, l'influence de la hauteur hydrostatique ne peut être négligée. Que soit modifiée la hauteur de la colonne d'eau ou la pression de vapeur, il en résulte une modification de la pression de saturation locale, du degré de sous-refroidissement maximal ainsi que du gradient de sous-refroidissement. Cette spécificité du milieu d'ébullition a une influence non négligeable sur la taille et la forme des bulles : cette influence est analysée. Les courbes d'ébullition pour des pressions allant de 0.8 kPa à 100 kPa sont tracées. Puisque de fortes fluctuations de la surchauffe pariétale sont observées pour certaines gammes de flux imposés, ces courbes sont tracées en tant que flux instantané en fonction de la surchauffe pariétale pour un flux donné aux cartouches chauffantes. Afin d'être ensuite plus proche d'une configuration d'échangeur à plaques, l'ébullition en vase de l'eau dans un premier temps sans puis avec confinement est étudiée. Des courbes d'ébullition sont tracées pour différentes pressions de vapeur et différentes hauteur de la colonne d'eau. Puis, six différents espaces de confinement sont testés pour des pressions allant de 1.2 kPa à 5 kPa. Les courbes obtenues sont tracées et analysées. Un régime d'ébullition spécifique à la basse pression et déjà observé en configuration horizontale apparaît lorsque l'espace de confinement diminue. L'influence de l'apparition de ce régime sur le transfert de chaleur est montrée. Enfin, des expériences utilisant la PIV rapide ont été réalisées afin de mettre en évidence « l'effet pompe » pour de faibles espaces de confinement. Les résultats sont présentés et traités. La signification du nombre de Bond, nombre incontournable lorsque l'ébullition confinée est étudiée, est également abordée.

Le deuxième banc expérimental permet d'observer la vaporisation de l'eau dans un canal d'évaporateur à plaques de dimension standard (0.2 m de large x 0.5 m de haut) dans des conditions similaires à celles obtenues dans une climatisation à absorption (pressions de travail variant de 16 kPa à 0.85 kPa, remplissage de la plaque variant de 1/2 à 1/10 de la hauteur totale de la plaque). Un plan d'expérience est réalisé pour un espacement entre deux plaques de 2 mm et 4 mm. Lors des expériences réalisées, trois principaux régimes d'ébullition ont été identifiés ainsi que trois différentes zones de travail : une zone d'ébullition en vase, une zone d'évaporation en film et une zone de vapeur. Il a été mis en évidence que la majorité du transfert de chaleur a lieu dans la zone d'évaporation en film. Le film observé dans cette partie est créé suite à la rupture de la membrane d'une bulle de plusieurs centimètres ayant pris naissance dans la partie d'ébullition en vase. Des puissances frigorifiques allant de 0 à 503 W ont été mesurées. Les conditions pour obtenir la meilleure puissance frigorifiques possible sont déterminées. Enfin, dans une première tentative vers un dimensionnement des échangeurs compacts basse pression, un coefficient de transfert global a été estimé et des premières réflexions basées sur des nombres adimensionnels ont été proposés.

Mots clefs : évaporateurs compacts, pressions subatmosphérique, études expérimentales, vaporisation de l'eau, ébullition en vase, machine frigorifique à sorption.

CONTENT

CONTENT	11
LIST OF FIGURES.....	15
LISTE OF TABLES.....	20
NOMENCLATURE	23
INTRODUCTION	27
1 LITERATURE REVIEW	31
1.1 Absorption cooling machines	32
1.2 Low pressure evaporators.....	36
1.2.1 Technology survey	36
1.2.2 Compact subatmospheric pressure evaporators.....	41
1.2.2.1 Effect of the operating pressure.....	41
1.2.2.2 Effect of the superheating temperature.....	42
1.2.2.3 Effect of the low vapor density.....	42
1.2.2.4 Effect of the feed fluid flow rate	43
1.2.2.5 Effect of the boiling regime.....	43
1.3 Free boiling phenomena	44
1.3.1 Nucleation	44
1.3.1.1 Liquid-vapor phase change.....	44
1.3.1.2 Immersed bubble equilibrium in a liquid	45
1.3.1.3 Nucleation theory	46
1.3.2 Bubble dynamics	48
1.3.2.1 Bubble growth	48
1.3.2.2 Bubble cycle at subatmospheric pressure.....	49
1.3.2.3 Detachment.....	52
1.3.3 Boiling curve	54
1.3.4 Boiling curve in transient boiling	57
1.4 Boiling phenomena in narrow spaces.....	58
1.4.1 Influence of the confined space in the heat exchange	58
1.4.2 Boiling regime in confined space	60
1.4.3 Parameters of influence	64
1.5 Two-phase flow and flow boiling in vertical tubes	65
1.5.1 Flow patterns	65
1.5.2 Heat transfer coefficient	69

1.6	Falling film evaporation	71
1.6.1	Falling film regimes	71
1.6.2	Wettability and Dry patch	73
1.7	Closing remarks.....	75
2	FUNDAMENTAL APPROACH OF PHASE-CHANGE PHENOMENA AT SUBATMOSPHERIC PRESSURE: BOILING ON A HORIZONTAL PLANE SURFACE.....	77
2.1	Experimental test setup and procedures	78
2.1.1	Experimental test facility.....	78
2.1.1.1	The vessel.....	78
2.1.1.2	The sample	79
2.1.1.3	The visualization test facility.....	79
2.1.2	Experimental procedures.....	80
2.1.3	Measurement techniques	80
2.1.3.1	Experimental heat flux and boiling surface temperature estimation	81
2.1.3.2	Image processing.....	83
2.2	Non-homogeneity of the boiling environment	83
2.3	Pool boiling in horizontal copper plane surface	85
2.3.1	Bubbles dynamics.....	85
2.3.1.1	Bubble shape	85
2.3.1.2	Bubble growth.....	87
2.3.1.3	Influence of the pressure on bubble size	89
2.3.2	Thermal analysis.....	91
2.3.2.1	Evidence of a new boiling regime at subatmospheric pressure.....	91
2.3.2.2	Influence of the pressure	96
2.3.2.3	Influence of the height of the liquid level.....	99
3	APPROACHING THE PHENOMENOLOGY OF PLATE-TYPE HEAT EXCHANGER: BOILING ON A VERTICAL PLATE	103
3.1	Subatmospheric water pool boiling in a vertical plane surface	104
3.1.1	Experimental setup	104
3.1.2	Visualization.....	104
3.1.2.1	Bubble shape	104
3.1.2.2	Bubble crisis	107
3.1.3	Thermal analysis.....	108
3.1.3.1	Boiling curve at $P_v = 1.2$ kPa.....	108
3.1.3.2	Influence of the vapor pressure	110
3.1.3.3	Influence of the height of the liquid level.....	113

3.2	Subatmospheric water pool boiling in a vertical narrow space	115
3.2.1	Experimental setup	115
3.2.2	Bond number limitation for the characterization of subatmospheric boiling phenomena in narrow channel	116
3.2.3	Effect of the confinement on experimental boiling curves.....	118
3.2.3.1	Influence of the thickness of the narrow channel	118
3.2.3.2	Influence of the vapor pressure	120
3.2.4	Highlight on the wake-induced flow by PIV analysis.....	123
4	WATER VAPORIZATION INSIDE A CHANNEL OF A SMOOTH PLATE	129
4.1	Experimental test facility.....	130
4.1.1	Experimental setup	130
4.1.1.1	The test bench.....	130
4.1.1.2	Evaporator	131
4.1.1.3	Instrumentation.....	132
4.1.1.4	The visualization test facility.....	133
4.1.2	Experimental procedure.....	134
4.1.2.1	Preparation and commissioning	134
4.1.2.2	Test campaign.....	134
4.2	Overall approach by the method of experiments (DOE).....	134
4.2.1	Methodology	135
4.2.2	Presentation of the design of experiments	135
4.3	Design of experiments results	140
4.3.1	Flow regimes	140
4.3.1.1	Flow observed	140
4.3.1.2	Influence of the flow patterns on heat transfer	146
4.3.2	Results' analysis for a thickness of the channel of 4 mm.....	148
4.3.3	Impact of the channel thickness	152
4.3.3.1	Visualization.....	153
4.3.3.2	Design of Experiments	155
4.3.4	Comparison of results obtained for $e = 4$ mm and $e = 2$ mm	158
4.4	Discussion	162
4.4.1	Simplified temperatures profile inside the evaporator	162
4.4.2	Overall heat transfer coefficient	163
4.4.3	Dimensionless numbers.....	168
5	PRELIMINARY EXPERIMENTAL INVESTIGATION OF WATER BOILING PHENOMENA IN A THIN LIQUID LAYER	177

5.1	Visualization: the occurrence of two typical behaviors.....	178
5.2	Experimental boiling curves.....	182
CONCLUSION AND PERSPECTIVES		185
	Synthesis.....	185
	Perspectives	187
References		189
APPENDIX A: Boiling phenomena hysteresis on bubble size and boiling curves.....		197
APPENDIX B: Uncertainties on the calculation of heat fluxes and uncertainties associated with the heat storage term		199
APPENDIX C: Boiling curves obtained in horizontal orientation for $h_1 = 150$ mm and five different vapor pressures		200
APPENDIX D: Boiling curves obtained in horizontal orientation for $h_1 = 100$ mm and five different vapor pressures		201
APPENDIX E: Water vaporization inside a channel of a smooth plate- Results obtained with the first version of the plate and comparison with result introduced in the main text.....		202
APPENDIX F: Responses to tests realized for the experimental design and error calculation.....		211
APPENDIX G: Void and mass fraction obtained		214
APPENDIX H: Uncertainties on the calculation of heat fluxes at different spot of the central plate		215
APPENDIX I: Simulation with Star CCM+ of the temperature distribution inside the central plate of the evaporator		217
APPENDIX J: Comparison of flow regime obtained for $e = 4$ mm and $e = 2$ mm.....		221
APPENDIX K: Plot of the evolution of the cooling capacity with dimensionless numbers.....		222

LIST OF FIGURES

Figure 1.1: Schematic of a) a single-effect H ₂ O/LiBr absorption machine cycle and b) the Dühring diagram associated	32
Figure 1.2: Schematic of a) a double- effect H ₂ O/LiBr absorption machine cycle and b) the Dühring diagram associated	34
Figure 1.3: Profile of the water saturation temperature along the vertical axis for a vapor saturation pressure of 1.2 kPa (T _{sat} = 9.7 °C).....	36
Figure 1.4: Schematic of principle of shell and tubes evaporator	37
Figure 1.5: Example of capillary structure (micro-fin-structured tube) (Schnabel <i>et al.</i> , 2011)	37
Figure 1.6: Schema of principle of capillary assisted evaporator in pool boiling operation mode used by Schnabel <i>et al.</i> (2011)	38
Figure 1.7: Falling film evaporator at the outlet surface of the tube a) in horizontal orientation b) in vertical orientation	38
Figure 1.8: Horizontal U-tube falling film evaporator with fins	39
Figure 1.9: falling film evaporator at the inlet of the tube a) global scheme b) operating principle	39
Figure 1.10: Influence of the filling level on the saturation temperature (Leprieur, 2014).....	41
Figure 1.11: Evolution of the saturation pressure with the saturation temperature for water	42
Figure 1.12: Consecutives snapshots obtained by Chang <i>et al.</i> (2012) over on entire cycle.....	43
Figure 1.13: Clapeyron diagram (Siedel, 2012).....	45
Figure 1.14: Apparent contact angle in conical cavities (Collier and Thome, 1994)	47
Figure 1.15: Conditions for the entrapment of gas in the advance of a semi infinite liquid sheet by Bankoff (1958).....	47
Figure 1.16: Schematic of the bubble growth at the vicinity of a wall by Carey (1992).....	49
Figure 1.17: Mushroom shape bubble observed by Van Stralen <i>et al.</i> (1975) at 2.04 kPa	50
Figure 1.18: Bubble curvature for an axisymmetric bubble by Ginet (1999).....	52
Figure 1.19: Boiling curves at a) imposed heat flux and b) imposed temperature	55
Figure 1.20: Boiling curves for water at 101 kPa, 9 kPa and 4 kPa by McGillis <i>et al.</i> (1991a).....	56
Figure 1.21: Transient boiling curve (Héas, 2001 from Sakurai <i>et al.</i> , 1970).....	58
Figure 1.22: Evolution of the wall superheat with the plate height for different imposed heat fluxes (Xia <i>et al.</i> , 1996)	59
Figure 1.23: Change in the concave shape of the boiling curve (Stutz <i>et al.</i> , 2009)	60
Figure 1.24: Flow map of boiling regime occurring in a narrow space (Bonjour and Lallemand, 1998)	62

List of Figures

Figure 1.25: Evolution of the maximal and minimal interface velocity obtained in the channel for different wall superheat (Ait Ameer, 2006).....	63
Figure 1.26: Pressure fluctuations inside the channel for $\frac{\dot{q}}{\dot{q}_{crit,e}} \approx 0.85$ (Ait Ameer, 2006).....	63
Figure 1.27: Enhancement factor in vertical and horizontal heated surface for different spacing of the confined space (Bonjour <i>et al.</i> , 1997).....	65
Figure 1.28: Two-phase flow patterns during evaporation in vertical flow (Collier and Thome, 1994).....	66
Figure 1.29: Flow regimes along the tube in the case of a vertical upward flow for different heat flux densities (Visentini, 2012, from Roshenow <i>et al.</i> , 1998).....	67
Figure 1.30: Cross-sectional void fraction (Revellin, 2005).....	68
Figure 1.31: Flow pattern map for R-22 and horizontal flow (Wojtan <i>et al.</i> , 2005). S=stratified flow, SW=stratified-wavy flow, I=intermittent flow, A=annular flow, M=mist flow and D= transition zone between annular and mist flow.....	68
Figure 1.32: a) Comparison of experimental heat transfer data on a horizontal flow with new prediction method b) Corresponding flow patterns map for horizontal flow.....	69
Figure 1.33: a) Schematic of the typical heat transfer coefficient trends depending on the saturation pressure and b) information reported on experimental conditions (at the bottom) (Charnay, 2014).....	70
Figure 1.34: Schematic of a film flowing down on a vertical plate.....	71
Figure 1.35: Pictures of inertial and capillary waves (Koffman, 2014).....	72
Figure 1.36: Stable dry patch following the breakup of a liquid film flowing down a vertical surface a) observed in a two-phase thermosyphon b) shown schematically (El-Genk and Saber, 2001).....	74
Figure 2.1: Detail of the pool boiling device in horizontal configuration.....	78
Figure 2.2: Detail of a) the copper block, b) the whole test heater.....	79
Figure 2.3: Visualization facility.....	80
Figure 2.4: Positions of the thermocouples along the copper block for a) the row 1 b) the row 2.....	81
Figure 2.5: Test sample thermocouples temperature example.....	81
Figure 2.6: Definition of notations used.....	83
Figure 2.7: Profile of the water saturation temperature along the vertical axis for a vapor saturation pressure of 1.78 kPa ($T_{sat} = 15.7 \text{ }^\circ\text{C}$).....	84
Figure 2.8: Evolution of the maximal subcooling degree versus the vapor saturation pressure and the liquid height.....	84
Figure 2.9: Profile of subcooling degree along the vertical axis for vapor saturation pressure of (1) 3 kPa ($T_{sat} = 24 \text{ }^\circ\text{C}$), (2) 7 kPa ($T_{sat} = 39 \text{ }^\circ\text{C}$) and (3) 11 kPa ($T_{sat} = 48 \text{ }^\circ\text{C}$) at the free surface level ($z = 0$).....	85
Figure 2.10: Bubble growth with liquid and vapor jets following the bubble departure ($P_v = 1.2 \text{ kPa}$, $T_l = 10^\circ\text{C}$, $h_l = 200 \text{ mm}$, $q = 22.6 \text{ W.cm}^2$).....	86

Figure 2.11: Bubble growth velocity for a) $h_1 = 200$ mm; b) $h_1 = 150$ mm ($P_v = 1.2$ kPa, $T_1 = 10^\circ\text{C}$, $\dot{q}_1 = 8.6$ W.cm⁻², $\dot{q}_2 = 16.9$ W.cm⁻², $\dot{q}_3 = 29.1$ W.cm⁻²) 88

Figure 2.12: Bubble growth velocity for 4 different vapor pressures ($h_1 = 200$ mm) 88

Figure 2.13: Correlations and experimental bubble diameters available in the literature 89

Figure 2.14: Bubble before detachment at a vapor saturation pressure of a) 100 kPa, b) 15 kPa, c) 4.2 kPa, d) 1.8 kPa, e) 1.2 kPa, f) 0.85 kPa, ($h_1 = 200$ mm; $\dot{q} = 10.2$ W.cm⁻²) 90

Figure 2.15: Evolution in time of the wall temperature and the instantaneous heat flux at subatmospheric pressure for three different heat flux imposed at the cartridges heaters of a) $\dot{q} = 11.6$ W.cm⁻²; b) $\dot{q} = 9.1$ W.cm⁻²; c) $\dot{q} = 22.1$ W.cm⁻² ($P_v = 1.2$ kPa, $h_1 = 200$ mm) 92

Figure 2.16: Evolution in time of the wall temperature and the instantaneous heat flux at atmospheric pressure for a) $\dot{q} = 11.5$ W.cm⁻²; b) $\dot{q} = 25.0$ W.cm⁻² ($P_v = 100$ kPa, $h_1 = 200$ mm) 92

Figure 2.17: Boiling curves for $P_v = 1.2$ kPa and $P_v = 100$ kPa ($h_1 = 200$ mm) 93

Figure 2.18: Pictures obtained during the phase (A) (B) and (C) ($P_v = 1.2$ kPa, $h_1 = 200$ mm, $\dot{q} = 11.6$ W.cm⁻²) 94

Figure 2.19: Boiling curves for three different imposed heat fluxes (6.3 W.cm⁻²; 17.8 W.cm⁻²; 27.4 W.cm⁻²), ($h_1 = 200$ mm, $P_v = 1.2$ kPa) 94

Figure 2.20: Heat transfer coefficients estimated at a) 18.5 W.cm⁻² with the three phase A, B, C of the cyclic boiling referred; b) different imposed heat flux ($P_v = 1.2$ kPa, $h_1 = 200$ mm) 95

Figure 2.21: Boiling curves for $h_1 = 200$ mm and a) $P_v = 100$ kPa; b) $P_v = 15$ kPa; c) $P_v = 4.2$ kPa; d) $P_v = 3$ kPa; e) $P_v = 1.8$ kPa; f) $P_v = 1.2$ kPa; g) $P_v = 0.8$ kPa 97

Figure 2.22: Heat transfer coefficient during one cycle (if any) for $h_1 = 200$ mm and a) $P_v = 100$ kPa, b) $P_v = 15$ kPa, c) $P_v = 4.2$ kPa, d) $P_v = 3$ kPa, e) $P_v = 1.8$ kPa, f) $P_v = 1.2$ kPa, g) $P_v = 0.8$ kPa 98

Figure 2.23: Boiling curves for $P_v = 1.2$ kPa and a) $h_1 = 200$ mm, b) $h_1 = 150$ mm, c) $h_1 = 100$ mm 100

Figure 2.24: Heat transfer coefficient during one cycle (if any) for $P_v = 1.2$ kPa and a) $h_1 = 150$ mm b) $h_1 = 100$ mm 100

Figure 3.1: Detail of the pool boiling device 104

Figure 3.2: Visualization of bubble growth ($P_v = 1.8$ kPa, $h_1 = 167$ mm, $\dot{q} = 7.0$ W.cm⁻²) 105

Figure 3.3: a) Evolution in time of the maximal horizontal diameter and maximal vertical diameter of the bubble; b) Schematic of the notation used 105

Figure 3.4: Schematic of the mains moments of the bubble growth 106

Figure 3.5: Visualization of “bubbles crisis” ($P = 1.8$ kPa, $T_1 = 15^\circ\text{C}$, $h_1 = 167$ mm, $\dot{q} = 12.7$ W.cm⁻²) 107

Figure 3.6: Evolution in time of the wall temperature and the instantaneous heat flux for $\dot{q} = 7.7$ W.cm⁻² and $h_1 = 156$ mm 108

Figure 3.7: Boiling curves for $h_1 = 156$ mm and $P_v = 1.2$ kPa 109

Figure 3.8: Comparison of boiling curves obtained in vertical and horizontal orientation 109

List of Figures

Figure 3.9: Comparison of the probability density functions (noted PDF) of the experimental heat transfer coefficient estimated at $P_v = 1.2$ kPa on a) vertical orientation, $h_l = 200$ mm b) horizontal orientation, $h_l = 156$ mm.....	110
Figure 3.10: Boiling curves obtained in vertical orientation for 5 different vapor pressures	111
Figure 3.11: Comparison of the probability density functions (noted PDF) of the experimental heat transfer coefficient estimated $h_l = 156$ mm and a) $P_v = 5.0$ kPa, b) $P_v = 4.0$ kPa, c) $P_v = 3.0$ kPa, d) $P_v = 1.8$ kPa, e) $P_v = 1.2$ kPa.....	112
Figure 3.12: Visualization of the microlayer ($P = 1.3$ kPa, $h_l = 50$ mm, $\dot{q} = 2.9$ W.cm ⁻²).....	113
Figure 3.13: Boiling curves obtained in vertical orientation for 4 different heights of the liquid level	113
Figure 3.14: Evolution of the subcooling degree with the liquid depth for the five vapor pressures investigated and three heights of the liquid level	114
Figure 3.15: Comparison of boiling curves obtained for $P_v = 3.0$ kPa, $h_l = 156$ mm and $P_v = 1.8$ kPa, $h_{liq} = 115$ mm, i.e. for a same maximal subcooling degree of 34 K	115
Figure 3.16: Detail of a) the pool boiling device b) the confinement plate.....	116
Figure 3.17: Picture of bubble formed inside the narrow space created ($P_v = 5$ kPa, $h_l = 156$ mm, $e = 11.5$ mm)	116
Table 3.1: Value of usual dimensionless numbers used to give the proportionality of different forces just before detachment at 1.8 kPa, 15 kPa and 100 kPa	118
Figure 3.18: Experimental boiling curves for different channel thicknesses ($P_v = 1.2$ kPa, $h_l = 156$ mm)	119
Figure 3.19: Probability density functions (noted PDF) of the experimental heat transfer coefficient for three channel thicknesses a) $e = \infty$, b) $e = 7.7$ mm and c) $e = 2$ mm ($P_v = 1.2$ kPa, $h_l = 156$ mm).....	120
Figure 3.20: Influence of the pressure on experimental boiling curves for different vapor pressures imposed and a) $e = \infty$, b) $e = 7.7$ mm, c) $e = 5.9$ mm and d) $e = 2.9$ mm ($h_l = 156$ mm)	121
Figure 3.21: Probability density functions (noted PDF) of the experimental wall superheat (on left), experimental instantaneous heat flux (on right) for 3.0 kPa, 4.0 kPa and 5.0 kPa ($h_l = 156$ mm, $e = 2.9$ mm)	122
Figure 3.22: Probability density functions (noted PDF) of the experimental wall superheat (on left), experimental instantaneous heat flux (on right) for 1.2 kPa and 1.8 kPa ($h_l = 156$ mm, $e = 2.9$ mm)	123
Figure 3.23: Schema of the experimental PIV device	124
Figure 3.24: Schematic general trend for the time evolution of the liquid velocity and associated phenomenology	125
Figure 3.25: Velocity curve versus dimensionless time at a) 30 W.cm ⁻² , b) 12 W.cm ⁻² and c) 6 W.cm ⁻² ($h_l = 77$ mm, $P_v = 1.8$ kPa)	126
Figure 3.26: Boiling curves with data corresponding to velocity curves plotted for $\dot{q} = 30$ W.cm ⁻² , $\dot{q} = 12$ W.cm ⁻² and $\dot{q} = 6$ W.cm ⁻² circles with dashed line ($h_l = 77$ mm, $P_v = 1.8$ kPa)	127
Figure 4.1: Drawing of the experimental test setup	130
Figure 4.2: Schematic of the evaporator	131

Figure 4.4: Schematic of the visualization test facility	133
Figure 4.5: Factors of the design of experiments on the drawing of the experimental test setup.....	136
Figure 5.1: Bubble growth in a liquid layer of 3 mm with a breaking of the bubble at the interface liquid/vapor ($P_v = 3$ kPa, $T_1 = 24$ °C, $h_l = 3$ mm, $\dot{q} = 1.6$ W.cm ⁻²)	178
Figure 5.2: Bubble growth in a liquid layer of 3 mm with thick top of the bubble falling down its center ($P_v = 3$ kPa, $T_1 = 24$ °C, $h_l = 3$ mm, $\dot{q} = 1.6$ W.cm ⁻²)	179
Figure 5.3: Bubble growth in a liquid layer of 7 mm without breaking of the bubble ($P_v = 1.25$ kPa, $T_1 = 10$ °C, $h_l = 7$ mm, $\dot{q} = 17.8$ W.cm ²).....	181
Figure 5.4: Boiling curves for $P_v = 1.2$ kPa and a) $h_l = 200$ mm, b) $h_l = 50$ mm, c) $h_l = 20$ mm, d) $h_l = 15$ mm, e) $h_l = 10$ mm, f) $h_l = 3$ mm.....	182
Figure A.1: Boiling curves at increasing and decreasing imposed heat flux and pictures of bubbles associated (vertical orientation, $P_v = 1.7$ kPa, $h_l = 167$ mm)	197
Figure A.2: Boiling curves at increasing and decreasing imposed heat flux (vertical orientation, $P_v = 1.2$ kPa, $h_l = 200$ mm)	196
Figure C.1: Boiling curves for $h_l = 150$ mm and a) $P_v = 4.2$ kPa; b) $P_v = 3$ kPa; c) $P_v = 1.8$ kPa; d) $P_v = 1.2$ kPa; e) $P_v = 0.8$ kPa.....	200
Figure D.1: Boiling curves for $h_l = 100$ mm and a) $P_v = 4.2$ kPa; b) $P_v = 3$ kPa; c) $P_v = 1.8$ kPa; d) $P_v = 1.2$ kPa; e) $P_v = 0.8$ kPa.....	201
Figure I.1: Boundaries chosen for the simulation on the schematic of the central plate of the evaporator	217
Figure I.2: Results of the Star CCM+ simulation of the temperature field for a portion of the central plate and the secondary fluid	218
Figure I.3: Results of the Star CCM+ simulation of the temperature field in the vapor part of the central plate	219
Figure I.4: Results of the Star CCM+ simulation of the temperature field in the film evaporation part of the central plate	219
Figure I.5: Results of the Star CCM+ simulation in the liquid part of the central plate.....	220
Figure K.1: Evolution of the cooling capacity achieved with the equivalent radius of the large bubble estimated	222
Figure K.2: Evolution of a) the cooling capacity achieved and b) the specific cooling capacity achieved with the Rayleigh Number	222
Figure K.3: Evolution of a) the cooling capacity achieved and b) the specific cooling capacity achieved with the Grashof Number.....	222
Figure K.4: Evolution of a) the cooling capacity achieved and b) the specific cooling capacity achieved with the Weber Number	223

LISTE OF TABLES

Table 1.1: Evaporators' performance	40
Table 3.1: Value of usual dimensionless numbers used to give the proportionality of different forces just before detachment at 1.8 kPa, 15 kPa and 100 kPa	118
Table 4.1: Specification of the different measuring devices	133
Table 4.2: Analysis of factors influencing the cooling capacity	137
Table 4.3: Experimental tests for $e = 4$ mm with associated driving pressure	137
Table 4.4: Corresponding absorber operating conditions (Abs) for given experimental operating conditions (Exp).....	139
Table 4.5: Tests realized and response obtained	149
Table 4.6: Coefficients of the mathematical model (Eq. 4.3) obtained by the design of experiments	149
Table 4.7: Model verification tests.....	150
Table 4.8: Tests realized and response obtained for $e = 2$ mm	156
Table 4.9: Coefficients of the mathematical model obtained by the design of experiments for $e = 2$ mm and $e = 4$ mm.....	157
Table 4.10: Experimental results of the highest theoretical cooling capacity achievable for the four driving pressures investigated.....	159
Table 4.11: Experimental results of the highest theoretical cooling capacity achievable in the experimental field for $e = 2$ mm and $e = 4$ mm	160
Table 4.12: Cooling capacity obtained in the apparent evaporator 3 with a) the ΔT_{LM} method assuming an overall falling film heat transfer coefficient (h_3) b) using Chang <i>et al.</i> (2012) correlation (h_{Chang}).....	167
Table E.1: Tests realized and response obtained.....	204
Table E.2: Coefficients of the mathematical model obtained by the experimental design.....	205
Table E.3: Model's verification tests	205
Table E.4: Favorable and theoretical liquid height for different $T_{cond}^{c,fs}$ and ΔP	206
Table E.5: Coefficients of the mathematical model obtained by the experimental design for $e = 2$ mm and $e = 4$ mm.....	207
Table E.6: Coefficients of the mathematical model obtained by the experimental design before (V_1) and after (V_2) experimental setup changes.	209
Table F.1: Results of the experimental design for $e = 2$ mm and the first version of the prototype (V_1)	211
Table F.2: Results of the experimental design for $e = 4$ mm and the first version of the prototype (V_1)	211
Table F.3: Results of the experimental design for $e = 2$ mm and the second version of the prototype (V_2)	212

Table F.4: Results of the experimental design for $e = 4$ mm and the second version of the prototype (V2)	213
Table F.5: Standard error of the estimate and mean absolute error calculated for the four experimental designs realized	213
Table G.1: Void and mass fraction calculated for the both version of the experimental setup (V1 and V2), for $e = 4$ mm and $e = 2$ mm.....	214
Table J.1: Flow regime observed for $e = 4$ mm and $e = 2$ mm.....	221

NOMENCLATURE

Latin letters

A	sectional area	m^2
b	experimental design coefficient	
C	drag coefficient	
C _p	specific heat capacity	$J.kg^{-1}.K^{-1}$
D	bubble diameter	m
d	distance	m
F	force	N
e	channel thickness	m
E _f	formation energy	N
f	frequency	Hz
g	gravity acceleration	$\approx 9.8 m.s^{-2}$
	free enthalpy	$kJ.kg^{-1}$
G	mass velocity	$kg.m^{-2}.s$
h	enthalpy	$J.kg^{-1}$
	heat transfer coefficient	$W.m^{-2}$
H	height	m
h _{cg}	height of the center of gravity	m
h _l	height of the liquid level	m
K	overall heat transfer coefficient	$W.m^{-2}.K^{-1}$
k _B	Boltzmann's constant	$\approx 1.38.10^{-23} J.K^{-1}$
L _c	capillary length	m
M	molar mass	$kg.kmol^{-1}$
\dot{m}	mass flow rate	$kg.m^{-3}$
n	number of molecules	mol
P	pressure	kPa
\dot{Q}	heat flux	W
\dot{q}	heat flux density	$W.m^{-2}$
R	radius	m
R _{cav}	radius of the nucleation site	m
S	entropy	$J.K^{-1}$
	exchange area	m^2
T	temperature	K
t	time	s
u	velocity	$m.s^{-1}$
V	volume	m^3
v	specific volume	$m^3.kg^{-1}$
W	width	m
\dot{W}_{elec}	electrical power	W
x	vapor quality	
X	centered factor	
	mass fraction	

Nomenclature

Y	response	
z	depth	m

Greek letters

α	angle	rad
	thermal diffusivity	$\text{m}^2 \cdot \text{s}^{-1}$
β	thermal expansion coefficient	K^{-1}
ϕ	diameter	m
δ	liquid film thickness	m
δ_{th}	thermal boundary layer	m
ε	void fraction	
Γ	dimensionless flow rate per unit perimeter	
λ	thermal conductivity	$\text{W} \cdot \text{m}^{-1} \cdot \text{K}^{-1}$
μ	dynamic viscosity	$\text{kg} \cdot \text{m}^{-1} \cdot \text{s}^{-1}$
μ_c	chemical potential	$\text{J} \cdot \text{mol}^{-1}$
ρ	density	$\text{kg} \cdot \text{m}^{-3}$
σ	surface tension	$\text{N} \cdot \text{m}^{-1}$
θ	contact angle	rad
ν	kinematic viscosity	$\text{m}^2 \cdot \text{s}^{-1}$
φ	phase	

Subscripts

abs	relative to the absorber
adim	dimensionless
att	relative to the waiting time
b	relative to the bubble growth
B	relative to the bubble
	relative to thermostatic bath
buoy	buoyancy
c	critical
cv	convective
Cu	relative to copper
cond	relative to the condenser
cool	cooling
crit	relative to the critical heat flux
d	at the detachment or departure
D	drag
des	desorption
eq	equivalent
ev	relative to the evaporator
f	relative to the coldest source
	frictional
fs	relative to the secondary fluid
g	gravitational
h	hydraulic
in	relative to the inlet

inst	instantaneous
int	relative to intermediate source
i	relative to the factor i
l	relative to the liquid phase
LI	liquid inertia
LiBr	relative to Lithium Bromide solution
M	Marangoni
min	minimum
nb	nucleate boiling
out	relative to the outlet
proj	projected
pump	relative to the pump
refr	relative to the refrigerant
rej	rejected
sat	saturation
sc	relative to the warmest source
sub	subcooling
th	thermal
	theoretical
v	relative to the vapour phase
w	wall
wet	relative to wetted area
x	at the location x
$ _0$	central point of the experimental design
∞	far field

Superscripts

*	centered value at the nucleation site level
c	setting value
fs	secondary fluid

Dimensionless numbers

Bo	Bond number
	Boiling number
Eö	Eötvös number
Fr	Froude number
I _R	Robinson and Judd criterion
Ja	Jacob number
Nu	Nusselt number
Pr	Prandtl number
Re	Reynolds number
St	Stephan number
We	Weber number
δ^+	Dimensionless thickness

INTRODUCTION

According to numerous studies (ADEME, CERN, CENERG, etc.), air-conditioning systems market is an important and still growing market. In 2011, the world market for air conditioning was valued at US\$ 88.2 billion compared to US\$ 55 billion in 2006 (i.e. an increase by 60 % - Seiler *et al.*, 2013). This fad for air conditioning system has as a consequence an increased of the consumption of electrical energy that was estimated to 22 TWh in 2005 in Europe (Grignon-Massé, 2010). This amount of energy consumed for space cooling and refrigeration accounted for 24.8 % of the total energy consumption in the United States for commercial and residential building (Brown and Domanski, 2014) and for 23.3 % of household electrical consumption in France in 2008 (ENERTECH/CEREN). These numbers probably have increased nowadays as more and more buildings are equipped with air-conditioning systems due to the increase of thermal loads, living standards and occupant comfort demands (Henning, 2007).

This high electrical consumption is mainly due to the dominant position in this market of vapor compression equipment as it presents the three following advantages: low cost, higher efficiency and good personal safety record (Grignon-Massé, 2010). To a lesser extent, pollution, green house effect, presence of several air-cooling systems at a given location (block of flats) participate to the increase of the ambient temperature (heat island effect) and thus to the increase of the energy consumption for cooling.

Among this large amount of electrical energy consumption worldwide, the commonly air-conditioning (AC) systems commercialized by the manufacturers consist in classical compression refrigeration cycle using halogenated alkanes or hydrofluorocarbons (HFCs) as refrigerants. These fluids contribute to greenhouse effect and global climate change. This technology of AC systems is not only used for commercial and residential building but it also commonly used for mobile air-conditioning. In 2003, the quantity of R134a estimated to be released into the atmosphere, per year and per car equipped with AC system, amounted to 93g (ADEME, 2003). This could be equivalent to an extra carbon dioxide emission of 10 g.km^{-1} for a car travelling 12 000 km per year (Goulet, 2011). These leaks of refrigerant to the atmosphere must be added to the release of extra pollutant emissions due to the extra fuel consumption that AC system engenders. This extra fuel consumption is estimated to be of 31 % for urban route and 16 % for extra urban driving (INRETS, 2007 cited by Goulet, 2011).

Due to these observations and as environmental regulations involving gas emissions, nature of refrigerants, electricity consumption (and more generally energy consumptions) becomes increasingly restrictive, air-conditioning systems requiring less electrical power and using environmentally friendly refrigerant should be considered.

In this context, sorption systems seem to be a good alternative to vapor compression equipment as the major part of their power energy needed to operate is provided by thermal energy. This thermal energy can be supplied by exhausted gas, solar energy and waste energy in general. Another advantage of these systems is the use of natural fluid, fluid with low GWP (Global Warming Potential) and zero-

ODP (Ozone Depletion Potential), such as ammonia or water¹. Using water as refrigerant presents also the advantage to use a non toxic fluid and an almost endless resource.

Absorption chillers represent already a large fraction of chillers sold in Japan and China (Brown and Domanski, 2014). They also are already the content of many patents especially in mobile systems for which a regulation for air-conditioning systems will be effective in 2020 (Zur and Shechtman, 1995; Miskimin and Edberg, 1998; Boudard and Bruzzo, 2009). These systems will probably continue to be used and expand into applications where management of peak electricity demand is important, for which sources of waste heat are readily available or in solar applications (Brown and Domanski, 2014). However, unless the cost mix of primary energy significantly increases, absorption and adsorption cooling will retain a small share in most markets due to their investment cost, their size and their weight, especially for low cooling capacity. Indeed, in 2008, for a cooling capacity below 17.5 kW, the cost of a “split” system was equal to 177 €₂₀₀₈.kW⁻¹ whereas the cost of a sorption machines was superior to 1500 €₂₀₀₈.kW⁻¹ (Grignon-Massé, 2010). Makni (2012) compared two air cooling systems, one classical air cooling machine manufactured by Mitsubishi Electric of 14 kW, and an adsorption air-cooling machine manufactured by SorTech AG of 15 kW and found that in the first case the compactness was 0.027 m³.kW⁻¹ and 8.29 kg.kW⁻¹ whereas in the second case the compactness was 0.099 m³.kW⁻¹ and 39.3 kg.kW⁻¹, i.e. around four times heavier and bigger than the conventional air-cooling systems. But, the weight and the size are not only a challenge to be competitive with usual vapor compression system, it is also a big challenge to overcome in order to allow the use of sorption system in cars and more generally in mobile applications.

As, compactness and cost are known to be the two main drawbacks for the development of small cooling power sorption systems, the design of such machines must be optimized. Apart from those dedicated to sorption (absorber, generator, etc.), evaporator is the other component which needs to be improved. Thus, compact evaporator like plate-type heat exchangers can play a significant role in reducing the investment cost of low cooling power sorption systems. But, although compact heat exchanger has been pointed out as a key factor to allow the development of these systems, the studies remain scarce so far (Schnabel *et al.*, 2008, Estiot *et al.*, 2008, Clause *et al.*, 2011). Knowledge on heat transfer phenomena and geometry at operating pressure usually encountered in sorption chiller (i.e. around 1.2 kPa at the evaporator for sorption systems using water as refrigerant) is insufficient and thus, the design of evaporators mainly remains empirical. In consequence their geometry is not optimized for such operating conditions.

Due to the current lack of data and characterization of evaporation at low pressure, the objective of this PhD thesis is to go further in the understanding of phenomena occurring in compact evaporator either from a fundamental point of view than from an applicative point of view. In that goal, two experimental test setups were designed and built. They allow the observation of the water behavior at subatmospheric pressure at the bubble scale and at the scale of the evaporator. Such an experimental strategy has been set up in order to achieve the following objectives:

- To characterize the influence of the pressure on the heat transfer coefficient and on the bubble dynamics.
- To identify the driving parameters influencing plate heat-exchangers performances when used as evaporator in sorption chiller using water as refrigerant.

¹ The ODP and GWP of water and ammonia are equal to 0 whereas the GWP of the R134a, often used as reference, is equal to 1430 kg_{CO2}.kg⁻¹.

Works conducted to achieve these objectives are reported in this present thesis. This manuscript is divided into five chapters with several appendices:

- Chapter 1 reviews current low pressure evaporators used in industrial processes and introduces fundamental concepts that are necessary to understand the results presented.
- Chapter 2 presents the experimental test facility used to study the influence of the pressure on the heat transfer coefficient and on the bubble dynamics at the bubble scale. It also presents results obtained when studying pool boiling of water on a horizontal plane surface of copper of 19.6 cm² at subatmospheric pressure.
- Chapter 3 focuses on results obtained under the same conditions but for vertical orientation. The influence of the confinement on heat transfer achieved and on boiling regime observed is also discussed.
- Chapter 4 presents results obtained when studying the vaporization of water inside the channel of an evaporator of standard dimension. The experimental setup used is introduced. Flow regimes and heat transfer coefficients observed are analyzed and discussed. Preliminary studies for dimensioning such evaporator are also investigated.
- Chapter 5 presents a track for futures researches after the present study. Preliminary results obtained by studying boiling in a liquid layer whose height is lower than the bubble departure diameter are introduced.

1 LITERATURE REVIEW

The objective of this section is to provide the necessary information to understand the background of results presented in this work. The first part of this section is dedicated to the comprehension of absorption system (section 1.1). Then, the review focuses on evaporators used in these systems. After introducing subatmospheric evaporators usually encountered in industrial processes, the unusual behavior of these one is highlighted (section 1.2). The four other parts are dedicated to the understanding of mechanisms involved in these evaporators: the generation of a bubble in a free (section 1.3) or in a confined space (section 1.4), in the absence or in the presence of a flow rate (section 1.5) and the falling film evaporation (section 1.6).

1.1 Absorption cooling machines

Liquid adsorption uses the ability of some fluids to absorb (exothermic reaction) or desorb (endothermic reaction) a vapor phase. The solubility of the vapor phase inside the liquid phase depends on the pressure and temperature of the system.

This ability of some fluids to absorb or desorb a vapor phase is used in absorption system. The condenser, the evaporator and the valve are common to both cycles and only the refrigerant circulates inside. The only differences lies in the fact that the mechanical compressor is replaced by a chemical part (composed by an absorber and a desorber) coupled with a liquid pump and that the working fluid in this part is a solution of two constituents where one constituent is more volatile than the other. The more volatile constituent is used as refrigerant (Fig 1.1).

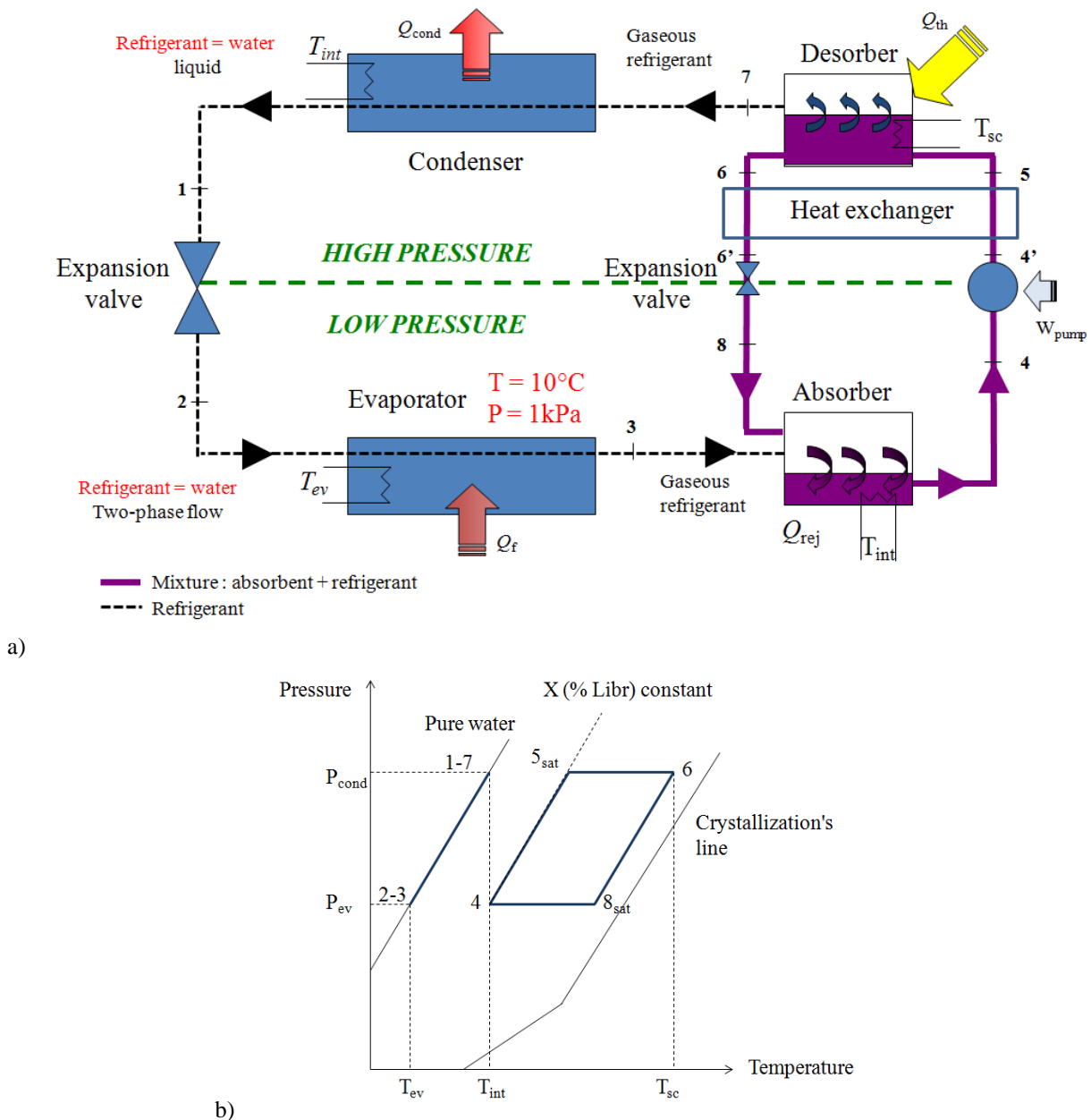


Figure 1.1: Schematic of a) a single-effect H₂O/LiBr absorption machine cycle and b) the Dühring diagram associated

The vapor flows from the evaporator to the absorber. Here, the vapor is absorbed by the weak solution coming from the desorber. As this reaction is exothermic, the heat produced by this reaction of absorption is removed thanks to a transfer fluid at a temperature T_{int} . At the outlet of the absorber, the solution thus rich in water is pumped to the desorber. The solution is then heated by a fluid which circulates at a temperature T_{sc} . This implies the desorption of a part of the refrigerant trapped in the solution. The vapor then flows to the condenser whereas the solution now poor in water goes back to the absorber. At the condenser, the vapor condenses into liquid. During this exothermic step, heat (Q_{cond}) is removed to the heat sink at a temperature T_{int} . The temperature T_{int} imposes the temperature of condensation of the fluid and thus the higher pressure of the cycle. Then the refrigerant passes through the valve and goes back to the evaporator. As the refrigerant is expanded through a valve, the fluid might enter the evaporator with a given void fraction depending on the subcooling at the condenser outlet. The temperature of evaporation of the liquid phase (T_{ev}) imposes the low pressure of the cycle.

The use of absorption machines rises two points:

- 1) As mentioned above, since the solution is liquid, a liquid pump is used to bring the fluid pressure from the low pressure (P_{ev}) to the high pressure (P_{cond}). The amount of energy thus required is much smaller than the energy required for the same evolution at the vapor state, like it is the case in the classical vapor compression system.
- 2) Working with water as refrigerant implies the following constraint:
 - First, since the triple point of water is reached at 611 Pa and 0 °C, couple as H₂O/LiBr cannot be used for applications which required working at temperature below 0 °C. This pair is thus mainly used for air-conditioning systems.
 - Second, air-conditioning refrigeration implies using refrigerant at a temperature of around 10 °C. For water, this implies a working pressure at the evaporator of 1 kPa (10 mbar). If water condenses at 35 °C, the high pressure would reach 5.6 kPa (56 mbar) which is still a pressure relatively low compared to usual working pressures for refrigeration. Problems of gas tightness and maintenance could be encountered. Moreover, in relation with the low pressure in the system, the pressure drop could rapidly lead to a decrease of the performance of the machine as it would induce a noticeable decrease of the saturation temperature (cf. section 1.2.2.3.).
 - Third, as the temperature increases, the solubility of lithium bromide inside the water decreases. Hence there is a risk of fouling because of LiBr crystallization.

To compare the performance of refrigeration systems, the common tool used is a first law-based efficiency named the Coefficient of Performance (COP). In the case of absorption systems the COP is thus:

$$COP = \frac{Q_f}{W_{pump} + Q_{th}} \quad (1.1)$$

According to Henning (2007), under normal operations (i.e. driving heat temperature of 80-100 °C) and for a system using the solution H₂O/LiBr, a COP of around 0.7 could be achieved.

A higher efficiency could be reached using double-effect cycle (Fig. 1.2). These systems use two generators in series working at different temperatures. The cycle is described in the Fig. 1.2. Chillers using such cycle are available and permit to achieve a COP in range of 1.1-1.2. However, driving temperatures in the range of 140-160 °C are required for those chillers.

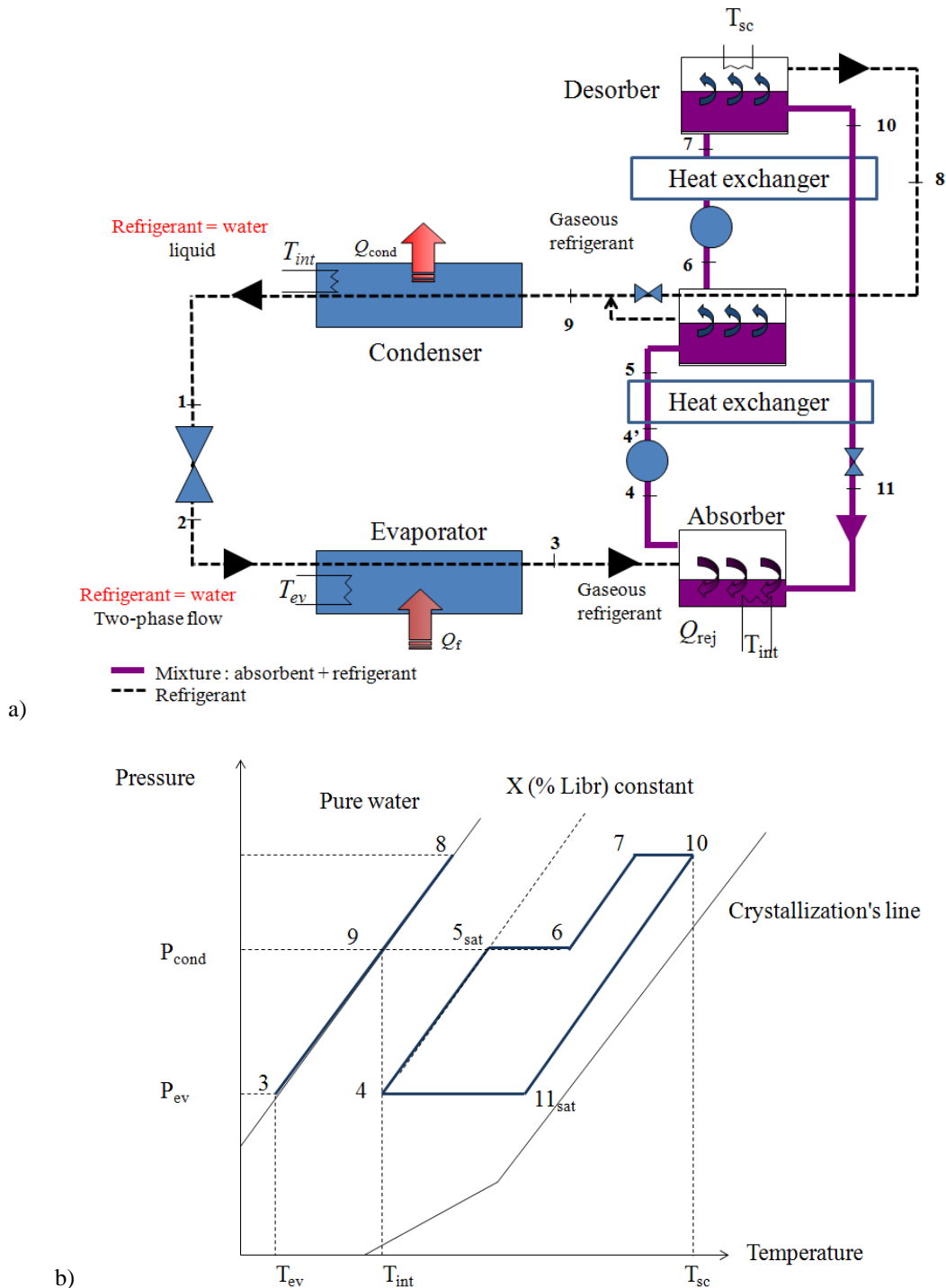


Figure 1.2: Schematic of a) a double- effect H₂O/LiBr absorption machine cycle and b) the Dühring diagram associated

Many others cycles were designed but still remain combinations of elementary cycle (Niebergall, 1959 cited by Ziegler, 2014). Such cycles improve the efficiency but also the temperature lift and, as more

components are needed, increase the total cost of the system. The cheapest absorption chiller designable is thus an elementary cycle running ideally with low cold source and intermediate temperatures and a high driving temperature. As a small change in temperatures impacts strongly the power density, the best way to improve the performance of existing systems is to improve the heat and the mass transfer (Ziegler, 2014). According to Ziegler (2014), no major improvement could come from the fluid as, unless finding a fluid contradicting Trouton's rule² and thus allowing the reshape of isotherms, water is the fluid having the lowest ratio heat capacity versus latent heat of vaporization. Indeed at a temperature of 10 °C, this ratio is 2.25 higher for ammonia than for water. His demonstration lies in the fact that the COP could be written as a function of the Stephan number.

$$\text{COP} = \frac{q_{\text{ev}}}{q_{\text{des}} + q_{\text{sub}}} = \frac{\Delta h_{\text{lv}} (1 - \text{St}_{\text{ev}})}{f(\text{St}_{\text{sub}}, \text{St}_{\text{poor}})} \quad (1.2)$$

With

$$\text{St} = \frac{C_{p1} \Delta T}{\Delta h_{\text{lv}}} \quad (1.3)$$

This function is minimal when the Stephan number is minimal and so, when the heat capacity is low and the latent heat of vaporization is high.

Water is thus one of the best fluids to use as refrigerant in sorption systems in addition to the fact that it is a natural fluid. However using this refrigerant requires working at operating pressure close to 1 kPa in the evaporator. At such low pressure range, working with water could significantly affect the evaporator behavior as:

- The vapor density is low. This could result in:
 - high velocity vapor stream and consequently high pressure drops
 - the formation of large diameter bubbles with consequently a risk of wall drying out in the evaporator
- The weight of the liquid column height induces a hydrostatic pressure which could be of the same order of magnitude of the free surface saturation pressure. This strongly impacts the saturation temperature inside the liquid column (depending on the operating conditions but typically 3 to 5 K for each 5 cm of liquid column height – Fig. 1.3) and could result in:
 - evaporation failure
 - the impossibility to generate spontaneously a bubble

² Trouton's rule is based on the empirical observation made by Trouton that the standard entropy change of vaporization is the same for most of the fluids. From Clapeyron's equation, this rule imposes that the slope of isotherms is more or less constant, as $\frac{d \ln P}{d(-1/T)} \cong \frac{\Delta h_{\text{lv}}}{R} \cong \frac{T_{\text{sat}} \Delta s}{R}$ with $\Delta s = \text{cst}$.

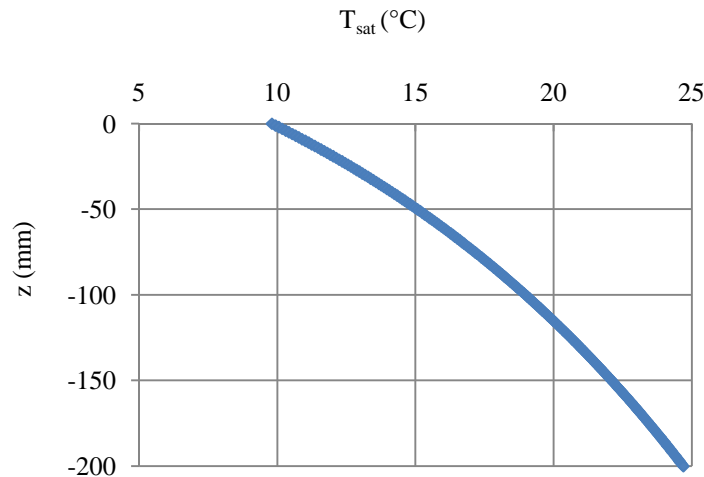


Figure 1.3: Profile of the water saturation temperature along the vertical axis for a vapor saturation pressure of 1.2 kPa ($T_{sat} = 9.7$ °C)

Due to these aspects and the lack of scientific knowledge at subatmospheric pressure, compact heat exchangers operating at low pressure are mainly designed empirically. Their size and cost are thus not optimized although an optimization of their design is necessary to make sorption systems competitive compared to vapor compression systems.

Thus, after introducing low-pressure evaporators used currently in industrial processes, achievement and problems found in the literature regarding the conception of compact evaporators are introduced.

1.2 Low pressure evaporators

1.2.1 Technology survey

Subatmospheric pressure evaporators are mainly used in three areas: air cooling refrigeration, electrical component cooling and desalination process. In order to avoid evaporator failure, these evaporators are often flooded heat exchangers or falling film heat exchangers. Capillary effect heat exchangers are also often encountered as they allow to achieve higher heat transfer coefficients.

The flooded evaporators studied by Rahman *et al.* (2003) and used for a desalination process are shell and tubes heat exchangers (Fig. 1.4). The working fluid enters at a temperature of 30 °C and flows vertically upward inside the tubes of the evaporator. Hot water maintained at a temperature of 53 °C flows in countercurrent outside the tube. Only a part of the feed water is evaporated. A blowdown pump recirculates the remaining water that is not evaporated. The cooling power obtained with this heat exchanger is 91.8 kW for a heat exchanger of 0.5 m high and 0.4 outer diameter. The power density is thus 1461 kW.m⁻³ and the power-weight ratio 5.19 kW.kg⁻¹. The working pressure is 8 kPa.

Capillary assisted evaporators could be of each type of heat exchangers as long as capillary patterns are manufactured or stuck on the operating area (Fig. 1.5).

These structures foster the evaporation of the fluid as the capillary forces induce a motion of the fluid which then covers the operating surface. A liquid film is thus created and vaporized around the operating surface. Several studies on capillary assisted evaporators could be found in the literature:

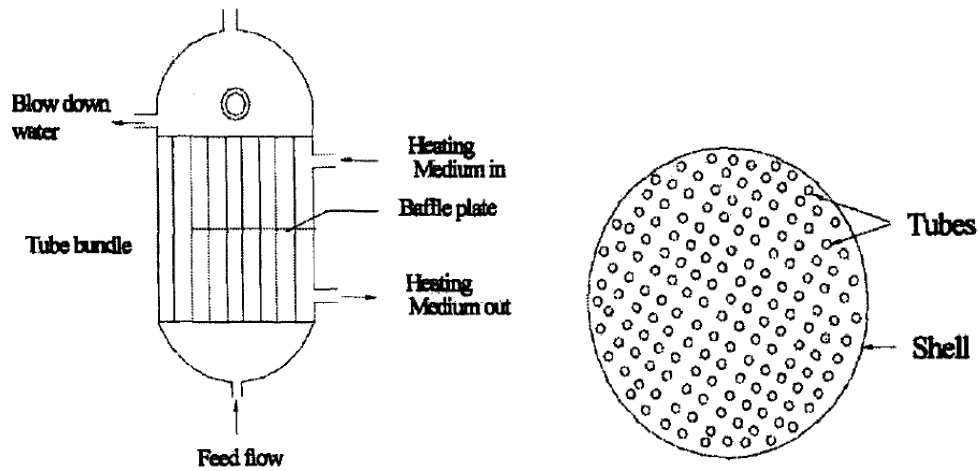


Figure 1.4: Schematic of principle of shell and tubes evaporator

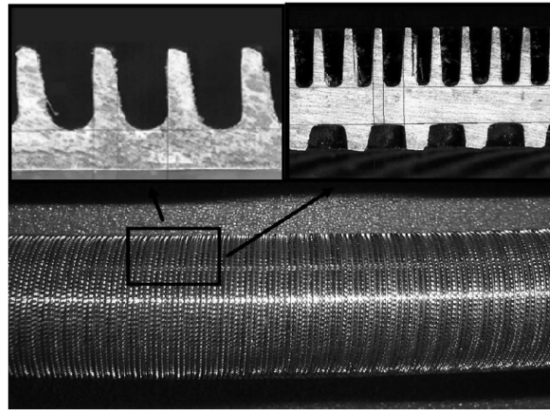


Figure 1.5: Example of capillary structure (micro-fin-structured tube) (Schnabel *et al.*, 2011)

- Sabir and Bwalya (2002) and Sabir and Elhag (2007): In the heat exchanger described in their papers, channels are manufactured on the internal surface of tubes. Both are made with copper and are water to air heat exchanger. In the first paper, the operating pressure is set at 1.65 kPa and the cooling capacity achieved is 0.7 kW for a volume of 0.042 m³. In the second case, the operating pressure is set at 1.45 kPa and the power ranges from 0.5 to 1.6 kW. The power density is thus 17 kW.m⁻³ and the power-weight ratio 0.20 kW.kg⁻¹ in the first case whereas a power density of 38 kW.m⁻³ and a power-weight ratio is 0.25 kW.kg⁻¹ are achieved in the second case.
- Schnabel *et al.* (2011): The authors studied the influence of different capillary structures on the outlet surface of 4 tubes of copper of 400 mm long and connected together. The cooling power achieved varies from 400 to 1200 W for a feed water temperature of 15, 18 or 22 °C and saturation pressure ranging from 1.1 to 1.7 kPa. The power density achieved is 200 kW.m⁻³.

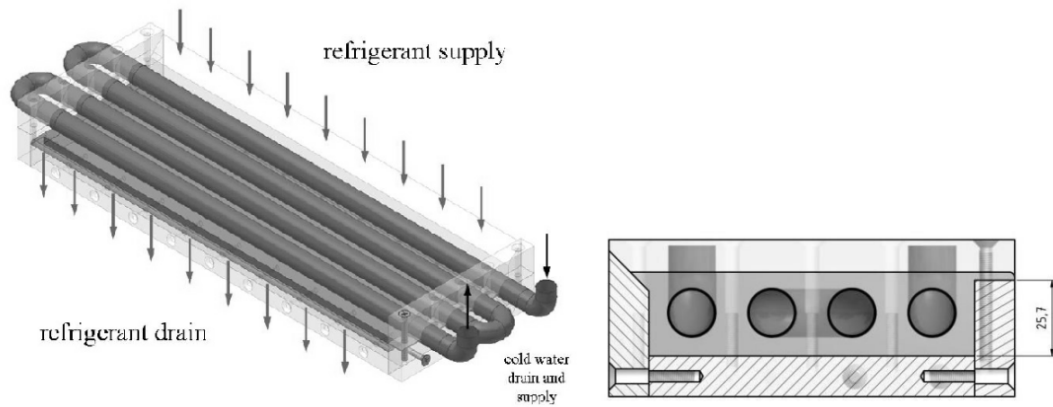


Figure 1.6: Schema of principle of capillary assisted evaporator in pool boiling operation mode used by Schnabel *et al.* (2011)

The last type of evaporator often encountered in subatmospheric process are falling film evaporators. They are commonly encountered in $H_2O/LiBr$ absorption machine. The falling film could be distributed on tubes or on vertical plates. In the first case, the refrigerant could be distributed at the outer surface of tube (Bell *et al.*, 1996, Castro *et al.*, 2008, Florides *et al.*, 2003) or at their inner surface (Morison *et al.*, 2006). The tubes orientation could be horizontal or vertical. A distributor is needed in order to homogeneously distribute the refrigerant.

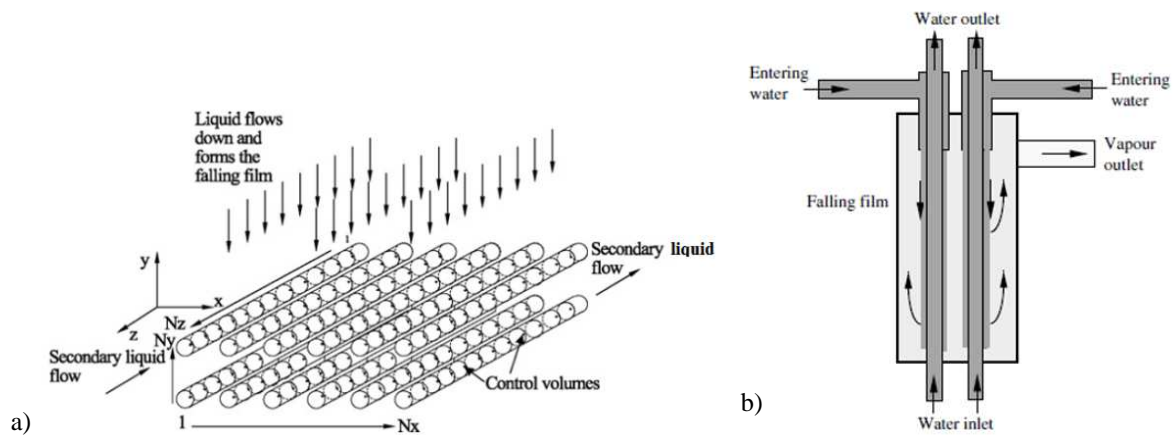


Figure 1.7: Falling film evaporator at the outlet surface of the tube a) in horizontal orientation b) in vertical orientation

Several falling film evaporators could be found in the literature:

- Bell *et al.* (1996): The authors used a copper horizontal U-tube evaporator with fins. The operating pressure is set at 0.87 kPa. The refrigerant is a solution of lithium bromide and the heat transfer fluid is water. The volume of this evaporator is 0.0034 m^3 for a weight of 5.84 kg. The cooling power achieved is not mentioned.



Figure 1.8: Horizontal U-tube falling film evaporator with fins

- Castro *et al.* (2008): The authors study horizontal coil stainless steel evaporators. The achieved cooling power is 2 kW for a power density of 178 kW.m^{-3} and a power-weight ratio of 0.52 kW.kg^{-1} . The refrigerant is a lithium-bromide solution and the heat transfer fluid is air entering at a temperature of $30 \text{ }^\circ\text{C}$. The evaporation pressure is 1 kPa.
- Florides *et al.* (2003): The authors study a falling film evaporator made with copper and placed in vertical orientation. The operating pressure is set at 0.93 kPa. The refrigerant is a solution of lithium bromide entering at a temperature of $13 \text{ }^\circ\text{C}$. The heat transfer fluid is water. The cooling power achieved in this study is 1 kW; the power density is 147 kW.m^{-3} and the power-weight ratio 0.23 kW.kg^{-1} .
- Kim *et al.* (2008) study a falling film evaporator made with vertical stainless steel plates of 90 mm x 540 mm. The cooling power obtained ranges between 0.1 and 0.5 kW. The power densities thus range between 89 and 557 kW.m^{-3} .
- Morison *et al.* (2006): the evaporator studied in this paper is constituted by a single stainless steel tube of 1 m height and 72 mm inner diameter. The fluid is homogeneously distributed at the inner surface of the tube and the vapor create circulate at the center of the tube. The total weight of this evaporator is 16.65 kg and its volume is 0.0041 m^3 .

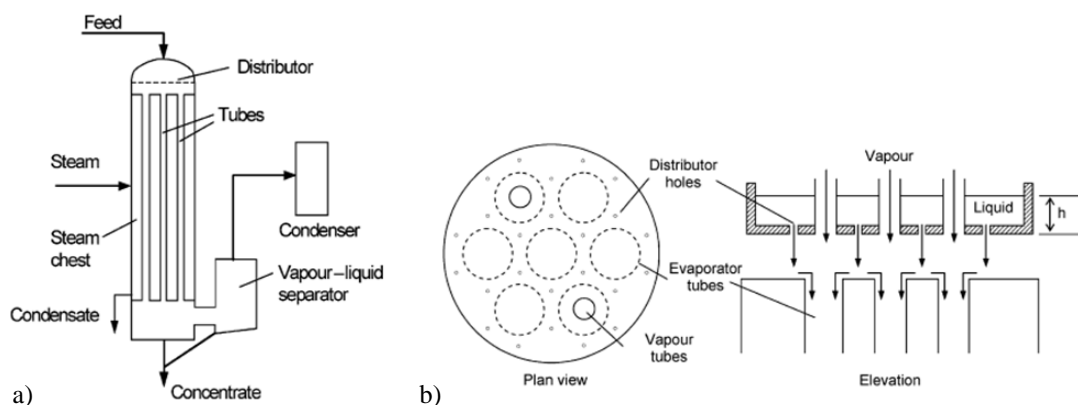


Figure 1.9: falling film evaporator at the inlet of the tube a) global scheme b) operating principle

The performance of the previously mentioned evaporators and their respective technologies are gathered in Table 1.1.

Table 1.1: Evaporators' performance

Authors	Rahman <i>et al.</i> (2003)	Sabir and Bwalya (2002)	Sabir and Elhag (2007)	Schnabel <i>et al.</i> (2011)	Castro <i>et al.</i> (2008)	Florides <i>et al.</i> (2003)	Kim <i>et al.</i> (2008)
Technology	Flooded/ Shell and tubes	Capillary assisted /outer surface of tube	Capillary assisted /outer surface of tube	Capillary assisted /outer surface of tube	Falling film/ coil	Falling film /vertical tubes	Falling film/ vertical plate
Maximal cooling power (kW)	91.8	0.7	1.6	1.2	2	1	0.016
Operating pressure (kPa)	8	1.65	1.46	1.1-1.7	1	0.9	1.5
Volume (m ³)	0.06	0.042	0.042	0.01	0.011	0.0068	0.0009
Weight (kg)	17.69	39.95	6.48	ND	3.84	4.39	ND
Material	aluminium	copper	copper	copper	stainless steel	copper	stainless steel
Refrigerant	H ₂ O	H ₂ O	H ₂ O	H ₂ O	LiBr/ H ₂ O	LiBr/ H ₂ O	LiBr/ H ₂ O
Heat transfer fluid	H ₂ O	air	air	H ₂ O	air	H ₂ O	H ₂ O
Refrigerant temperature (°C)	30	13-15	10-15	ND	6	6	13
Heat transfer fluid temperature (°C)	53	ND	25-30-35	15-22	30	13-11	25- 30
Power density (kW.m ⁻³)	1461	17	38	200	178	147	557
Power-weight ratio (kW.kg ⁻¹)	5.19	0.02	0.25	ND	0.52	0.23	ND

Most of the industrial processes using low pressure evaporators used tubular heat exchangers. However tubular design has limitations in the reduction of size and cost for small absorption chiller. It is thus believed, for a small cooling power, that a plate-type design would allow a more compact and cost-effective machine as the typical area density of a compact plate heat exchanger is in the order of 1000 m².m⁻³ and as it is suitable for automated fabrication. However, plate heat exchanger are rarely used in sorption refrigeration as problems such as the difficulty to wet the whole heat transfer surface, excessive pressure drop due to small hydraulic diameter or distribution problems occurred. As efforts have to be done to optimized subatmospheric evaporator for sorption systems to be competitive, few studies reported some achievements and problems with compact subatmospheric pressure evaporators. Main results of these studies are introduced in the following part.

1.2.2 Compact subatmospheric pressure evaporators

Two main different technologies are studied in order to optimize the size and the cost of subatmospheric evaporators: plate heat exchangers (used as falling film evaporators or used as bubble evaporators) and capillary assisted evaporators (used as flooded evaporators or used as falling film evaporators). As mentioned above, the low operating pressure results on a non-conventional behavior of these evaporators. This behavior is observed whichever the technologies used. Major effects observed on the evaporator behavior are listed thereafter.

1.2.2.1 Effect of the operating pressure

A limitation on the performance of subatmospheric pressure evaporators is the working pressure imposed.

Schnabel *et al.* (2008) studied water boiling on a flooded evaporator of copper on different structured surfaces and for vapor pressure varying between 1 kPa and 2 kPa. They observed that doubling the pressure from 1 kPa to 2 kPa permits to nearly double heat fluxes at the same wall temperature whereas they noted nearly no difference for the calculations. This observation is in agreement with Chang *et al.* (2012) who conducted experiments in an evaporator constituted by a pair of parallel stainless steel plates and also observed that the wall temperature superheat needed to obtain a given heat flux decreases as the pressure increases. According to Xia *et al.* (2008), the increase of the vapor pressure can bring two benefits as this leads to the increase of liquid thermal conductivity and to the decrease of kinetic viscosity and surface tension: one is the increase of evaporation mass flux across the curved liquid-vapor interface; the other is the increase of the liquid flow rate in the evaporation thin film region encountered both in pool boiling evaporator and falling film heat exchanger.

Another way to vary the working pressure is to vary the hydrostatic pressure by varying the filling ratio (Fig. 1.10). The significant influence of the filling ratio on the heat transfer rate is also often mentioned in the literature (Xia *et al.*, 2008, Schnabel *et al.*, 2011, Clausse *et al.*, 2011, Chang *et al.*, 2012, Lanzerath *et al.*, 2014). In flooded evaporators, the filling level strongly influences the evaporation capacity of the evaporator. This observation is partly explained by Xia *et al.* (2008): heat is transferred by natural convection in the part of the tube outside surface under the free liquid surface whereas at the tube outside surface over the free liquid surface heat is transferred by thin film evaporation.

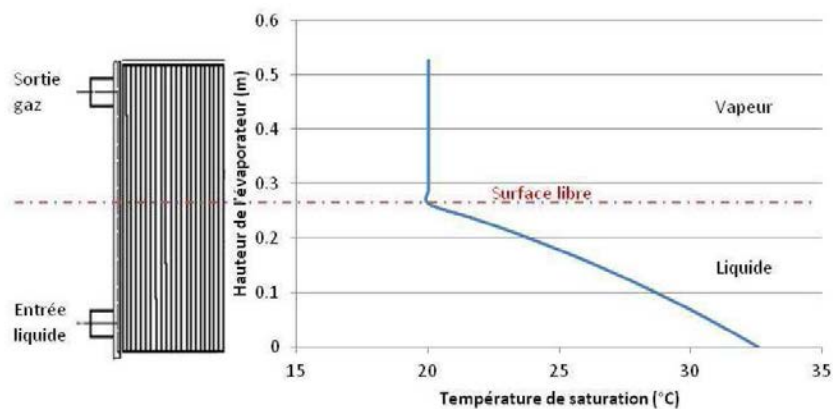


Figure 1.10: Influence of the filling level on the saturation temperature (Leprieur, 2014)

1.2.2.2 Effect of the superheating temperature

A parameter often studied for its influence on the heat transfer is the effect of the superheating temperature. For a given evaporation temperature, a significant influence of the secondary fluid temperature is observed. Rahman *et al.* (2003), observed a significant increase in vapor generation and heat flux as the secondary fluid temperature increases. This observation is in agreement with the observation of Kim and Kang (2003). Lanzerath *et al.* (2014), explained that as a change in the thermophysical properties of water results in a higher Reynolds numbers and thus in an enhancement of the inner heat transfer. Besides, as the viscosity of the fluid is lower at higher pressure and higher temperature, the evaporation is promoted.

1.2.2.3 Effect of the low vapor density

The particularities of subatmospheric water vaporization are mainly due to the variation of water thermophysical properties in this range of pressure and more specifically to the low vapor density ($\rho_v = 0.0092 \text{ kg.m}^{-3}$ at 1.2 kPa and $\rho_l = 999.68 \text{ kg.m}^{-3}$).

Due to the low vapor density, high velocities of vapor stream are usually reached and thus high pressure drops are observed. At such low pressure, the resulting pressure drops have a significant influence on the evaporator performance and on the performance of the machine since a small decrease of the saturation pressure induces a significant decrease of the saturation temperature. This is all the more significant that the pressure is low. As an example, a pressure drop of 0.4 kPa at 1.2 kPa induces a decrease of the saturation temperature of 5.9 K. This same pressure drops at 5 kPa will leads to a decrease of the saturation temperature of 1.5 K (Fig. 1.11).

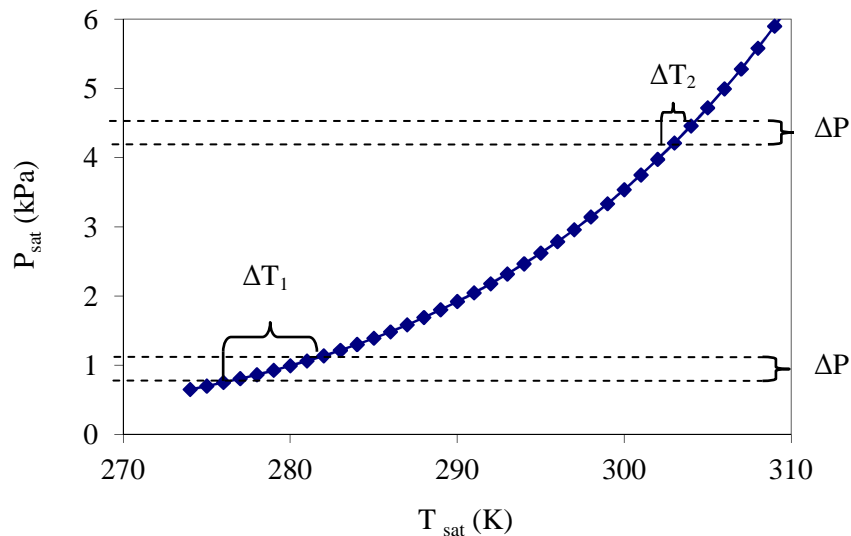


Figure 1.11: Evolution of the saturation pressure with the saturation temperature for water

The high velocity vapor flow generated could also, in some configurations, interact with the countercurrent liquid flow (falling film, two-phase thermosyphon, etc.) leading to high drag flow instabilities. Golobic and Gaspersic (1997), studying a method for the prediction of performance limit in a two-phase closed thermosyphon, have noticed a decrease of the maximum heat flux achieved with the increase of pipe length-to-diameter ratio due to these flow instabilities.

The low vapor density also allows the creation of bubble with centimeter size (Van Stralen *et al.*, 1975, Rullière *et al.*, 2012). During their experiments on flooded evaporators, Schnabel *et al.* (2008)

observed bubbles with diameters ranging between 40 mm to 60 mm. Clausse *et al.* (2011) used an industrial plate heat exchanger for which it was not possible to observe boiling phenomena but they noted that a too high secondary fluid temperature decreases the evaporator performance. This might be due to a dry out caused by the presence of a bubble of centimeter size in a channel of millimeter size. Another effect of the creation of such large bubbles in a very short time is the difficulty to maintain a stable refrigerant flow (Goulet, 2011).

1.2.2.4 Effect of the feed fluid flow rate

Few studies focus on this issue probably because of the difficulty to maintain a constant and stable refrigerant flow. However it is interesting to notice that Rahman *et al.* (2003) observed that the vapor generation decreased significantly with the increasing of the feed water flow rate. They observed that the evaporation takes place at a greater distance from the inlet of the tube with the increase of the feed water flow rate. As there is an increase of the single-phase region inside the tube, the inside heat transfer coefficient as well as overall heat transfer coefficient decrease.

1.2.2.5 Effect of the boiling regime

Chang *et al.* (2012) studied the performance and the behavior of an evaporator constituted by a pair of parallel stainless steel plates of 138 x 20.8 mm² each with channels of 10 mm. This evaporator was inserted in a two-phase thermosyphon loop. The pressure varied between 2.1 kPa and 66.2 kPa. During their experiments, they observed the occurrence of a periodic regime which led to three distinct flow regions with various heat transfer properties. This boiling regime is characterized by the periodical growth of a bubble at a nucleation site. Once the buoyancy force overcomes the surface tension, the bubbles escape from the nucleation site and continue expanding during their rise. When such an elongated bubble then surges out of the liquid, the liquid film that encapsulated the bubble is spread onto the evaporator wall above the liquid level. The splashed liquid droplets evolve into a liquid film above the newly formed liquid level and an evaporation process takes place (Fig. 1.12). This cycle is repeated in a periodical manner. The author noticed that during the cycle almost 44 % of the time is characterized by boiling activities and 56 % of the time is characterized by waiting time.

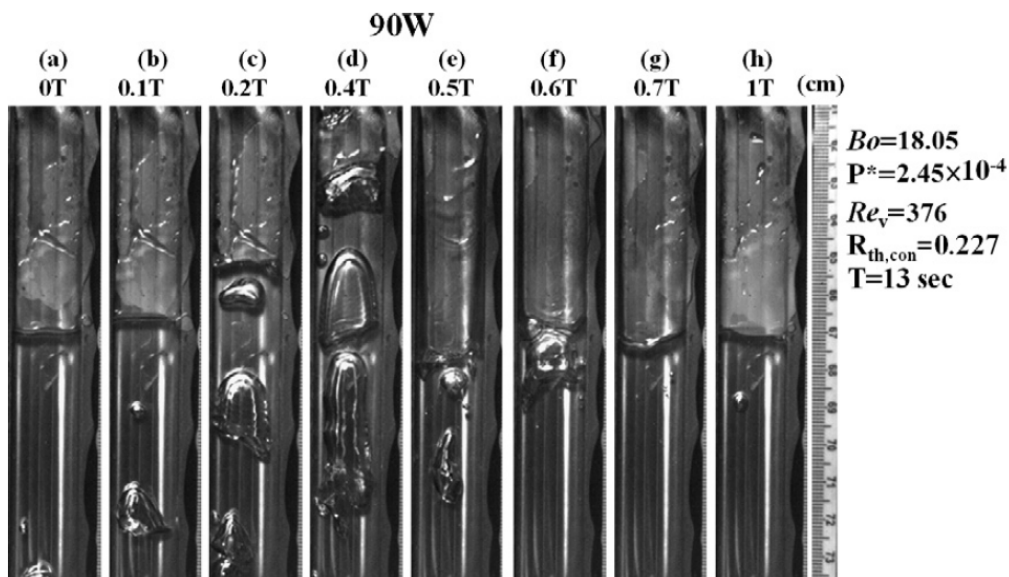


Figure 1.12: Consecutive snapshots obtained by Chang *et al.* (2012) over an entire cycle

Three distinct zones of flow region were identified: a pool boiling region above the free liquid surface, an intermittent region where the liquid oscillates and a vapor region. Empirical correlations were developed for these three zones (Eq. 1.4 to 1.6). Wall temperature fluctuations were detected on each of these zones.

$$h_{\text{Pool Boiling region}} = (1.951 \times 10^6 \dot{q}^{-0.26}) P^{0.508 - 5.9 \times 10^{-6} \dot{q}} \quad (1.4)$$

$$h_{\text{Intermittent Region}} = (2 \times 10^6 \dot{q}^{-0.325}) P^{0.449 - 7.08 \times 10^{-6} \dot{q}} \quad (1.5)$$

$$h_{\text{Vapor Region}} = (2 \times 06.10^6 \dot{q}^{-0.412}) P^{0.441 - 7.08 \times 10^{-6} \dot{q}} \quad (1.6)$$

P^* is the dimensionless evaporator pressure defined as the ratio of the evaporation pressure to the critical pressure of the working fluid and \dot{q} the heat flux density.

In spite of their practical interest, such studies remains scarce and many problems still need to be solved. The reported works highlight a high sensitivity of the evaporator performance to operating conditions (operating pressure, secondary fluid temperature, filling level, etc.) as well as the difficulties to obtain stable conditions (observation of cycling boiling regime, difficulty to maintain a constant feed flow). Moreover, few studies focused on phase-change phenomena occurring inside these evaporators (boiling and falling film evaporation) despite the observation of evaporation failure. A better knowledge on these points thus seems important to acquire in order to be able to design optimized subatmospheric evaporators.

The next parts of this chapter are therefore dedicated to the understanding of these phenomena, i.e. at the understanding of the two-phase flow phenomena that may occur at the evaporator, at the generation of the first bubble and at the falling film evaporation process. These points are based on the observation of Chang *et al.* (2012): a bubble needs to be generated to induce a vapor flow by evaporation. Due to the size of bubbles observed at such low pressure, the boiling phenomena occurring in confined space have to be as well understood. This will bring us to give some background information on free boiling phenomena, boiling in narrow space, fundamentals of flow boiling and finally falling film evaporation.

1.3 Free boiling phenomena

1.3.1 Nucleation

1.3.1.1 Liquid-vapor phase change

In a Pressure, Volume, Temperature diagram of a pure substance, different areas are represented. These different areas represent the conditions for the compound to be a solid, a liquid, a vapor or be at the equilibrium between two phases. The curve which represents the border of two-phase region is called the binodal curve. Fig. 1.13 is a Clapeyron diagram of the liquid-vapor region of a fluid.

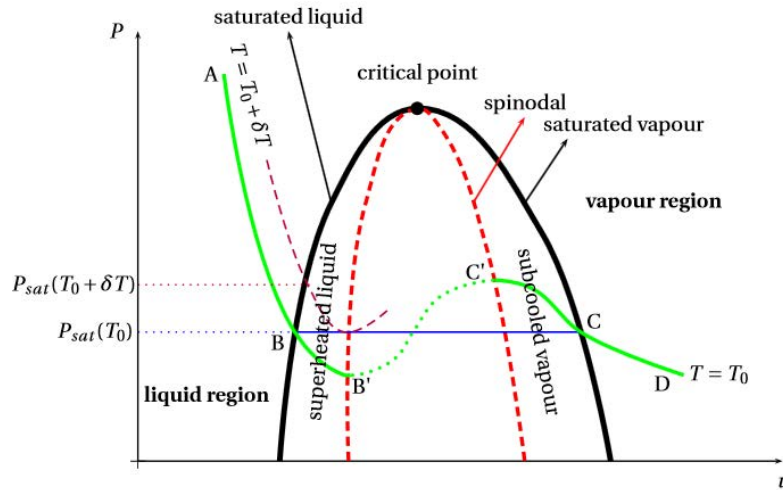


Figure 1.13: Clapeyron diagram (Siedel, 2012)

The fluid is at a stable liquid state between A and B along the isotherm curve. It is at a stable vapor state between C and D. In the first case one would say that the liquid is subcooled. In the second case the vapor is superheated. On the straight line between B and C, liquid and vapor phases coexist in stable thermodynamics equilibrium. The amount of vapor compared to the amount of liquid could be calculated. As the pressure is uniform in the two phases, the liquid-vapor interface is a flat interface.

These represent conditions of existences of vapor, liquid or both states in a thermodynamic equilibrium. Other states of liquid or vapor can exist. For a given temperature, the volume of the saturated liquid phase can be increased from B to B' (this leads to a decrease of the pressure) without any phase change. The liquid is at a metastable state. The same phenomenon appears for the vapor phase between C and C'. Here again, the vapor is at a metastable state. However, these metastable states are limited by the spinodal curve (dashed line in Fig. 1.13). Liquid and vapor spinodal curves represent respectively the minimum and maximum of each isotherm where a single phase state could exist.

A metastable fluid can change of phase. This is typically what could happen when considering a heating transformation at a constant bulk pressure of $P = P_{sat}(T_0)$. Vapor and liquid phases will coexist and be at the same temperature. The liquid is thus superheated. The pressure in each phase will however be different. The liquid will be at bulk pressure $P_{sat}(T_0)$ and the vapor will be at a higher pressure $P_{sat}(T_0 + dT)$ corresponding to the saturation pressure of its temperature. A radius curvature will be observed at the liquid-vapor interface in order to balance mechanical forces acting on it. The difference between the two pressures at the interface and the amount of liquid superheat could be determined by thermodynamical concepts.

1.3.1.2 Immersed bubble equilibrium in a liquid

In the following part, a spherical bubble with a volume V , a temperature T_v , a pressure P_v immersed in a liquid at a metastable state and at a temperature T_l and pressure P_l imposed by external conditions is considered.

The Helmholtz free energy of formation of the bubble can be expressed as the difference of energy between the system bubble – liquid and the system liquid without bubble (Papon and Leblond, 1990).

$$\Delta E_f = n_v (\mu_{c,v} - \mu_{c,l}) + (T_v - T_l)S_v - (P_v - P_l)V + A_l \sigma \quad (1.7)$$

With n_v the mol number of fluid in the bubble, $\mu_{c,v}$ and $\mu_{c,l}$ the chemical potential of the vapor and the liquid respectively, S_v the entropy of the bubble and A_i the area of the interface. The immersed bubble is in equilibrium with its environment when the free energy of formation of the bubble is null (i.e. $\Delta E_f = 0$). The realization of this condition leads to the three following equations:

$$\mu_{c,v} = \mu_{c,l} \quad \text{chemical equilibrium} \quad (1.8)$$

$$T_v = T_l \quad \text{thermal equilibrium} \quad (1.9)$$

$$(P_v - P_l) = \frac{2\sigma}{R} \quad \text{mechanical equilibrium (Laplace equation)} \quad (1.10)$$

With R the bubble radius at equilibrium.

Assuming that the chemical equilibrium and the thermal equilibrium are reached, the equation of Helmholtz free energy of bubble formation depends on the value of R . For $R=R_c$, the value of this equation is maximal. This means that an unstable equilibrium is reached. As it corresponds to an unstable equilibrium, this radius is called the critical radius. If the radius R is inferior to R_c , the bubble will condense. On contrary, if the radius R is superior to R_c , the bubble will grow. The growth of the bubble will be then limited by either the liquid inertia (boiling at low pressure, cavitation), the thermal diffusion (boiling in general), the mass diffusion (presence of incondensable), the fluid viscosity. The critical radius could be predicted by the Young-Laplace equation and write as followed:

$$R_c = \frac{2\sigma}{P_{\text{sat}}(T_\infty) - P_\infty} \quad (1.11)$$

This critical radius thus decreases with the liquid superheat and with the bulk liquid pressure.

1.3.1.3 Nucleation theory

Literature distinguishes two kinds of nucleation: the homogeneous nucleation and the heterogeneous nucleation. The homogeneous nucleation refers to the spontaneous growth of a vapor bubble in a metastable liquid. In this metastable liquid, thermal fluctuations occur. Due to these thermal fluctuations, several molecules could join and form a vapor embryo of the size of the equilibrium nucleus. However, the probability of forming a vapor embryo of $1 \mu\text{m}$ (order of magnitude of the critical radius for water at atmospheric pressure) is very small. Moreover, if the liquid pressure is far away from the critical pressure of the fluid, the wall superheat required to create a bubble is typically several hundreds of Kelvin (220.7 K for water at atmospheric pressure), which is more than one order of magnitude above the superheat usually encounter in experiments. In experiments, the onset of boiling is actually usually due to the growth of a vapor nucleus on a solid surface, on particles or on entrapped incondensable gases. This nucleation is then called heterogeneous nucleation.

The heterogeneous nucleation thus requires less energy than the homogeneous nucleation. This is due to the presence of a catalyst and more precisely to the presence of a triple interface between the solid/particles, the liquid and the gas/vapor. The formation energy of the bubble is calculated thermodynamically in the same way as explained in the previous part. The equation thus obtained could be written as the bubble formation energy in homogeneous nucleation multiplied by a function depending on the contact angle at the triple line θ (Bankoff, 1957, Cole, 1974).

$$\Delta E_f(R) = \frac{4\pi R^2}{3} \sigma_{lv} f(\theta) \quad (1.12)$$

With for flat smooth surface:

$$f(\theta) = \frac{2 + 3\cos\theta - \cos^3\theta}{4} \quad (1.13)$$

θ characterizes if the fluid is a wetting fluid or not. It depends on the fluid/wall pair. Usually, the value of θ ranges between 0 and 100 °. If the liquid is completely wetting the solid surface ($\theta = 0$), $f(\theta) = 1$ and the required superheat necessary to nucleate a bubble is identical to the one required in homogeneous nucleation. In theory, if $\theta = 180$ °, $f(\theta) = 0$ and no liquid superheat is required.

In the case of nucleation on natural surface, nucleation occurs in pits or cavities present in the surface. The presence of such cavities facilitates nucleation for two reasons:

- The apparent contact angle is increased as the contact line between the vapor, liquid and solid phase is located within a cavity (Fig. 1.14 - Collier and Thome, 1994).

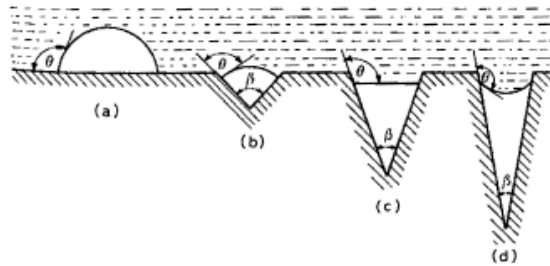


Figure 1.14: Apparent contact angle in conical cavities (Collier and Thome, 1994)

- The presence of cavity allows the presence of entrapped gas or vapor as the liquid does not fill the entire cavity. An ordinary surface is first empty of liquid. When the liquid then moves forward, vapor or liquid will be trapped if the liquid touches the opposite side of the cavity before touching the bottom of the cavity. The superheat needed to nucleate a bubble in such cavities is usually further reduced with respect to the previous case. (Fig. 1.15 – Bankoff, 1958)

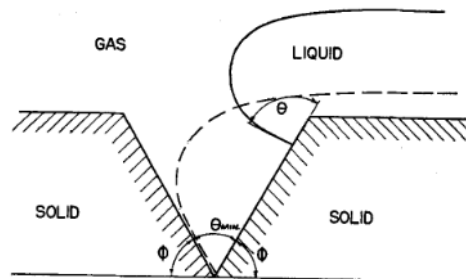


Figure 1.15: Conditions for the entrapment of gas in the advance of a semi infinite liquid sheet by Bankoff (1958)

Actually, when an initially dry wall is wetted, different cases could be observed. The cavity can be wholly overflowed and in that case it will be difficult to activate it. On the contrary, geometrical

conditions of the cavity and/or value of the surface tension can help trap some gas or vapor. This pocket of gas/vapor is then the embryo of vapor needed for the activation of the site and subsequent bubble growth. Once a cavity with entrapped gas is activated, bubbles detach and evacuate slowly the gas until only vapor remains trapped in the cavity.

Several experiments and theoretical studies were conducted to predict the geometrical conditions of a cavity to activate it. It has been shown that the shape and the size of the cavity have a significant influence. For a conical site, only cavities of a narrow range of size are the location of bubble nucleation. Hsu (1962) shows that the cavity radius shall be no less than a minimal radius ($r_{cav\ min}$) and no more than a maximal radius ($r_{cav\ max}$). These two extremes could be calculated as follow:

$$r_{cav,min} = \frac{\delta_{th}}{4} \left[1 - \frac{T_{sat}(P_1) - T_{\infty}}{T_w - T_{\infty}} - \sqrt{\left(1 - \frac{T_{sat}(P_1) - T_{\infty}}{T_w - T_{\infty}}\right)^2 - \frac{12.8\sigma T_{sat}(P_1)}{\Delta h_{lv}\rho_v\delta_{th}(T_w - T_{\infty})}} \right] \quad (1.14)$$

$$r_{cav,max} = \frac{\delta_{th}}{4} \left[1 - \frac{T_{sat}(P_1) - T_{\infty}}{T_w - T_{\infty}} + \sqrt{\left(1 - \frac{T_{sat}(P_1) - T_{\infty}}{T_w - T_{\infty}}\right)^2 - \frac{12.8\sigma T_{sat}(P_1)}{\Delta h_{lv}\rho_v\delta_{th}(T_w - T_{\infty})}} \right] \quad (1.15)$$

At subatmospheric pressure, due to the decreases of the vapor densities and of the saturation temperature with the pressure, less and less activation sites are likely be activated. The difference between the boiling performance on a raw surface and on a polished surface is thus less significant than at atmospheric pressure.

1.3.2 Bubble dynamics

Once a bubble is created, it will grow, detach and then rise in the liquid bulk.

1.3.2.1 Bubble growth

A typical cycle of bubble growth is represented on Fig. 1.16 (Carey, 1992). Just after the departure of a bubble (Fig. 1.16.a), the far field liquid bulk rewets the wall. As the temperature of the surrounding liquid $T_{l,\infty}$ is lower than the wall temperature T_w , an amount of time t_{att} is needed to establish the thermal boundary layer that was destroyed by the departure of the preceding bubble before the next bubble can be created. The heat is transferred by convection and/or transient conduction in the liquid film. Then, the bubble embryo starts to grow, absorbing the energy necessary to the vaporization both from the wall and from the surrounding superheated liquid. At the very first moment of the growth, as the bubble radius is small, surface tension forces are important. According to Lee and Merte (1996), the bubble growth is slow. This growth period is named the delay period. As it lasts less than 1 ms for water at atmospheric pressure, this period of the bubble growth is often negligible and will be neglected in the following description. Then, when the bubble is large enough for inertial forces to control the bubble growth, the bubble growth is accelerated with respect to the growth during the delay period. The radius varies linearly with the growth time. This is the inertial phase of the growth. The growth of the bubble is due to extreme temperature gradients and thus to extreme mass transfer. During the inertial growth, the bubble has a hemispheric shape. Once the inertial growth is finished, the interface temperature decreases as a result of the large amount of heat that was consumed to vaporize the liquid. The growth is slowed down and controlled by heat diffusion from the liquid to the bubble. Surface tension tends to give a spherical shape to the bubble. The increase of the bubble radius follow a law $R \approx t^n$ with n generally equal to 0.5.

This classical description of bubble growth is currently being subject of debate in the scientific community. For example, Siedel *et al.* (2008) observed an evolution closer to $n = 0.2$ than to $n = 0.5$. In addition, in their experiments, as in the classical description of bubble growth, the growth rate is much faster during the initial stage of bubble growth than at the end of the growth.

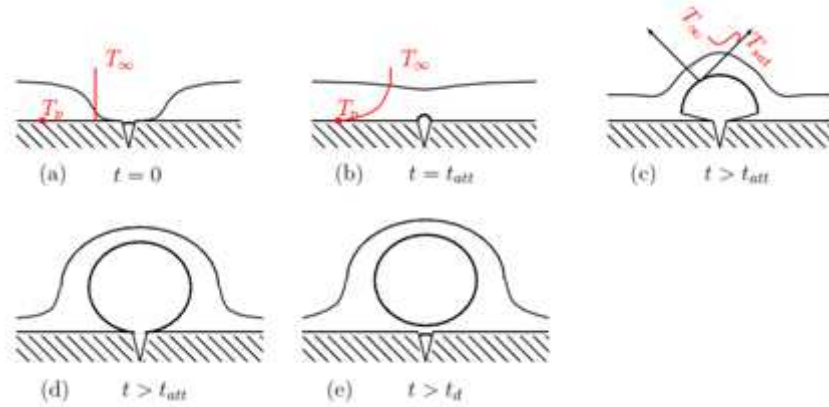


Figure 1.16: Schematic of the bubble growth at the vicinity of a wall by Carey (1992)

The first part of the bubble growth is often proposed to be modeled by the Rayleigh equation. This equation expresses the liquid kinetic energy variation inside the boiling environment. The bubble growth controlled by diffusion can be modeled by a thermal balance at the interface of the bubble. However, the bubble growth is actually much more difficult to comprehend. The shape of the bubble is rarely spherical, the temperature field around the bubble is non-uniform, and several authors mentioned the existence of a thin liquid film between the wall and the vapor called microlayer. The evaporation of this microlayer could actively foster the bubble growth. Several equations could be found in the literature. Some of them do not consider the microlayer (Zuber *et al.*, 1961), others only this one (Copper and Lloyd, 1969), some taking into account the effect of the microlayer and the heat and mass transfer around the bubble (Buyevich and Webbon, 1996). Numerical models with fewer assessments could be also found in the literature (Fujita and Bai, 1997; Son and Dhir, 1998).

1.3.2.2 Bubble cycle at subatmospheric pressure

During the inertial growth, the variation of the bubble radius is proportional to $P^{0.5}$ (mentioned in Ginet, 1999). Thus, the duration of the inertial growth compared to the whole time required for the bubble growth is more significant as the pressure decreases. Moreover, this growth phase is all the more significant when the Jacob number is high. Indeed, a high Jacob number means an intensification of the heat transfer at the top of the bubble (Ginet, 1999). This leads to a quicker growth and thus to the predominance of inertial forces. Based on a ratio of inertia velocity scaling and diffusion velocity scaling, Robinson and Judd (2004) developed a number in order to provide an indication if the bubble growth is inertia-controlled or diffusion-controlled:

$$I_R = \frac{4}{27} \left(\frac{\sigma}{\rho_l \alpha^2} \right) \frac{R_{cav}}{Ja^2} \quad (1.16)$$

With $Ja = \frac{\rho_l C_{p1} (T_w - T_{sat})}{\rho_v \Delta h_{lv}}$. If $I_R \ll 1$, the bubble growth is controlled by inertia; if $I_R \gg 1$, the

bubble growth is controlled by diffusion. In the case of water boiling at subatmospheric pressure, this number is very small compared to 1. The bubble growth is thus controlled by inertia.

This conclusion is confirmed by the pictures obtained by Van Stralen *et al.* (1975) for water at pressure ranging from 2 kPa to 26 kPa. Indeed these pictures show the hemispherical shape expected during the inertial growth. As the bubble growth governed by the thermal diffusion was never reached, the bubble never achieved an almost spherical shape in Van Stralen's experiments. But the shape of the bubble is not the only difference observed on the bubble cycle at subatmospheric pressure. According to these authors, bubbles observed for pressure ranging from 2 kPa to 8 kPa were centimeter size (15.39 cm at 2.04 kPa). Moreover, just after the departure of the large bubble, the growth of a vapor column was observed conferring to the bubble a "mushroom shape" (Fig. 1.17). Similar pictures were obtained by Rullière *et al.* (2012).

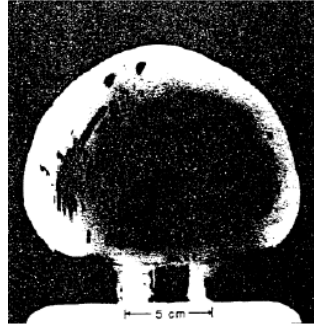


Figure 1.17: Mushroom shape bubble observed by Van Stralen *et al.* (1975) at 2.04 kPa

The behavior of the vapor column conferring to the bubble the "mushroom shape" can be thought to present analogies with cavitation. As a dry spot beneath the center of the growing primary bubble should remain, the local depression increases the superheating at this spot and causes a rapid growth of the secondary bubble. The width of this secondary bubble is limited to the size of the dry spot beneath the primary bubble. This secondary bubble disappears at higher pressure (13 kPa). This can be explained by the diminishing radius of the dry area in combination with the decreasing relative depression in the wake.

Another difference between subatmospheric bubble cycle and usual observation in boiling cycle is the bubble frequency of detachment. The frequency of bubble appearance (f_d) depends on the nucleation site, the heat flux and the diameter of bubble at detachment. During the inertial growth the ratio $f_d d_d$ is constant, with f_d defined as follows:

$$f_d = \frac{1}{t_d - t_{att}} \quad (1.17)$$

During the isobaric growth (other name for the thermal diffusion controlled growth), the ratio $f_d^{1/2} d_d$ is constant. t_d corresponds to the time during which the bubble grows. t_{att} is the waiting time. This latter represents the time between the detachment of the bubble and the beginning of the growth of the succeeding bubble. These times were measured by Cusursuz *et al.* (2001) for an isolated bubble of n-pentane at atmospheric pressure. The waiting time and the growth time measured were around 16 and 330 ms for a wall superheat of 3 K and around 4 and 30 ms for a wall superheat of 7.5 K. As the pressure decreases, both the waiting time and the bubble growth time increase. Van Stralen *et al.* (1975) reported waiting time values between 10 and 100 s at 2 and 4 kPa. McGillis *et al.* (1991a), also studying water pool boiling at subatmospheric pressure, found the same order of magnitude in the same range of pressure. Using the solution for the temperature distribution during the transient conduction of heat into a semi-infinite solid, they developed a correlation valid at such low pressure to estimate the waiting time:

$$t_{\text{att}} = \frac{\pi \lambda_1 \rho_l C_p}{4 \dot{q}^2} \left(\frac{1.6 \sigma T_{\text{sat}}}{R_{\text{cav}} \rho_v \Delta h_{\text{lv}}} + \frac{R_{\text{cav}} \dot{q}}{\lambda_1} \right)^2 \quad (1.18)$$

The increase of the waiting time with the decrease of the pressure could be explained by two phenomena, both due to the decrease of the vapor density:

- the occurrence of large bubbles: when leaving the wall, large bubbles are replaced by a large amount of cold liquid; the larger this amount of liquid, the longer the time required to superheat it during the waiting time.
- an increase in the theoretical wall superheat required for nucleation for a given cavity size. Bubble growth is expected to take place from an active cavity when the surrounding liquid reaches the required superheat. An estimation of superheat required for the onset of nucleation can be obtained from an immediate derivation of the Clausius-Clapeyron equation combined with the expression for the mechanical equilibrium of a vapor bubble:

$$\Delta T_{\text{sat}} = \frac{1.6 \sigma T_w}{R_{\text{cav}} \rho_v \Delta h_{\text{lv}}} \quad (1.19)$$

This increase in the required wall superheat leads to an increase in the required time to superheat the liquid, for a given heat input rate.

According to McGillis *et al.* (1991a), the time for bubble growth could be expressed by the following correlation:

$$t_d = 0.266 P^{-0.565} \quad (1.20)$$

with P in kPa. This correlation is in good agreement with subatmospheric data obtained by McGillis *et al.* (1991a) and Van Stralen *et al.* (1975). Typical bubbles growth times at such low pressure are 50-100 ms (Yagov, 2001).

If the waiting time is greater than the time for bubble growth and release, the boiling is considered as “intermittent”. Significant oscillations in the wall temperature occur. These oscillations are all the more significant as the pressure decreases due to the high superheat required for the onset of the nucleation and the intermittent downwash of cool liquid. Van Stralen *et al.* (1975) recorded wall temperature fluctuations up to 11 K. The local temperature drops simultaneously during the bubble growth and increases again during the succeeding waiting time, i.e during the amount of time required to superheat the liquid in the vicinity of the wall. For the authors, these periodic temperature fluctuations inside the copper (a highly conducting material) are a proof that the so-called “superheating enthalpy” of the microlayer is consumed for the greater part to support the bubble growth. McGillis *et al.* (1991a&b) also observed such fluctuations, but they explained them as a consequence of the liquid motion around the bubble at its departure. The departure of a bubble creates a wake which induces a liquid recirculation and hence a removal of liquid superheated from the surface. The sudden increase in pressure that occurs during the bubble expansion provides an increase in the local saturation temperature which causes an instantaneous subcooling of the liquid (McGillis *et al.*, 1991b). This subcooled liquid then mixes in the wake of the large departing bubble cooling the surface. The wall temperature then increases during the waiting time until a bubble departs. The magnitude of these oscillations depends on the thermal diffusivity of the solid. However, it could be preferable for many applications to avoid these wall temperatures fluctuations and to reach a continuous boiling. The criterion $t_{\text{att}} = t_d$ predicts the transition to this regime. McGillis *et al.* (1991a)

found that at very low pressure a heat flux level of 60 W/cm² is required to produce a departure frequency high enough to maintain continuous boiling and steady wall temperatures. They found good agreement between experiments and heat flux predicted by this criterion.

1.3.2.3 Detachment

The detachment of a bubble partly depends on the balance of forces that act on it. There are two kinds of forces: static forces corresponding to forces applying on the motionless bubble (buoyancy force, contact force, surface tension force, thermocapillary convection) and dynamic forces due to the motion of the bubble (inertial and added mass forces, drags force, lift force). For an axisymmetric bubble, only the vertical component of the force is considered. Only this one is considered thereafter.

- Buoyancy force: The buoyancy force is considered as the resultant of the hydrostatic pressure forces on the bubble surface. It is due to the vertical pressure gradient caused by gravity. If an homogeneous vapor and liquid density is assumed, and if it is assumed that the bubble is fully submerged, the buoyancy force can be written as follow³:

$$F_{\text{buoy}} = (\rho_l - \rho_v)gV_B \quad (1.21)$$

- Contact force: As the bubble is not completely immersed in the liquid but attached to a surface, the buoyancy is actually higher due to the contact area with the surface. Moreover, the vapor pressure being higher than the pressure around the bubble, wall reaction has to be considered. These two effects are included in the contact force. This contact force can be expressed as follow:

$$F_{\text{contact}} = \sigma \left(\frac{1}{R_{1B}} + \frac{1}{R_{2B}} \right) \pi R_B^2 \quad (1.22)$$

With R_{1B} and R_{2B} the two curvatures of the bubble as shown in Fig. 1.18.

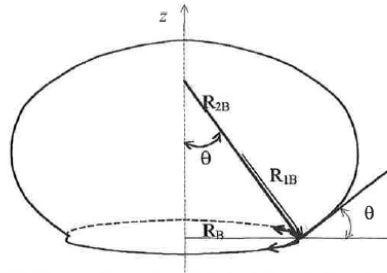


Figure 1.18: Bubble curvature for an axisymmetric bubble by Ginet (1999)

- Triple line surface tension: This force represents the interactions between two molecules of different states. It is governed by the surface tension between the liquid and vapor phases and the wettability of the liquid over the solid surface. It tends to maintain the bubble on the wall. If an axisymmetric bubble is considered, the triple line surface tension can be expressed as follow:

$$F_{\sigma} = -2\pi R_B \sigma \sin\theta \quad (1.23)$$

- Thermocapillary or Marangoni force: This force represents the driving force which allows the movement of the liquid when there is a surface tension gradient. If the surface tension gradient

³ This force can be expressed differently if the calculation starts from an integral momentum balance.

is due to a gradient of concentration, this force is called “Marangoni force”. If this gradient is due to a gradient of temperature, this effect is called thermocapillary force. In the case of a bubble formed on a heated surface, the surface tension gradient is due to the non-homogeneous field of temperature. The liquid is then moved from the base of the bubble to the top of this one.

$$F_M = \int_{s_b} \frac{d\sigma}{dt} \sin\alpha \cdot 2\pi r dx \approx R_B \Delta\sigma \quad (1.24)$$

Thermocapillary effect is usually taken as negligible for low wall superheat conditions and in the presence of gravity. In the case of highly subcooled boiling it will however play a prominent role (Siedel *et al.*, 2013).

- Inertial force and added mass force: As the bubble grows, the interface pushes away the surrounding liquid. The liquid inertia and added mass force correspond to the liquid reaction to its acceleration caused by the motion of the interface.

$$F_{LI} = K_1 \rho_l \frac{dh_{cg}}{dt} \frac{dV}{dt} + K_2 \rho_l V \frac{d^2 h_{cg}}{dt^2} \quad (1.25)$$

For the case of a hemispherical bubble growing on a wall, $K_1 = 2$ and $K_2 = 4$ (Klausner *et al.*, 1993)

- Drag force: viscous stress is caused by the motion of the bubble. The force induced could be expressed as

$$F_D = -\frac{1}{2} C_D \rho_l A_{mc} u^2 \quad (1.26)$$

With C the drag coefficient and A_{mc} the maximal area normal to the bubble movement. In the case of centimeter size bubble with mushroom shape, $C = 2.6$ and does not depend on the size of the bubble (Haberman and Morton, 1953, cited by Ginot, 1999).

- Lift force: When two bubbles are very close to each other, the flow carried by the wake of the first one can impact the next growing bubble. The resultant of this force is approximated by the expression of Zeng *et al.* (1993):

$$F_{Lift} = \frac{75}{16} \rho_l u^2 R_B^2 \left(\frac{R_B}{L}\right)^8 \quad (1.27)$$

This force is often negligible but it needs to be taken into account in the case of very low pressure when a vapor jet follows the first large bubble.

Two different modes of thinking could be found in the literature regarding the detachment of the bubble. The first one is commonly encountered and widely used to develop correlations: bubble detachment occurs when the force balance is null. The second one is a new mode of thinking and it is based on the mechanical equilibrium of the bubble and on the mechanical stability of the triple line: detachment occurs when the mechanical equilibrium of the bubble and its stability at the triple line are not achieved any more. In the case of the first mode of thinking, not all the forces have to be considered to estimate when the detachment will occur. At the first order, it is commonly admitted that detachment will occur when buoyancy force and surface tension are balanced. However, several authors showed that the growth velocity has a significant influence on the bubble detachment. The detachment will be governed by buoyancy and surface tension forces in the case of a slow growth

whether it will be governed by inertial force in the case of a high speed bubble growth. Inertial forces will thus predominate in case of high wall superheat, high subcooled boiling or low pressure.

Most of the correlations used to predict bubble departure diameter were developed for a spherical bubble with a relatively slow growth. Some of the widely used correlations are introduced thereafter.

The most known correlation to predict the detachment diameter is the one established by Fritz in 1935. As mentioned above, this correlation is based on a balance between buoyancy forces and surface tension forces:

$$D_d = 0.02080 \sqrt{\frac{\sigma}{g(\rho_l - \rho_v)}} \quad (1.28)$$

Where θ is the angle of wettability in degree. However, this correlation does not explicitly depend on the pressure and it has been shown to overestimate the bubble departure diameter at high pressure. Cole and Schulman (1966) suggested using the following equation to explicitly consider the pressure:

$$D_d = \frac{133322}{P} \sqrt{\frac{\sigma}{g(\rho_l - \rho_v)}} \quad (1.29)$$

Cole and Roshenow (1969) developed a correlation in which the effect of the pressure is considered through the density of the vapor by adding a term similar to the Jacob number:

$$D_d = 1.5 \times 10^{-4} \sqrt{\frac{\sigma}{g(\rho_l - \rho_v)}} \left(\frac{\rho_l C_p T_{sat}}{\rho_v \Delta h_{lv}} \right)^{5/4} \quad (1.30)$$

Nishikawa *et al.* (1976) empirically suggested using the following equation:

$$D_d = \sqrt{\frac{\sigma}{g(\rho_l - \rho_v)}} \left(0.12 + 0.08 \left(\frac{C_p (T_p - T_{sat})}{\Delta h_{lv}} \right)^{2/3} \right) \quad (1.31)$$

Borishanskiy *et al.* (1981) developed a correlation introducing the Boltzmann's constant and the molar mass of the fluid:

$$D_d = 5 \times 10^5 \left(\frac{P}{P_c} \right)^{-0.46} \left(\frac{k_B T_c}{P_c M} \right)^{1/3} \quad (1.32)$$

Jensen and Memmel (1986) based their correlation on the previous equation and on numerous experimental data. They adjusted the empirical exponent and coefficient to:

$$D_d = 2.97 \times 10^4 \left(\frac{P}{P_c} \right)^{-1.09} \left(\frac{k_B T_c}{P_c M} \right)^{1/3} \quad (1.32)$$

1.3.3 Boiling curve

From a macroscopic point of view, boiling on a heated wall could be described from a curve plotting the heat flux as a function of the wall superheated. This representation is usually referred to as "boiling curve". The boiling heat transfer was first described that way by Nukiyama (1934). He obtained two

different boiling curves depending on whether a temperature or a heated flux is imposed on the heated surface (Fig. 1.19).

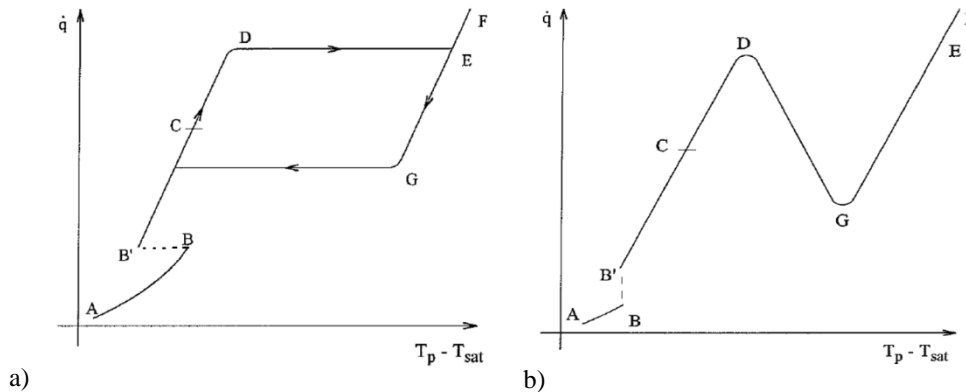


Figure 1.19: Boiling curves at a) imposed heat flux and b) imposed temperature

Each area described thereafter is characterized by a specific boiling regime.

Natural convection (A-B): The heated wall has a temperature superior to the surrounding liquid. The temperature of the liquid surrounding the surface thus increases. A thermal boundary layer is formed. Heat is exchanged by natural convection and then by evaporation at the free surface.

Onset of the boiling (B-B'): The surface temperature is sufficient for bubbles to nucleate. Heat transfer is enhanced as a part is transferred by phase-change. At imposed heat flux, a temperature drop is thus observed. At imposed temperature, a sudden increase of heat flux is observed. First bubbles are often due to entrapped gas in cavities.

Isolated bubble regime (B'-C): Bubbles are generated from isolated sites. The surface temperature rises very slowly with the heat flux. More and more nucleation sites become active on the surface. Part of the heat flux is transferred by phase-change whereas the other part is convected into the liquid bulk. The heat transfer is enhanced due to the growth and the departure of bubbles which induces a liquid motion. The liquid motion induces a cyclic destruction of the thermal boundary which is then carried by the wake of the bubble and allows the far field liquid bulk to wet the wall. Mechanism of destruction and reestablishment of the thermal boundary enhance significantly the heat transfer. The diameter of detachment of the bubble and their frequency of detachment depends on the heat flux.

Fully developed nucleate boiling regime (C-D): the heat flux is high enough to activate many nucleation sites. They get close enough to each other to allow the merger of neighboring bubbles. The frequency of bubble detachment increase as well. Horizontal and vertical bubbles merger are observed (called also respectively lateral coalescence and vertical coalescence). Large masses of vapor are created. The liquid motion close to the heated surface is restricted and the heat transfer is starts to level off or even decrease slightly.

Critical heat flux (D-E): This point marks the end of the nucleate boiling regime. Vapor masses above the surface prevent any liquid to rewet the surface. A vapor film is formed on the surface leading to a sudden rise of the wall temperature.

Film boiling regime (E-G): Heat exchange occurs by conduction and radiation through the vapor film. As the temperature increases with the heat flux, radiative transfer through the vapor film becomes a major heat transfer mode. The vapor layer formed becomes stable for heat flux inferior to the critical

heat flux. As a stable film boiling regime has been established, even if the heat flux is decreasing and the temperature is decreasing as well, the same regime of film boiling regime is observed far below the CHF temperature. The wall can be damaged if the wall temperature reaches the melting temperature of the material. This regime remains stable until reaching a critical value called Leidenfrost point.

Leidenfrost point (G): The Leidenfrost point represents a transition back to the isolated bubble regime. The heat flux is low enough to allow a break in the vapor film. Liquid can rewet the surface. The heat transfer is enhanced and a sudden temperature drop is observed.

The use of such boiling curve allows to identify rapidly the area of heat transfer effectiveness. Isolated bubble and fully developed boiling regimes are thus really interesting as they allow to release high heat flux to the fluid for relatively low wall superheat.

McGillis *et al.* (1991a) studied the effect of the pressure only for this interesting part of the boiling curve (Fig. 1.20). They observed that a reduction in the pressure shifted the boiling curve to higher wall superheat. Indeed, as mentioned previously, lower pressure increases the minimum superheat required for nucleation and thus delays the onset of nucleate boiling. It is also interesting to notice that they marked the Onset of the Continuous Boiling (OCB). Contrary to what happens at atmospheric pressure (101 kPa), once the boiling is triggered, an intermittent regime is observed (i.e the waiting time is longer than the bubble growth time). Heat is transfer by transient conduction, convection and phase change. This observation is in agreement with the conclusion reached by Gorenflo (2013) who predicted for different fluids (but experimented it only which methanol for the lowest pressure of $P/P_c = 0.02$) that at subatmospheric pressure the “vigorous convection induced by the (few) big fast-growing and fast-moving bubbles” become the dominant heat transfer phenomenon compared to heat transfer induced by nucleation. This regime may be the unstable boiling observed by Wu *et al.* (1982) and by Labuntsov *et al.* (1978) marked by an irregular unsteady character.

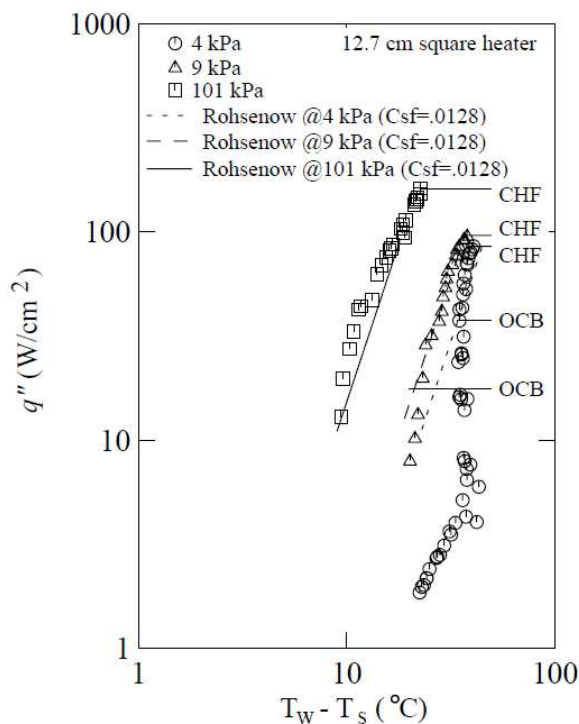


Figure 1.20: Boiling curves for water at 101 kPa, 9 kPa and 4 kPa by McGillis *et al.* (1991a)

During this regime, usual correlations for fully developed to nucleate boiling cannot be applied (Mc Gillis *et al.*, 1991a, Kim *et al.*, 2007).

1.3.4 Boiling curve in transient boiling

Studies on transient boiling started with the desire to understand what would happen on a nuclear plant during an extremely high and sudden rise in wall temperature. Opposal to studies conducted in steady state boiling introduced previously, where a steady state is obtained before any type of measurements, most of the studies of transient boiling are realized by imposing a chosen heating mode evolution in time on the sample and by measuring the instantaneous heat flux and surface temperature obtained at each time step. Many studies focused on the exponential heating of a metal film in water at atmospheric pressure. However, Sakurai *et al.* (1970) among other extended these studies to other heating mode, especially on heating ramps. Nevertheless they still used metallic wire or film and few studies focused on the transient heating of a large sample (Héas, 2001).

According to these studies, the most significant characteristic of the transient boiling is the delay of the onset nucleate boiling compared to steady state boiling and thus the high wall superheat reached. The higher the heating rate, the higher the temperature required to set nucleate boiling on and the higher the wall superheat reached. Due to the difference of boiling phenomena involved in transient heating compared to steady state boiling and due to the delay of the onset of nucleate boiling, the shape of the boiling curves obtained at transient heating is different than that obtained at steady state boiling.

Sakurai *et al.* (1970) plotted the boiling curve obtained during a relatively slow exponential heating of a metal foil immersed in water at atmospheric pressure (Fig. 1.21). They observed that before the onset of the boiling, the variation of the surface temperature is similar to that obtained in transient conduction. Once boiling is triggered (point B on the Fig. 1.21), the temperature of the metal foil keeps rising up to the point C. The heat transfer enhancement due to liquid motion near the heated foil permits a decrease of the foil temperature to D. According to the authors, the amplitude of the CDE cycle depends on the heat capacity of the foil: the higher its heat capacity, the smaller the temperature difference between CD and DE.

Héas (2001) studied transient boiling of pentane occurring on a 90 mm high and 30 mm diameter cylinder when imposing a heat flux step set to $21.6 \text{ W}\cdot\text{m}^{-2}\cdot\text{K}^{-1}$ for most of his experiments. This heat flux step was imposed by two cartridges heaters placed in the cylinder at the opposite part of the boiling surface in order to impose the heat flux at a certain distance of the boiling surface. Among other, he showed that the initial conditions severely affect results, making it difficult to obtain a good repeatability. However, after developing a preliminary procedure to avoid these problems, for the part of the boiling curves studied (he did not reach the critical heat flux), the shape of boiling curves obtained remained similar to those obtained for the exponential heating of a foil. He observed that once boiling is triggered, the boiling regime is characterized by a partial dry out of the heated surface. Then, the size and the frequency of the vapor masses diminish slowly. At the point D of the Fig. 1.21, nucleate boiling regime is fully established. Héas also noticed that before the trigger of boiling, the release of energy to the fluid is inferior to the energy stored into the sample.

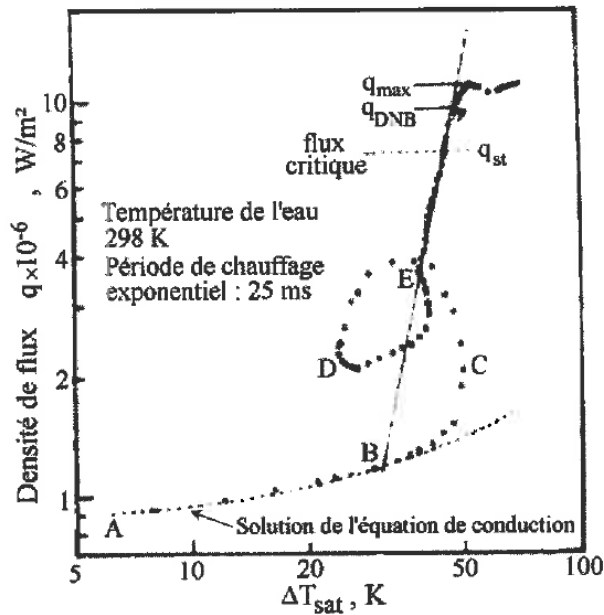


Figure 1.21: Transient boiling curve (Héas, 2001 from Sakurai *et al.*, 1970)

In transient boiling the liquid surrounding the bubble is less superheated than in saturated boiling. Thus, the wall superheat required to initiate boiling is higher in the latter than in the former case. Due to the high wall superheat required, a change from conduction/convection regime to film boiling regime could be observed.

According to several authors who propose an analogy between transient boiling and subcooled boiling, increasing the subcooling also leads to a delay of the onset of nucleate boiling and thus to an increase in the wall superheat required to initiate boiling.

1.4 Boiling phenomena in narrow spaces

Boiling phenomena in narrow spaces also named “confined boiling” refers to the boiling phenomena occurring in an environment where at least one dimension of the flow is narrow enough to change heat transfer mechanisms with respect to boiling in a large (“infinite”) volume of liquid. Different configurations of narrow space were studied in the literature; among which parallel plates, annular channels or circular microchannels.

1.4.1 Influence of the confined space in the heat exchange

Several studies showed an enhancement of the heat transfer when decreasing the channel thickness at low heat fluxes and a reversal trends at high heat fluxes. However, when a very narrow space is given, the heat transfer is degraded whichever the given heat flux (Katto and Yokoya, 1966, Bonjour, 1996, Ait Ameer, 2006).

Katto and Yokoya (1966) first studied the boiling of water between two circular horizontal plates. They observed that for a narrow space thickness greater than 2 mm, the boiling curve obtained is similar to that for free boiling. However at a given heat flux, the wall superheat monitored decreases when decreasing the channel thickness, reaches a minimum and then increases dangerously. They explained the enhancement of the heat transfer as an increase of the length of

the microlayer trapped between the liquid and the wall. Due to the presence of the confined plate, the bubble is deformed and the microlayer enlarged. This fosters the evaporation of the microlayer and highly enhances the heat transfer. When the microlayer is entirely evaporated and the liquid cannot rewet the heated surface, the heat transfer is rapidly deteriorated. Ait Ameer (2006) gave an alternative interpretation of this decrease of the heat transfer: he stated that the feeding in liquid of the confined space is reduced for a very low spacing of the channel because of increased friction at the inlet.

Rampisela (1993) compared the enhancement of the heat transfer between two parallel plates for R113 and water at atmospheric pressure. The channel thickness varied between 1 and 5 mm. He observed that the heat transfer enhancement can reach 600 % for water at low heat fluxes and small confined space but no significant enhancement is observed for R113. He assumed that this difference is due to the heat transfer by latent heat as the water latent heat is much higher than the latent heat of R113.

Xia *et al.* (1996) experimentally studied saturated boiling of R113 at atmospheric pressure between two vertical parallel plates. The height of the plates varied between 56 to 197 mm and the confined space from 0.8 to free boiling. They plotted the local wall superheat versus the plate height for different imposed heat fluxes (Fig. 1.22). For low heat flux, the maximal wall superheat is located at the entrance of the channel where the heat is transferred by single phase convection. The location of this maximal wall superheat moved until reaching the top of the plate at high heat fluxes. This is due to the increase of the void fraction at the top of the plate. The authors found that an optimal design of the confined space exists to enhance heat transfer. This one depends on the fluid and the heat flux but also on the ratio H/e .

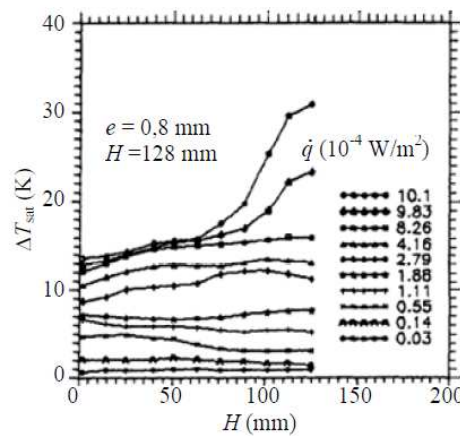


Figure 1.22: Evolution of the wall superheat with the plate height for different imposed heat fluxes (Xia *et al.*, 1996)

Stutz *et al.* (2009), experimentally studied the boiling of saturated n-pentane between two circular horizontal plates. As Bonjour *et al.* (1997) before them, they used the Bond number in order to characterize the effect of the confined space on bubbles.

$$Bo = \frac{e}{\sqrt{\frac{\sigma}{g(\rho_l - \rho_v)}}} = \frac{e}{L_c} \quad (1.33)$$

e is the thickness of the channel and L_C the capillary length. For a Bond number greater than unity, bubbles are not affected by the confinement. However, heat transfer is degraded as the confined plate prevents both the formation of convective cells above the heated surface and the rise of vapor masses created. For Bond number lower than unity, bubbles are flattened and the enlarged microlayer fosters the evaporation at low heat fluxes. Due to these change in heat transfer mechanisms, they observed different shapes for the boiling curves depending on this Bond number (Fig. 1.23). Bonjour (1996), as he studied R113 boiling between two vertical plates, also observed different shapes of the boiling curves, especially depending on the Bond number.

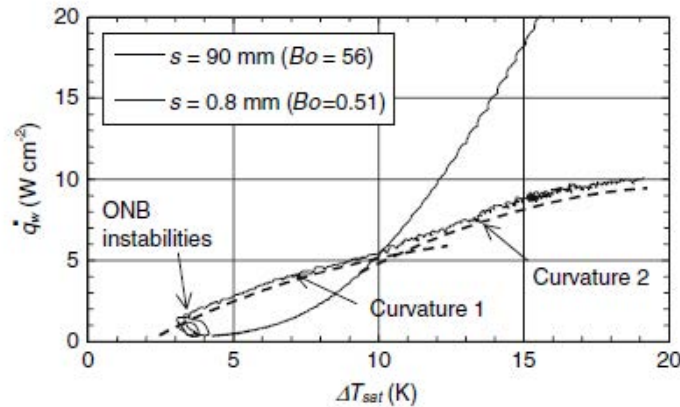


Figure 1.23: Change in the concave shape of the boiling curve (Stutz *et al.*, 2009)

The enhancement of the heat transfer in confined space is due to several mechanisms:

- As bubble is flattened due to the presence of the confined wall, site-seeding is fostered. Vapor remains trapped in nucleation site. These sites are then activated more easily. Moreover, due to the confinement, the heat cannot be released to the far field liquid bulk; more sites can thus be activated.
 - The increase of liquid motion due to the raise and departure of bubbles. To a certain extent the heat transfer by convection induced by the liquid motion is enhanced with the decreasing spacing of the narrow space. Indeed, as the confined space decreases, the entrance area decreases as well and the fluid velocity increases. Moreover, buoyancy force are more significant as for a given heat flux, both the liquid average temperature and the void fraction are higher.
- However, Ait Ameer (2006) observed a decrease of the fluid velocity with the decreasing spacing of the narrow space. For this author, the enhancement of the heat transfer at low heat flux and low spacing cannot be explained by the enhancement of the convective effect: the viscous effects limit the increase of the velocity for very small channels thicknesses.
- The evaporation of the microlayer trapped between the crushed bubble and the heated surface.

The influence of each mechanism depends on the boiling regime considered.

1.4.2 Boiling regime in confined space

Three main boiling regimes are usually identified in a confined space constituted by two vertical plates: nucleate boiling with deformed bubbles, nucleate boiling with bubbles merger and partial dry out of the wall. These three main regimes were identified by high speed camera or pictures by many authors for a Bond number close to or less than the unity.

- **Deformed bubbles nucleate boiling:** this regime appears at low heat fluxes. Isolated bubbles are crushed to the plate. These flattened bubbles grow rapidly and keep growing during their raise inside the channel. They are thus larger at the top of the channel. As the bubble is crushed to heated wall, heat transfer is enhanced due to the fostered evaporation of the microlayer. The higher the evaporation rate is, the larger the bubble diameter.

- **Nucleate boiling with bubbles merger:** As the heat flux increases, the amount of vapor generated increase as well. Deformed bubbles merge together but a thin film of liquid is always observed between the wall and vapor masses. As the velocity of the fluid is relatively high, the far field liquid bulk wets the wall with a high heat transfer coefficient. Bonjour and Lallemand (1998) suggested the following correlation for this regime:

$$Nu = \frac{hR_{cav}}{\lambda_1} = K\Pi_1^{n_1}\Pi_2^{n_2}\Pi_3^{n_3} \quad (1.34)$$

With:

$$\Pi_1 = \frac{\dot{q}\rho_v\Delta h_{lv}}{\lambda_1\sigma\Delta T_{sat}} R_{cav}^2 \quad \text{characterizing the nucleation} \quad (1.35)$$

$$\Pi_2 = \frac{\rho_l C_{p,l}\sigma T_{sat}}{(\rho_v\Delta h_{lv})^2 R_{cav}} \quad \text{being the ratio between the sensible heat and the latent heat} \quad (1.36)$$

$$\Pi_3 = R_{cav} \sqrt{\frac{P(\rho_l - \rho_v)\rho_l}{\rho_v}} \quad \text{taking into account the influence of the pressure} \quad (1.37)$$

$$K=2.49 \times 10^{-4}, n_1 = 1.039, n_2 = 0.154, n_3 = 0.575 \text{ for } Bo > 0.5$$

$$K=2.19 \times 10^{-4}, n_1 = 0.832, n_2 = 0.076, n_3 = 0.659 \text{ for } Bo < 0.5$$

$$R_{cav} = \frac{2\sigma T_{sat}(\rho_l - \rho_v)\delta_{th}}{\rho_l\rho_v\Delta h_{lv}\Delta T_{sat}} \quad \text{is an estimate of the radius of activated sites} \quad (1.38)$$

$$\delta_{th} = \frac{\lambda_1}{h_{cn}} \quad \text{is a scaling for the thermal boundary layer thickness} \quad (1.39)$$

$$h_{cn} = \frac{\lambda_1}{e} \left[\frac{24H}{eRa_e} + 2.51 \left(\frac{H}{eRa_e} \right)^{2/5} \right]^{-1/2} \quad (1.40)$$

is an estimate of the single phase heat transfer coefficient and

$$Ra_e = \frac{g\beta\dot{q}e^4}{\lambda_1 a_1 \nu_1} \quad \text{is a modified Rayleigh number} \quad (1.41)$$

This correlation shows good agreement with experimental results for a large range of pressure and thickness of the narrow space either for different fluid.

- **Partial dry out of the wall:** For high heat fluxes, the thin liquid film trapped between the wall and the vapor is rapidly evaporated, leading to a temporary and local dry out of the wall. As liquid rewets periodically the heated wall, the wall temperature is almost steady but the heat transfer coefficient is degraded.

These three different regimes were also studied through local measurements of the void fraction, oscillation of the wall temperature or travel time of liquid/vapor structure. This latter measurement was done by Bonjour and Lallemand (1998). They recorded bubble crossing time as well as void fraction for different given heat fluxes. They were able to identify the transitions between these three regimes. A map flow was thus realized (Fig. 1.24). The upper curve represents the ratio between critical heat flux in confined space and critical heat flux in free boiling. They showed that the transition between isolated deformed bubbles and isolated merger bubble could be represented by the curve $\frac{\dot{q}}{\dot{q}_{crit,e}} = 0.2$ and the transition between isolated merger bubble and partial dry out by the

$$\frac{\dot{q}}{\dot{q}_{crit,e}} = 0.7 .$$

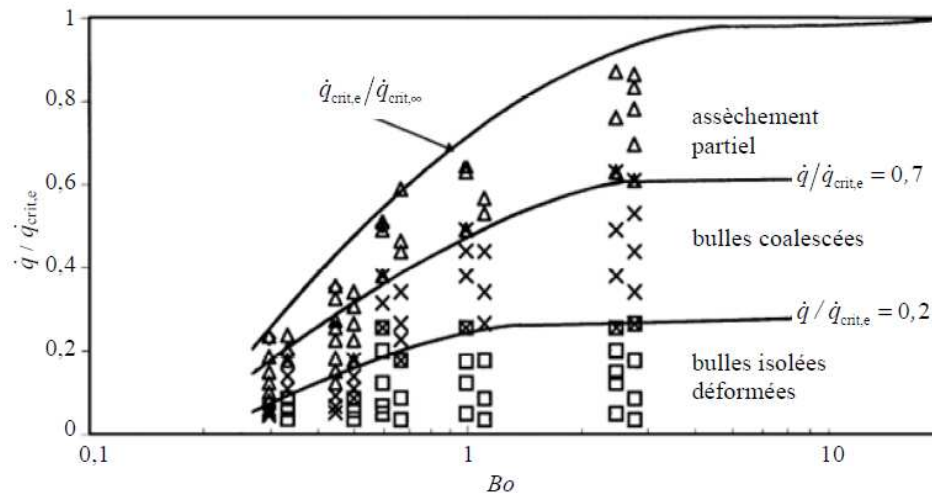


Figure 1.24: Flow map of boiling regime occurring in a narrow space (Bonjour and Lallemand, 1998)

Ait Ameer (2006) proceeded differently to characterize the boiling regime. He identified only two boiling regimes in his study of the boiling of pentane between two vertical plates of 120 mm x 60 mm forming a rectangular channel either open laterally or closed laterally. He characterized these regimes as a “steady rising boiling regime” and a “pulsating regime”.

- The **steady rising boiling** appears at low heat flux $\frac{\dot{q}}{\dot{q}_{crit,e}} < 0.2$. The flow is divided in two areas: a liquid area in the lower third of the plate; a two-phase area in the upper part of the plate. In this second area, isolated bubbles are observed. They merge and raise rapidly. During this flow regime, the flow is always ascendant.
- The **pulsating regime** appears for $\frac{\dot{q}}{\dot{q}_{crit,e}} > 0.2$. The appearance of instabilities leading to the pulsating regime is due to the rapid expansion of the vapor phase and to friction and capillary effects small enough to allow an efficient liquid feeding at the lower end of the channel.

Boiling is characterized by a cyclic liquid feeding and periodic passage of ascending two-phase flow. The rapid expansion of vapor structure leads to a reduction and then to a stop of the liquid feeding ($30 < t < 60$ ms). The two-phase flow is then expelled at the upper end, lower end and eventually on the side of the confined space. In the channel, the two-phase fluid flows downwards in the lower third part of the channel and upwards otherwise. The border of these two areas is named as the centre of expansion and is characterized by a zero velocity. The evolution of the maximal and minimal interface velocity obtained in the channel for different wall superheat is represented in the Fig. 1.25. Velocity up to 2.5 m.s^{-1} and below -0.6 m.s^{-1} could be monitored. Pressure fluctuations up to 3 kPa were also monitored during the study (Fig. 1.26). The monitored over pressure corresponds to stop of liquid feeding. The increase of the over pressure when increasing the heat flux shows a vaporization more and more violent in the channel.

The mass flow rate at the lower part of the channel increases with the thickness of the narrow space due to the decrease of the friction and singular pressure drops.

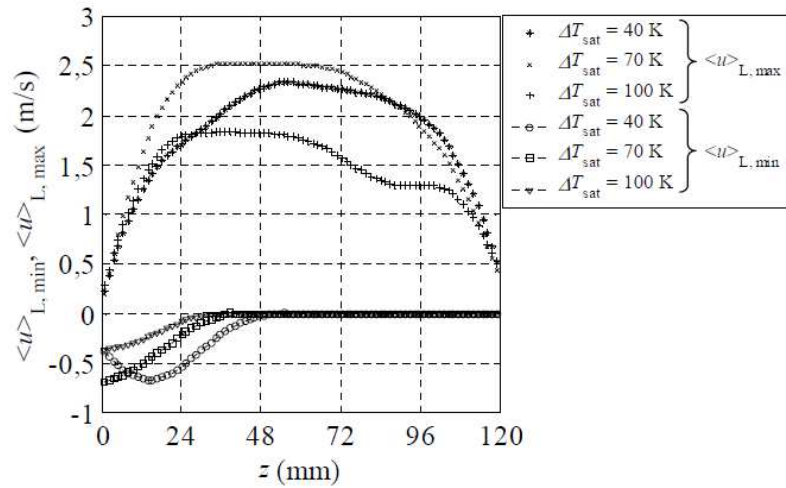


Figure 1.25: Evolution of the maximal and minimal interface velocity obtained in the channel for different wall superheat (Ait Ameer, 2006)

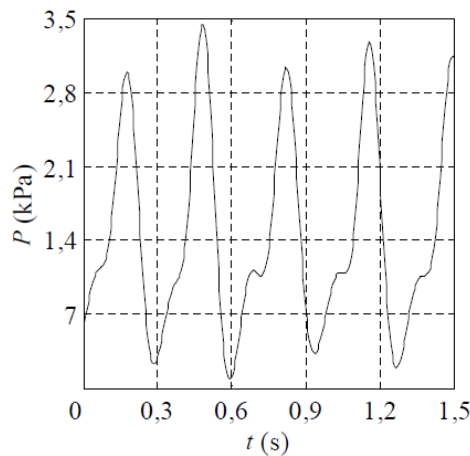


Figure 1.26: Pressure fluctuations inside the channel for $\frac{\dot{q}}{\dot{q}_{\text{crit,e}}} \approx 0.85$ (Ait Ameer, 2006)

According to this author, the heat transfer is optimal for a Bond number of 0.25 but for such confinement, velocity measurements show a decrease of the interface velocity when decreasing the thickness of the narrow space. Thus, the enhancement of the heat transfer (up to 600 % compared to free boiling) cannot be due to the convective effect enhancement but rather to the fostered phase-change (evaporation of the microlayer, fostered nucleation of bubbles). For channel thickness greater than the capillary length, the enhancement of the heat transfer could be only due to the enhancement of convective effect.

1.4.3 Parameters of influence

Influence of surface tension: even if surface tension plays an important role in the bubble curvature and bubble diameter of detachment, studies show that there is no significant influence of surface tension on boiling in confined space once nucleate boiling is onset. However, as heat transfer is enhanced for Bond number inferior to the unity, i.e. for a channel thickness smaller than the capillary length, it has an influence on the value of the optimal thickness that maximizes the heat transfer.

Influence of geometry: Yao and Chang (1983) did not observe any significant influence of the plate height on the heat transfer. However, Bonjour (1996), Xia *et al.* (1992) and Fujita and Uchida (1995) observed that for some height, the heat transfer is enhanced. An optimal height exists. They showed that this optimum depends on the imposed heat flux and on the channel thickness.

Boundary conditions of the narrow space also have an influence on the heat transfer. Closing the channel sides or its lower end enhances heat transfer at low heat flux. Fujita *et al.* (1988) explained this observation as the velocity of the two-phase flow is thus limited. As a matter of fact, bubbles spend more time in the channel which fosters the evaporation of the microlayer. However, the difficulty for the liquid to feed the channel leads to a decrease of the heat transfer at higher heat fluxes.

Influence of the confined space inclination: Fujita *et al.* (1988) showed that for a channel thickness lower than the bubble departure diameter, the inclination of the heated surface has an influence on the driving pressure. Liquid motion is thus limited and heat transfer degraded. Several authors observed that the heat transfer coefficient increases from a horizontal heated surface to a vertical heated surface. Bonjour *et al.* (1997) reached such a conclusion by comparing

an “enhancement factor” $FA = \frac{h_e - h_\infty}{h_\infty}$ in these two heated wall orientation (Fig. 1.27).

In horizontal space, the fluid is at rest and the presence of the confined plate disturbs the evacuation of the vapor phase. Indeed, by contrast with the vertical configuration, the microlayer is rapidly evaporated and a dry out of the wall is observed. As the two mechanisms which enhance significantly the heat transfer in confined space are the evaporation of the enlarged microlayer and the enhancement of convective effect inside the narrow space, the heat transfer coefficient is higher in vertical configuration than in other configuration. Moreover, due to the buoyancy force, in vertical orientation the bubbles are deformed even if the confined space is large and the bubble slides along the wall carrying liquid in its wake and allowing an evaporation of the microlayer during its raise.

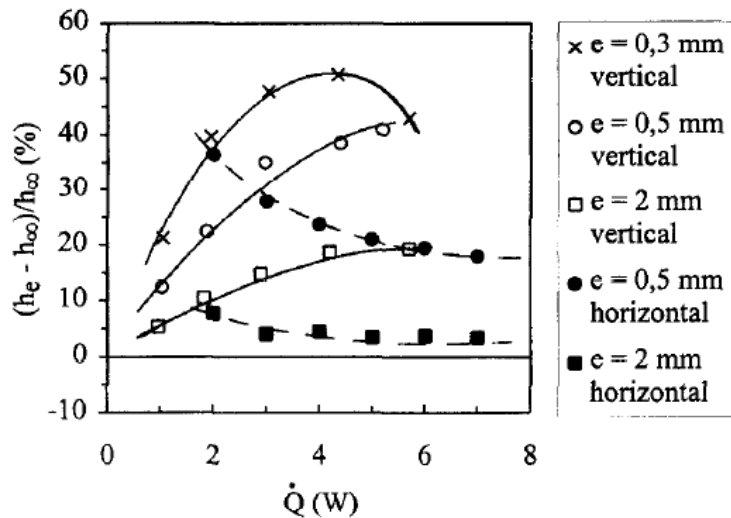


Figure 1.27: Enhancement factor in vertical and horizontal heated surface for different spacing of the confined space (Bonjour *et al.*, 1997)

Influence of the subcooling: Passos *et al.* (2004) performed experiments on subcooled nucleate pool boiling of FC72 and FC87 on a downward facing surface. They observed that the effect of the confined space on the heat transfer is opposite to that for saturated boiling, i.e. the heat transfer coefficient is degraded when the confinement is increased. This observation could be due to the fact that in subcooled boiling, bubbles grow up at their nucleate site prior to collapsing, i.e. without sliding along the wall. This is in agreement with the observations of Yuan *et al.* (2011) who observed that less and less bubbles slide along the wall as the subcooling degree increases. However, they also observed that increase of the heat flux or an increase of the pressure induces an increase of the percentage of sliding bubbles. Thus, above 0.6 MPa, all bubbles grow and slide along the wall.

In these previous studies, the flow is induced by the growth and the rise of the bubbles. However, in the evaporator implemented on cooling machines, the motion of the refrigerant may also be induced by an external component. Despite the similarity of phase-change phenomena between free boiling and forced convective boiling more usually named “flow boiling”, some differences could be noticed. These differences are introduced thereafter.

1.5 Two-phase flow and flow boiling in vertical tubes

1.5.1 Flow patterns

In presence of a forced flow inside a channel, different boiling regimes may take place depending on the pressure, the geometry of the tube, the flow rate, the subcooling, etc. The generally accepted flow patterns in a vertical upward flow are shown in Fig. 1.28 and are described below:

- **Bubbly flow:** The flow distribution during this regime is characterized by the presence of discrete bubbles dispersed in a continuous liquid flow. The sizes and the shape of the bubbles may be different for each of them but they all are smaller than the diameter of the tube.
- **Slug flow:** This regime occurs when the vapor quality increase. The bubbles coalesce and form larger bubbles. The diameter of these elongated bubbles, also named Taylor bubbles, becomes similar to the channel diameter. The elongated bubbles formed during this regime have a characteristic spherical nose and their bases are flattened. They are separated from the wall by a thin liquid film and are separated from each other by liquid slugs which may carry smaller bubbles in them.
- **Churn flow:** When the velocity of the flow is increased, formation of a seemingly unstable flow of vapor and liquid occurs. During this regime, the liquid is displaced to the tube wall.
- **Wispy-annular flow:** This regime occurs at high mass velocity. A considerable amount of liquid is entrained in the vapor core forming droplets. These liquid droplets may coalesce to form larger liquid wisps.
- **Annular flow:** The liquid forms a continuous film around the perimeter of the pipe. The interface between the liquid and the vapor is disturbed by small amplitude waves and droplets may be dispersed in the vapor. At very high velocities, vapor rips the liquid film off from the wall and most of the liquid is entrained as a spray by the vapor. When this occurs, the flow regime is named **Mist flow**.

Annular flow appears at large vapor flow rate.

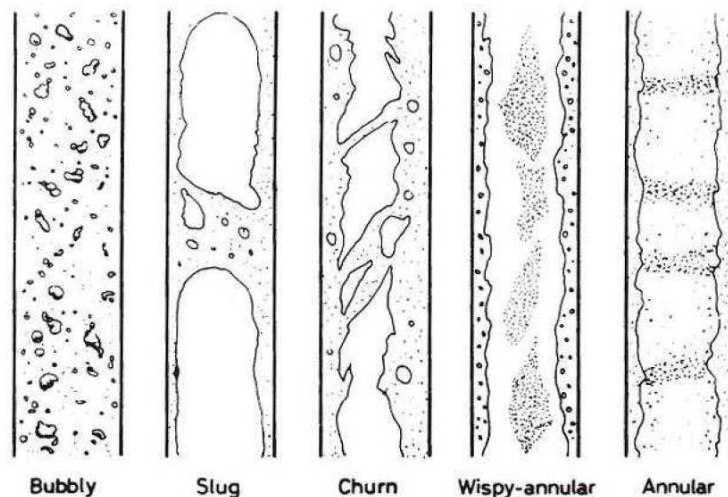


Figure 1.28: Two-phase flow patterns during evaporation in vertical flow (Collier and Thome, 1994)

In horizontal tube, two-phase flow characterization is complicated by the influence of the gravity which causes an asymmetry of the flow distribution. Flow regimes observed are thus different than those observed in vertical orientation. Regimes such as the stratified flow during which a complete separation of the vapor and liquid occurs could be for example observed.

If phase-change occurs in the channel, the vapor quality increases in the direction of the flow. The occurrence of the different flow regimes then depends on the location along the channel (Fig. 1.29).

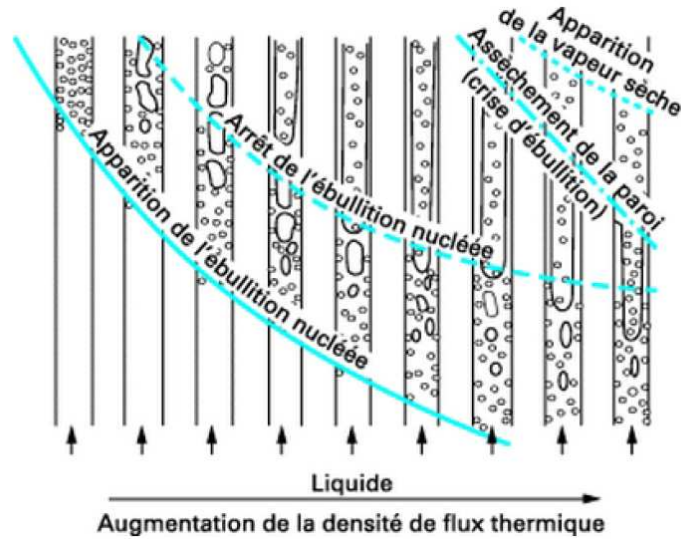


Figure 1.29: Flow regimes along the tube in the case of a vertical upward flow for different heat flux densities (Visentini, 2012, from Roshenow *et al.*, 1998)

Assuming a subcooled flow feeding the channel, heat is thus first transferred by forced convection at the lower part of the channel. As the liquid is slowly heated by the wall during the fluid rise, boiling is set on at the wall surface. The bubbles then detach and may condense. It is the occurrence of the bubbly flow introduced previously. As the liquid continues rising, the slug flow, the churn flow and then the annular flow are observed. If the heat flux density increases, these flow regimes are translated closer to the lower part of the channel.

The local flow pattern occurring in the tube can be predicted using a flow patterns map knowing the vapor quality and the mass velocity of the flow. The vapor quality is defined as follows:

$$x = \frac{\dot{m}_v}{\dot{m}_v + \dot{m}_l} = \frac{\dot{m}_v}{\dot{m}} \quad (1.42)$$

With \dot{m}_v the mass flow rate of the vapor and \dot{m}_l the mass flow rate of the liquid (Fig. 1.30).

And the mass velocity is defined as follows:

$$G = \frac{\dot{m}}{A_v + A_l} \quad (1.43)$$

With A_v the cross-sectional area occupied by the vapor and A_l the cross-sectional area occupied by the liquid (Fig. 1.30).

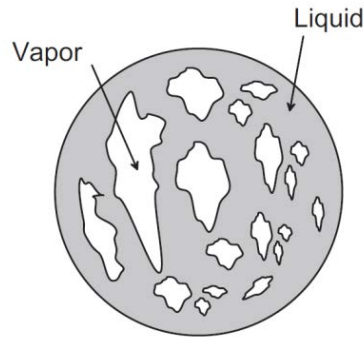


Figure 1.30: Cross-sectional void fraction (Revellin, 2005)

A variety of flow pattern maps are proposed in the literature. Those developed by Wojtan *et al.* (2005) are today often considered as being of reference. For the purpose of illustration, such a map is shown in Fig. 1.31 for specific operational conditions.

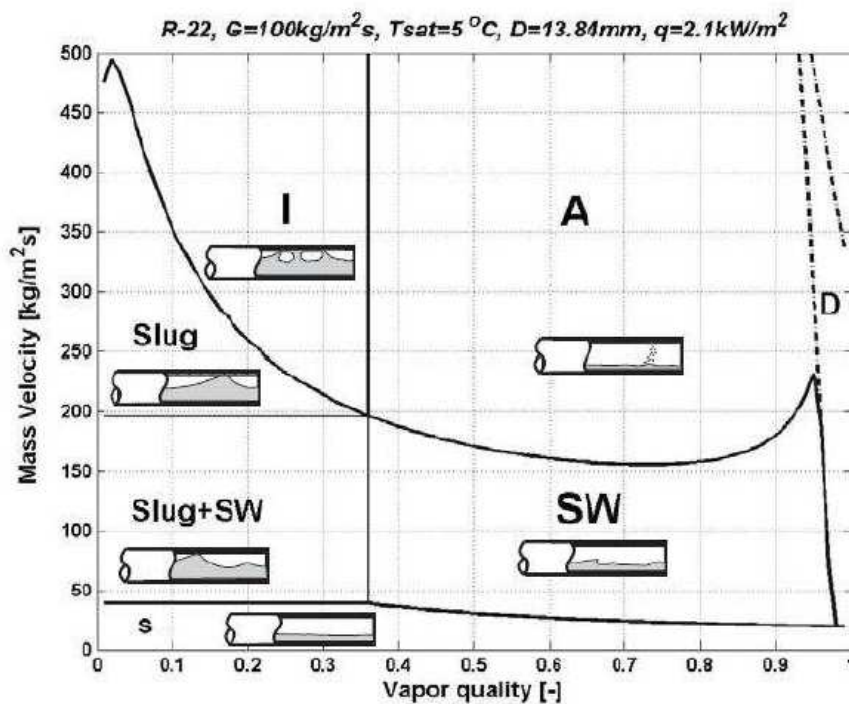


Figure 1.31: Flow pattern map for R-22 and horizontal flow (Wojtan *et al.*, 2005). S=stratified flow, SW=stratified-wavy flow, I=intermittent flow, A=annular flow, M=mist flow and D= transition zone between annular and mist flow.

Wojtan *et al.* (2005) method for preparing flow pattern maps covers a large area of operating conditions and fluids. However, to date and to our knowledge, no study was conducted for flow boiling regime under the operating conditions which would be encountered in typical sorption refrigeration systems (low reduced pressure ranging from $2 \cdot 10^{-4}$ to $5 \cdot 10^{-5}$ depending on the fluid nature and on the evaporation temperature) and thus, no flow pattern map seems to be validated in these conditions. Nevertheless, few studies have been carried out to investigate the effect of the saturation temperature on the two-phase flow structure. The few studies on this subject suggest that the saturation temperature may be an important factor on the bubble dynamics, especially regarding the transition to annular flow and dry out flow (Revellin *et al.*, 2008; Charnay *et al.*, 2013).

1.5.2 Heat transfer coefficient

In two-phase flow, heat transfer is driven by two main mechanisms: nucleate boiling and convective boiling. These heat transfer mechanisms are strongly dependent on the flow patterns parameters (mass velocity, heat flux and vapor quality). When the nucleate boiling is dominant, i.e. the heat transfer is related to the formation of bubble at the tube, the heat transfer coefficient depends on the heat flux and the saturation pressure level. When convective boiling is dominant, i.e. heat transfer is related to conduction and convection through a thin liquid film with evaporation at the liquid-vapor interface, heat transfer coefficient depends on the mass flux and on the vapor quality. When both mechanisms are of the same order of importance, heat transfer coefficient depends on the heat flux, mass velocity and vapor quality. Heat transfer is enhanced when bubbles are formed but is degraded when liquid film is displaced from the wall and replaced by vapor.

Various models exist in the literature in order to evaluate the heat transfer depending on the flow patterns (Gungor and Winterton, 1986; Groeneveld, 1973; Groeneveld and Delorme, 1976). A “Universal” model was also developed after the creation of the first flow patterns map (which was then significantly improved with the time until the last significant change made by Wojtan *et al.* in 2005). Fig. 1.32 shows as an illustration the results obtained with the prediction method of Kattan-Thome-Favrat (1998) compared to experimental data and the corresponding flow patterns map.

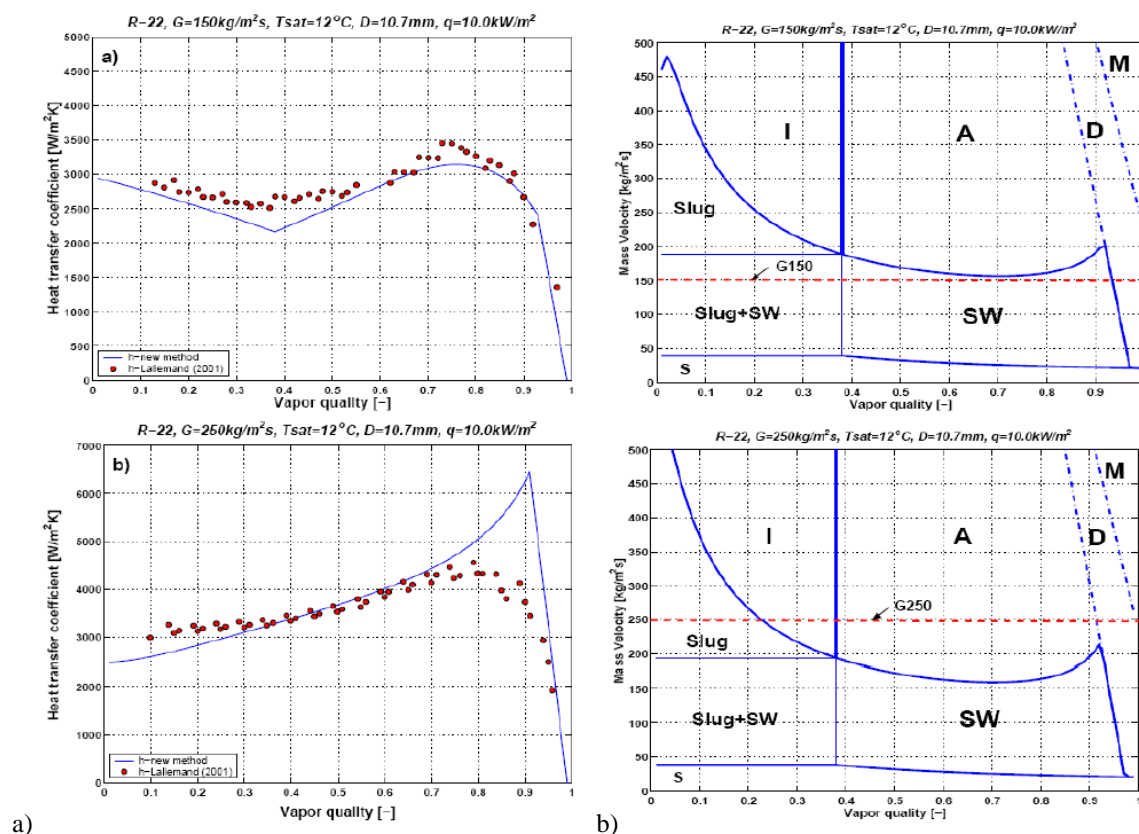
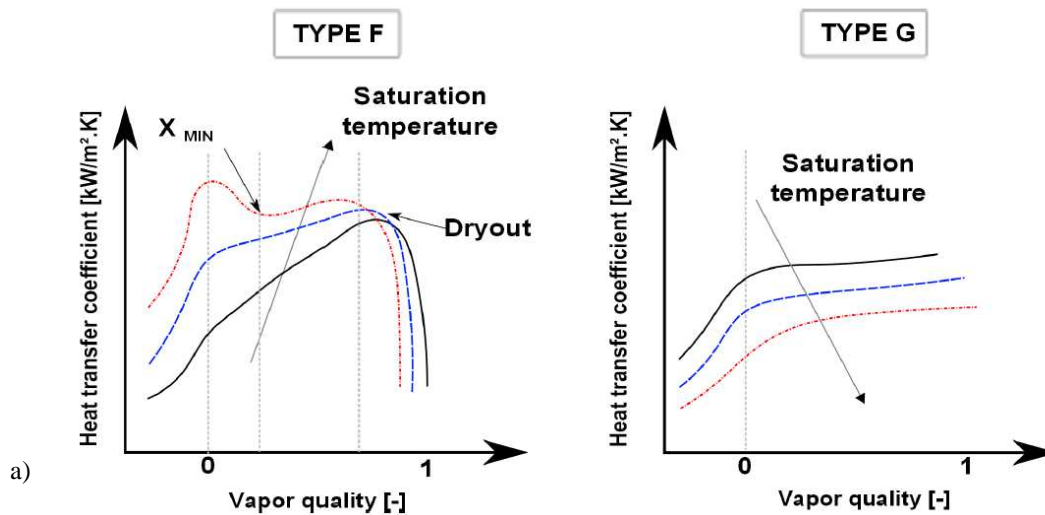


Figure 1.32: a) Comparison of experimental heat transfer data on a horizontal flow with new prediction method
 b) Corresponding flow patterns map for horizontal flow

This association of maps and models usually offer a good representation of physical phenomena. However as already mention for the flow pattern maps, they may not have been validated for the

operating conditions which would be encountered in typical sorption refrigeration systems. Nevertheless, recent papers reported data on the influence of saturation temperature on the heat transfer coefficient. These data were gathered and handled by Charnay (2014). In his thesis, Charnay reported two opposite trends of evolution of the heat transfer coefficient with the saturation temperature: an increase of the heat transfer coefficient when increasing saturation temperature (noted “Type F” on Fig. 1.33) and a decrease of the heat transfer coefficient when increasing the saturation temperature (noted “Type G”). The schematic evolution of the heat transfer coefficient with the influence of saturation temperature as well as the experimental conditions for which these results were obtained are shown on Fig. 1.33.



Author	Fluid	Geometry	d_h [mm]	\dot{q} [kW/m ²]	G [kg/m ² ·s]	T_{sat} [°C]	x [-]	TYPE
[Greco and Vanoli (2005)]	R-410A/R-404A	circular	6.0	11-39	290-1100	-15-23.5	0-1.0	F
[Da Silva Lima et al. (2009)]	R-134a	circular	13.84	7.5-17.5	300-500	5-20	0.01-0.99	F
[Del Col (2010)]	(*)	circular	8.0	9-53	200-600	25-45	0-1.0	F
[Tibiricá and Ribatski (2010)]	R-134a/R-245fa	circular	2.3	5-55	50-700	31-68	0.05-0.99	F
[Agostini et al. (2008)]	R-245fa	rectangular	0.336	36-1900	281-1501	24-44	0.15-1.0	F
[Vakili-Farahani et al. (2013)]	R-245fa/R-1234ze	rectangular	1.3-1.45	3-107	50-400	30-70	0-1.0	F
[Ong and Thome (2011b)]	(**)	channel	1.03-3.04	4.8-221.5	200-1290	31-35	0-1.0	F
[Ali et al. (2011)]	R-134a	circular	1.70	2-156	50-600	27-32	0-1.0	F
[Basu et al. (2011)]	R-134a	circular	0.5-1.6	0-350	300-1500	15-45	0-1.0	F
[Grauso et al. (2013)]	CO ₂ /R-410A	circular	6.0	5-20	150-500	5-42	0-1.0	F
[Saisorn et al. (2010b)]	R-134a	circular	1.75	1-83	200-1000	31-50	0-0.95	G
[Choi et al. (2007b)]	CO ₂	circular	1.5-3	20-40	200-600	-10-10	0-1.0	G
[Kaew-On and Wongwises (2009)]	R-410A	rectangular	3.48	5-14.25	200-400	10-30	0-1.0	G

(*) R-22/R-134a/R-125/R-410A - (**) R-134a/R-236fa/R-245fa

b)

Figure 1.33: a) Schematic of the typical heat transfer coefficient trends depending on the saturation pressure and b) information reported on experimental conditions (at the bottom) (Charnay, 2014)

Although most of the experiments analyzed by Charnay were conducted for saturation temperatures close to the operating saturation temperature usually encountered in the evaporator of sorption systems, the corresponding reduced pressures are higher than the reduced pressure encountered in sorption machines using water as refrigerant. Besides, almost none of these studies were done with water as the working fluid. As liquid-vapor phase-change phenomena depend on the fluid density, surface tension and viscosity, the flow boiling heat transfer characteristics observed in low pressure evaporators are quite different than those reported above. Indeed, probably also due to the low evaporation mass flow rate, a flow regime more similar to falling film evaporation than annular flow could be observed in the upper part of the tube (Chang *et al.*, 2012). Thus, falling film evaporation phenomena are introduced thereafter.

1.6 Falling film evaporation

In technical processes, evaporation generally takes place from liquid films, drops or jets. Films may flow on a heated surface as a result of gravity or of vapor shear. As a liquid flows down due to the gravity, different falling film regimes could appear.

1.6.1 Falling film regimes

Falling film regimes depend on the temperature of the fluid and the mass flow rate. Three main flow regimes are commonly accepted depending on the local Reynolds number (Eq. 1.44): the turbulent flow, the wavy-laminar flow and the laminar flow.

$$\text{Re}_x = \frac{\rho u \delta_x}{\mu} \quad (1.44)$$

As generally the fluid mass flow rate decreases along with the process of evaporation (Fig. 1.34), the Reynolds number decreases and so, the flow tends to progress from turbulent to wavy-laminar and then to laminar. The progression from the turbulent flow to the wavy-laminar flow takes place continuously without any possibility to define a clear boundary between these two regimes.

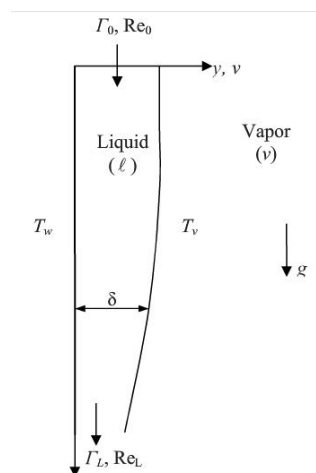


Figure 1.34: Schematic of a film flowing down on a vertical plate

Regarding heat transfer, heat is transferred to the film surface by conduction and/or convection and by evaporation processes that take place at the surface of the film. The magnitude of the phase-change is directly related to the film thickness and whether the film is laminar or turbulent (Thome, 2004).

The three regimes commonly accepted and some correlations of heat transfer developed for each of these regimes are described thereafter. The values of the local Reynolds number given by Eq. 1.44 to define the transition between the different falling regimes were given by Grossman (1986) but these values may vary from one source to one another.

- **Laminar falling film regime - $\text{Re}_x < 20$:** This regime is obtained when the film flows down without any perturbations on its liquid-vapor interface. It is well described by Nusselt's model although this model was developed for falling film condensation (Thome, 2004; Claudaze, 1996). The dimensionless thickness of the film can thus be calculated as follows:

$$\delta^+ = \delta \frac{u^*}{\nu} = 0.866 \text{Re}_x^{0.5} \quad (1.45)$$

With δ the average thickness of the film and u^* the friction velocity:

$$u^* = \sqrt{\frac{\mu \left(\frac{du}{dz} \right)_w}{\rho_1}} \quad (1.46)$$

According to the Nusselt theory, the heat flux could be calculated as follow:

$$\dot{q} = h_x (T_{\text{sat}} - T_w) = \frac{\lambda_1}{\delta_x} (T_{\text{sat}} - T_w) \quad (1.47)$$

- **Wavy-laminar falling film regime - $20 < \text{Re}_x < 1600$:** During this regime, capillary and inertial waves are flowing down on the surface of the film (Fig. 1.35). The heat transfer achieved during this regime depends on the Reynolds number and thus on the location along the plate. It could be enhanced due to the development of surface waves.

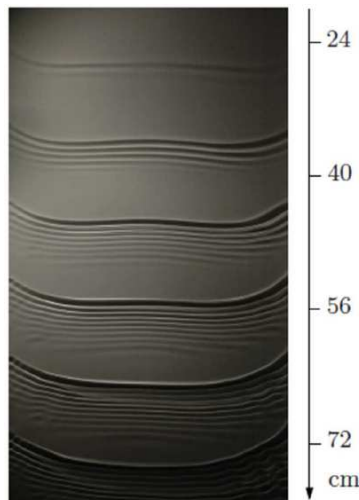


Figure 1.35: Pictures of inertial and capillary waves (Koffman, 2014)

Despite the presence of such waves, Nusselt's model can also be applied for this regime (Clauzade, 1996) and the dimensionless thickness of the film can thus be calculated as follows:

$$\delta^+ = \delta \frac{u^*}{\nu} = 0.7746 \text{Re}_x^{0.5} \quad (1.49)$$

The heat transfer could be also calculated using the Kudateladze theory:

$$\frac{\bar{h}_H (v^2/g)^{1/3}}{\lambda_1} = \frac{\text{Re}_{\delta_x}}{1.08 \text{Re}_{\delta_x}^{1.22} - 5.2} \quad (1.50)$$

With

$$\text{Re}_{\delta_x} = \frac{4 \dot{M}_x}{W \cdot \mu_1} \quad (1.51)$$

And
$$\dot{M}_x = \rho_1 \cdot \frac{\rho_1 - \rho_v}{\mu_1} \cdot W \cdot g \cdot \frac{\delta_x^3}{3} \quad (1.52)$$

- **Turbulent flow - $Re_x > 1600$:** During this regime, the number of waves observed increases. They overlap with one another and the whole plate is covered with waves. No clear transition is observed between the wavy-laminar regime and the turbulent flow pattern. The heat transfer could be calculated using the Labunstov theory:

$$\frac{\bar{h}_H (v^2 / g)^{1/3}}{\lambda_1} = \frac{Re_{\delta_x}}{8750 + 58 \cdot Pr_1^{-0.5} \cdot (Re_{\delta_x}^{0.75} - 253)} \quad (1.53)$$

Although these three regimes are commonly accepted and defined, the regimes experimentally observed are most of the time quite different. Indeed, formation of rivulets was reported by many authors as well as the presence of dry areas due to the presence of dry patches or due to the flow distribution. Besides, in the case of a film flowing on a vertical plate, even for low Reynolds number, inertial and capillary waves were observed. At $Re_x < 5$, these waves are 2D and then gradually 3D as the local Reynolds number increases (Nosoko *et al.*, 1996).

Different models were developed for the different falling film regimes. But, for all the models, the flow configurations simulated on flat plates are significantly different from those observed experimentally (formation of rivulets, dry patch, etc.). Results obtained from models were thus significantly different than experimental results.

Most of the experimental studies on falling film evaporators were performed with a binary mixture for which heat and mass transfer were coupled (Zaitsev *et al.*, 2004, Goulet, 2011, Flores, 2014, etc.) and/or with a pure component but for tube falling film evaporators. Review on these evaporators was proposed by Thome (2004) and Fernandez-Seara and Pardinias (2014). Few studies focused on falling film in vertical plate with a pure fluid as working fluid unless in order to compare binary mixtures evaporation performance with pure fluid evaporation performance (Kim and Infante Ferreira, 2008, Koffman, 2014). It seems however interesting to notice that several of these experimental studies revealed that the heat transfer coefficient of falling film evaporation is comparable or even greater than that of pool boiling (Chien and Tsai, 2011, Fernandez-Seara and Pardinias, 2014). It was also several times observed that the falling film heat transfer coefficient remains constant with heat flux (under non-boiling condition) and that it increases when the saturation temperature increases (Fernandez-Seara and Pardinias, 2014).

1.6.2 Wettability and Dry patch

During their experiments, Kim and Infante Ferreira (2008) observed that most of the time, the flow was wide at the top and narrower as it flowed down. Thus the plate was not completely wet. They noticed that the wet surface area changes with the flow rate and the heat flux. For water, they however found that for a Reynolds number above 200, the heat transfer area was completely wet.

The ability of a fluid to wet the surface or not is a consequence of the surface tension solid/liquid, liquid/gas, gas/solid. It can be expressed in an energy point of view since a geometrical change of shape of the fluid induces a change in its energy.

The liquid flows in a rivulet which can be locally stopped by a stagnation point (noted G on Fig. 1.36). The shape of the free surface at this point depends on the liquid flow rate. The falling film flow rate to avoid the breakdown of the film can thus be studied by analyzing the force balance at the stagnation

point and by analyzing the total energy of the rivulet. Thus, by minimizing the total energy of the rivulet, it is possible to determine the lowest flow rate needed to ensure that the surface remains covered by a continuous, thin liquid film. This is the MWR: Minimum Wetting Rate.

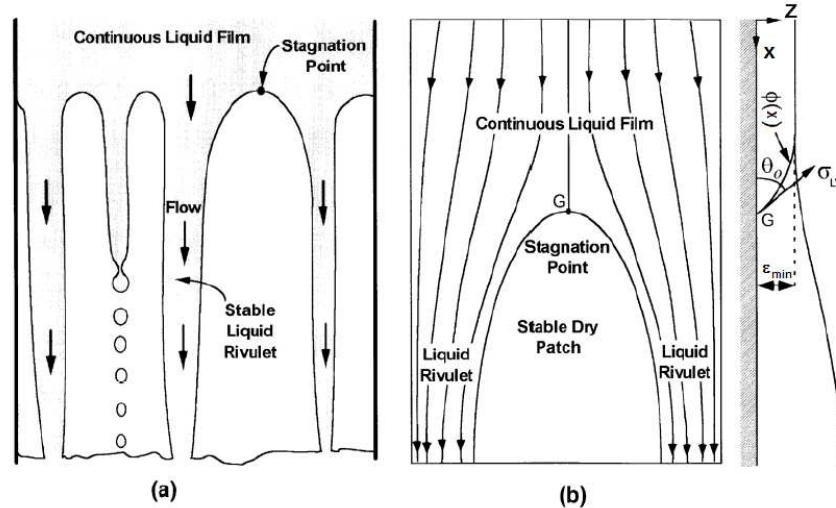


Figure 1.36: Stable dry patch following the breakup of a liquid film flowing down a vertical surface a) observed in a two-phase thermosyphon b) shown schematically (El-Genk and Saber, 2001)

El-Genk and Saber (2001) studied this minimum flow rate. As the total energy of a stable, symmetrical liquid rivulet is the sum of the kinetic energy and the interfacial energy, they tried to minimize these two quantities. They found that the total energy is minimized when the dimensionless film thickness is:

$$\delta_{\min}^+ = (1 - \cos \theta)^{0.22} \quad (1.54)$$

With θ the angle of wettability as defined in Fig 1.36, and that the MWR is:

$$\Gamma_{\min} = 0.67\delta_{\min}^{+ 2.83} + 0.26\delta_{\min}^{+ 9.51} \quad (1.55)$$

Kinetic forces are stabilizing the liquid film: inertia of the film tends to maintain its initial velocity profile. On the contrary, surface forces are destabilizing the liquid film in the case of liquid-wall contact. In the case of liquid-gas contact, surface forces could be stabilizing if the film is being cooled by the wall or if the vapor is condensing on the film. If the liquid rivulet is not stable, the rivulet will breakup when a perturbation will occur (local change of surface tension, etc.) and a dry patch will be formed (Fig. 1.36).

A dry patch can be the cause of instability as it affects the following forces that act on the film (Gross, 1994):

- Liquid inertia forces which favors the rewetting of the dry patch
- Surface tension forces which tend to enlarge the size of the dry patch

- Marangoni effect which tends to transport liquid away from the edge and thus enlarge the size of the dry patch
- Vapor inertia forces which help to increase or decrease the size of the dry patch depending on the direction of the vapor
- Interfacial shear forces which in one hand tend to spread the liquid and rewet its top edge and in the other hand, which tend to elongate its lower edge.

The formation of dry patch is responsible for a decrease of the heat transfer and must be avoided to ensure a high heat transfer coefficient.

1.7 Closing remarks

In order to optimize the size of compact subatmospheric evaporators, it is fundamental to know and comprehend two-phase phenomena occurring at such low pressure. This literature review thus provides a basic description of two-phase heat transfer mechanisms as they are currently understood. As a conclusion, several points could be highlighted:

- Few publications are found regarding boiling at subatmospheric pressure. General features of boiling at low pressure are the high bubbles growth rates, the large bubble volumes at detachment, the long waiting time between bubbles, and the deterioration of the boiling performance. Few studies focused on the fundamental phenomena of water pool boiling on a plain plate surface. The analysis of the entire bubble life cycle remains to be done despite its special fundamental interest because of the particular bubble mushroom shape at such low pressure.
- Boiling heat transfer in narrow space is enhanced when compared to free boiling at low heat fluxes. Vertical configuration should be favored in order to enhance the heat transfer.
- In flow boiling (forced convective boiling), the heat transfer achieved depends on the flow regime and on the saturation temperature. To date, no studies of two-phase flow phenomena cover the operating conditions which would be encountered in typical sorption refrigeration systems (low reduced pressure ranging from $2 \cdot 10^{-4}$ to $5 \cdot 10^{-5}$ depending on the fluid nature and on the evaporation temperature and low mass flow rate).
- According to Chang *et al.* (2012), in the channel of a plate evaporator, periodic appearance of a bubble is observed. As the bubble grows, a motion of the free surface is observed. The bubble then surges out and the liquid that encapsulated the bubble is spread on the wall. A liquid film is formed and evaporation immediately takes place. To go further in the understanding of phenomena occurring inside compact heat exchangers, it thus seems fundamental to understand falling film phenomena at such low pressure. But here again, studies focusing on the fundamental phenomena of falling film evaporation on a vertical plate especially at low pressure are scarce. Heat transfer correlations developed shows high discrepancy with experimental data due to the complexity of falling regime observed. Indeed, the formation of a dry patch and/or a rivulet is often observed due to a local change of surface tension, liquid thickness, evaporation process, etc. disturbing the flow. This observed flow,

much more complicated than stabilized flow, is thus significantly different than the flow configuration often simulated.

There is a notable lack on fundamental knowledge on two-phase phenomena at subatmospheric pressure. This lack of knowledge impacts on the design and on the understanding of phenomena occurring in low pressure evaporators. The aim of the present work is to go further in the understanding of the physical phenomena ruling the behavior of the subatmospheric evaporator. In this purpose, phase-change phenomena are studied in two different scales:

- At the bubble scale: an experimental test bench was built to study the bubble dynamics and the heat transfer phenomena of water at a nucleation site created on the center of a copper horizontal plane surface.
- At the evaporator scale: a second experimental test setup was designed and built to allow the observation and the thermal study of the water vaporization in a channel of a plate heat exchanger of standard dimension.

2 FUNDAMENTAL APPROACH OF PHASE-CHANGE PHENOMENA AT SUBATMOSPHERIC PRESSURE: BOILING ON A HORIZONTAL PLANE SURFACE

The objective of this chapter is to highlight the specific characteristics of water pool boiling at subatmospheric pressure on a horizontal copper plane surface. Section 2.1 details the experimental test setup built to characterize the pool boiling of water at pressure down to 0.8 kPa and the procedure followed during the study. As the specificity of the water pool boiling at subatmospheric pressure lies in the non-homogeneity of the boiling environment, Section 2.2 is dedicated to the understanding of this phenomenon. Its influence on the bubbles size and on the bubble growth is analyzed (section 2.3). In this last section, as some authors mentioned significant fluctuations of the wall superheated in certain conditions of imposed heat flux (Van Stralen et al., 1975; McGillis et al., 1991a&b) boiling curves for pressures ranging from 0.8 kPa to 100 kPa were plotted as the instantaneous heat flux vs. the instantaneous wall superheat for a given heat flux imposed at the heater. Same kind of boiling curves were plotted for a vapor pressure of 1.2 kPa and height of the liquid level of 200 mm, 150 mm and 100 mm.

2.1 Experimental test setup and procedures

2.1.1 Experimental test facility

2.1.1.1 The vessel

The experimental test facility consists of a 200 mm inner diameter and 420 mm high stainless steel cylinder (Fig. 2.1). Four circular viewports (diameter 100 mm) arranged on the side face of the chamber allow observing the sample as well as visualization and recording of the images. A fifth viewport of the same diameter is located at the base of the vessel and can be used to insert the test sample into the vessel.

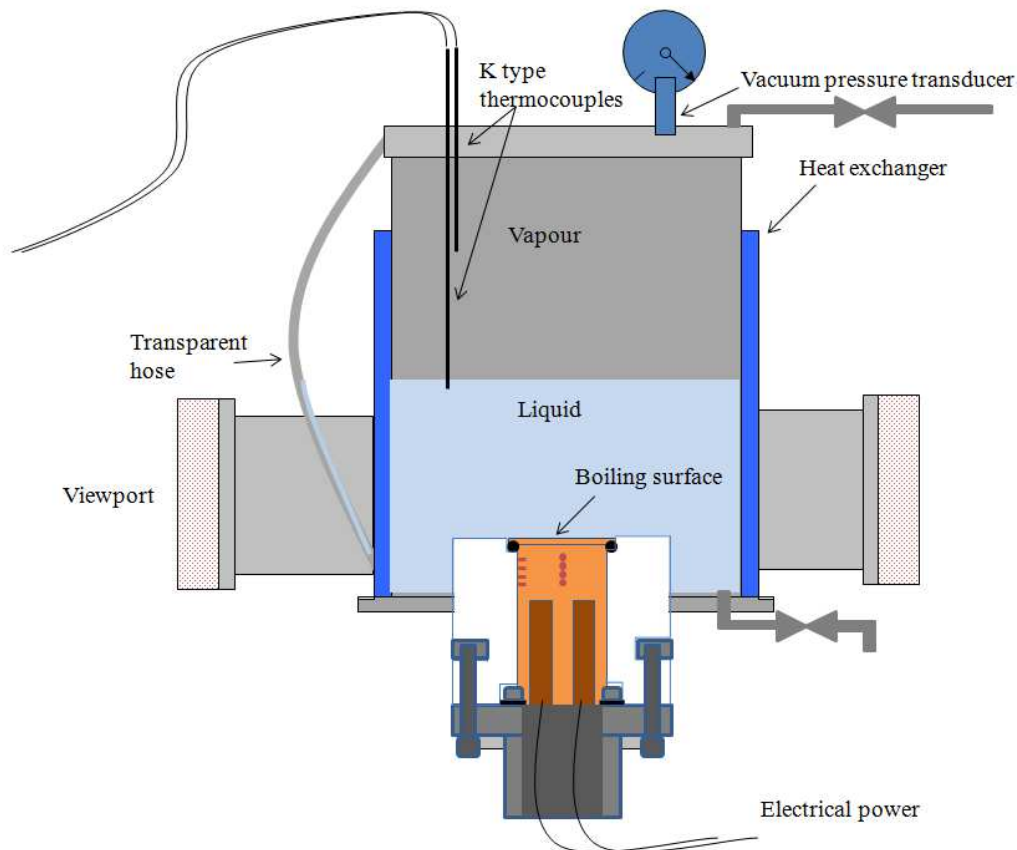


Figure 2.1: Detail of the pool boiling device in horizontal configuration

In the present study, all experiments are performed using distilled water as the working fluid. A valve connected to a vacuum pump at the top of the vessel allows the emptying of the chamber with gas. Another valve situated at the bottom of the vessel allows the filling and the emptying of the chamber with the working fluid. In order to estimate the height of the liquid level filled in the vessel, a transparent hose is connected to the chamber. A heat exchanger located inside the wall of the boiling vessel through which circulates cooling water allows controlling the fluid temperature between 0 °C to 35 °C. Two thermocouples are placed into the chamber to measure the vapor and the liquid temperatures. The latter thermocouple is located at a distance of 150 mm from the bottom of the vessel (i.e. at a distance of 100 mm from the surface boiling). Two vacuum pressure transducers Kobold SEN type with a working pressure range of 0 – 1 bar and 0 – 0.16 bar are used to measure the pressure of vapor.

All components assembled to form the experimental test setup are made in vacuum technology (ISO-K) to ensure high gas tightness.

2.1.1.2 The sample

The test heater is a 40 mm diameter and 78 mm high cylindrical copper block (Fig. 2.2a). Two cartridges heaters of 600 W each are inserted at the bottom of the cylinder in order to impose an electrical heat flux. Two rows of four K-type thermocouples are located along this copper block to allow the estimate of the instantaneous wall temperature and heat flux at the boiling surface by means of an inverse heat conduction method and the Fourier's law. Heat fluxes thus estimated are referred thereafter as instantaneous heat fluxes. A fin (thickness = 1.5 mm, diameter = 50 mm) is located at the extremity of the copper block in order to avoid nucleation at the periphery of the fin and therefore promote nucleate boiling on an artificial nucleation site created by mechanical indentation at the center of the disk. The nucleation site is conical and has a diameter of 110 μm and a depth of 73 μm . The boiling surface is polished with a diamond paste until reaching a mean roughness of $R_a = 0.4 \mu\text{m}$ (measured with a confocal microscope). The entire area of the boiling surface is equal to 19.6 cm^2 .

The test heater is insulated on its perimeter with PTFE and fixed to a stainless steel flange (Fig. 2.2b). The outer edge of the boiling surface is also sealed with a cyanoacrylate adhesive to prevent the liquid from leaking. An O-ring seal is placed between the copper block and the PTFE in order to ensure gas-tightness. For the same purpose, a plate seal is placed between the bottom of the block copper/PTFE and the stainless steel flange. The stainless steel flange permits to insert the test heater at a certain distance from the bottom of the vessel in order to have the best view of the boiling surface. The hole in the center of the flange is used as an open space for the passage of the thermocouples and the cables of the cartridges heaters.

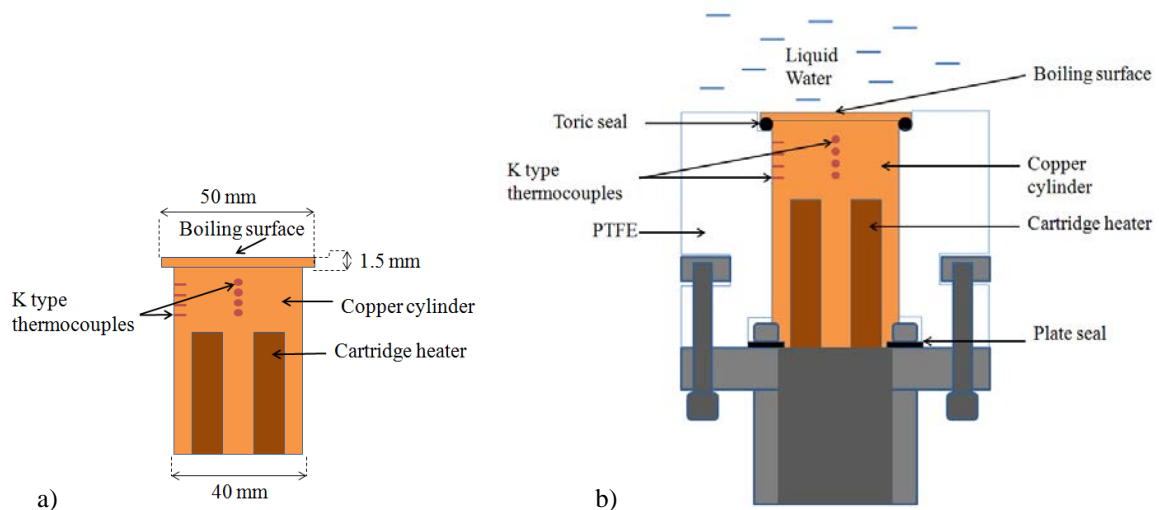


Figure 2.2: Detail of a) the copper block, b) the whole test heater

2.1.1.3 The visualization test facility

In order to capture pictures of bubbles growth and detachment, a Photron Fastcam 1024 PCI high speed camera is placed near one viewport. The boiling area is illuminated through the opposite viewport by means of a 400 W daylight metal halide lamp (Fig. 2.3). The frequency of this back-light is 200 kHz. A tracing paper placed against this opposite viewport is used to disperse the light

homogeneously. The acquisition frequency of the camera is set to 1000 images per second to obtain the best trade-off between acquisition speed and image size (1024 x 1024 pixels).

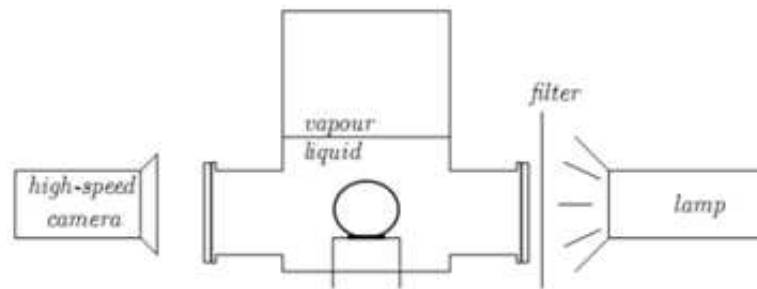


Figure 2.3: Visualization facility

2.1.2 Experimental procedures

Once the sample is inserted inside the vessel, the tank is evacuated and filled with the water. The tank containing the water is then maintained at the water vapor saturation pressure for 60 hours. During this lapse of time, the tank is periodically evacuated. The vapor pressure is then set to the desired value by controlling the fluid temperature that circulates in the doubled-skin of the boiling vessel. Once the thermal equilibrium is reached, the tank is evacuated another time. As a hysteresis effect had been observed, - which is a usual phenomenon in boiling due to nucleation site activation and de-activation and to boiling regime transition -, it was chosen to realize experiments at decreasing heat fluxes. Thus, an increasing electrical power is progressively set to the cartridge heaters. This electrical power is set by ramp. Steady state, i.e. stabilization of the pressure and temperature in the vessel, is waited before any increase of the electrical power imposed but the corresponding data are usually not recorded. Once the highest imposed heat flux needed for the study is reached and steady state obtained, the tank is evacuated one last time. Then one hour is waited before starting the acquisition. The points obtained for low heat flux were obtained by decreasing the electrical power imposed to the cartridge heater by ramp and then waiting at least one hour. Each point recorded for the study was collected every three seconds during ten minutes.

Example of hysteresis phenomena obtained during this study is shown on Appendix A.

2.1.3 Measurement techniques

Several temperature and pressure measurements are performed at different locations inside the vessel and inside the test heater. Regarding temperature measurements, two K-type thermocouples are placed in the vessel. One is placed in the vapor phase above the free surface, the other one in the liquid at a distance to the surface boiling of 100 mm. Two rows of four thermocouples are located along the copper block of the test heater. All ten thermocouples cold junctions are enclosed in an insulated box in which the temperature is measured by a platinum resistance thermometer Pt-100. All the thermocouples were calibrated together with their acquisition chains. They were immersed in a stirred bath with controlled temperature and their voltages were measured at 13 different temperatures from 0 °C to 200 °C to obtain their calibration curves. The absolute uncertainties on the temperature were estimated to be ± 0.1 K.

All measurements are performed by a Keithley 2700 acquisition unit which is controlled by a Labview program.

2.1.3.1 Experimental heat flux and boiling surface temperature estimation

The heat flux dissipated to the fluid by the boiling surface and the boiling surface temperature are estimated by means of an inverse method using the two rows of four thermocouples along the copper block of the test sample. In order to determine with accuracy the position of these thermocouples, the variation of altitude along the rod is measured with a confocal microscope for the two rows (Fig 2.4). The heat flux across a section of the copper cylinder is assumed to be uniform. The thermal conductivity of the copper is assumed constant and equal to $398 \text{ W.m}^{-1}.\text{K}^{-1}$ within the temperature range investigated.

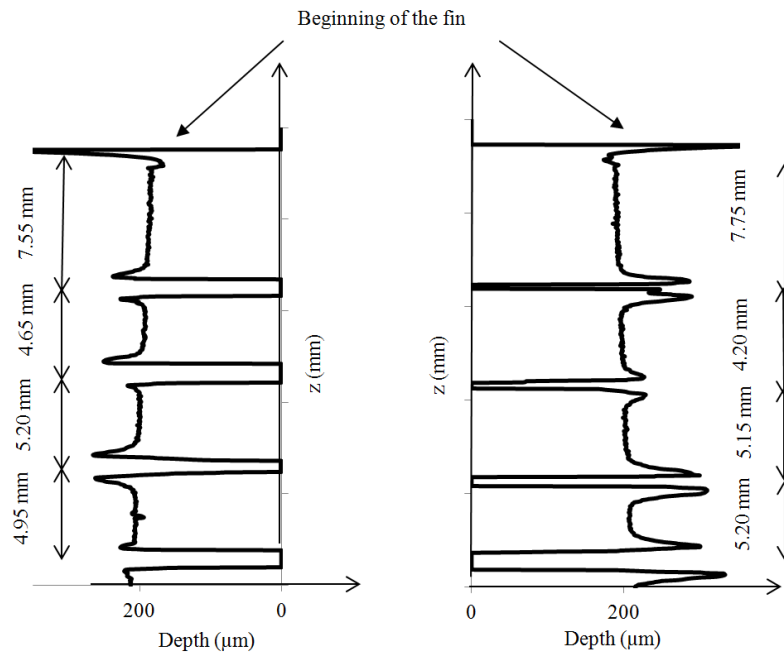


Figure 2.4: Positions of the thermocouples along the copper block for a) row 1 b) row 2

An example of temperature data obtain from these two rows is shown on the figure 2.5.

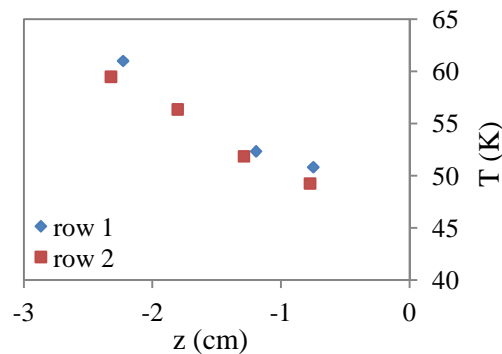


Figure 2.5: Test sample thermocouples temperature example

Assuming a uniform heat flux across a section of the copper cylinder and a constant copper thermal conductivity within the temperature range investigated, the temperature along the z-axis can be written as follow:

$$T(z) = az^2 + bz + c \quad (2.1)$$

In this case, c is temperature of the boiling surface.

From the four temperature measurements, a second order polynomial data fit allows the determination of the coefficient a, b and c and thus the determination of the temperature of the boiling surface and the heat flux at the boiling surface. Indeed, the surface heat flux is academically calculated from the Fourier's law:

$$\dot{q}(z) = -\lambda_{Cu} \left. \frac{dT}{dz} \right|_{z=0} \quad (2.3)$$

As the temperature along the z-axis can be fitted by Eq. 2.1, Fourier's law can be written in this case as:

$$\dot{q}(z) = -\lambda_{Cu} (2az + b) \quad (2.4)$$

The coefficient b determined previously thus represents the heat flux at the boiling surface.

By derivation of Eq. 2.1 a second time, one would obtain:

$$a = \frac{1}{2} \frac{d^2T}{dz^2} = -\frac{1}{2\lambda_{Cu}} \frac{d\dot{q}}{dz} \quad (2.5)$$

where $\frac{d\dot{q}}{dz}$ is the rate of heat flux dissipation along the rod. As the value of a is very low, heat fluxes dissipation can be neglected. A linear extrapolation assumption could thus be used to estimate the surface temperature and the heat flux. According to the criterion developed by Héas (2001),

$$\Delta t_i = \frac{\alpha \Delta t}{d^2} \quad (2.2)$$

this assumption is acceptable if the criterion Δt_i is higher than 1. Δt stands for the time step between the acquisition of two data and d for the distance between two thermocouples. As this criterion is always satisfied in this study this assumption is thus acceptable.

The respective uncertainties on the temperature and thermocouple position measurements are estimated to be ± 0.1 K and ± 0.4 mm. This leads to a heat flux uncertainty of 10 % for high heat flux and more than 50 % for very low heat flux (Appendix B). Additional error associated with the thermal conductivity of copper should be included but as this error has no influence on the temperature computations and is an offset error, it does not influence the differences in the observed trends.

If the eight thermocouples are operational, the heat flux dissipated to the fluid by the boiling surface and the boiling surface temperature are calculated for the both rows. The average value of the heat flux and the boiling surface temperature can then retained. However, due to the mounting procedure of the test sample to the stainless steel flange, breaking of thermocouples occurred. Thus, calculations obtained solely for a row with all the thermocouples operational was then retained.

2.1.3.2 Image processing

The numerical pictures are analyzed using a home-made image processing code developed under MATLAB® environment and inspired by the image processing code used by Siedel *et al.* (2008). The detection of the edge of the bubble permits to determine the bubble geometrical characteristics. As photos describe the bubble only in two dimensions, the bubble is divided into slices thick of one pixel to calculate its volume. The volume is thus the sum of each cylinder created. This method has the advantage of taking into account the whole contour of the bubble and the error on the volume determination remains low. Once the volume is estimated, if required, the value of the equivalent diameter can be calculated assuming a spherical bubble of same volume.

2.2 Non-homogeneity of the boiling environment

At subatmospheric pressure, as the pressure is very low, the static head imposed by the liquid height can be of the same order of magnitude as the fluid saturation pressure. As a consequence, the pressure and saturation temperature (or subcooling degree) fields of the bulk fluid in the vessel are highly non-homogeneous, which affects the bubble growth dynamics and the bubble shape. As the height of the liquid level is non negligible, a variation of the height of the liquid level also means a variation of pressure. The local pressure varies linearly with depth z ($z = 0$ refers to the free surface level). But, the local saturation temperature ($T_{\text{sat}}(z)$) follows a natural logarithm law with the local pressure. The variation of the local saturation temperature with the local pressure is thus highly significant at very low pressure compared to atmospheric pressure.

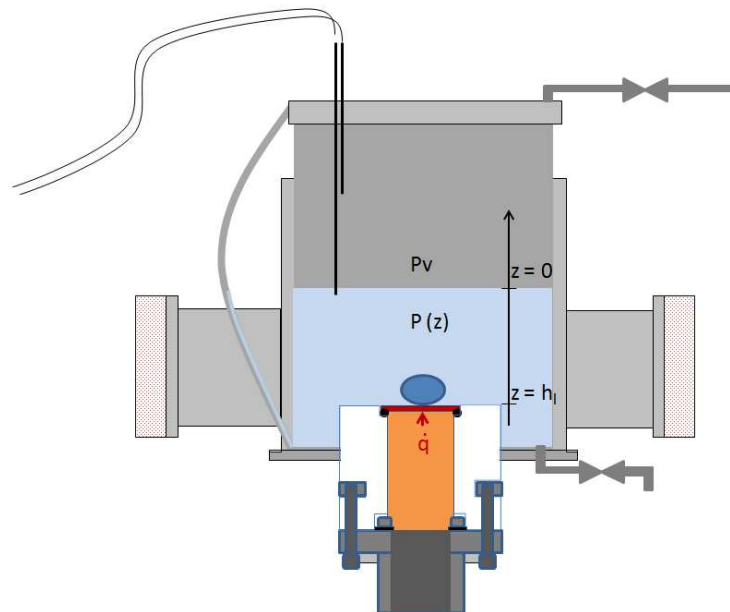


Figure 2.6: Definition of notations used

As one assumes that saturated conditions prevail in the vessel, the temperature at the free surface level is the saturation temperature of the vapor pressure. This temperature is also the temperature of the bulk liquid ($T_1 = T_{\text{sat}}(0)$). As the pressure is non homogeneous in the vessel, the saturation temperature and so, the subcooling degree ($T_{\text{sat}}(z) - T_1$) also strongly depends on the depth. The boiling environment is thus also non-homogeneously subcooled. The maximal subcooling degree is reached at the level of the boiling surface since the local pressure is maximal at this point. Fig. 2.7 shows the profile of the saturation temperature of water along the vertical axis, from the free surface level.

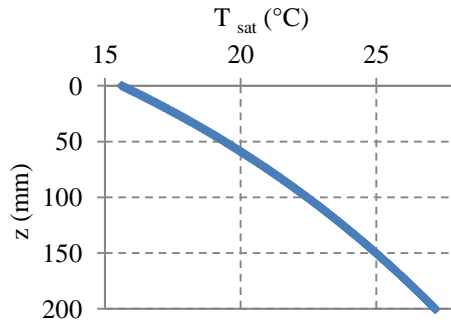


Figure 2.7: Profile of the water saturation temperature along the vertical axis for a vapor saturation pressure of 1.78 kPa ($T_{\text{sat}} = 15.7 \text{ }^\circ\text{C}$)

The non-homogeneity of the pressure and saturation temperature fields leads to the variation of the fluid thermophysical properties in the bulk fluid and thus to the observation of phenomena different than those observed at atmospheric pressure. However, the issue of the study of water pool boiling at subatmospheric pressure lies not only in the impact of the non-homogeneity on bubble growth and shape but also in the difficulties to impose comparables operating conditions. Vapor saturation pressure, pressure at the boiling surface, liquid height, subcooling degree ($T_{\text{sat}}(z) - T_1$) and subcooling gradient (dT_{sat}/dz) are dependent. Local pressure can be imposed by varying the saturation vapor pressure and/or by varying the height of the liquid level.

If one imposes a vapor saturation pressure and reduces the height of the liquid level, the local pressure at the boiling surface decreases. The same observation can be done if one imposes a height of the liquid level and reduces the vapor saturation pressure. But, in the first case, the subcooling degree would decrease whereas it would increase in the second case. Figure 2.8 shows that adjusting the two parameters (vapor saturation pressure and height of the liquid level) allows to obtain a given maximal subcooling degree. But as one does so, the pressure at the boiling surface level is not only different, but the gradient of subcooling degree is also different. For example, a given maximal subcooling degree of 9 K would be reachable for vapor saturation pressure of around respectively 3 kPa, 7 kPa and 11 kPa (noted 1, 2, 3 on fig. 2.8 and 2.9) for the three different heights of the liquid level (200 mm, 400 mm, 600 mm) (Fig. 2.8). But, the subcooling gradients near the boiling surface would however be respectively $3.7 \text{ K}\cdot\text{cm}^{-1}$, $1.8 \text{ K}\cdot\text{cm}^{-1}$ and $1.2 \text{ K}\cdot\text{cm}^{-1}$ (Fig. 2.9).

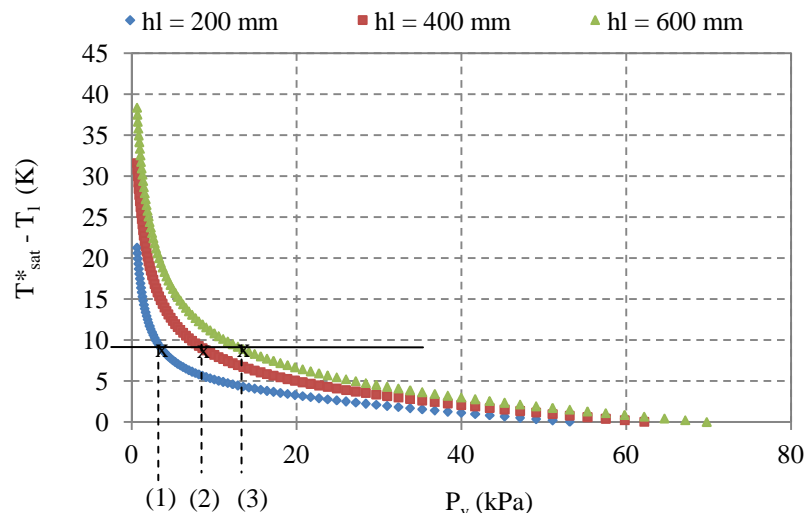


Figure 2.8: Evolution of the maximal subcooling degree versus the vapor saturation pressure and the liquid height

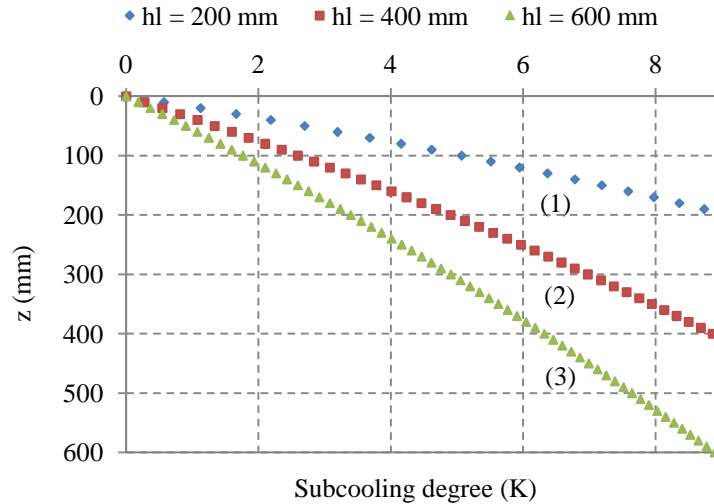


Figure 2.9: Profile of subcooling degree along the vertical axis for vapor saturation pressure of (1) 3 kPa ($T_{\text{sat}} = 24 \text{ }^\circ\text{C}$), (2) 7 kPa ($T_{\text{sat}} = 39 \text{ }^\circ\text{C}$) and (3) 11 kPa ($T_{\text{sat}} = 48 \text{ }^\circ\text{C}$) at the free surface level ($z = 0$)

The bubble growth dynamics depends on the heat and mass transfer at the bubble interface. As the bubble diameter in subatmospheric conditions can reach 15 cm, it is obvious that the analyses done under the assumption of small bubbles growing in fairly homogeneous saturation temperature and pressure field do not stand. The influence of the subcooling degree on bubble dynamics has as much importance as the change of fluid thermophysical properties like vapor density and surface tension due to the decrease of pressure.

2.3 Pool boiling in horizontal copper plane surface

2.3.1 Bubbles dynamics

2.3.1.1 Bubble shape

Experiments were conducted for pressure ranging mainly from 5 kPa to 0.8 kPa, heat flux ranging from $0.9 \text{ W}\cdot\text{cm}^{-2}$ to $30 \text{ W}\cdot\text{cm}^{-2}$ (critical heat flux not reached) and height of the liquid level ranging from 100 mm to 200 mm. Because of the highly non-homogeneous boiling environment, various shapes and sizes of bubbles in subatmospheric pressure pool boiling were observed. These shapes do not only depend on the pressure imposed but also on the history of the bubbles, i.e. size and frequency of preceding bubbles and on the movements of the free surface interface (due to the rise of bubbles). That is why even during a single experiment, diverse shape of bubbles can be observed. However, despite this diversity, some shapes can be regarded as characteristic of the subatmospheric pressure pool boiling (fig. 2.10).

At the first moments of the growth ($t < 10 \text{ ms}$), the bubble is hemispherical. As the volume of the bubble is increasing, the bubble turns to a flattened spheroid shape. The vertical curvature radius is becoming lower than the horizontal curvature radius. Then, the radius of the dry area decreases as the center of gravity of the bubble rises which results in the formation of a conical base. The bubble then detaches. As it detaches, a liquid jet following the ascension of the bubble is observed. This jet passes right through the bubble penetrating into its lower side.

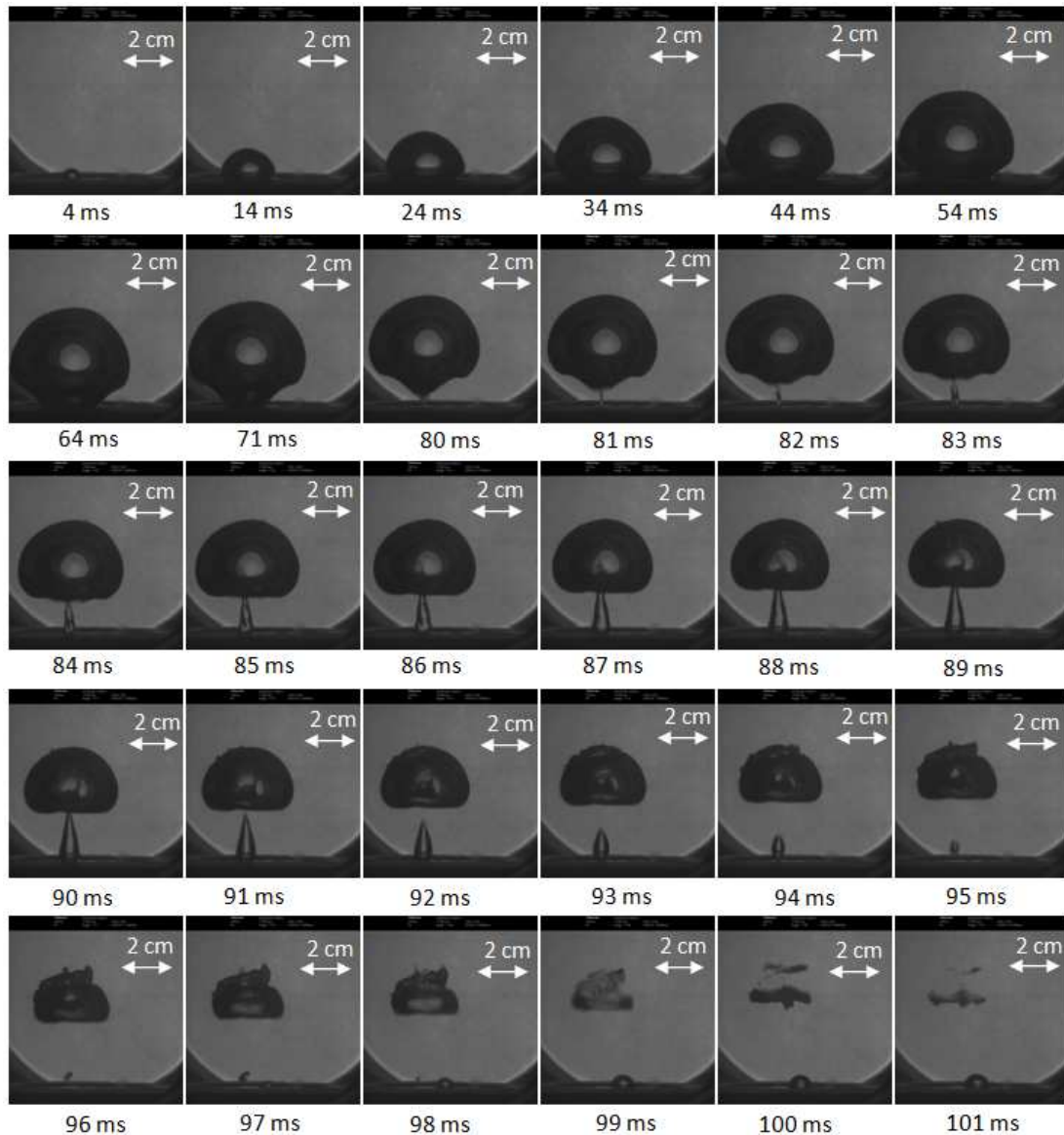


Figure 2.10: Bubble growth with liquid and vapor jets following the bubble departure ($P_v = 1.2$ kPa, $T_1 = 10^\circ\text{C}$, $h_1 = 200$ mm, $\dot{q} = 22.6$ W.cm²)

A vapor nucleus grows at the adjacent dry spot beneath the primary bubble quickly after the bubble departure ($t = 81$ ms) and follows the ascension of the bubble. It can reach the bubble before re-condensing or not, depending on the heat flux and the subcooling degree of the environment. The bubble then collapses, as a usual behavior in subcooled liquids because of the condensation of the vapor in the cold liquid.

During its growth, the bubble can reach several centimeters (from 1 to 15 cm).

The overall shape of the bubble is the same as observed by Van Stralen *et al.* (1975). According to Madjeski (1966) cited by Ginet (1999), the flattened spheroid shape observed from $t = 14$ ms to $t = 64$ ms is a usual shape observed in a boiling environment non-homogeneous in temperature. According to Van Leeuwen (1973) cited by Van Stralen *et al.* (1975), the liquid jet following the bubble is due to a depression after the bubble departure. The author explained that this liquid jet leads to a relatively large depression at the surface level and, as some superheated vapor remains trapped in the nucleation site after the departure of the bubble, a vapor nucleus grows quickly after the bubble

departure. Clark and Merte (1973; cited by Van Stralen *et al.*, 1975) also observed the growing of a succeeding secondary vapor bubble which confers to the bubble its “mushroom shape”. They stated that this second bubble is carried by a high momentum liquid jet formed by the wake of the first bubble. The width of this secondary bubble is limited to the size of the dry spot beneath the primary bubble (Van Stralen, 1979; Van Leeuwen, 1973).

The absence of a secondary bubble at higher pressure (13 kPa for Van Stralen, 1979; beneath 15 kPa in the present study) can thus be explained by the diminishing radius of the dry area in combination with the decreasing relative depression in the wake (Van Leeuwen, 1973). The difference between the upper pressure limit for which the secondary bubble is observed between Van Stralen (1979) and this study is certainly due to the difference of the height of liquid level imposed.

As suggested by the shape of the bubbles, the balance of forces applied on them is necessarily very different at sub- and at atmospheric pressure. As a matter of fact, inertial forces are proportional to the volume of the bubble, which is much greater at subatmospheric pressure. In addition, the surface tension force is proportional to the radius of the cavity, which is much smaller than the equivalent radius of the bubble at subatmospheric pressure. In other words, in subatmospheric conditions, the detachment is no more governed by the buoyancy and surface tension forces, but rather by the buoyancy and the inertial forces. This effect of inertia is all the more significant that at low pressure the boiling is subcooled and the Jacob number is high (Yagov, 2001, Robinson and Judd, 2004). The bubble shape is thus strongly impacted during its growth as the liquid inertia tends to deform and pull the bubble away from the heating surface (Zuber, 1959). According to McGillis *et al.* (1991b), this phenomenon is more significant since it is associated with the induced liquid flow around the bubble, which produces lift forces on it.

Due to these differences of forces applied on the bubble at subatmospheric pressure, correlations which take into account only surface tension forces and buoyancy forces to calculate the bubble diameter detachment could not be applied there. Moreover, the Laplace equation (Chap. 1, Eq. 1.11) often used as a scaling for the radius of the bubble for which stable equilibrium is reached cannot be applied either because of the size of the bubble. Indeed, the vapor pressure inside the bubble is probably non homogeneous. Besides, as the bubble grows in a highly non-homogeneous environment in pressure, the pressure of the liquid should be calculated by an integration of the pressure along the bubble curvature.

2.3.1.2 Bubble growth

By processing the pictures obtained with the MATLAB® program, the volume of the bubble for each time steps is calculated. Fig. 2.11 shows the evolution of the dimensionless volume depending on the dimensionless growth time for bubbles obtained at 1.2 kPa and $\dot{q} = 8.6 \text{ W.cm}^{-2}$, $\dot{q} = 16.9 \text{ W.cm}^{-2}$, $\dot{q} = 29.1 \text{ W.cm}^{-2}$. The dimensionless time and the dimensionless volume are calculated as the ratio of the value of the time/volume of the bubble at each time step to the value of the time at the moment of bubble detachment/maximum volume of the bubble during its growth.

The dimensionless volume of the bubble first increases with a dimensionless time dependency proportional to $V_{\text{adim}} \approx t_{\text{adim}}^{2.25}$. Then, for a dimensionless time of 0.2, the bubble growth follows a law close to $V_{\text{adim}} \approx t_{\text{adim}}^{1.5}$. At $t_{\text{adim}} \approx 0.5$, the bubble growth velocity slows down until the bubble reaches its highest volume at $t_{\text{adim}} \approx 0.7$. The volume of the bubble then decreases before detachment.

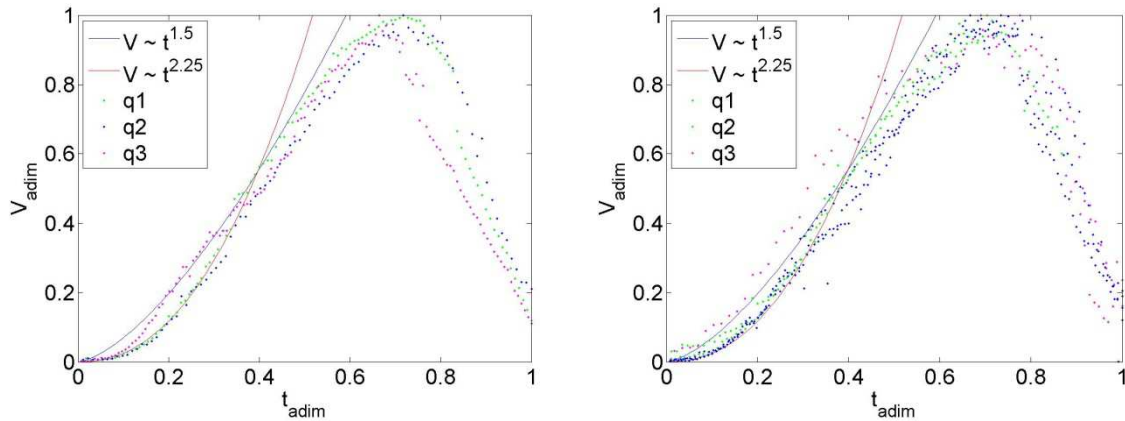


Figure 2.11: Bubble growth dimensionless velocity for a) $h_1 = 200$ mm; b) $h_1 = 150$ mm ($P_v = 1.2$ kPa, $T_1 = 10^\circ\text{C}$, $\dot{q}_1 = 8.6$ W.cm $^{-2}$, $\dot{q}_2 = 16.9$ W.cm $^{-2}$, $\dot{q}_3 = 29.1$ W.cm $^{-2}$)

This evolution of the bubble growth is observed for $h_1 = 200$ mm and $h_1 = 150$ mm but also for each experiments conducted at subatmospheric pressure as soon as the subcooling is sufficient. For vapor pressure investigated and for a height of the liquid level of 200 mm, this evolution was however not observed for vapor pressure of 15 kPa and higher, i.e. for a maximal subcooling degree lower than 2.6 K (Fig. 1.12). For these pressures, the volume increases more slowly than for the other pressures and it remains almost constant before the detachment. This maximal volume is reached at $t_{adim} \approx 0.9$.

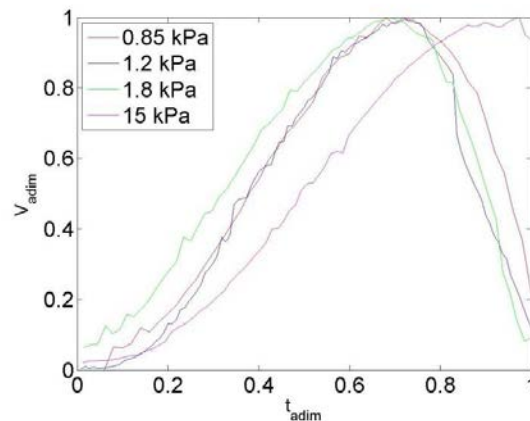


Figure 2.12: Bubble growth velocity for 4 different vapor pressures ($h_1 = 200$ mm)

For vapor pressure lower than 15 kPa, this particular evolution of the bubble growth curve was also observed by Rullière *et al.* (2012). It is probably due to the non-homogeneity of the environment and more specifically to the subcooling of the liquid close to the bubble during its growth. Due to the size of the bubble, the bubble rapidly emerges from the thermal boundary layer. The top of the bubble is then in contact with a liquid at a temperature lower than the saturation temperature of the fluid. A part of the vapor should then condense. This condensing of the vapor is balanced by the vaporization of the water near the triple line. However, as the bubble grows and as a consequence of the buoyancy force, the bubble rises, the diameter of the foot of the bubble decreases. As the diameter of the bubble foot decreases, cold liquid circulate around the bubble foot. This recirculation of the cold liquid fosters the condensation of the vapor and then balances the vaporization of the water at the triple line. When the amount of liquid vaporized is insufficient to balance the amount of liquid that condenses, the volume of the bubble decreases.

As mentioned in the literature review, during bubble growth controlled by diffusion, classical theory says that the increase of the bubble radius follows a law $R \approx t^{0.5}$ ($V \approx t^{1.5}$). During the bubble growth controlled by inertia, the increase of the bubble radius follow a law $R \approx t$ ($V \approx t^3$). As in subatmospheric pressure, the bubble growth is controlled solely by inertia, the increase of the bubble volume should follow a law close to $V \approx t^3$. The study shows that at the beginning of the growth the increase of the volume is smaller than the increase predicted by this law but is higher than the increase predicted in the case of a bubble growth controlled solely by diffusion. The bubble growth thus follows a law which is an intermediate between the bubble growth controlled by inertia and the bubble growth controlled by diffusion. This is in agreement with the law proposed by Yagov (2001): $R \approx t^{2.25}$, who studied water pool boiling at a pressure down to 1 kPa. Then, from $t_{adim} \approx 0.2$ to $t_{adim} \approx 0.5$, the increase of the volume of the bubble is close to $R \approx t^{0.5}$ and thus to the law proposed for the bubble growth controlled by diffusion. However, for $t_{adim} > 0.5$, the increase of the bubble volume is even smaller than the increase of bubble volume predicted by this law. This evolution of the dimensionless volume is probably due to the highly subcooling of the bubble environment and thus to the re-condensation of a part of the vapor generated.

2.3.1.3 Influence of the pressure on bubble size

According to the literature, the bubble departure diameter increases when decreasing the pressure. This statement is in agreement with the results obtained either by authors who conducted experimental studies (Van Stralen, 1979; Mc Gillis *et al.*, 1991a&b; Yagov, 2001; Rullière *et al.*, 2012) or by authors who performed mathematical studies in a uniformly superheated liquid (Fritz, 1935; Cole and Rohsenow, 1969; Nishikawa *et al.*, 1976; Borishanskiy *et al.*, 1981; Jensen and Memmel, 1986) or even in a non-uniform temperature field (Zuber, 1959). Fig. 2.13 shows the detachment diameter predicted by correlations developed by some of these authors and, when mentioned, experimental bubble diameters obtained from authors who conducted experimental studies. Bubbles diameters obtained during this study are also shown on this figure. However, due to experimental setup constraints, only bubbles small enough to be observed during the entire growth are shown. This remark is especially of importance for the departure diameter of bubble shown at 1.2 kPa, i.e. at a local pressure of 3.2 kPa. Indeed, bubbles with a departure larger diameter are also observed. The corresponding pressure is chosen to be the local pressure. As the height of the liquid level is not always mentioned in the literature, this pressure had sometimes to be taken as the vapor pressure. It is the case for Van Stralen's experiments.

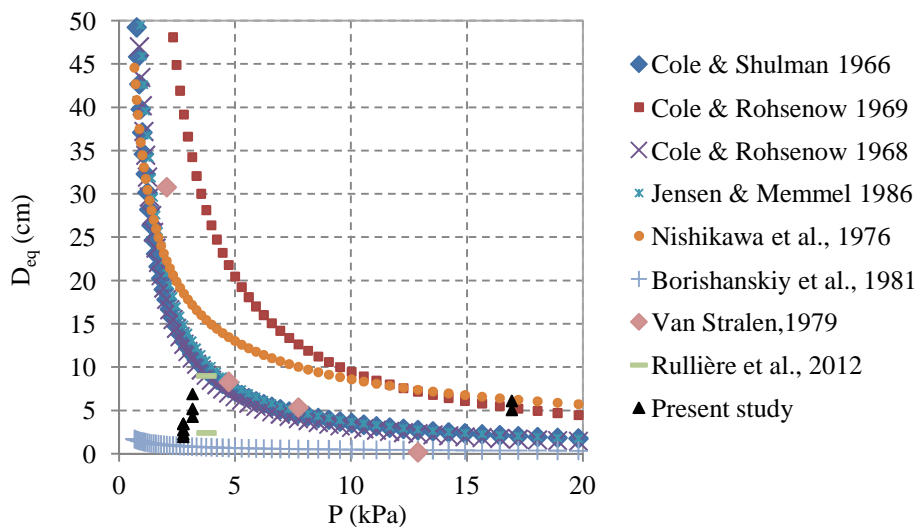


Figure 2.13: Correlations and experimental bubble diameters available in the literature

Bubble departure diameters measured by Van Stralen (1979) are in good agreement with the correlations developed by Cole & Shuman, Cole & Roshenow, and Jensen & Memmel. However, the diameter of the bubbles that were analyzed by Rullière *et al.* (2012) or during this study could be smaller than that predicted by these correlations. This holds especially true for bubbles obtained at a local pressure of 2.8 kPa, i.e. at a vapor pressure of 0.85 kPa ($h_l = 200$ mm).

This evolution of the bubble departure diameter for very low pressure (around 0.85 kPa) could be expected since the boiling environment is subcooled. This one is all the more subcooled that, for a given height of the liquid level, the vapor pressure decreases. Thus, there must be a pressure (for a given liquid height) for which the influence of the subcooling degree is more significant than the influence of other parameters (surface tension, vapor density, diffusivity, etc.). Figure 2.14 shows bubbles, just before their detachment, obtained for vapor saturation pressures of 100 kPa, 15 kPa, 4.2 kPa, 1.8 kPa, 1.2 kPa, 0.85 kPa and a given imposed heat flux of 10.2 W.cm^2 . The liquid height is constant and equal at 200 mm.

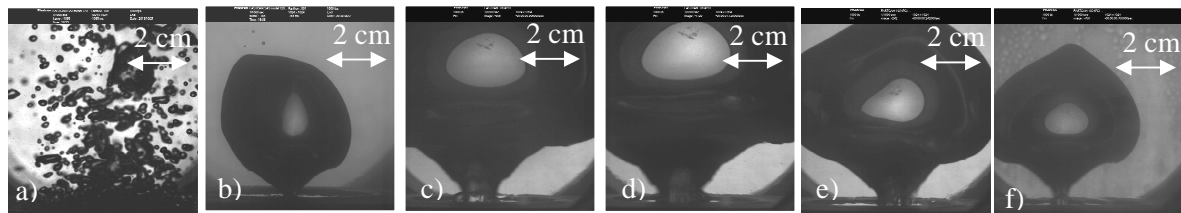


Figure 2.14: Bubble before detachment at a vapor saturation pressure of a) 100 kPa, b) 15 kPa, c) 4.2 kPa, d) 1.8 kPa, e) 1.2 kPa, f) 0.85 kPa, ($h_l = 200$ mm; $\dot{q} = 10.2 \text{ W.cm}^{-2}$)

As shown in figure 2.14, bubbles and regimes obtained at atmospheric pressure or at subatmospheric pressure for a given imposed heat flux are different. Many bubbles of millimeters size are observed at atmospheric pressure water pool boiling whereas single bubble with centimeters size (sometimes follows during a short time by others bubbles of centimeters size) are observed at subatmospheric pressure. As mentioned in the literature and as mentioned above, the departure diameter of these subatmospheric bubbles increases when decreasing the pressure. However, the opposite trend is observed for vapor pressures of 1.2 kPa and 0.85 kPa. For these two investigated pressures the departure diameter of bubbles decreases when decreasing the pressure. This decrease in the bubble detachment diameter could be explained by the difference of bubble growth pool boiling environment. The average subcooling degree is higher at 0.8 kPa than at 4.2 kPa and it becomes larger with decreasing pressure. At 0.8 kPa it even becomes high enough to counterbalance the effects of the low vapor density that are encountered at such low pressure. The vapor forming the bubbles thus tends to re-condense more easily at 0.8 kPa than at 4.2 kPa. Moreover, mechanisms of bubble growth change with the decreasing pressure. During his study on water bubble growth at decreasing subatmospheric pressure, Van Stralen (1979) noticed that the relative contribution of the microlayer evaporation to bubble growth increases until reaching a lower limit of pressure given by the author at 4 kPa. Then, at 2 kPa, the author observed another change in the mechanism of the bubble growth: below 2 kPa bubbles are “Rayleigh bubbles” and expand owing to an excess of pressure derived from the superheat of the heated wall. These two limits given by Van Stralen (1979) must however be used with caution. As mentioned before, liquid height and vapor saturation pressure must be known to well define running conditions and compare results. As the liquid height is not mentioned by the author, these limits can be quite different.

This change in the bubble growth mechanism could maybe also explain the difference in the bubble growth observed for a vapor pressure of 15 kPa (Fig. 2.12).

2.3.2 Thermal analysis

2.3.2.1 Evidence of a new boiling regime at subatmospheric pressure

With the decrease of the pressure (down to a certain pressure), larger and larger bubbles are observed. As these large subatmospheric bubbles grow and detach, some authors report large fluctuations of the wall temperatures (Van Stralen *et al.*, 1975; Mc Gillis *et al.*, 1991a; Mc Gillis *et al.*, 1991b). However, these wall fluctuations are explained only for a boiling regime named "intermittent boiling regime", i.e. when the waiting time is greater than the time for bubble growth and release. This intermittent boiling regime is thus characterized by the departure of a single bubble after a long waiting time. The frequency of detachment as well as the diameter of the bubble at detachment could be assumed constant. However, as mentioned by Labuntsov *et al.* (1978), Wu *et al.* (1982), and as observed in the present study, boiling at subatmospheric pressure seems to be irregular and unsteady especially at low heat fluxes and very low pressure range. This means that at such low pressure and for a given heat flux, bubbles seem to detach with irregular diameter of detachment (from 1 to 15 cm) and with irregular frequency of detachment (from more than 26 Hz to 5 mHz). Despite these different boiling regimes, cyclic wall fluctuations similar to those observed by Van Stralen *et al.* (1975) and McGillis *et al.* (1991a) were recorded in the present study (Fig. 2.15).

The cycle can be divided in two different parts: the increase of the wall temperature and then its drop. As shown on Fig. 2.15, the amplitude of the cycle does not significantly depend on the imposed heat flux. The variation of the wall temperature is almost of 25 K for the three imposed heat fluxes. However, the heat flux has an influence on the period of these two phases. The higher the heat flux, the lower the time-averaged value of the wall temperature. These temperature fluctuations are not observed for experiments conducted at atmospheric pressure (Fig. 2.16).

Another way to show these fluctuations for each imposed heat flux investigated is to plot the boiling curves. All the points shown on Fig. 2.15 and Fig. 2.16 (among others) are thus represented on Fig. 2.17 as boiling curves.

As more than 200 points are represented on Fig.2.17 for any of the imposed heat fluxes, it is clear that for some points no fluctuations of the wall temperature are seen. It is always the case at atmospheric pressure but it is also the case at subatmospheric pressure and low heat fluxes (below 6.3 W.cm^{-2}) or at 27.4 W.cm^{-2} . This could be explained by an analysis of the predominant regime of heat transfer. At atmospheric pressure, visualization with the high speed camera shows that heat is transferred by single phase natural convection for heat fluxes below 0.5 W.cm^{-2} . Beyond this point, heat is transferred by phase change. The wall superheat required to trigger the nucleate boiling is around 6 K. Once boiling starts, bubbles have a constant diameter of detachment and a constant frequency of detachment for a given heat flux. The bubble frequency increases when increasing the imposed heat flux. At 1.2 kPa, heat is also transferred by single phase natural convection at low heat fluxes but the transition between heat transfer by single phase convection and phase-change heat transfer appears for a heat flux higher than 6.3 W.cm^{-2} . The required wall superheat to trigger this transition is much higher than at atmospheric pressure (more than 30 K instead of 6 K as mentioned above). At 27.4 W.cm^{-2} , heat is transferred by fully developed boiling, i.e. the observed bubbles have a constant departure diameter and a constant frequency of detachment as observed at atmospheric pressure. Between these two regimes, before reaching 27.4 W.cm^{-2} , a boiling regime characterized by cyclic wall fluctuations is observed. This specific boiling regime is described thereafter.

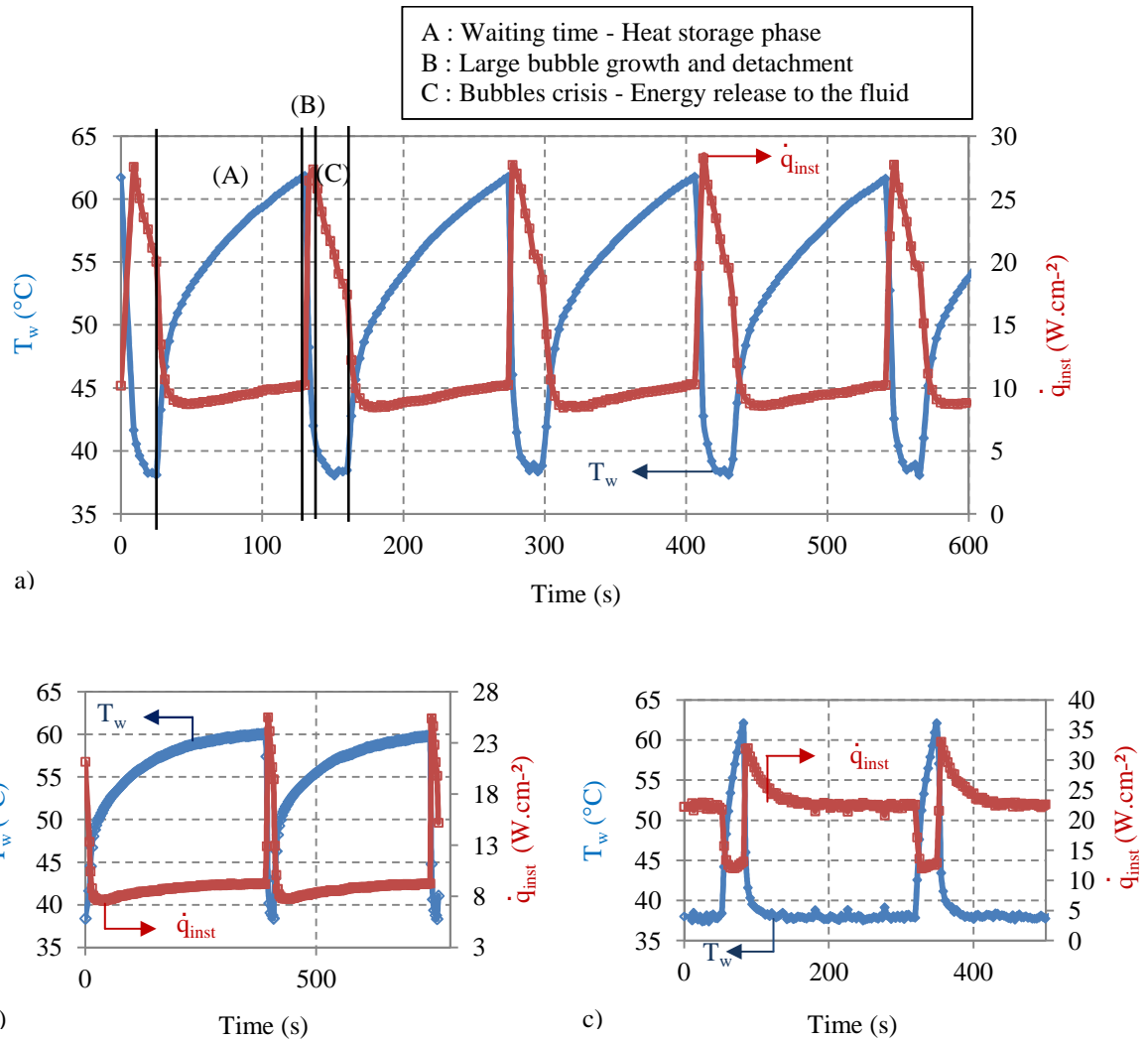


Figure 2.15: Evolution in time of the wall temperature and the instantaneous heat flux at subatmospheric pressure for three different heat flux imposed at the cartridges heaters of a) $\dot{q} = 11.6$ W.cm⁻²; b) $\dot{q} = 9.1$ W.cm⁻²; c) $\dot{q} = 22.1$ W.cm⁻² ($P_v = 1.2$ kPa, $h_l = 200$ mm)

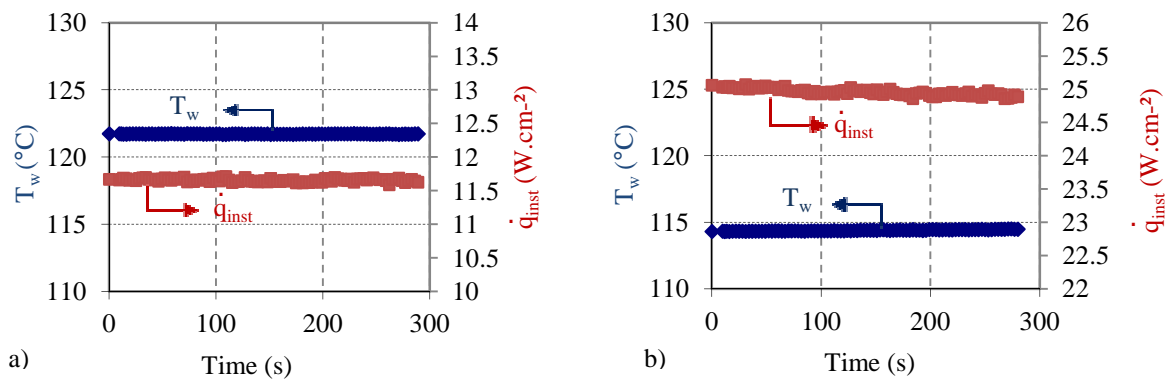


Figure 2.16: Evolution in time of the wall temperature and the instantaneous heat flux at atmospheric pressure for a) $\dot{q} = 11.5$ W.cm⁻²; b) $\dot{q} = 25.0$ W.cm⁻² ($P_v = 100$ kPa, $h_l = 200$ mm)

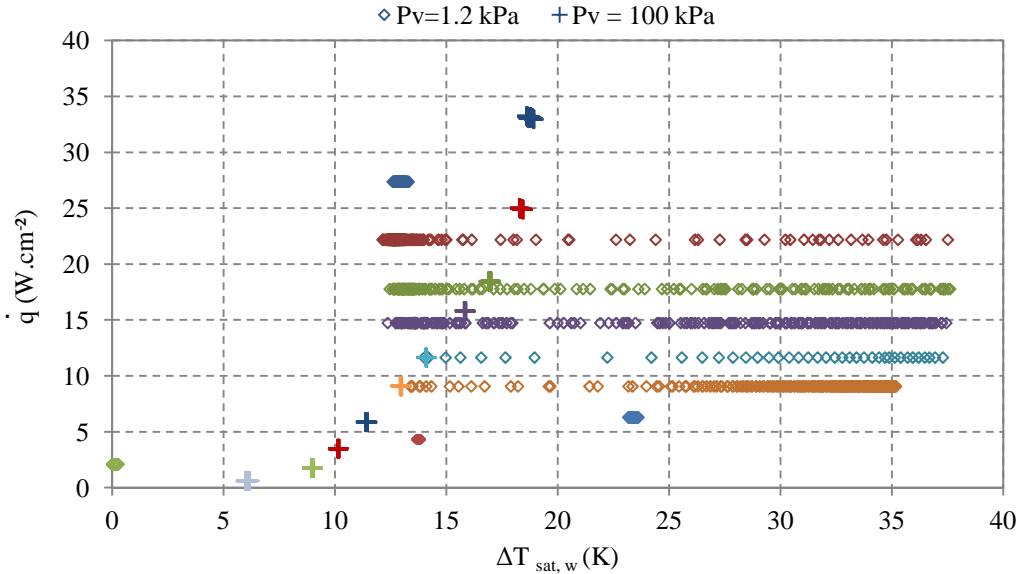


Figure 2.17: Boiling curves for $P_v = 1.2$ kPa and $P_v = 100$ kPa ($h_1 = 200$ mm)

During the first part of the cyclic pattern (noted A on Fig. 2.15, 2.18 and 2.19), the instantaneous heat flux passing through the wall is lower than the imposed heat flux (respectively 9 W.cm^{-2} and 11.6 W.cm^{-2} on Fig. 2.15). The thermal equilibrium is not reached and a part of the thermal energy is stored in the wall. Phase A may last more than 100 s. The wall superheat thus increases until reaching the temperature required to initiate nucleation (Fig. 2.15a). At this point, the wall temperature drops suddenly and a peak in the instantaneous heat flux is observed ($\dot{q}_{\text{inst}} = 26 \text{ W.cm}^{-2}$). The duration of this phase is less than 200 ms (phase noted B on Fig. 2.15, 2.18 and 2.19). The wall temperature then keeps decreasing as well as the instantaneous heat flux transferred to the fluid. All the stored energy is released to the fluid until the initial conditions of the cyclic pattern are recovered (phase named C on Fig. 2.15, 2.18 and 2.19). The duration of these three phases (A, B and C) depends on the given heat flux as shown on figure 2.15. At low imposed heat fluxes, the phase of storage (or phase A) last 40 times longer than the phase of release of energy to the fluid (phase C), while at higher imposed heat fluxes (Fig. 2.15c), phase C is longer than phase A. The duration as well as the amplitude of these oscillations may also strongly depend on the material used and on the surface finish even if, as mentioned by McGillis *et al.* (1991b), at such low pressure the influence of the surface finish on the heat transfer is less pronounced than at atmospheric pressure as only few sites can actually be activated. Regarding the material used, the periodic boiling phenomena would strongly depend on properties and size of the heater. A heater with a high thermal inertia would induce larger amplitudes than a heater with a lower thermal inertia. It is the case in our experiments: the heater is highly thermally capacitive. It is also the case with industrial heat exchangers and one can therefore expect that periodic boiling may also take place in real application.

Visualizations (Fig. 2.18) reveal that during the storage phase (phase A), a change in the refractive index environment is observed in the boiling vessel, which proves that a free single-phase convection is established. The thermal boundary is thus created during this phase and convective cells are visible. As the wall temperature keeps increasing and the wall superheat becomes sufficient (38 K), nucleation is then initiated which leads to the departure of a large bubble (up to 15 cm). The departure of this large bubble corresponds to the temperature drop of around 1 K and to a peak of heat flux transferred to the fluid around $\dot{q}_{\text{inst}} = 26 \text{ W.cm}^{-2}$ observed during the phase B. Many bubbles with different sizes and different frequencies of detachment are then created everywhere on the boiling surface (Fig.2.18).

At the end of phase C, the frequency of the bubbles detachment and their size decrease until nucleation stops. The cycle can then start again.

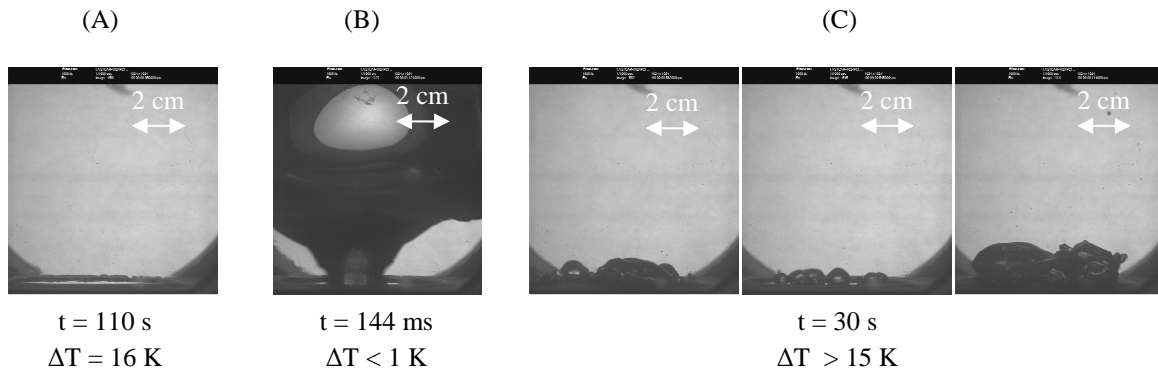


Figure 2.18: Pictures obtained during the phase (A) (B) and (C) ($P_v = 1.2$ kPa, $h_l = 200$ mm, $\dot{q} = 11.6$ W.cm⁻²)

These results can also be interpreted from graphs (called "instantaneous boiling curves", or for the sake of simplicity, "boiling curves") that represent the instantaneous heat flux as a function of the instantaneous wall superheat ($T_w - T_{sat}^*$). The blue circles on Fig. 2.19 correspond to points collected for an imposed heat flux of 17.8 W.cm⁻², i.e. for an imposed heat fluxes between heat fluxes imposed to collect data on Fig. 2.15b and Fig. 2.15c.

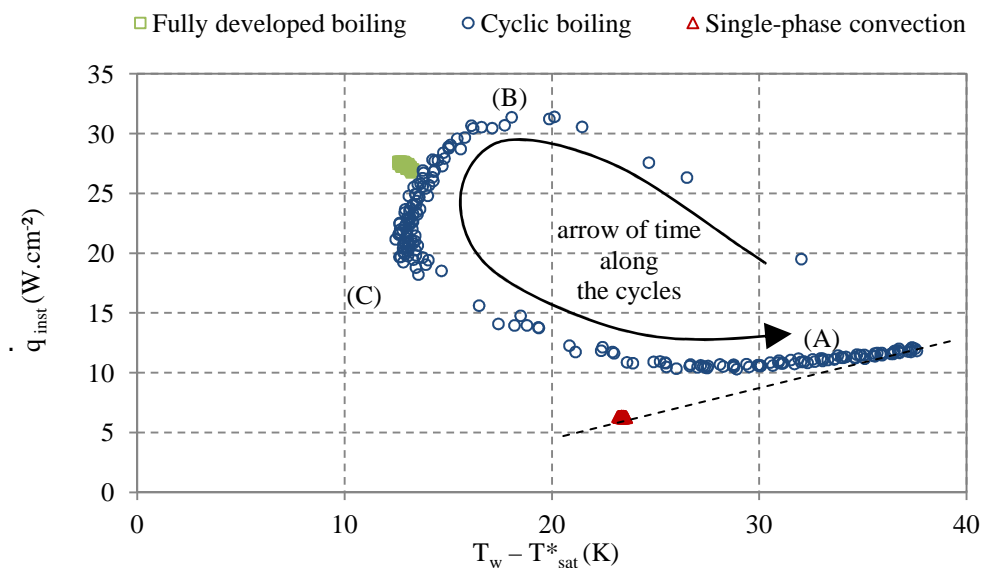


Figure 2.19: Boiling curves for three different imposed heat fluxes ($\triangle 6.3$ W.cm⁻²; $\circ 17.8$ W.cm⁻²; $\square 27.4$ W.cm⁻²), ($h_l = 200$ mm, $P_v = 1.2$ kPa)

Figure 2.19 is another way to highlight the occurrence of three main heat transfer regimes observed during this study. One, represented with red triangles, is a single-phase natural convection regime and the two others are boiling regimes: the fully-developed regime and the new regime named "cyclic boiling regime". As mentioned above, the fully developed boiling regime and the single-phase convection regime are similar to those observed at atmospheric pressure. They are characterized by very stable values of heat flux and wall superheat, so stable that hundreds of instantaneous measurements appear as a single point (red triangle) or almost (there is a limited scatter among the points represented by green squares on Fig. 2.19). Besides, the cyclic boiling appears to be specific to the subatmospheric boiling. During this regime analyzed previously, the creation of bubbles during the

cycle induces an increase of the phase change heat transfer, but also permits the destruction of the thermal boundary layer and to cool the wall surface by liquid recirculation. The single phase convection is thus unsteady whereas an overall steady state is nevertheless obtained for the single phase convection represented by the red triangles.

The shape of the boiling curves observed on Fig. 2.19 for the cyclic regime presents analogies with boiling curves obtained in transient heating. This observation may confirm that some analogies could be done between transient boiling and boiling in subcooled environment.

As three different boiling regimes are observed, different heat transfer coefficients are estimated. Fig. 2.20a shows the evolution of the heat transfer coefficient during the cycle for an imposed heat flux of 17.8 W.cm^{-2} . Fig. 2.20b shows this evolution with the dimensionless cycle time for all the heat fluxes investigated with $P = 1.2 \text{ kPa}$. This dimensionless time is calculated by dividing the time of acquisition by the time of the cycle (if any) for the given imposed heat flux. As the duration of the cycle is not the same for each imposed heat fluxes, plotting the evolution of the heat transfer coefficient with the dimensionless cycle time allow to compare heat transfer coefficients achieved during one cycle for each imposed heat fluxes but do not shows the frequency of the cycle.

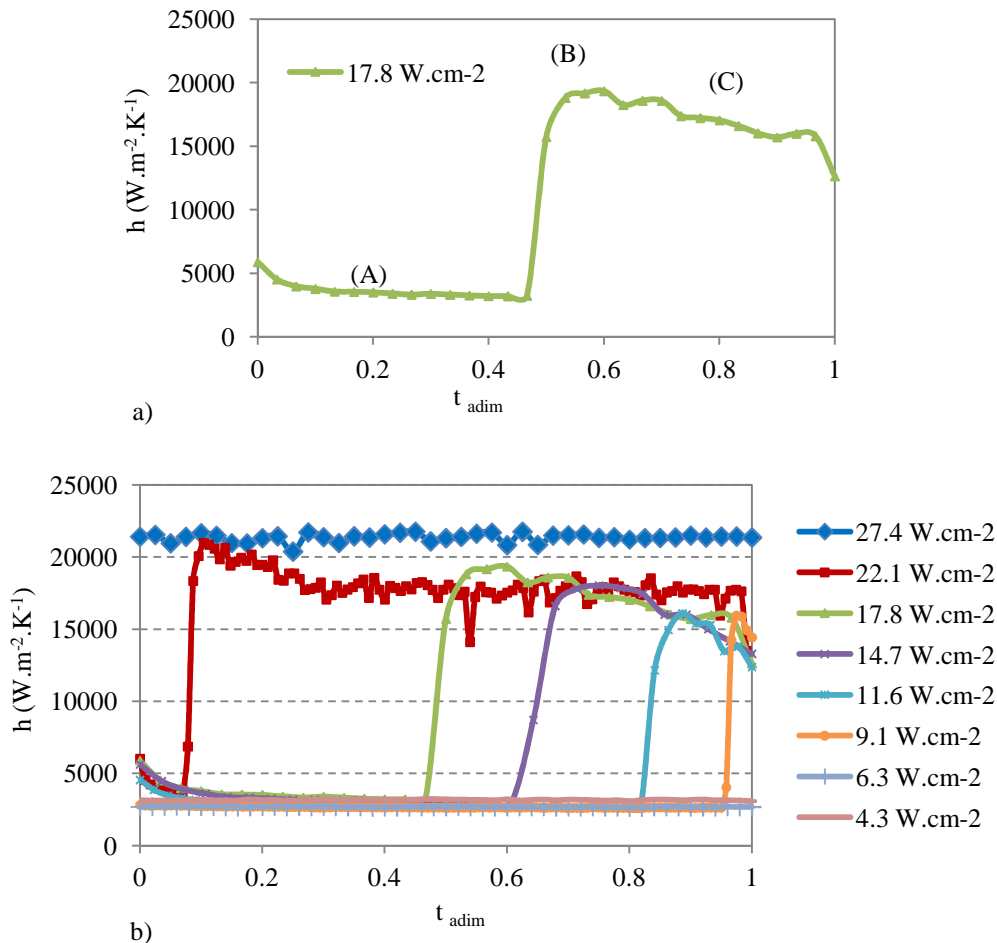


Figure 2.20: Heat transfer coefficients estimated at a) 18.5 W.cm^{-2} with the three phase A, B, C of the cyclic boiling referred; b) different imposed heat flux ($P_v = 1.2 \text{ kPa}$, $h_l = 200 \text{ mm}$)

The best heat transfer coefficient is obtained, as observed in atmospheric pressure, for the fully developed boiling regime. The same heat transfer coefficients can periodically be obtained during the phase B of the cyclic boiling regime at an imposed heat flux of 22.1 W.cm^{-2} . This maximal heat

transfer coefficient decreases when decreasing the imposed heat flux. An overall, high heat transfer coefficients could be achieved during the cyclic boiling regime, in spite of low heat transfer coefficient during the waiting time. The heat transfer estimated can thus vary from $21 \text{ kW}\cdot\text{m}^{-2}\cdot\text{K}^{-1}$ to $2.6 \text{ kW}\cdot\text{m}^{-2}\cdot\text{K}^{-1}$, depending on the heat flux imposed and on the phase of the cycle.

During this cycling regime, the heat transfer coefficient is severely affected with respect to the usual fully developed nucleate boiling. As fluctuations of 20 K could also be recorded, this regime must a priori be avoided. The influence of the pressure on the boiling performance and on the boiling regime is thus studied thereafter.

2.3.2.2 Influence of the pressure

Figure 2.21 displays the same kind of curves as figure 2.19, for a variety of imposed heat flux, for different vapor pressures in the range 0.85 - 100 kPa with a constant height of liquid level ($h_l = 200 \text{ mm}$).

The dispersion of experimental points for a given heat flux marks the occurrence of the previously described cyclic boiling regime. This dispersion is more and more pronounced with decreasing pressure, which reflects temperature fluctuations of progressively larger amplitude (up to 20 K). These variations severely affect the time-averaged heat transfer coefficient. However, even when the time-averaged heat transfer is reduced, the maximum instantaneous heat transfer coefficient achieved can be significantly increased.

Fig. 2.22 displays the same kind of curves as Fig. 2.20, for all the points recorded and shown on Fig. 2.21.

At atmospheric pressure, heat transfer coefficients from $1 \text{ kW}\cdot\text{m}^{-2}\cdot\text{K}^{-1}$ to $18 \text{ kW}\cdot\text{m}^{-2}\cdot\text{K}^{-1}$ were measured. These heat transfer coefficients are found to be generally lower at 15 kPa: they range from $13 \text{ kW}\cdot\text{m}^{-2}\cdot\text{K}^{-1}$ to $1.5 \text{ kW}\cdot\text{m}^{-2}\cdot\text{K}^{-1}$. Besides, with the decrease of the pressure, the occurrence of the cyclic boiling regime is observed, fluctuations on the heat transfer coefficients appear.

For the highest imposed heat flux (i.e. $27.4 < \dot{q} < 29.1 \text{ W}\cdot\text{cm}^{-2}$) and $P_v = 4.2 \text{ kPa}$ or $P_v = 3.0 \text{ kPa}$, the heat transfer coefficients show strong evolution with time, sometimes reaching very high values. The highest value is achieved for a pressure of 3.0 kPa ($24.4 \text{ kW}\cdot\text{m}^{-2}\cdot\text{K}^{-1}$). However, along the cycle, the heat transfer also reaches quit low values, down to $10 \text{ kW}\cdot\text{m}^{-2}\cdot\text{K}^{-1}$.

Although the given imposed heat flux is not exactly the same, for these highest heat fluxes, at 1.2 kPa, the highest heat transfer coefficient achievable is slightly lower with respect to heat transfer coefficients achieved at 3.0 kPa and 1.8 kPa ($21 \text{ kW}\cdot\text{m}^{-2}\cdot\text{K}^{-1}$ vs. $24 \text{ kW}\cdot\text{m}^{-2}\cdot\text{K}^{-1}$ and $23 \text{ kW}\cdot\text{m}^{-2}\cdot\text{K}^{-1}$, respectively) but as the boiling is fully established the time-averaged heat transfer coefficient is better ($21 \text{ kW}\cdot\text{m}^{-2}\cdot\text{K}^{-1}$ compared to $20.5 \text{ kW}\cdot\text{m}^{-2}\cdot\text{K}^{-1}$ and $18 \text{ kW}\cdot\text{m}^{-2}\cdot\text{K}^{-1}$). At $P_v = 0.85 \text{ kPa}$, the highest heat transfer coefficients achieved is lower than the highest heat transfer coefficient achieved for $P_v = 1.2 \text{ kPa}$ whereas a higher heat fluxes is imposed.

For imposed heat flux ranging from 23.2 to $8.7 \text{ W}\cdot\text{cm}^{-2}$, the heat transfer coefficient is generally greater when increasing the imposed heat flux. As the imposed heat flux decreases, no clear evolution of the influence of the pressure on heat transfer coefficient could be observed. This evolution becomes less and less predictable.

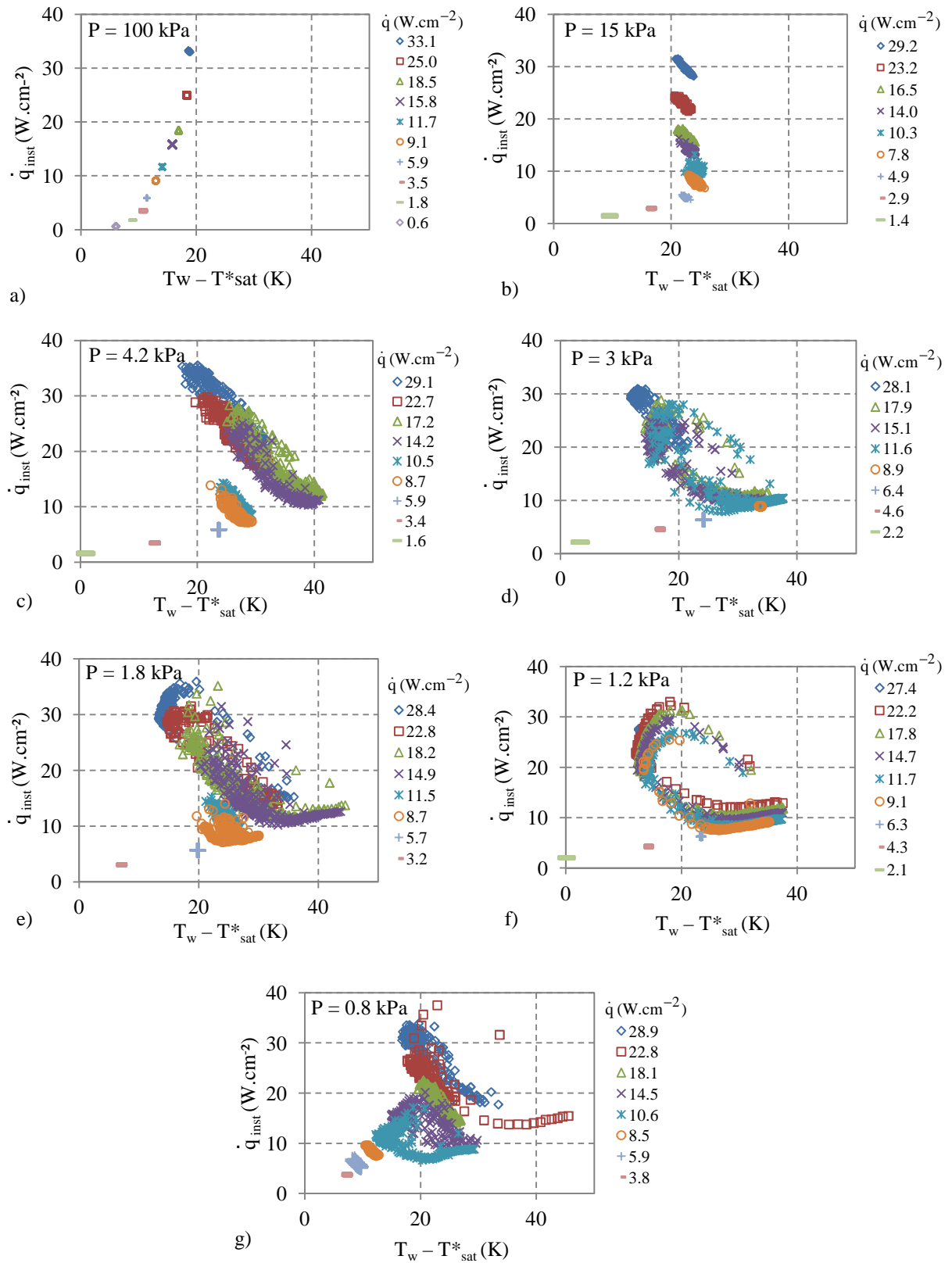


Figure 2.21: Boiling curves for $h_l = 200$ mm and a) $P_v = 100$ kPa; b) $P_v = 15$ kPa; c) $P_v = 4.2$ kPa; d) $P_v = 3$ kPa; e) $P_v = 1.8$ kPa; f) $P_v = 1.2$ kPa; g) $P_v = 0.8$ kPa

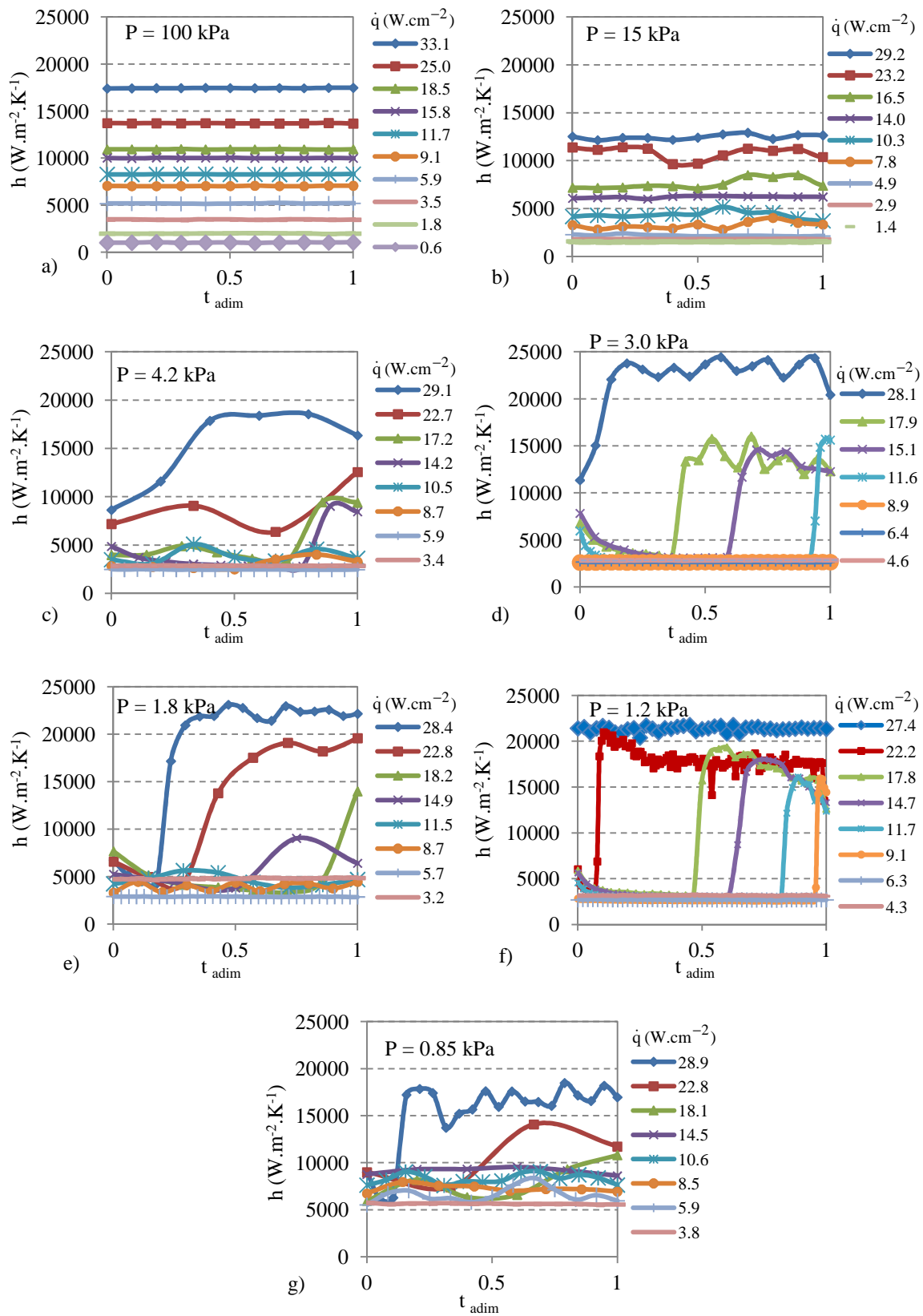


Figure 2.22: Heat transfer coefficient during one cycle (if any) for $h_1 = 200$ mm and a) $P_v = 100$ kPa, b) $P_v = 15$ kPa, c) $P_v = 4.2$ kPa, d) $P_v = 3$ kPa, e) $P_v = 1.8$ kPa, f) $P_v = 1.2$ kPa, g) $P_v = 0.8$ kPa

Significant decreases of the average heat transfer coefficient when decreasing the pressure were already mentioned in the literature by several authors (Chan *et al.*, 2010; Wu *et al.*, 1982; Mc Gillis *et al.*, 1991b). They linked this observation to the low vapor densities encountered at such low pressure. Indeed, as mentioned in the literature review, the decrease of the vapor density has two major consequences on the heat transfer:

1- the occurrence of large bubbles: when leaving the wall, large bubbles are replaced by a large amount of cold liquid; the larger this amount of liquid, the longer the time required to superheat this liquid during the waiting time.

2- an increase in the theoretical wall superheated required for nucleation for a given cavity size, as can be shown from an immediate derivation of the Clausius-Clapeyron equation combined with the expression for the mechanical equilibrium of a vapor bubble (Mc Gillis *et al.*, 1991b). This phenomenon also leads to an increase in the required time to superheat the liquid, for a given heat input rate.

This amount of time is all the more significant that the degree of subcooling degree for a given liquid height is higher when decreasing pressure, which also tends to increase the waiting time. As mentioned previously, during this waiting time, heat is transferred by transient conduction and then natural convection. As the pressure decreases, natural convection becomes the major phenomenon responsible for the heat transfer at a given heat flux. Although the amount of heat transferred by phase-change still remains significant for the heat transfer (as it is the motor of the bubble-induced convection and transient conduction to heat-up the cool liquid that replaces the leaving bubble), its contribution to the overall heat transfer becomes less important. This conclusion is in agreement with that reached by Gorenflo *et al.* (2013) who predicted for different fluids (but experimented it only with methanol for the lowest pressure of $P/P_c = 0.02$) that at subatmospheric pressure the “vigorous convection induced by the (few) big fast-growing and fast-moving bubbles” become the dominant heat transfer phenomenon compared to heat transfer induced by nucleation.

2.3.2.3 Influence of the height of the liquid level

For a height of the liquid level of 200 mm, for each imposed heat flux, the boiling regime observed is either natural convection, fully developed boiling or cyclic boiling as described above. However, for a vapor pressure of 1.2 kPa, as the height of the liquid level diminishes, the cyclic boiling regime is less and less pronounced (Fig. 2.23). The amplitude of wall temperature is smaller than for higher heights of the liquid level.

As this boiling regime is less apparent, periods of high and low heat transfer coefficient progressively diminish. The instantaneous value of the heat transfer coefficient (for a given imposed heat flux) is becomes more constant with time as the liquid height diminishes. The time-averaged heat transfer coefficient is severely reduced (Fig. 2.24).

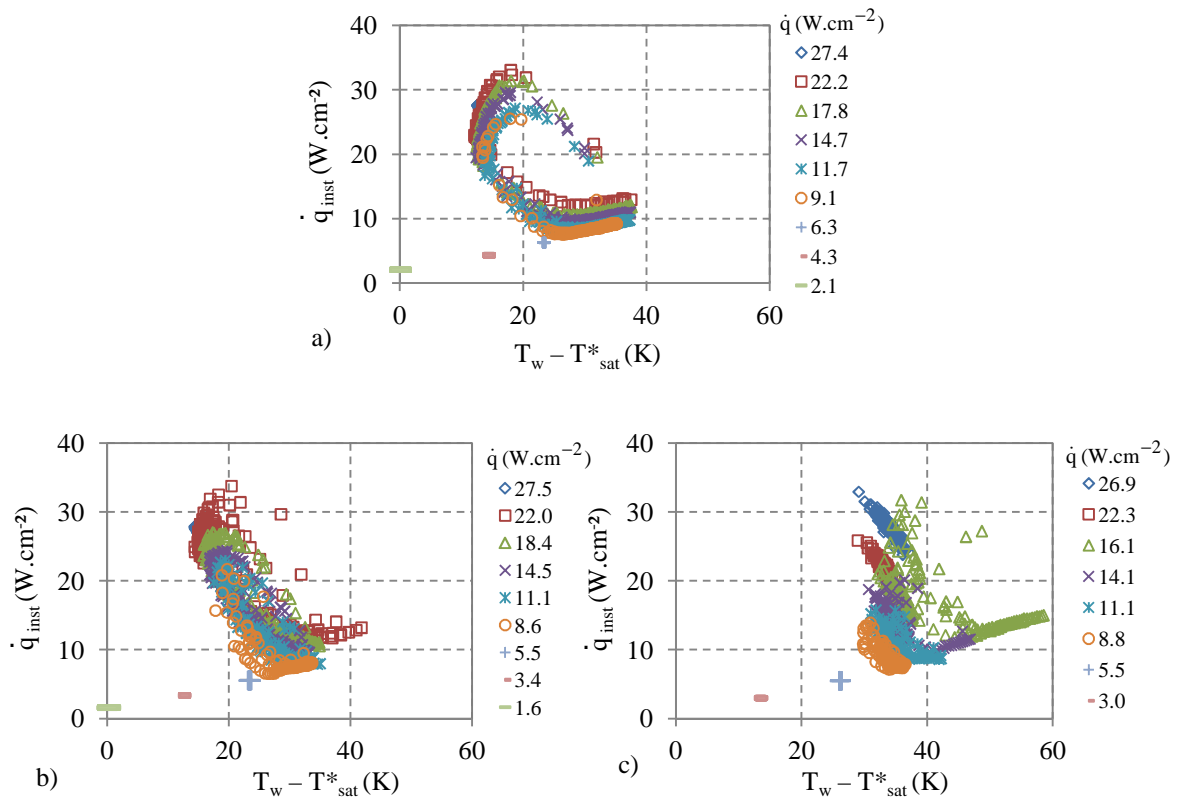


Figure 2.23: Boiling curves for $P_v = 1.2$ kPa and a) $h_l = 200$ mm, b) $h_l = 150$ mm, c) $h_l = 100$ mm

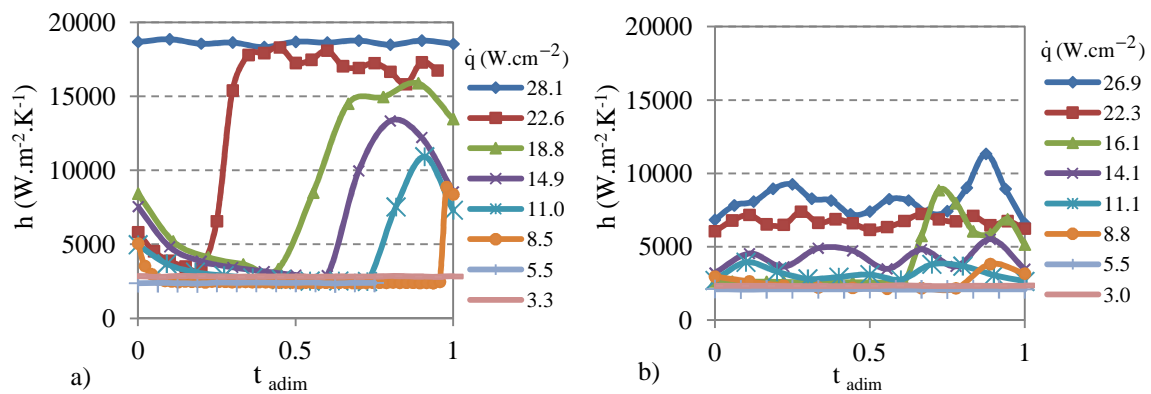


Figure 2.24: Heat transfer coefficient during one cycle (if any) for $P_v = 1.2$ kPa and a) $h_l = 150$ mm
b) $h_l = 100$ mm

For $h_l = 100$ mm, the boiling regime observed is no longer characterized by the periodic appearance of the large bubble followed by the appearance of many bubbles with different frequency of detachment and different diameter of detachment, but rather by the periodic appearance of a large bubble. This change of boiling regime when decreasing the height of the liquid level is due to the fact that, as the liquid height decreases, the difference between the vapor pressure and the pressure at the surface level decreases as well. Thus, the liquid in the pool is less subcooled compared to the saturation temperature at the surface level. This is also influenced by the fact that the height of the liquid level is of the same order of size as the bubble diameter of detachment, the far field liquid bulk cannot circulate as easily as it could with higher water level and thus the heating surface cannot be rewetted by cold liquid.

Conclusion

An experimental test setup was designed and built to study pool boiling of water over a large range of pressure (between 100 kPa and 0.85 kPa) on a horizontal heated copper disk.

It was shown that a major specificity of boiling at subatmospheric pressure lies in the non homogeneity of both saturation temperature and pressure of the boiling environment.

As it had sometimes been described in the literature, it was confirmed that at subatmospheric pressure, bubbles have centimeter size and present a particular shape of mushroom. The size of these bubbles increases when decreasing the pressure. It was however shown that this increase in the bubble detachment size when decreasing the pressure holds only down to a pressure of about 1.8 kPa. Below that pressure, the effect of the large degree of subcooling that are encountered in such conditions is no more counterbalanced by the evolution of the thermophysical properties (especially the decrease of the vapor density).

Instantaneous boiling curves obtained for pressures in the range 0.85-100 kPa were presented. As the pressure decreases, a new boiling regime appears. This regime is specific to the subatmospheric pool boiling and can be referred to as "cyclic boiling regime". During this regime, fluctuations of the wall temperature can reach 20 K. The heat transfer coefficient is thus severely affected with respect to the usual fully-developed nucleate boiling. Boiling curves for a pressure of 1.2 kPa and a height of the liquid level of 200 mm, 150 mm and 100 mm were also presented in order to observe the influence of the liquid height on the occurrence of this boiling regime. As the height of the liquid level diminishes, the cyclic boiling regime is less and less pronounced. This is due to the decrease of the subcooling degree when decreasing the pressure.

In the future, more experiments should be done in order to characterize operating conditions in which this specific regime appears and a flow pattern map could be drawn.

3 APPROACHING THE PHENOMENOLOGY OF PLATE-TYPE HEAT EXCHANGER: BOILING ON A VERTICAL PLATE

In order to be closer to a plate-type heat exchanger configuration, boiling on a vertical plane surface is studied, first without confinement and then with confinement. Bubble shape during the bubble growth and its influence on heat transfer during free boiling are discussed (section 3.1.2 and 3.1.3). Boiling curves for different vapor pressures and heights of the liquid level are plotted and compared with those obtained in horizontal configuration (section 3.1.3). Before studying boiling in narrow space, the meaning of the Bond number for characterizing boiling heat transfer at subatmospheric pressure is discussed (section 3.2.2). Then, boiling curves for different channel thicknesses and for pressure ranging from 1.2 kPa to 5 kPa are plotted and analyzed (section 3.2.3). Experiments with high speed PIV were conducted to highlight the influence of the wake-induced flow for very narrow channels. Results are presented and discussed (section 3.2.4).

3.1 Subatmospheric water pool boiling in a vertical plane surface

3.1.1 Experimental setup

The experimental setup is the same as that used previously. The only difference lies in the fact that the sample is not inserted by the viewport located at the bottom of the vessel but by one of the four viewports arranged on the side face of the chamber (Fig. 3.1).

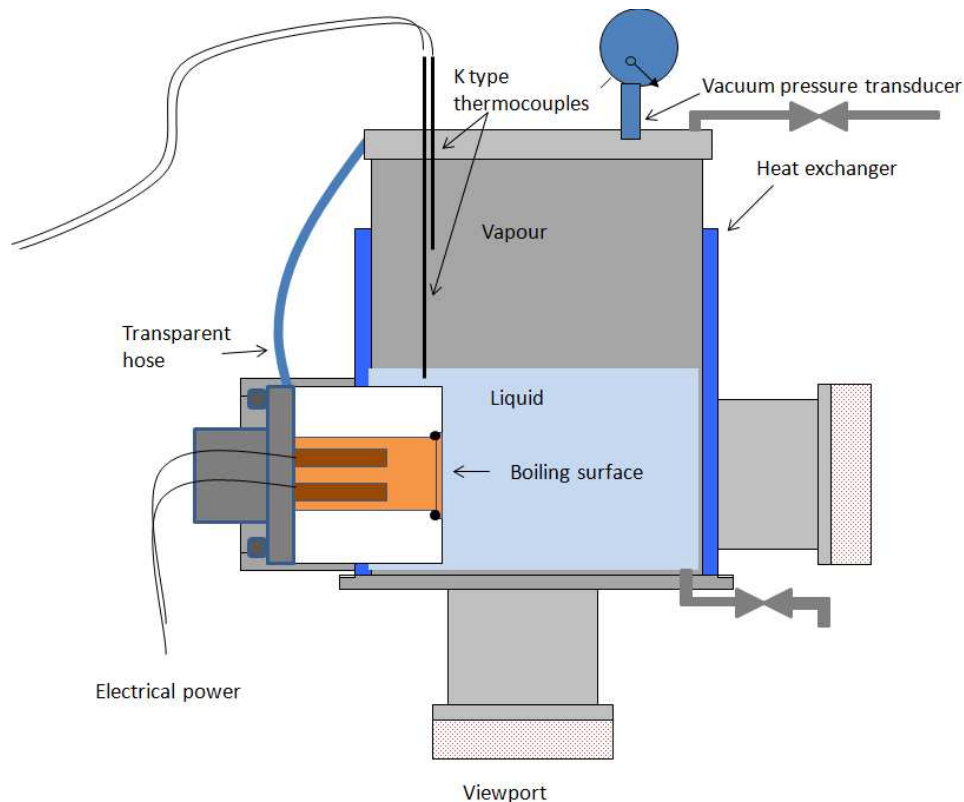


Figure 3.1: Detail of the pool boiling device

The sample, the visualization facility and the experimental procedure are exactly the same as those described in the previous chapter (Chap. 2, section 2.1).

As it is important to well determine the experimental conditions in order to precisely characterize the boiling environment, the height of the liquid level mentioned thereafter refers to the vertical distance from the center of the test heater (location of the nucleation site) to the free surface level.

3.1.2 Visualization

3.1.2.1 Bubble shape

Like in horizontal configuration, various shapes and sizes of bubbles are observed. However, in this orientation also, some shapes can be regarded as characteristic of the subatmospheric pressure pool boiling in vertical orientation. Fig. 3.2 shows the bubble growth on a vertical heat surface at $P_v = 1.8 \text{ kPa}$ and $\dot{q} = 7.0 \text{ W.cm}^{-2}$.

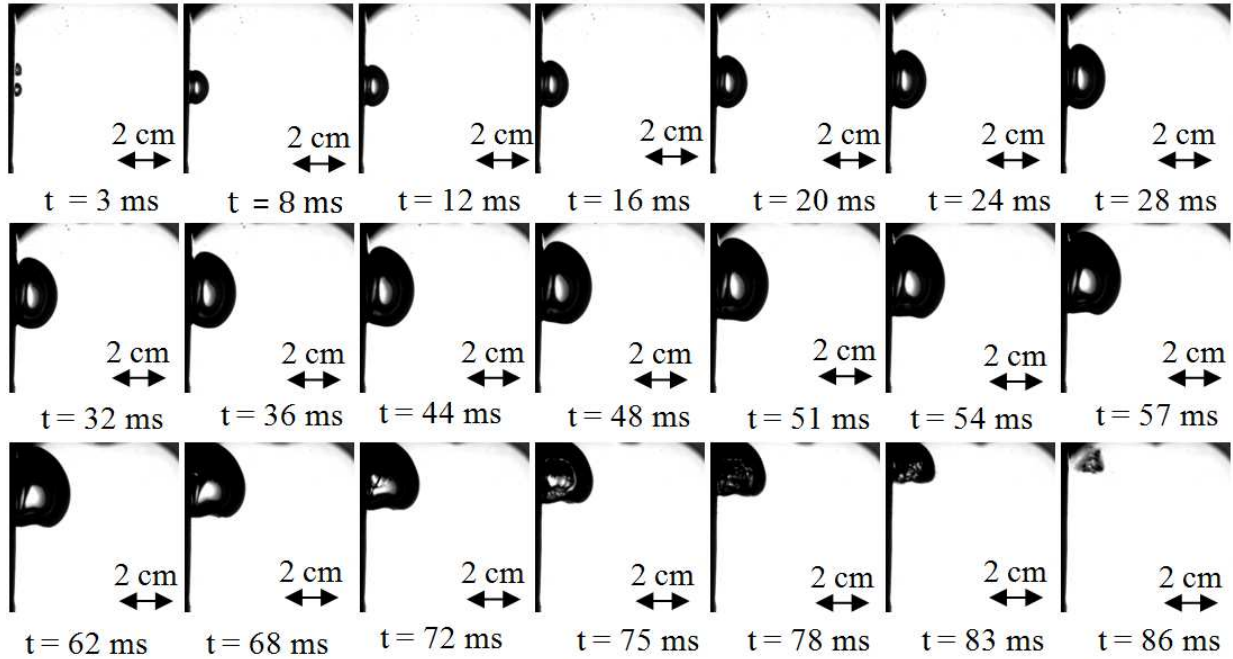


Figure 3.2: Visualization of bubble growth from a lateral view ($P_v = 1.8 \text{ kPa}$, $h_1 = 167 \text{ mm}$, $\dot{q} = 7.0 \text{ W}\cdot\text{cm}^{-2}$)

At the first moments of the growth, the bubble is hemispherical ($t < 16 \text{ ms}$). The maximum width of the bubble increases quicker than the maximum height (Fig. 3.3). The radius of the dry heated zone increases. As the bubble keeps growing a flattening of the base is observed ($t > 44 \text{ ms}$). The maximum vertical curvature decreases whereas the maximal horizontal curvature keeps on increasing and then remains constant. The dry heated zone remains at a fixed location until the flattened base reaches that specific location as depicted schematically on Fig. 3.4 ($t \geq 48 \text{ ms}$). Then, the bubble starts sliding upward along the heated surface before collapsing as usual behavior in subcooled liquids.

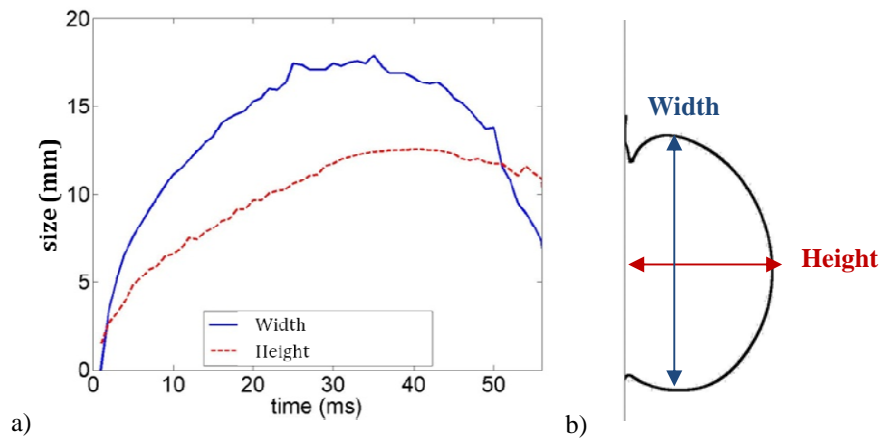


Figure 3.3: a) Evolution in time of the maximum height and maximum width of the bubble; b) Schematic of the notation used

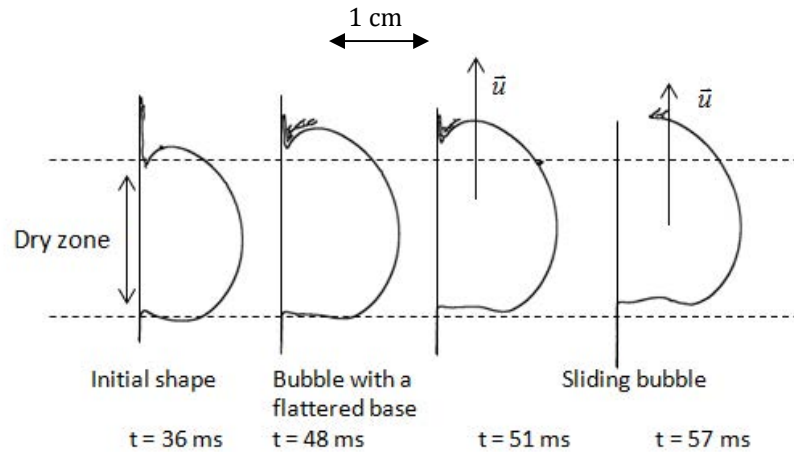


Figure 3.4: Schematic of the main moments of bubble growth

As for bubbles observed in the horizontal orientation, bubbles have centimeter sizes. However, the behavior of these bubble and their shape are quite different. According to Katto *et al.* (1970), the flattening of the base is due to the buoyancy force. The bubble has not reached its departure diameter but keeps growing. As the mass of vapor tends to keep on increasing, the bubble shape changes towards minimizing its surface energy. The difference of shape between the two orientations could be also due to the difference of liquid recirculation around the bubble. Indeed, in horizontal orientation, intense motion of the liquid from the far field liquid bulk to the base of the bubble tends to pull the bubble up. This liquid motion impacts on the shape of the bubble around its foot. In vertical orientation, the fluid cannot recirculate as easily as in horizontal orientation. As the bubble grows, the liquid is pushed on the lateral side of the bubble and up.

Another difference between bubble growth on a vertical plane surface and on a horizontal plane surface is the absence of a liquid jet in the first case when the bubble detaches (cf. section 2.3.1.1.: in horizontal orientation, when the bubble detaches, a liquid jet following the ascension of the bubble is observed. This jet penetrates into the lower side of this latter.). However, a presence of a vapor nucleus growing right after the sliding of the primary large bubble was sometimes observed as it could be observed in horizontal configuration.

The bubble sliding velocity observed in the vertical orientation depends on the size of the bubble. Generally, the sliding velocity decreases when the pressure increases, although for a same experiment a certain dispersion of the bubbles size could be observed. Nevertheless, for example a sliding velocity of around $240 \text{ mm}\cdot\text{s}^{-1}$ at $\dot{q} = 2.65 \text{ W}\cdot\text{cm}^{-2}$ and $P^* = 3.0 \text{ kPa}$ was measured whereas a sliding velocity of around $470 \text{ mm}\cdot\text{s}^{-1}$ was measured at $P^* = 1.7 \text{ kPa}$. In the first case bubbles had a maximal horizontal diameter of 15 mm whereas the maximal horizontal diameter was 36 mm in the second case. The same trend is observed for the maximal vertical diameter (22 mm in the first case, 41 mm in the other). Advancing and receding angles were the same in both cases: around 20° and around 48° , respectively.

Due to the non-homogeneity of the environment and as the bubble is stuck on a vertical heated wall, the bubble size and shape observed from a lateral point of view are not the same as the bubble size and shape observed from a frontal point a view. In this case, the volume of the bubble could not be estimated assuming an axisymmetric shape of the bubble. Thus, unless developing an experimental setup allowing the visualization of the bubble from a lateral and a frontal points of view at the same time (with several mirrors for example), the volume of the bubble as well as the evolution in time of this volume cannot be known.

3.1.2.2 Bubble crisis

As in the horizontal configuration, different boiling regimes were observed and characterized mostly by bubble size and bubble departure frequency. For a specific area of the boiling curve, the flow pattern is similar to the cyclic boiling regime observed in horizontal configuration. This means that no bubble is observed during a long waiting time (up to 120 s) and then a large bubble departs followed immediately after by a lot of bubbles which pop up on the entire heated surface (Fig. 3.5). These bubbles have different sizes and collapse relatively quickly. Contrary to what happens on horizontal configuration, no liquid jet is observed.

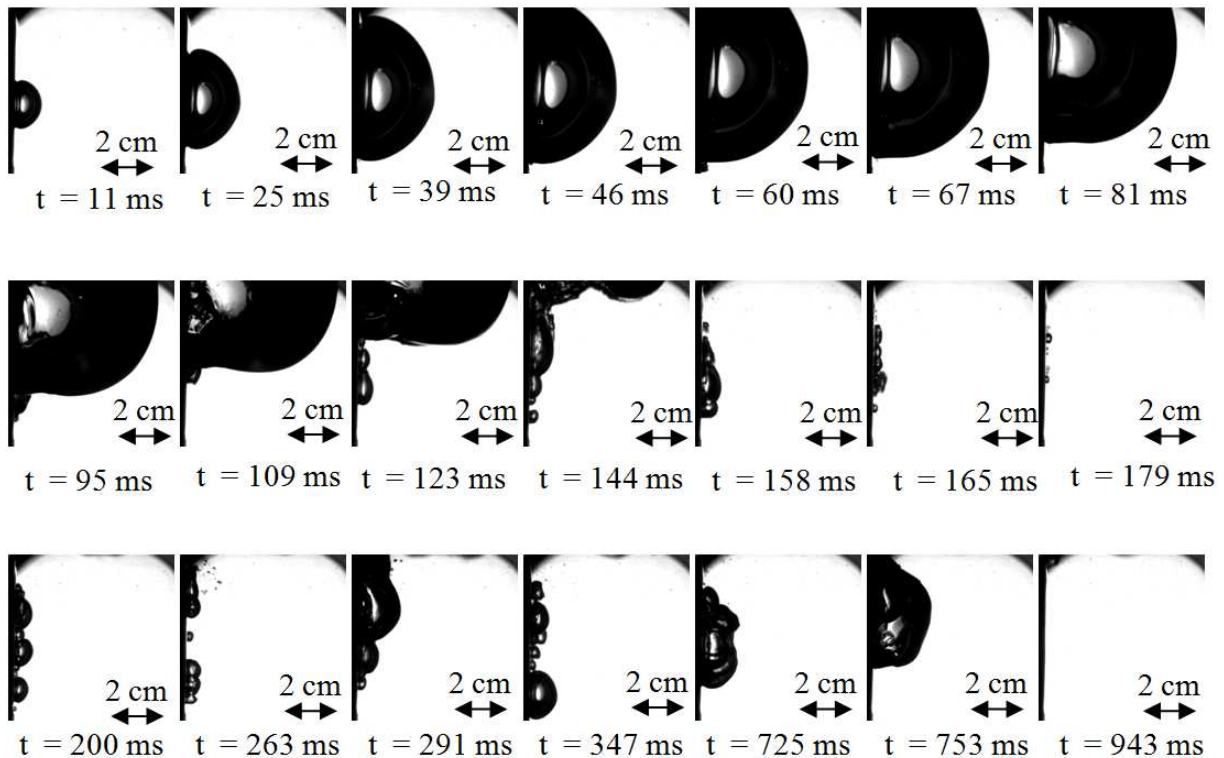


Figure 3.5: Visualization of “bubbles crisis” ($P = 1.8 \text{ kPa}$, $T_1 = 15^\circ\text{C}$, $h_1 = 167 \text{ mm}$, $\dot{q} = 12.7 \text{ W.cm}^{-2}$)

Although the surface is polished, this boiling regime is probably partly due to the phenomenon of “site seeding” as described by Eddington and Kenning (1978). During the growth of a large bubble, a microlayer is formed and then evaporated. The dry spot completely covers sites free of vapor which are still inactive. The bubble departure leaves a residue of vapor in these inactive sites, which are then able to promote bubbles nucleation. Judd and Lavdas (1980), who studied the formation of a large bubble like in the present study, agreed with this explanation. However, this formation of a bubble can also be partly due, as in horizontal configuration and despite the absence of the liquid jet, to a depression created by the rise of the bubble⁴. Lastly, as bubble collapse, an acoustic wave is generated. The formation of the following bubbles could also be fostered by acoustic cavitations. The same phenomenon must occur in horizontal configuration.

⁴ Assuming a velocity of the liquid equal to 0.6 m.s^{-1} when the bubble departed (Fig. 3.24), this depression was estimated roughly at 0.18 kPa i.e. about 10 % of the vapor pressure. It was calculated using the theorem of Bernoulli and neglecting heat transfer.

3.1.3 Thermal analysis

3.1.3.1 Boiling curve at $P_v = 1.2$ kPa

As mentioned by Shi *et al.* (1993), when vapor is trapped in inactive sites, a decrease in the surface heat flux and a decrease in the wall superheat for the next generation are observed. Such trends were observed during our experiments like in horizontal configuration. These fluctuations are shown on Fig. 3.6.

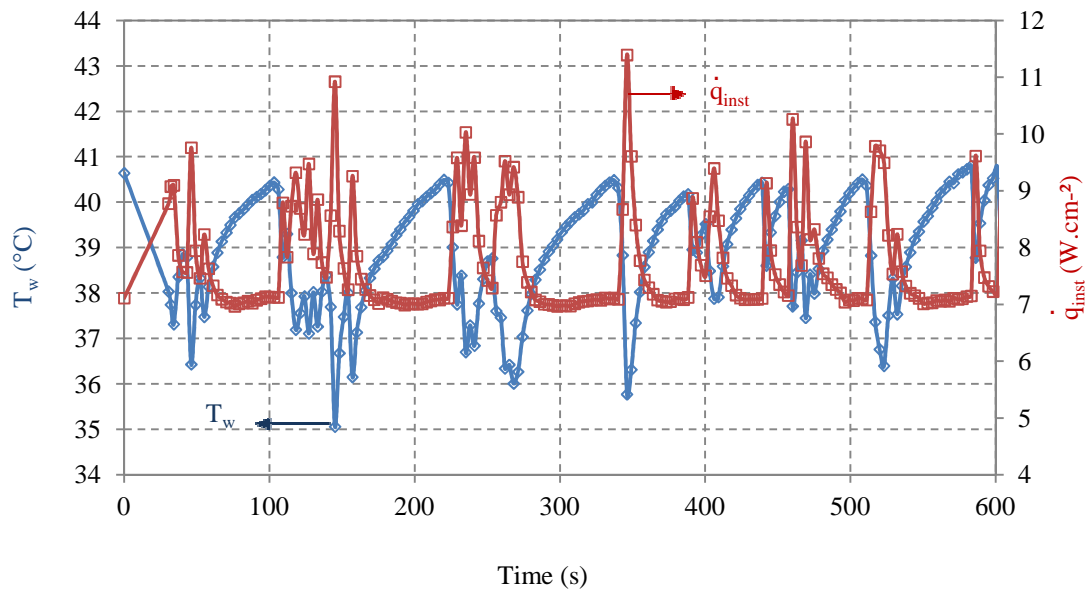


Figure 3.6: Evolution in time of the wall temperature \diamond and the instantaneous heat flux \square for $\dot{q} = 7.7 \text{ W.cm}^{-2}$ and $h_l = 156 \text{ mm}$

Despite the presence of flow patterns similar to the flow patterns observed in horizontal configuration, the cyclic boiling regime marked by fluctuations of the instantaneous heat flux and of the wall superheat is less significant. No dominant period of the boiling cycle could be defined whereas the vessel is fully thermalized. As these fluctuations are less significantly observed, the characteristic shape of the boiling curve marking the occurrence of the cyclic boiling regime is less significantly observed (Fig. 3.7).

The shape of the obtained boiling curves in vertical orientation are more similar to those obtained with the horizontal configuration at 1.2 kPa but for a height of the liquid level of 100 mm or less (cf Fig. 2.23 and Appendix C and D). The same conclusion as for $h_l = 100 \text{ mm}$ can thus be drawn: as the cyclic boiling regime is less apparent in vertical orientation than in horizontal orientation for $h_l = 200 \text{ mm}$ or even $h_l = 150 \text{ mm}$, the instantaneous value of the heat transfer coefficient (for a given imposed heat flux) is more constant along the time and the time-averaged heat transfer coefficient is severely degraded (Fig. 3.8 and 3.9).

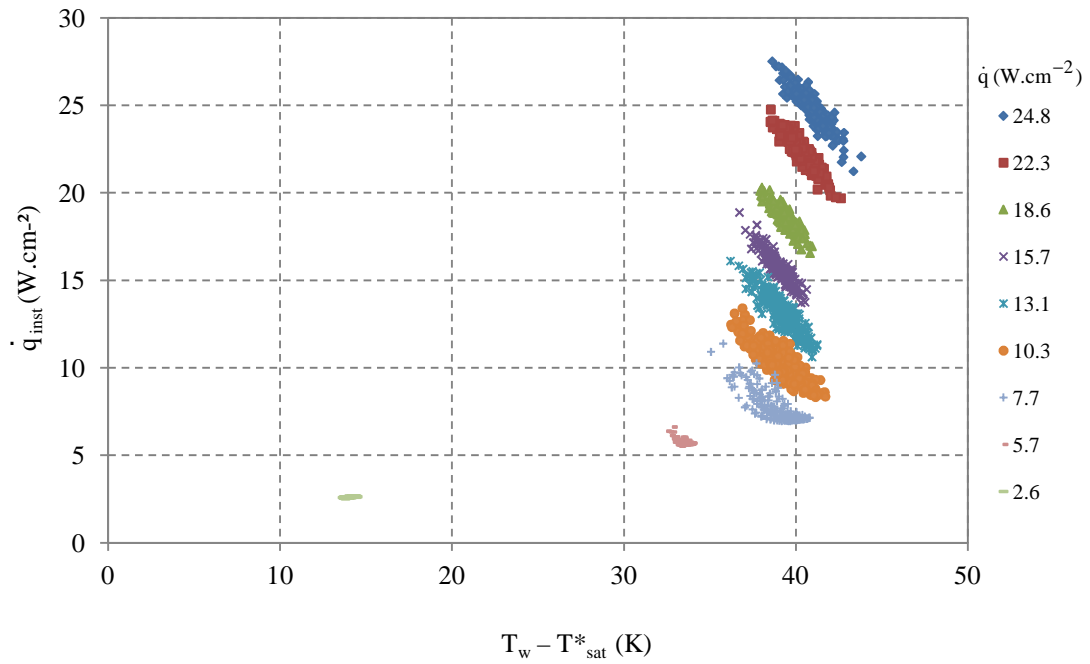


Figure 3.7: Boiling curves for $h_l = 156$ mm and $P_v = 1.2$ kPa

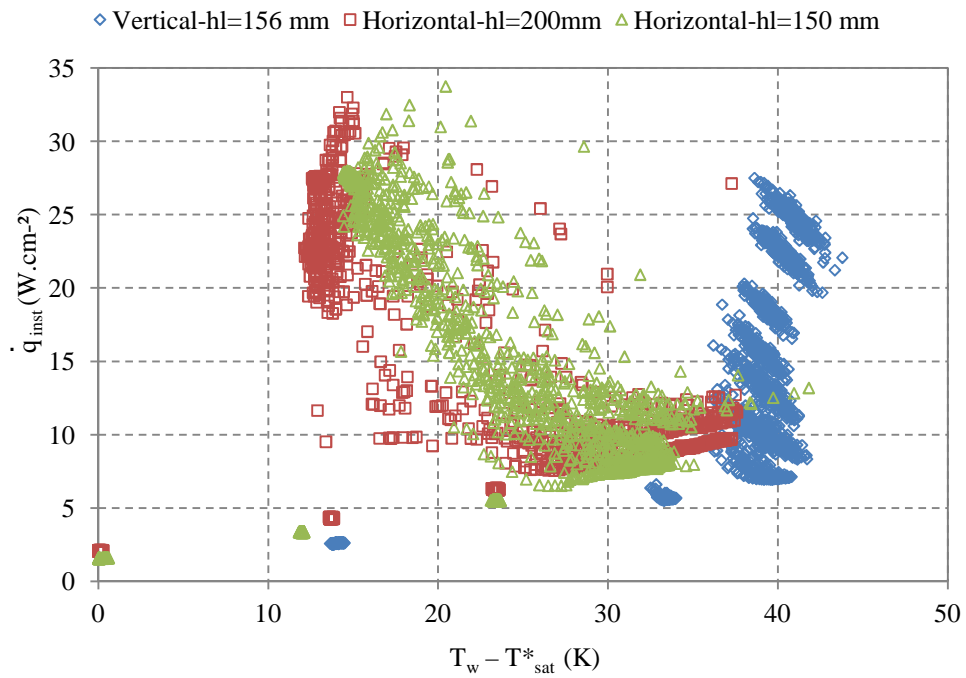


Figure 3.8: Comparison of boiling curves obtained in vertical and horizontal orientation

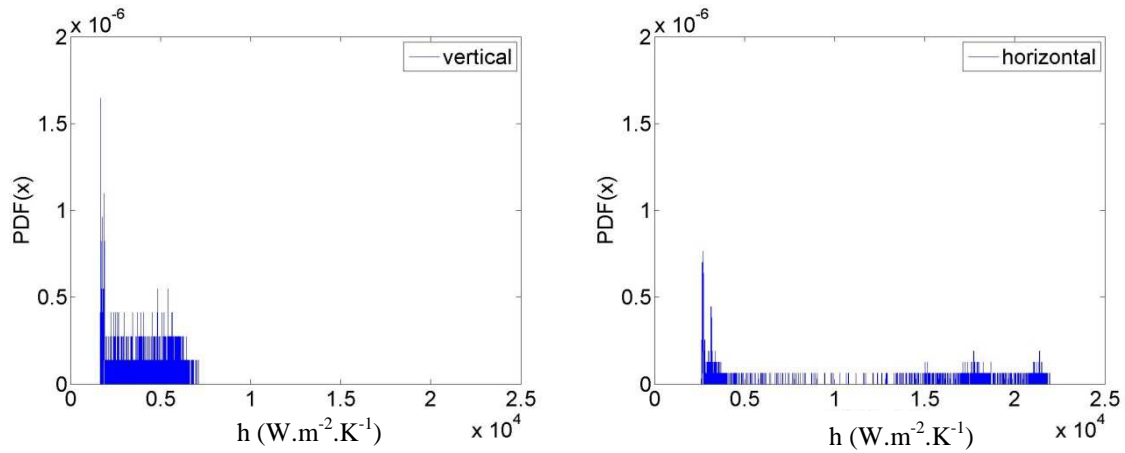


Figure 3.9: Comparison of the probability density functions (noted PDF) of the experimental heat transfer coefficient estimated at $P_v = 1.2$ kPa on a) vertical orientation, $h_l = 200$ mm b) horizontal orientation, $h_l = 156$ mm

Indeed, at low imposed heat flux, the heat transfer coefficient is similar for both orientations (below $5 \text{ kW.m}^{-2}.\text{K}^{-1}$) but then as the imposed heat flux increases, the difference in the heat transfer coefficients estimated between the two orientations becomes more and more significant. At imposed heat fluxes of 27.4 W.cm^{-2} and 22.1 W.cm^{-2} , the mean heat transfer coefficient achieved in horizontal orientation is close to $19 \text{ kW.m}^{-2}.\text{K}^{-1}$ and $16 \text{ kW.m}^{-2}.\text{K}^{-1}$ respectively, whereas in vertical orientation the heat transfer coefficient achieved is $6.2 \text{ kW.m}^{-2}.\text{K}^{-1}$. In vertical orientation, for $P_v = 1.2$ kPa and $h_l = 156$ mm, the heat transfer coefficients thus range from $1.8 \text{ kW.m}^{-2}.\text{K}^{-1}$ to $6.2 \text{ kW.m}^{-2}.\text{K}^{-1}$ whereas in horizontal orientation, for $P_v = 1.2$ kPa and $h_l = 200$ mm, the heat transfer coefficients range from $3.2 \text{ kW.m}^{-2}.\text{K}^{-1}$ to $23 \text{ kW.m}^{-2}.\text{K}^{-1}$ for imposed heat flux ranging from 0.6 W.cm^{-2} to 24.8 W.cm^{-2} .

This difference in heat transfer coefficients achieved could be due to the difference of fluid recirculation between the two orientations. In the vertical orientation, the liquid which rewets the surface is located below the bubble whereas in horizontal orientation the liquid comes from the far field liquid bulk (the liquid located at the vicinity of the bubble is carried away by the wake of the preceding bubble when this bubble detaches). Thus, the liquid which rewets the surface is warmer in the former than in the latter case. Fluctuations of the wall temperature are less significant and the cyclic boiling regime is less apparent. This conclusion is in agreement with results obtained in horizontal configuration but for height of the liquid level equal or lower than 100 mm. As a matter of fact diminishing the height of the liquid level allows diminishing the subcooling of the boiling environment, which prevents the far field liquid bulk from easily rewetting the boiling surface.

3.1.3.2 Influence of the vapor pressure

As in horizontal orientation, the influence of the vapor pressure on boiling curves is studied. Fig. 3.10 displays boiling curves obtained for vapor pressures of 5.0 kPa, 4.0 kPa, 3.0 kPa, 1.8 kPa and 1.2 kPa with a constant height of liquid level of 156 mm.

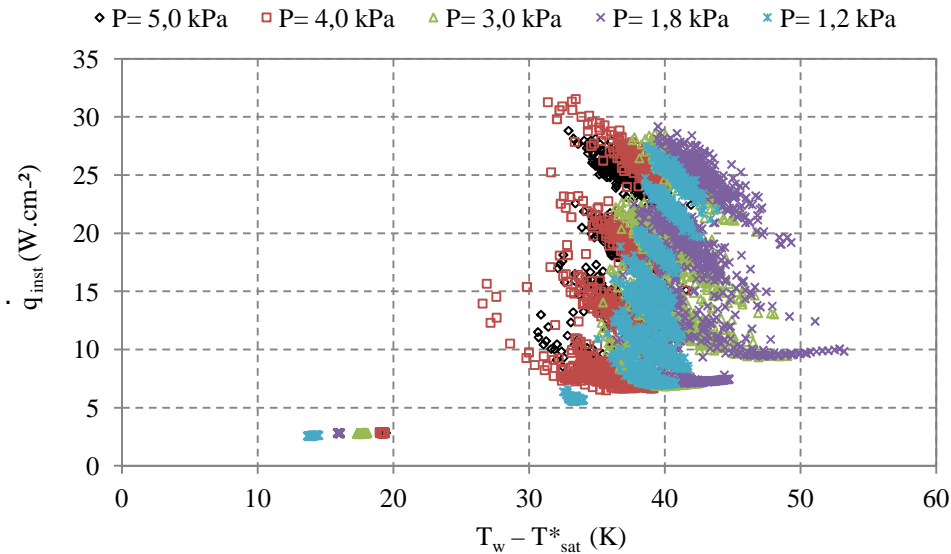


Figure 3.10: Boiling curves obtained in vertical orientation for 5 different vapor pressures

Similar shape of the boiling curves is observed whatever the pressures investigated. The dispersion of experimental points for a given heat flux is slightly different between each curves but no clear cycle can be observed. Due to the scatter of the experimental data, instantaneous heat transfer coefficients slightly higher for $P_v = 5$ kPa and $P_v = 4$ kPa could be achieved from time to time but the instantaneous heat transfer achieved remains of the same order of magnitude as for the other pressures investigated (9 to 10 $\text{kW}\cdot\text{m}^{-2}\cdot\text{K}^{-1}$ vs. 7.5 $\text{kW}\cdot\text{m}^{-2}\cdot\text{K}^{-1}$ for the other pressures investigated, cf. Fig. 3.11). The influence of the pressure on the time-average heat transfer is negligible.

According to the literature, in the vertical orientation, three main phenomena improve the heat exchange: convection phenomena, bubbles shape and wake-induced flow. Convection phenomena are due to inhomogeneous density of the fluid along the heat surface. The bubble shape fosters the evaporation of the microlayer (Bonjour *et al.*, 1997) and the slide of the bubble along the heated wall. As the bubble slides, cool liquid is carried up by the bubble's wake. This is what we call in the present work the wake-induced flow. The higher is the sliding velocity, the greater the motion of the liquid in the wake of the bubble and thus the higher the convective effects due to the wake-induced flow.

The negligible influence of the pressure on the heat transfer at subatmospheric pressure could be explained by a balance between these phenomena and those due to the subcooling of the environment. Indeed, as the vapor pressure decreases for a given height of the liquid level, the maximal subcooling degree of the environment increases. A part of the vapor generated re-condenses and higher wall superheated is required to set boiling on. But, as the pressure decreases (down to a certain pressure not reached in this study), the bubble diameter increases (Van Stralen *et al.*, 1975, Zuber 1959, Cole and Rohsenow, 1969). Due to the bubble size and shape, the length of the microlayer increases with the decrease of the pressure (Fig. 3.12). The evaporation of this microlayer is fostered. As the bubble is larger, the sliding velocity of the bubble along the wall is higher and convective effect due the wake-induced flow increases. These two phenomena (increase of the microlayer length and of convective effects due to wake-induced flow) enhance the heat transfer.

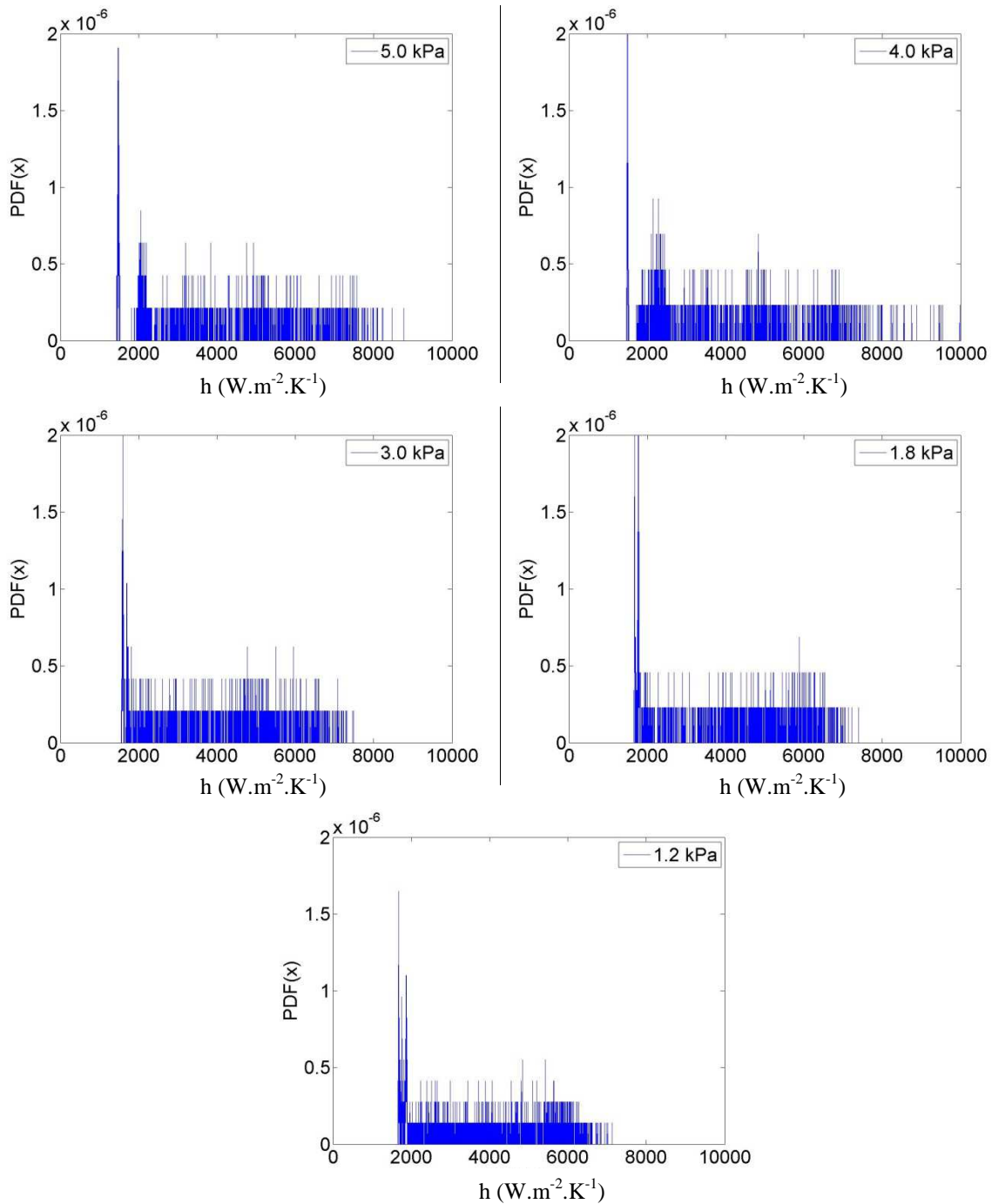


Figure 3.11: Comparison of the probability density functions (noted PDF) of the experimental heat transfer coefficient estimated $h_1 = 156$ mm and a) $P_v = 5.0$ kPa, b) $P_v = 4.0$ kPa, c) $P_v = 3.0$ kPa, d) $P_v = 1.8$ kPa, e) $P_v = 1.2$ kPa

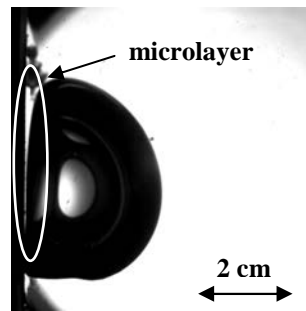


Figure 3.12: Visualization of the microlayer ($P = 1.3 \text{ kPa}$, $h_l = 50 \text{ mm}$, $\dot{q} = 2.9 \text{ W.cm}^{-2}$)

3.1.3.3 Influence of the height of the liquid level

The influence of the height of the liquid level on heat transfer was also studied. Fig. 3.13 shows boiling curves obtained for vapor pressures of 1.2 kPa and a height of liquid level of 74 mm, 115 mm and 167 mm.

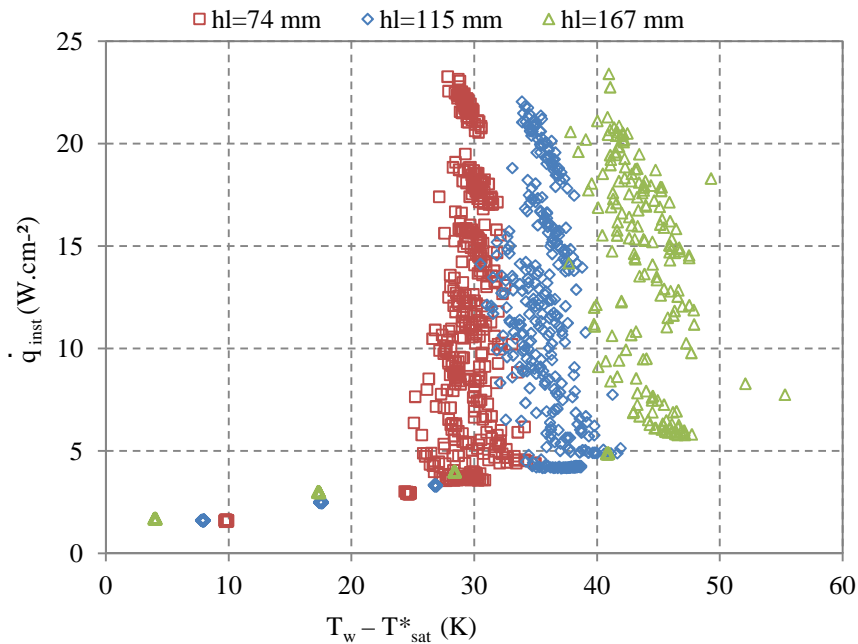


Figure 3.13: Boiling curves obtained in vertical orientation for 4 different heights of the liquid level

The minimum wall superheat required to maintain nucleation increases with the liquid height. At 74 mm, the wall superheat required to set boiling on is around 30 K whereas a wall superheat of around 47 K is required for a height of the liquid level of 167 mm. This observation is in agreement with the literature regarding boiling in subcooled environment as the onset of nucleate boiling is delayed when increasing the subcooling, i.e. when increasing the height of the liquid level.

According to these results, the height of the liquid level has a significant impact on the heat transfer whereas the vapor pressure imposed has a negligible influence on it, despite the fact that in each case the subcooling degree of the environment is changed.

These different trends observed when varying the liquid height or when varying the vapor pressure can be explained by analyzing the conditions encountered in the boiling environment (Fig. 3.14). Indeed,

for a given height of the liquid level, as the vapor pressure decreases, thermophysical properties of the water varies. These variations could be negligible for the thermal conductivity, latent heat or surface tension but they become rapidly significant for the vapor density. As the pressure decreases, the boiling environment is more subcooled but bubbles formed are larger. Thus, as mentioned before, phenomena due to the subcooling degree of the environment and phenomena due to the bubble shape and growth are balanced. On contrary, for a given vapor pressure, as the height of the liquid decreases, the local pressure decreases as well as the subcooling degree of the boiling environment. Thus, as the liquid height decreases, bubbles are larger and the subcooling is lower. Both phenomena induce a decrease of wall superheat required to set boiling on.

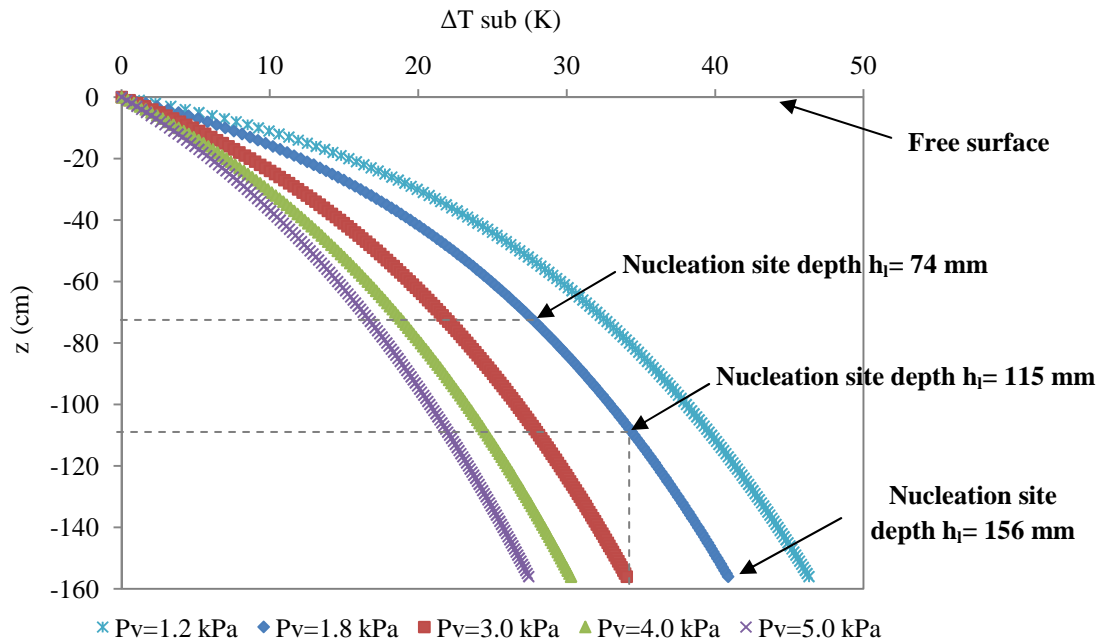


Figure 3.14: Evolution of the subcooling degree with the liquid depth for the five vapor pressures investigated and three heights of the liquid level

In order to illustrate the impact of the water thermophysical properties on heat transfer, Fig. 3.15 shows boiling curves obtained for $P_v = 3.0$ kPa, $h_{liq} = 156$ mm and $P_v = 1.8$ kPa, $h_l = 115$ mm, i.e. for experimental conditions for which a same maximal subcooling degree is given (namely $\Delta T_{sb} = 34$ K).

Although the same maximal subcooling degree is reached at the level of the nucleation site, the heat transfer is higher for $P_v = 1.8$ kPa, $h_l = 115$ mm than for $P_v = 3.0$ kPa, $h_l = 156$ mm. Different phenomena could explain this observation. First, even if the same maximal subcooling degree is reached, the subcooling gradient (dT_{sat} / dz) is not the same. For a same Δz , the ΔT_{sat} will be higher in the first case than in second case. This variation of the subcooling degree with the liquid depth must have an influence on the amount of vapor which condenses. Second, the imposed vapor pressure is not the same in both cases and the temperature of the liquid and the local saturation temperature are not the same either. The thermophysical properties of the water are thus not the same although this evolution is negligible for the thermal conductivity, the surface tension and the latent heat (-0.42 %, +0.35 % and +0.15 % respectively between conditions imposed by setting $P_v = 3.0$ kPa, $h_l = 156$ mm and conditions imposed by setting $P_v = 1.8$ kPa, $h_l = 115$ mm). For the vapor density however, this evolution is more significant as a decrease by 8.3 % is calculated.

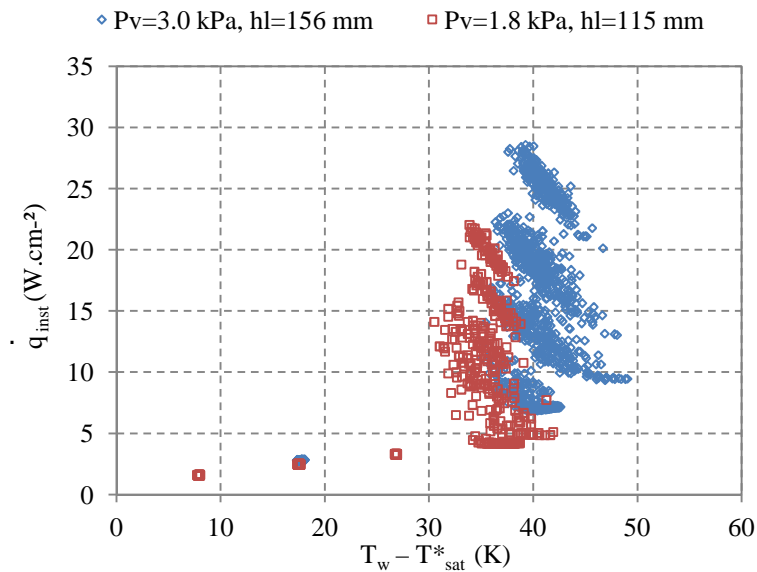


Figure 3.15: Comparison of boiling curves obtained for $P_v = 3.0$ kPa, $h_l = 156$ mm and $P_v = 1.8$ kPa, $h_l = 115$ mm, i.e. for a same maximal subcooling degree of 34 K

This value of the vapor density should have an impact on the volume of the bubble and on the sliding velocity. As explained above, as the bubble is larger, the evaporation of the microlayer is fostered, the sliding velocity is higher then, the wake-induced flow is fostered. As same maximal subcooling degree is reached, these phenomena are not balanced in the same way by phenomena due to the difference in subcooling gradient.

Another interesting result to mention is, as observed just above, that the heat transfer is enhanced with the decrease of the height of the liquid level in vertical orientation. In horizontal orientation, the opposite trend is observed (Chap 2, section 2.3.2.3). This is due to the difference of heat transfer mechanisms and bubble growth between these two configurations.

3.2 Subatmospheric water pool boiling in a vertical narrow space

3.2.1 Experimental setup

In order to be closer to the configuration encountered in plate-type heat exchangers, experiments were conducted for the study of boiling in a narrow vertical space. For these studies, the previous experimental setup was equipped with a truncated conical unheated and transparent PVC plate placed parallel to the heating surface in order to confine the fluid in the vicinity of the boiling surface, i.e. to form a vertical channel open at its circular periphery (Fig. 3.16).

The truncated conical unheated PVC plate used presented a cone angle of 45° and a diameter of 45 mm at the surface closest to the heated sample. The gap size of the narrow channel created is adjusted as wished by means of three threaded steel rods crossing the PVC plate. The narrow channel thus created is accurately measured by means of an optical device.

As the sample with is confined plate is inserted in the vessel, great care is taken to locate the threaded steel rods in order to avoid any disturbance of the upward flow (Fig. 3.17).

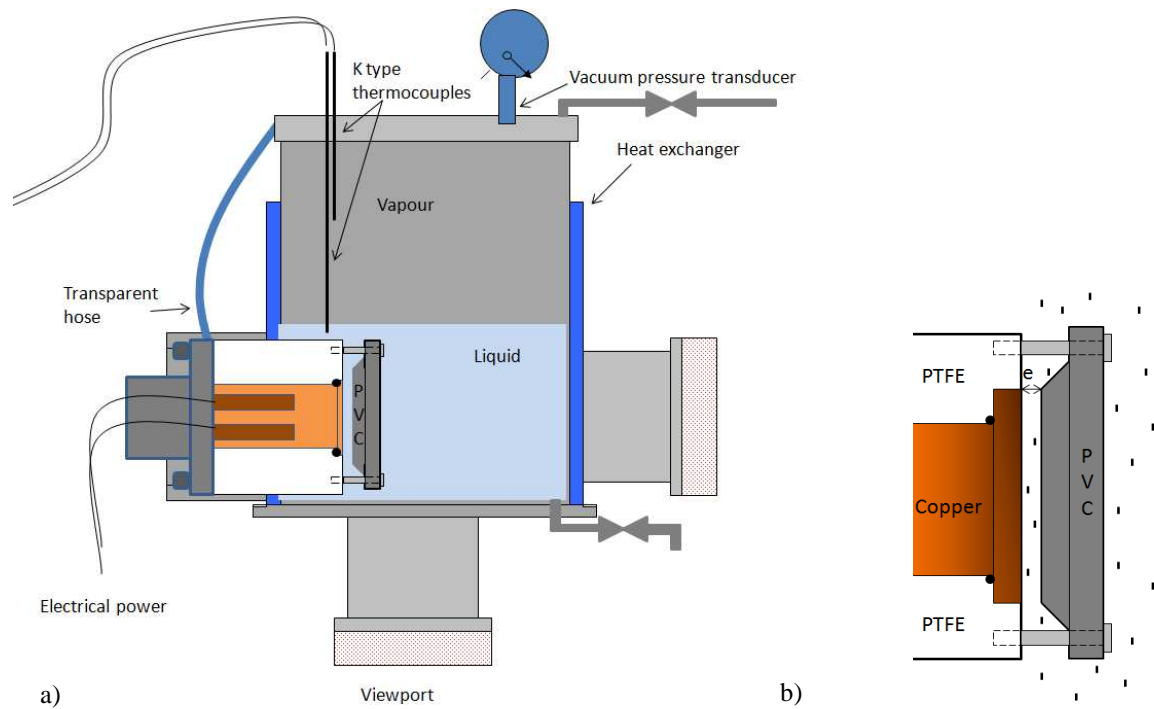


Figure 3.16: Detail of a) the pool boiling device b) the confinement plate

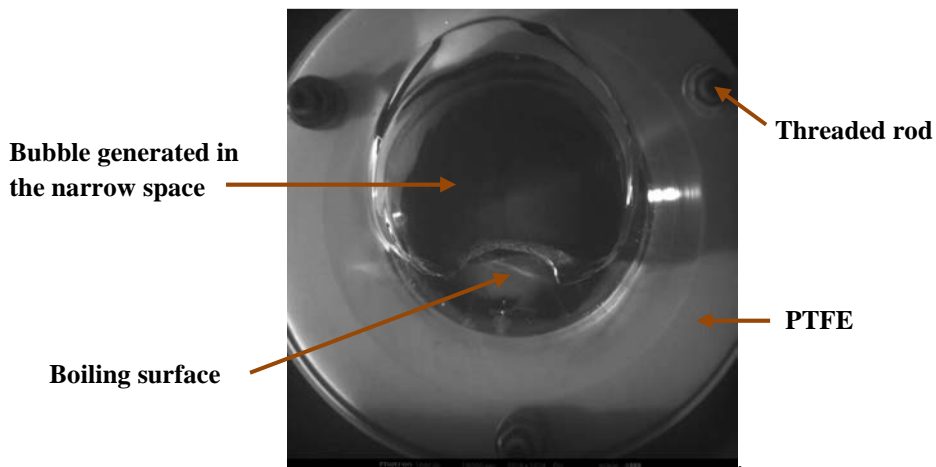


Figure 3.17: Picture of bubble formed inside the narrow space created ($P_v = 5$ kPa, $h_1 = 156$ mm, $e = 11.5$ mm)

3.2.2 Bond number limitation for the characterization of subatmospheric boiling phenomena in narrow channel

As it could be observed in the literature review, in order to characterize the effect of the confined space on bubble, the Bond number is widely used. However, it has been shown that at low pressure range bubbles have centimeter size and that the force balance at the detachment is different than at atmospheric pressure. The meaning of the Bond number for characterizing boiling heat transfer at subatmospheric pressure thus need to be discussed as a background before introducing the results obtained.

The Bond number stems from the Eötvös number (Eo) or gravity-based Bond number (Bo_g) defined as $Eo = Bo_g = \frac{\rho g R^2}{\sigma} = Bo^2$. The Eötvös number gives the proportionality between buoyancy forces and surface tension forces. It was used by Bretherton in 1961 as he studied the free rise of a bubble in a vertical tube in a theoretical point of view. His study was motivated by the fact that many experimental results revealed the existence of two regions with different behavior of the boiling phenomena in narrow channels. The author noted that if the gravity-based Bond number is inferior to 0.842, then the bubble should not rise. A limit value of 2 could be also found in the literature. Nevertheless, this dimensionless number was then used to determine the transition between a behavior governed by capillary effects and a behavior governed by viscous boundary layer phenomenon (Moriyama and Inoue, 1996). As an image, this transition is given for a tube diameter of the same size as the bubble diameter.

Based on the Eötvös number, the Bond number known nowadays is defined as $Bo = \frac{e}{L_c}$. This Bond number is often defined as a scaling for the ratio between the thickness of the narrow channel and the departure diameter of a bubble. Indeed, the bubble detachment diameter is commonly determined by equating the resultants of the buoyancy and surface tension forces (Buyevich and Webbon, 1996). This means that at the detachment of the bubble, the ratio of the Eötvös number (which gives the proportionality between buoyancy forces and surface tension forces) is equal to unity. Thus, based on this number, the bubble departure diameter should be close to $\sqrt{\frac{\sigma}{g(\rho_l - \rho_v)}}$, which is also known as the capillary length (L_c).

According to classical correlations (Cole and Rohsenow, 1969; Jensen and Memmel, 1986) or to experiments (Van Stralen, 1975; Rullière *et al.*, 2012), bubbles departure diameters have centimeter size at subatmospheric pressure while the capillary length is of a few millimeters (e.g. 2.7 mm at 2 kPa). There is thus a factor 100 between the capillary length and the bubbles departure diameter observed by Van Stralen (1975) or in this study. This is due to the fact that the bubble detachment at subatmospheric pressure is no longer mostly governed by the balance between buoyancy forces and the capillary forces, but rather mainly by the buoyancy forces and the inertial forces. In order to illustrate this change in governing factors, the three dimensionless numbers $We = \frac{\rho_l R u^2}{\sigma}$, $Ca = \frac{\mu_l u}{\sigma}$,

$Bo_g = \frac{\rho_l g R^2}{\sigma}$ used respectively to give roughly the magnitude of inertial, viscous and gravitational forces relative to surface-tension forces and the number $I_R = \left(\frac{4}{27}\right) \left(\frac{\sigma}{\rho_l \alpha^2}\right) \frac{R_{cav}}{Ja^2}$ developed by

Robinson and Judd (2004) are given in Table 3.1 for a variety of conditions. As the velocity of the bubble growths is needed to conduct this analyze, bubbles characteristics obtained by processing pictures obtained in horizontal configuration (Chap. 2) with the MATLAB® program are used (bubbles named B1 and B2 in this study). The experimental data needed for the bubble at atmospheric pressure (bubble B3) were estimated from the experimental study done by Mukherjee and Dhir (2004). Due to the non-homogeneity of the boiling environment imposed by the static head at low pressure, a rigorous analysis of the force balance during the bubble growth at subatmospheric pressure would require an integration of each thermophysical property along the bubble curvature. As the aim of the present analysis is to compare the influence of the different forces through usual dimensionless

numbers, the approach is simplified. The thermophysical properties of the fluid are assumed to be constant along the curvature of the bubble and the radius of the bubble is calculated assuming a sphere of equal volume.

Table 3.1: Value of usual dimensionless numbers used to give the proportionality of different forces just before detachment at 1.8 kPa, 15 kPa and 100 kPa

Dimensionless Number	Formula	B1 P _v = 1.8 kPa R = 1.74 cm u = 0.295 m/s	B2 P _v = 15 kPa R = 3.00 cm u = 0.395 m/s	B3 P _v = 100 kPa R = 0.17 cm u = 0.3 m/s
We	$We = \frac{\rho_l R u^2}{\sigma}$	20	62	$2 \cdot 10^{-3}$
Gravity-based Bo	$Bo_g = \frac{\rho_l g R^2}{\sigma}$	40	130	0.4
Ca	$Ca = \frac{\mu_l u}{\sigma}$	$5 \cdot 10^{-3}$	$3 \cdot 10^{-3}$	$5 \cdot 10^{-5}$
I _R	$I_R = \left(\frac{4}{27}\right) \left(\frac{\sigma}{\rho_l \alpha^2}\right) \frac{R_{cav}}{Ja^2}$	$3 \cdot 10^{-3}$	0.12	3

As inertial, viscous and buoyancy forces are the governing forces for the detachment of bubbles at subatmospheric pressure (Table 3.1), an inertial and viscous term should be added to the Bond number in the case of the characterization of subatmospheric boiling in narrow channels. Simplifying these four mains forces to:

- buoyancy force $\approx g(\rho_l - \rho_v)R^3$
- viscous force $\approx \mu u R$
- inertial force $\approx \rho_l u^2 R^2$
- surface tension $\approx \sigma R$

and assuming that the detachment would occur when the sum of these four simplified forces becomes null, a new characteristic length can be defined:

$$L_m = \frac{u^2}{2g} + \sqrt{\left(\frac{u^2}{2g}\right)^2 + L_c^2 + \frac{\mu u}{(\rho_l - \rho_v)g}} \quad (3.1)$$

With this number, for the experimental conditions of the bubble named B1 and the bubble named B2, this length is equal to 3.9 cm and 5.7 cm respectively while values of 3.4 cm and 6.0 cm were obtained experimentally. Due to the low value of the viscous term $\frac{\mu u}{(\rho_l - \rho_v)g}$, the latter could be neglected in these calculations.

3.2.3 Effect of the confinement on experimental boiling curves

3.2.3.1 Influence of the thickness of the narrow channel

In the following study, the thickness of the narrow channel varies from 7.7 mm to 2 mm with the following discrete values: 7.7 mm, 5.9 mm, 3.7 mm, 2.9 mm and 2 mm. Fig. 3.18 shows the

experimental boiling curves obtained for the six spacing mentioned above and for a vapor pressure P_v of 1.2 kPa. Pool boiling without confinement ($e = \infty$) is used as reference. For each channel thicknesses, six different heat fluxes are imposed at the cartridges heaters: 3 W.cm^{-2} , 6 W.cm^{-2} , 9 W.cm^{-2} , 14 W.cm^{-2} , 20 W.cm^{-2} and 25 W.cm^{-2} .

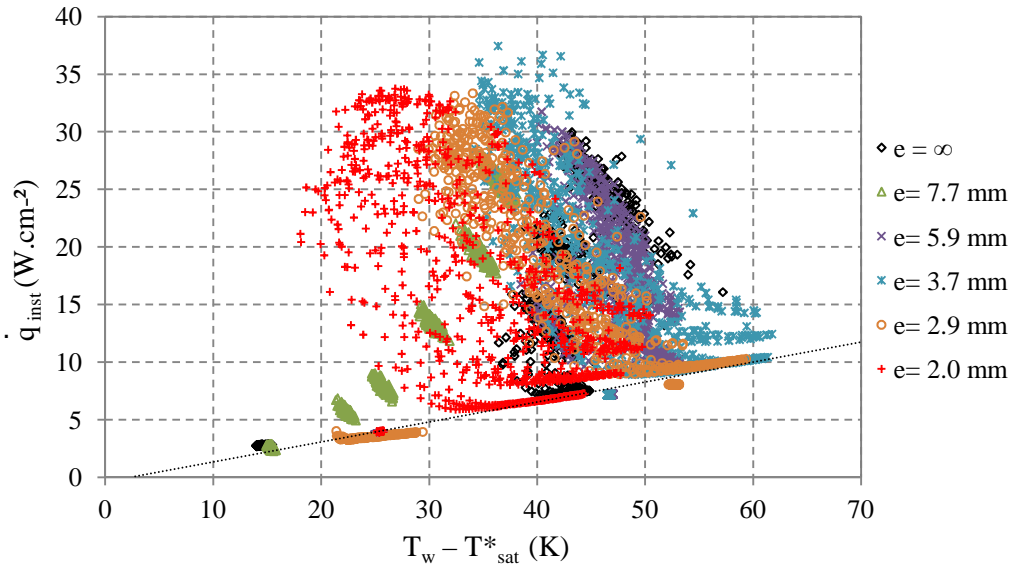


Figure 3.18: Experimental boiling curves for different channel thicknesses ($P_v = 1.2 \text{ kPa}$, $h_1 = 156 \text{ mm}$)

For a channel thickness of 7.7 mm, heat transfer is enhanced compared to the free boiling ($e = \infty$, Fig. 3.18 and 3.19). Visual observations revealed that for $e = \infty$, the diameter of detachment of the bubble at 1.2 kPa can reach up to 15 cm. Besides, the calculation in section 3.2.1 led to a theoretical value of a few centimeters. Therefore, this is in agreement with the literature (Aoki *et al.*, 1982, Fujita *et al.*, 1988, Bonjour *et al.*, 1997), as the bubble is flattened in the narrow channel, the evaporation of its microlayer is facilitated and thus the heat transfer is enhanced. However, as the size of the channel keeps decreasing the boiling regime seems more chaotic (high dispersion of the experimental points). This leads to a large range of instantaneous heat transfer coefficients (Fig. 3.19). The heat transfer coefficient is mostly degraded but periodically high heat transfer coefficients are achieved compared to heat transfer coefficient obtained for less chaotic boiling regimes. Despite these periodical high values of the heat transfer coefficient, the general trend for 5.9 mm is a degraded heat transfer even compared to the free boiling. Even though another heat transfer improvement is observed again when decreasing the channel thickness from 2.9 to 2 mm, for low imposed heat fluxes, the best heat transfer performance is still achieved for a thickness of 7.7 mm, i.e. for a less chaotic boiling regime.

The chaotic boiling regime characterized by the dispersion of the experimental points for a given heat flux marks the occurrence of the same cyclic boiling regime as obtained previously for a same vapor pressure but for a horizontal heated surface. For a given heat flux (imposed by the cartridges heaters) and for a given channel thickness, periods of low heat transfer coefficient are observed (dotted line on Fig. 3.18). Heat is transferred by unsteady natural convection due to the previous arrival of cold far field liquid. Once the convective cells are established and the wall superheat is high enough, a large bubble filling quickly the channel thickness appears followed by many bubbles of different diameter of detachment and different frequency of detachment, which improves the heat transferred. Then, as the energy stored in the wall is released to the fluid and the departure of the bubbles brings cold liquid, time is needed to reheat the liquid and reach the wall superheat needed to onset the boiling again. This last phase of the cycle can take more than 200 s as well as only a few seconds.

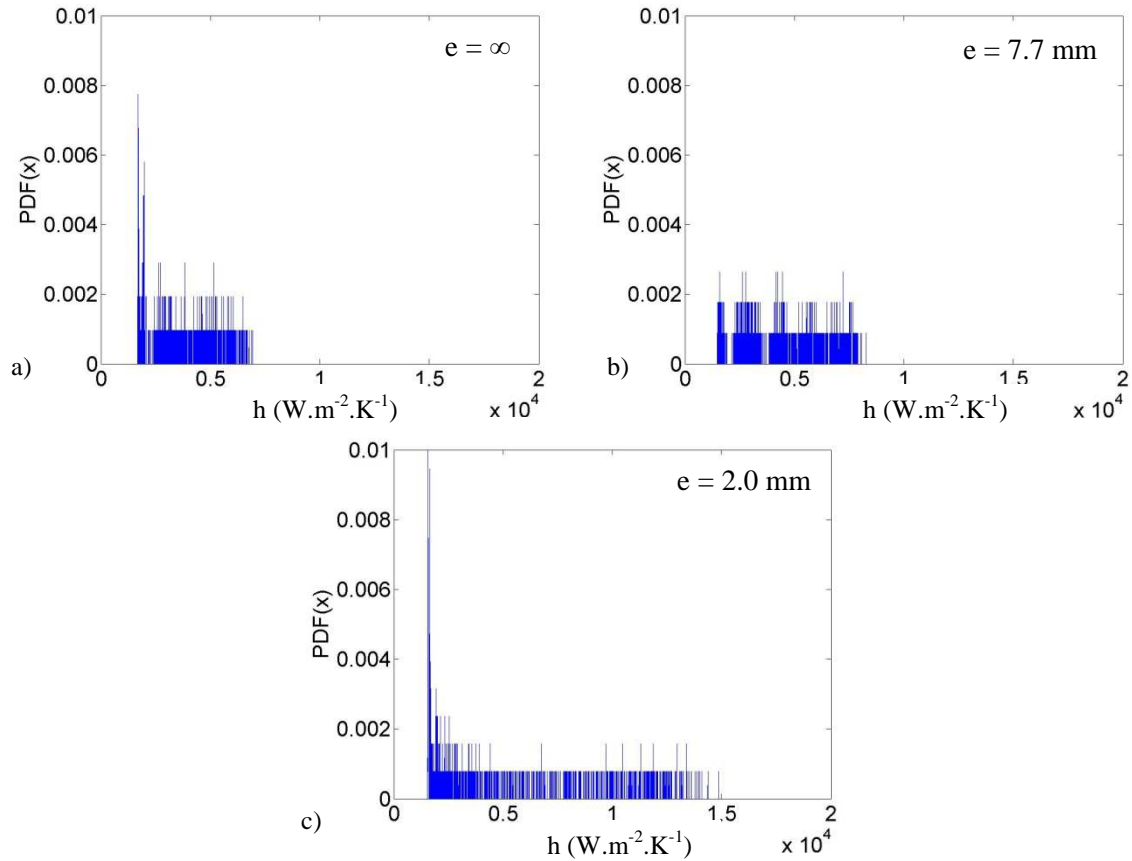


Figure 3.19: Probability density functions (noted PDF) of the experimental heat transfer coefficient for three channel thicknesses a) $e = \infty$, b) $e = 7.7$ mm and c) $e = 2$ mm ($P_v = 1.2$ kPa, $h_l = 156$ mm)

The scatter of the experimental data is linked to this waiting time. A long time between two bubbles implies a high scatter of the experimental data. This cycle is more or less significant depending on the channel thickness.

3.2.3.2 Influence of the vapor pressure

In the study of boiling in horizontal orientation (Chap. 2), it was observed that the appearance of the cyclic boiling depends on the imposed vapor pressure. This also holds true in the present cases of confined boiling. Fig. 3.20 shows the appearance of this cyclic regime with the decreasing pressure for the free boiling ($e = \infty$), $e = 7.7$ mm, $e = 5.9$ mm and $e = 2.9$ mm.

At subatmospheric pressure, the influence of the pressure on the heat transfer in a narrow channel is negligible until, for a given channel thickness, the cyclic boiling regime is set on. For the investigated pressures (from 5 down to 1.2 kPa), the influence of the pressure on the heat transfer is thus negligible for free boiling and for $e = 7.7$ mm (Fig. 3.20a and b). But for narrower channels, the cyclic boiling regime occurs for lower pressures. Thus, for a channel thickness of 5.9 mm, cyclic boiling appears for pressure of 1.8 kPa and 1.2 kPa. It is clearly seen on Fig. 3.20c that this change in the boiling regime has a significant effect on the heat transfer. The wall superheat increases significantly as this boiling regimes appears. The cyclic regime is then obtained for all of the investigated pressures for channel narrower thicknesses than 3.7 mm.

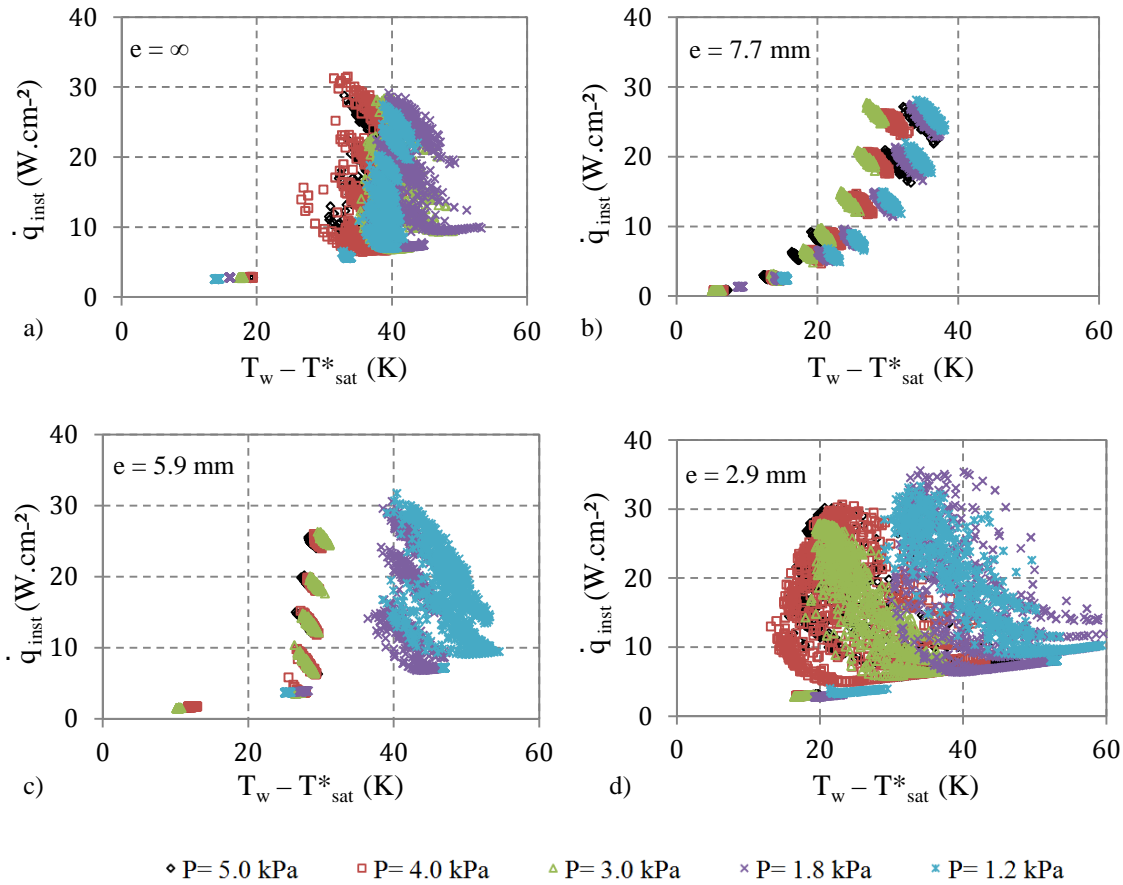


Figure 3.20: Influence of the pressure on experimental boiling curves for different vapor pressures imposed and a) $e = \infty$, b) $e = 7.7$ mm, c) $e = 5.9$ mm and d) $e = 2.9$ mm ($h_l = 156$ mm)

For a given channel thickness, if the cycling boiling regime occurs whatever the pressure, the pressure has an influence on the waiting time and thus on time-averaged heat flux and the time-averaged wall superheat (Fig. 3.21 and Fig. 3.22). Thus, for a thickness of 2.9 mm, for pressures of 3.0 kPa, 4.0 kPa and 5.0 kPa the wall superheat is around 20 K most of the time (Fig. 3.21). On the contrary at 1.2 and 1.8 kPa, the probability density functions of the experimental wall superheat present a peak around 55 K (Fig. 3.22). The same difference occurred regarding time-averaged heat flux. At 5 kPa the major part of the heat transferred to the fluid corresponds to the heat flux imposed by the cartridge heater (few cycles of storage and release of energy). Heat is thus mainly transferred by steady convection at low heat fluxes and then by fully developed boiling at higher heat fluxes. Below 5 kPa, at higher heat fluxes, the probability density function of the instantaneous heat flux recorded is smooth (no peak corresponding to the value of heat flux that is imposed by the heater is observed). Heat is thus mainly transferred by unsteady natural convection leading to high wall superheat and dominance of low instantaneous heat fluxes.

As the channel thickness and the pressure have a significant influence on the boiling regime and thus on the heat transfer, the general trend of the heat transfer variations with the decrease of the channel thickness and/or with the decrease of the pressure depends on both parameters. Thus, two different trends were observed for the smallest thicknesses ($e = 3.7$ mm, $e = 2.9$ mm and $e = 2$ mm) depending on the pressure:

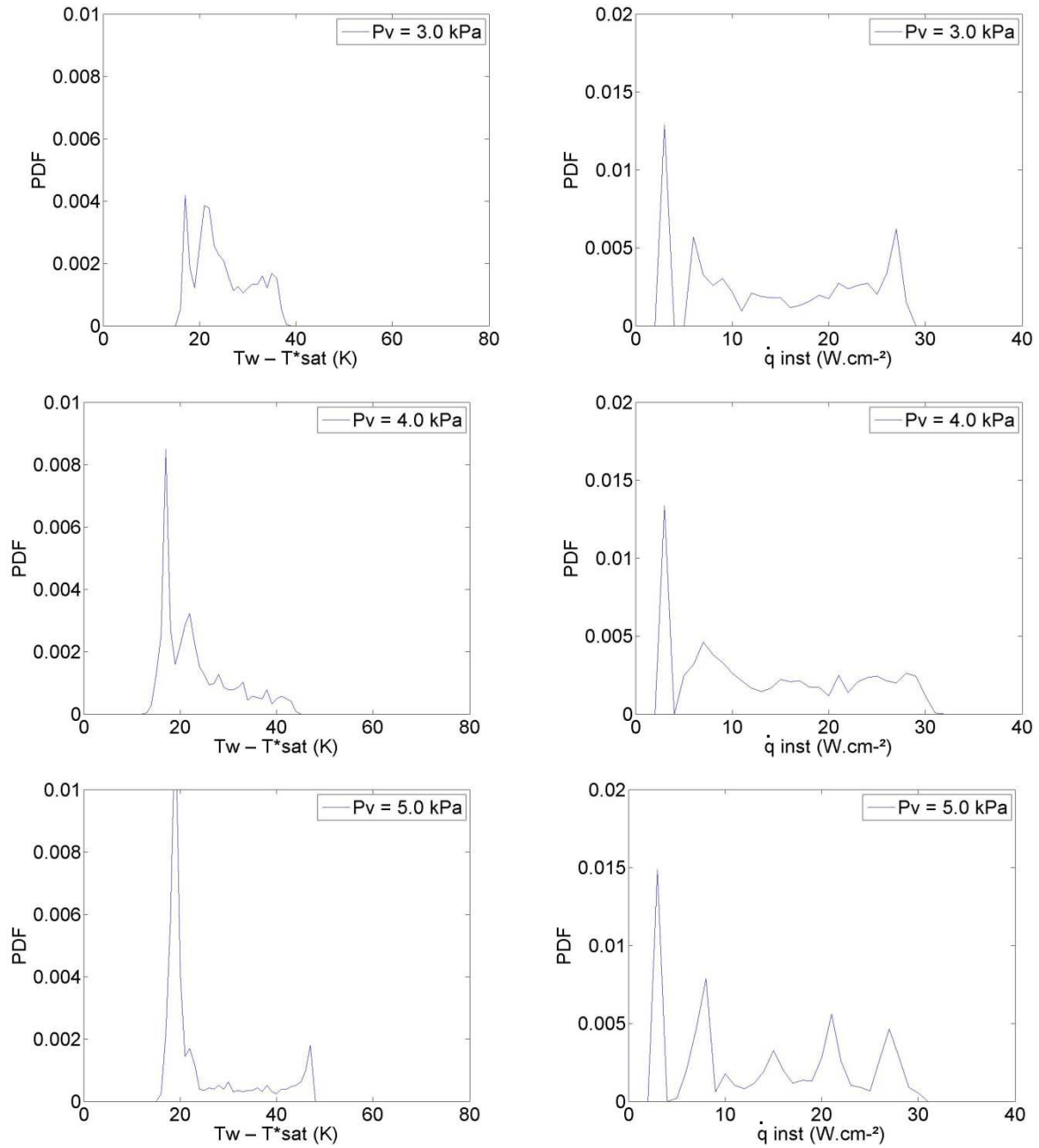


Figure 3.21: Probability density functions (noted PDF) of the experimental wall superheat (on left), experimental instantaneous heat flux (on right) for 3.0 kPa, 4.0 kPa and 5.0 kPa ($h_1 = 156$ mm, $e = 2.9$ mm)

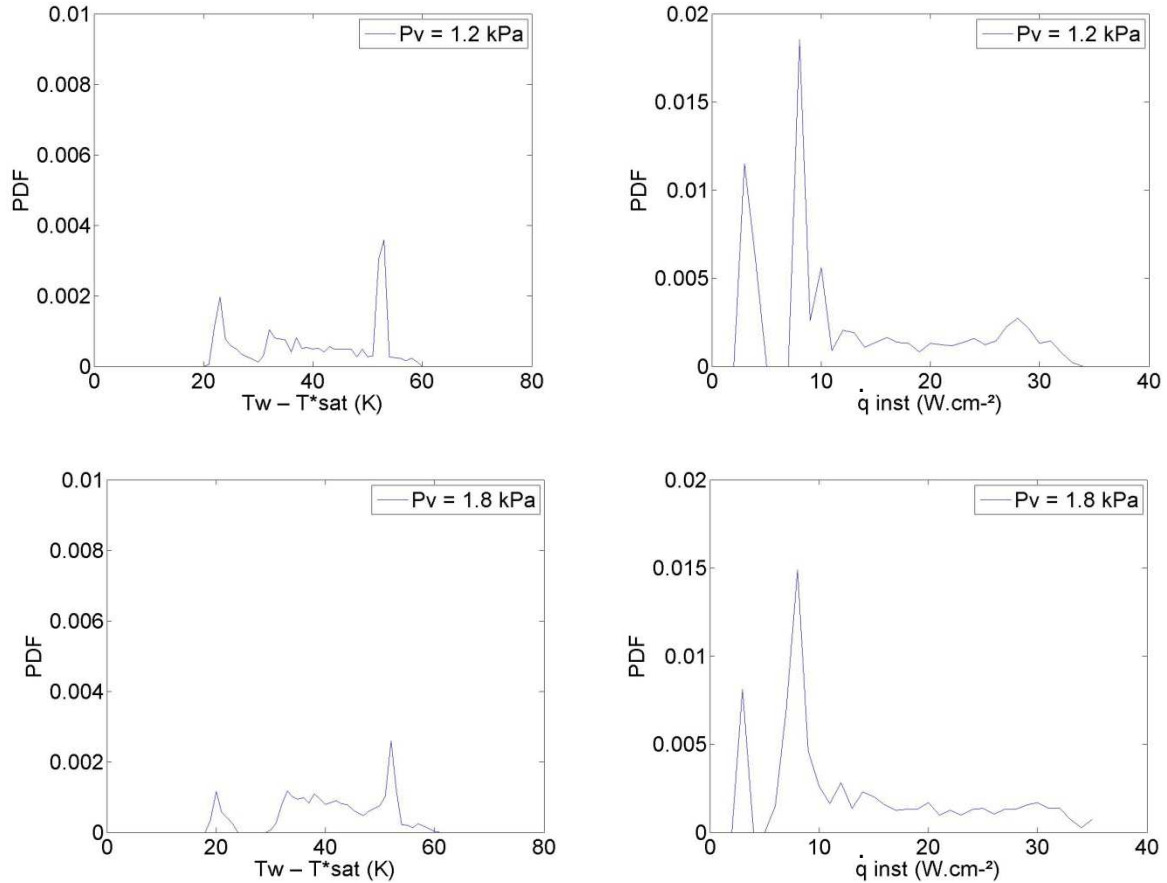


Figure 3.22: Probability density functions (noted PDF) of the experimental wall superheat (on left), experimental instantaneous heat flux (on right) for 1.2 kPa and 1.8 kPa ($h_1 = 156$ mm, $e = 2.9$ mm)

- For pressures ranging from 5 to 3 kPa: with respect to 5.9 mm, heat transfer is degraded for $e = 3.7$ mm whereas it is enhanced for $e = 2$ mm. Similar heat transfer coefficients are achieved for $e = 3.7$ mm and $e = 2.0$ mm.
- For the lowest pressures ($P_v = 1.8$ kPa or $P_v = 1.2$ kPa): heat transfer is enhanced as the channel thickness decreases.

For the largest channels ($e = 5.9$ mm and $e = 7.7$ mm) and for each pressure investigated, the general trends observed are the same as observed in Fig. 3.18. The heat transfer is first enhanced for a channel thickness of 7.7 mm with respect to free boiling, then the heat transfer is reduced for $e = 5.9$ mm.

3.2.4 Highlight on the wake-induced flow by PIV analysis

Different explanations for the changing heat transfer mechanisms when decreasing the thickness of the channel at low heat fluxes could be found in the literature. One suggests that the flatten shape of the bubble fosters site-seeding and the evaporation of the microlayer. Another suggests that, when reducing the channel thickness, i.e. the cross-section for fluid flow, convective effects induced by the bubbles growth and rise are increased. However, for Ait Aneur (2006), the heat transfer enhancement in narrow channel is linked to the boiling regime obtained. For this author, the enhancement of the heat transfer at low heat flux and low spacing cannot be explained by the enhancement of the convective effect as he observed a decrease of the fluid velocity when decreasing the thickness of the channel.

As at subatmospheric pressure bubbles obtained have centimeter size while the channel thicknesses in the present study have millimeter size, the influence of the pressure and the channel thickness on the heat transfer cannot be only due to the first mechanism. The influence of the boiling regime on the heat transfer has been confirmed in the previous part: observations are in agreement with those of Ait Ameur (2006). It remains the explanation of an enhancement of the heat transfer due to wake-induced flow. In order to verify this assumption, a Particle Image Velocity (PIV) device was implemented.

The PIV device comprises a continuous ND-Yag laser beam (wavelength of 532nm, power of 5 W), a sheet generator, a mirror and a high velocity camera (Fig. 3.23). The mirror is located just below the viewport situated at the bottom of the vessel and an angle of 45 °C is imposed between the mirror and the vertical line. The laser sheet thus created passes through the fluid, perpendicularly to the heated surface and the PVC plate. A high velocity camera is placed near one vertical viewport in order to observe the channel. During the experiments, the acquisition frequency of the camera was set to 3000 images per second. The tracing particles were Polyamide Seeding Particles PSP-5 ($\phi = 5 \mu\text{m}$, $\rho = 1.03 \text{ kg.m}^{-3}$).

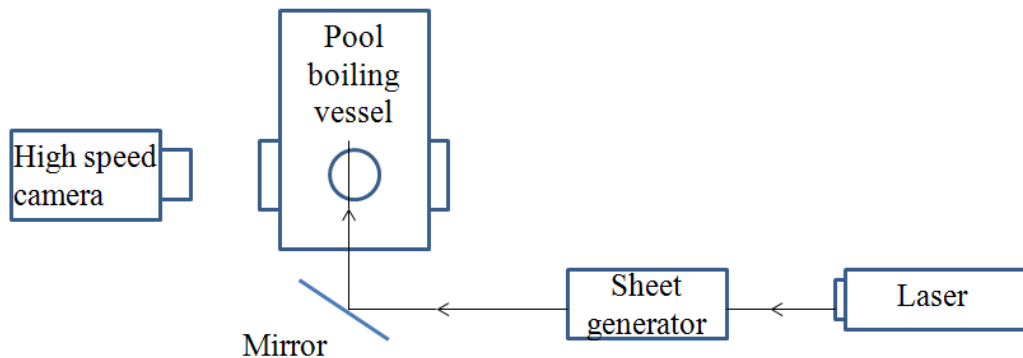


Figure 3.23: Schema of the experimental PIV device

In order to limit the mirage effect, temperature gradient inside the channel should be as small as possible. As in vertical configuration, the wall superheat required to trigger boiling decreases when decreasing the height of the liquid level (section 3.1.3.3.), experiments were conducted for a height of the liquid level of 77 mm and a vapor saturation pressure at the free level surface of 1.8 kPa. The choice of this height for the liquid level also allows diminishing the subcooling degree of the boiling environment and thus obtaining a less chaotic boiling regime. The occurrence of the cyclic boiling regime is thus avoided. Two different channel thicknesses ($e = 4.44 \text{ mm}$ and $e = 2.24 \text{ mm}$) for three different imposed heat fluxes (30 W.cm^{-2} , 12 W.cm^{-2} and 6 W.cm^{-2}) are analyzed. In order to reduce the error due to the high reflection of light (due to the presence of bubbles) and the error due to mirage effect, data are collected in a measurement window placed at the bottom of the channel. In particular, a distance of $800 \mu\text{m}$ is respected between the channel walls and the edge of this observation area. Fig. 3.24 represents the general trend for the time evolution of the liquid velocity in the measurement window. A negative velocity ($u < 0$) refers to a flow downwards while a positive velocity refers to the rise of the liquid. This trend can be associated to a typical phenomenology of boiling in narrow channel.

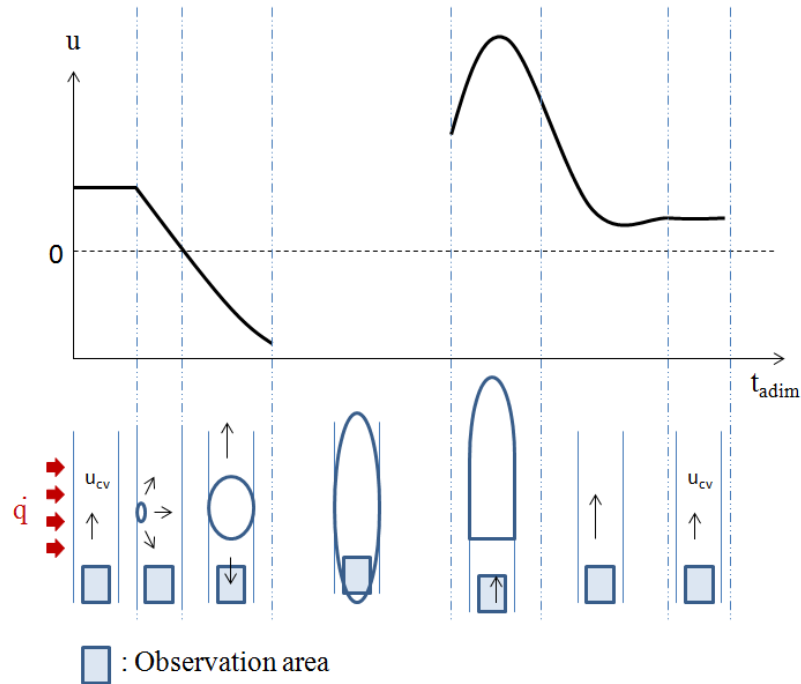


Figure 3.24: Schematic general trend for the time evolution of the liquid velocity and associated phenomenology

When there is no bubble in the narrow channel, the velocity measured by the PIV system is the free convection velocity. At a certain time, the liquid slows down and stops as a bubble starts its growth. As the bubble keeps growing, the liquid exits the channel from the bottom. The measured velocity is thus negative. As the front of the bubble reaches the bottom of the channel no measurement of the liquid velocity can be made. This lack of data continues until the bubble, led by the buoyancy force, leaves the observation area. As the bubble is leaving, the velocity of the liquid at the bottom of the channel is increased. When the entire vapor has left the narrow channel, the liquid velocity then decreases until reaching the free convection velocity.

Each curve shown thereafter (Fig. 3.25) represents the liquid velocity versus dimensionless time. This dimensionless time is defined as the ratio of the time to the time during which some vapor is present in the channel (i.e. as counted from the beginning of the bubble's growth to the time at which the whole amount of vapor has left the channel). Different series of measurements, possibly for identical conditions, are given on the same graphs for the sake of comparison or in order to check their consistency.

At 30 W.cm^{-2} , as the liquid leaves the channel from the bottom, the absolute liquid velocity recorded is highly diminished for a thickness of 2.24 mm (less than 0.2 m.s^{-1}) with respect to the liquid velocity of 0.44 m.s^{-1} recorded at 4.44 mm . This low negative liquid velocity is probably due to the viscous effect at these conditions. As the thickness of the narrow channel decreases, it creates more friction. No conclusion could be drawn for the two others imposed heat fluxes due to the lack of data for a thickness of 4.4 mm .

A significant difference between the upward and downward velocities can be observed at 30 W.cm^{-2} for a thickness of $e = 2.24 \text{ mm}$, but not for the two other imposed heat fluxes investigated. For these two heat fluxes, the liquid velocity is roughly the same whether the liquid feeds or leaves the channel (around 0.4 m.s^{-1} for $\dot{q} = 6 \text{ W.cm}^{-2}$).

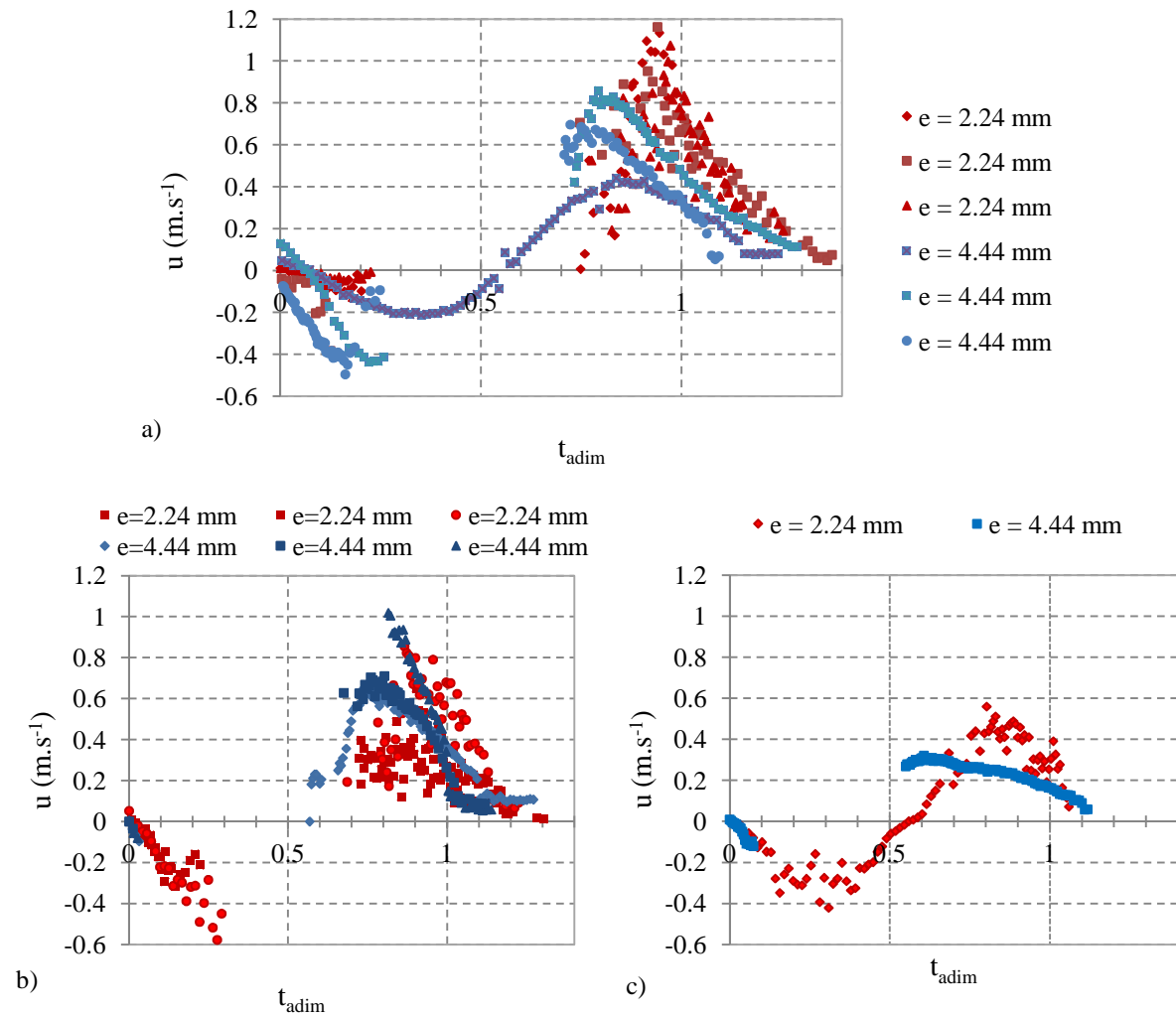


Figure 3.25: Velocity curve versus dimensionless time at a) 30 W.cm^{-2} , b) 12 W.cm^{-2} and c) 6 W.cm^{-2} ($h_1 = 77 \text{ mm}$, $P_v = 1.8 \text{ kPa}$)

This could be explained as the liquid is warmer at the top of the channel compared to its bottom (due to the difference of fluid density). The liquid is thus more easily pushed up than down at 30 W.cm^{-2} . The effect of the viscosity is not seen for the two other imposed heat fluxes investigated as the difference of liquid viscosity between the top and the bottom of the channel is probably less significant.

As the vapor leaves the narrow channel (positive velocity), the liquid velocity at the bottom of the channel increases when decreasing the thickness of the channel for a given heat flux of 30 W.cm^{-2} and 6 W.cm^{-2} . This increase with the decreasing thickness is less significant for an imposed heat flux of 12 W.cm^{-2} , with a mean of maximal values of 0.77 m.s^{-1} for $e = 2.24 \text{ mm}$ and of 0.62 m.s^{-1} for $e = 4.44 \text{ mm}$.

At this imposed heat flux of 12 W.cm^{-2} the heat transfer is the same for $e = 2.24 \text{ mm}$ and $e = 4.44 \text{ mm}$ (Fig. 3.26). As the liquid velocity is similar for both thicknesses, the wake-induced flow could not have an influence on it. The heat transfer is however greater for $e = 2.24 \text{ mm}$ than for $e = 4.44 \text{ mm}$ at 30 W.cm^{-2} which is in agreement with the enhancement of the convective effect measured. The opposite trend is observed for a heat flux of 6 W.cm^{-2} : the heat transfer is greater for $e = 4.44 \text{ mm}$ than for $e = 2.24 \text{ mm}$. Although this observation contradicts the observations of Ait Ameer (2006), this is in

agreement with the literature as, as explained by Fujita *et al.* (1988), at low heat fluxes the velocity of the rising bubble is limited, i.e the bubble spends a longer time in the channel and thus the evaporation of the microlayer is favored.

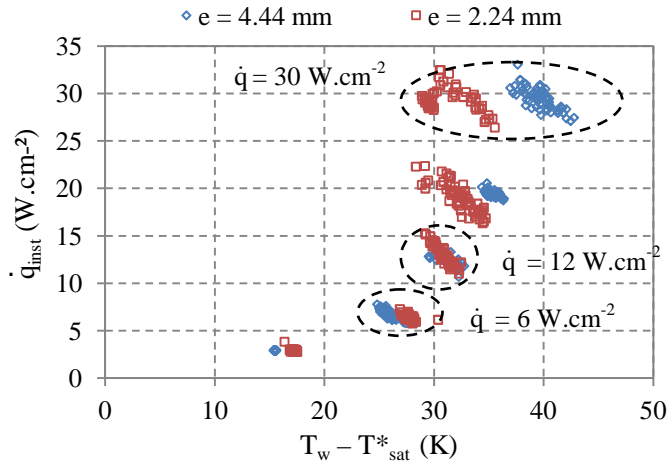


Figure 3.26: Boiling curves with data corresponding to velocity curves plotted for $\dot{q} = 30 \text{ W.cm}^{-2}$, $\dot{q} = 12 \text{ W.cm}^{-2}$ and $\dot{q} = 6 \text{ W.cm}^{-2}$ circles with dashed line ($h_1 = 77 \text{ mm}$, $P_v = 1.8 \text{ kPa}$)

In all cases, Fig. 3.24 shows an inversion of the flow (characterized by negative and positive values of the velocity) due to the expansion of the bubbles. This inversion of the flow fosters the heat transfer as it destroys the thermal and the dynamic boundary layers. This phenomenon is similar to the phenomenon observed by Ait Ameer (2006) and referred as a “pulsating regime”.

Thus, for low vapor pressure (around 1.8 kPa) and for a channel thickness in the range of 2.0 - 5.9 mm, the enhancement of the heat transfer at middle and high heat fluxes could be partly due to the enhancement of the convective effect.

The significant reduction of the heat transfer for channel thickness of 5.9 mm could not be firmly explained yet. According to thermophysical properties of water at such low pressure and assuming that the heated surface is a vertical flat plate, the dynamic boundary layer can be calculated as equal to 5.5 mm. As during the cyclic boiling regime, heat is mainly transferred by convection rather than by phase change, a channel thickness of 5.9 mm could disturb the establishment of the dynamical boundary and thus significantly degrade the heat transfer. This phenomenon could be then balanced by the convective effect as the thickness of the channel decreases, explaining the existence of an optimal channel thickness. The existence of this optimal channel thickness was already mentioned in the literature at atmospheric pressure conditions (Fujita and Uchida, 1990; Bonjour, 1996; Ait Ameer, 2006).

Conclusion

The experimental test setup was slightly modified to study water pool boiling in vertical orientation with or without confinement and at subatmospheric pressure (from 5 to 1.2 kPa) on a heated copper disk.

In free boiling conditions (i.e. without confinement), bubbles with centimeters size and with a flattened base were observed. Despite the high subcooling degree of the environment, a sliding of these bubbles was observed prior to their collapse. The sliding velocity depends mainly on the volume of the bubble. The cyclic boiling regime observed in horizontal orientation was also observed during visualization but the boiling curve shape characteristic of this regime was less significantly observed. No clear cycle for the cyclic regime could be defined although the chamber was fully thermalized. It was also shown that the vapor pressure has a negligible influence on the heat transfer whereas a decrease of the height of the liquid level for a given pressure significantly improves heat transfer. This is due to the balance between heat transfer mechanisms in vertical orientation and phenomena due to subcooling of the environment. As the pressure decreases, the boiling environment is more subcooled but bubbles formed are larger. The evaporation of the microlayer is fostered, the sliding velocity of the bubble is higher and so are the convective effects due to the wake-induced flow. Thus, phenomena due to the subcooling degree of the environment and phenomena due to the bubble shape and growth are balanced. On contrary, for a given vapor pressure, as the height of the liquid decreases, the local pressure decrease as well as the subcooling degree of the boiling environment. Thus, as the liquid height decreases, bubbles are larger and the subcooling is lower. Both phenomena induce a decrease of wall superheat required to set boiling on.

From the present study of boiling in narrow spaces, it was shown that the heat transfer is enhanced for a channel thickness of 7.7 mm when compared to free boiling but degraded for a thickness of 5.9 mm. The heat transfer is then enhanced again for channel thickness of 2.9 mm. For a channel thickness of 2 mm, two different trends were observed depending on the pressure: for pressures of 5 and 3 kPa, the heat transfer is globally degraded; for pressures of 1.8 kPa and 1.2 kPa, the heat transfer is globally enhanced. As the pressure and the channel thickness decrease, the occurrence of the cyclic boiling regime was also shown. This chaotic regime is similar to the cyclic boiling regime observed during boiling on a horizontal surface and it is responsible for a degradation of the heat transfer. Depending on the pressure and on the channel thickness, the cyclic boiling regime could be characterized by more or less significant fluctuations of the wall superheat and instantaneous heat flux leading to different time-averaged heat transfer coefficients. The influence of the pressure on the heat transfer is not significant when this cycling boiling regime does not take place. As the effect of the boiling regime has been shown, a Particle Image Velocity system was implemented on the experimental setup in order to shed light on the role of the convective effects on the enhancement/degradation of the heat transfer. An increase of the velocity of the liquid feeding the channel was shown with the decreasing thicknesses for the two thicknesses of the channel investigated ($e = 2.24$ mm and $e = 4.44$ mm) and for a vapor pressure of 1.8 kPa. Lastly, this experimental study also led to discuss the significance of the Bond number, which is usually used to relate the channel thickness to the bubble length or to the fluid capillary length, in operating conditions for which the capillary length and the channel thickness are of a few millimeters - while the bubble diameter can reach up to 15 cm in the present operating conditions -. This discussion brought to the role of dynamic forces in the bubble detachment process at subatmospheric pressure in addition to the usual capillary and buoyancy forces.

4 WATER VAPORIZATION INSIDE A CHANNEL OF A SMOOTH PLATE

Due to the lack of knowledge about water behavior in conditions that might occur in sorption chillers using water as refrigerant, designing compact heat exchangers remains mainly empirical. Furthermore, fundamental studies about boiling phenomena near vacuum pressures highlighted difficulties to overcome: centimeter size of bubbles which could cause high wall superheat, large fluctuations of the wall temperature could result in material fatigue, a non homogeneous boiling environment in pressure and subcooling making the onset of nucleate boiling very sensitive to experimental conditions, etc.

The objective of this chapter is to gain further understanding of the phenomena occurring in compact plate-type evaporators. In that goal, an experimental test setup was designed and built (section 4.1). It allows the observation of the water vaporization in a channel of a plate heat exchanger of standard dimension (0.2 m width x 0.5 m height) under various operating conditions. As nearly no compact heat exchangers have been tested for low-pressure evaporation this far, the behavior of plate-type heat exchangers in these pressure ranges is difficult to understand. Thus, a campaign based on design of experiments (DOE) methodology was established in order to assess the maximal cooling capacity under constraints and apprehend the interactions between different experimental factors (section 4.2). The design of experiments results obtained for a thickness of the channel of 4 mm and 2 mm are analyzed and discussed (section 4.3). Flow patterns observed are introduced and conditions to obtain the best cooling capacity are searched. Finally, an overall heat transfer coefficient for the evaporator is estimated and the variation of the cooling capacity obtained with various dimensionless numbers is plotted for the first time as an approach for the design of such compact evaporators (section 4.4).

4.1 Experimental test facility

4.1.1 Experimental setup

The prototype design⁵ allows the study of water vaporization inside a channel of a smooth plate-type evaporator in absorption and adsorption configuration. As only the absorption configuration was studied during this work, only this configuration will be introduced. Moreover, due to the problems encountered during experiments some changes had to be made. These changes regard the liquid supply line and the evaporator. The first version of the entire test bench and results obtained with this prototype are presented in appendices (Appendices E and F). Only the second version of the test bench and results obtained with this one will be introduced hereafter.

4.1.1.1 The test bench

The entire test bench is constituted by a condenser, a smooth stainless steel plate evaporator, a liquid supply line and a vapor exhaust line (Fig. 4.1).

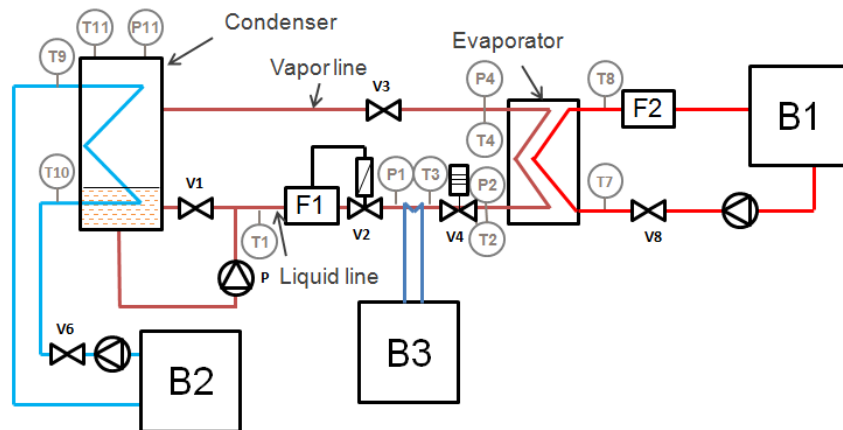


Figure 4.1: Drawing of the experimental test setup

The absorber is simulated by the condenser for which the saturation temperature is set at a lower value than the evaporation temperature. The experimental test setup thus built operates as a pump-assisted closed-loop thermosyphon. Varying the temperature at the condenser allows to simulate an absorption chiller with diverse driving forces for vapor flow between the evaporator and the absorber. The saturation temperatures are set by means of two heating/cooling devices (B1 and B2). The heating/cooling device B1 is used to set the high temperature source whereas the heating/cooling device B2 is used to set the low temperature source (B2). A third heating device (B3) is used to set a fluid temperature which could correspond to the temperature of the refrigerant in an absorption chiller before its expansion.

The working fluid is deionized water. It circulates from the condenser to the evaporator in a liquid line of 5 mm inner diameter. In this liquid line, a liquid pump (P) is added at the outlet of the condenser, before entering the mass flow meter, in order to overcome the pressure losses due to the presence of the mass flowmeter (F1). The mass flow rate is solely controlled by the mass flow controller. The refrigerant which circulates in the line can be heated or not before being expanded through the throttling valve (V4). The refrigerant is then fed into the evaporator by three tubes of 2 mm inner

⁵ The prototype was designed and mounted by an engineering assistant at CNAM, Pierrick Vallon.

diameter. Once the refrigerant is vaporized, the fluid flows back to the condenser through a vapor line of 52 mm inner diameter for further cycling.

The condenser is a stainless steel vessel of 300 mm inner diameter and 720 mm height. An oversized copper-tube coil heat exchanger is located inside the container in order to condense the vapor refrigerant along the outer surface of the tube and in order to store the refrigerant at liquid state. The total length of the tube coiled in the condenser is 7 m. The temperature of the water circulating inside the heat exchanger is controlled by the thermostatic bath B2.

4.1.1.2 Evaporator

The evaporator (Fig.4.2) is constituted by two stainless steel plates and one PMMA (Polymethyl methacrylate) plate of 500 mm height and 200 mm width. These three plates formed two rectangular channels in which the refrigerant and the secondary fluid flows. The PMMA plate is used as the external plate on the refrigerant side in order to observe boiling phenomena. The central plate is made of stainless steel and has a thickness of 6 mm in order to allow the insertion of 44 thermocouples (22 homogeneously distributed for each surface of the central plate). The secondary fluid circulates on the other side of the central plate.

Two different spacings can be chosen between the PMMA plate and the central plate (refrigerant side): 2 mm and 4 mm. These two different spacings are imposed by two different spacers and two different toric seals. For the sake of simplicity, the word “channel” used thereafter referred to the narrow channel thus created in which the vaporization of the refrigerant takes place.

The spacing between the two stainless steel plates (secondary fluid side) is set at 1 mm.

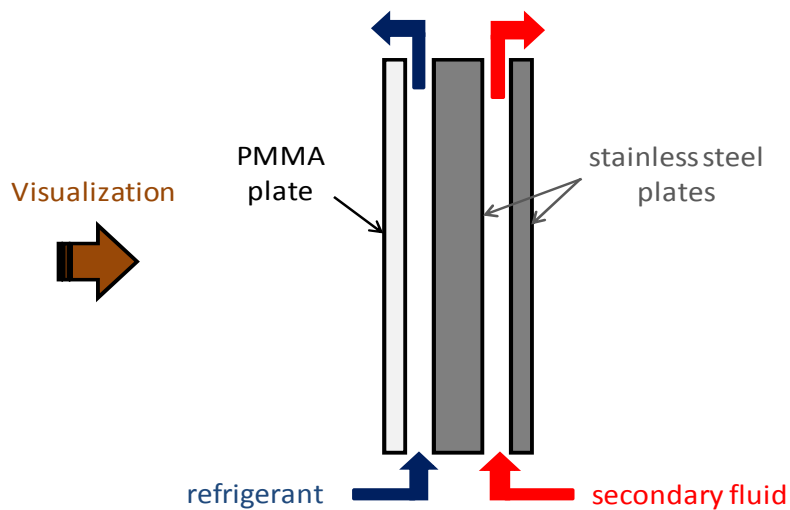


Figure 4.2: Schematic of the evaporator

The thermocouples located on the central plate are placed face to face on each side of the plate. They are used to determine the heat flux from the secondary fluid to the refrigerant at different spots by means of the Fourier’s law (cf. Chap 2 section 2.1.3.1.). Uncertainties estimated on the heat fluxes are discussed in the Appendix H. A simulation with Star-CCM+® was realized to check that the heat transfer is generally monodimensional and that the influence of the environment is negligible (Appendix I). Notches (depth of 1 mm) had to be manufactured in order to insert these thermocouples. They were backfilled with tin. The locations of these thermocouples are shown in Fig. 4.3.

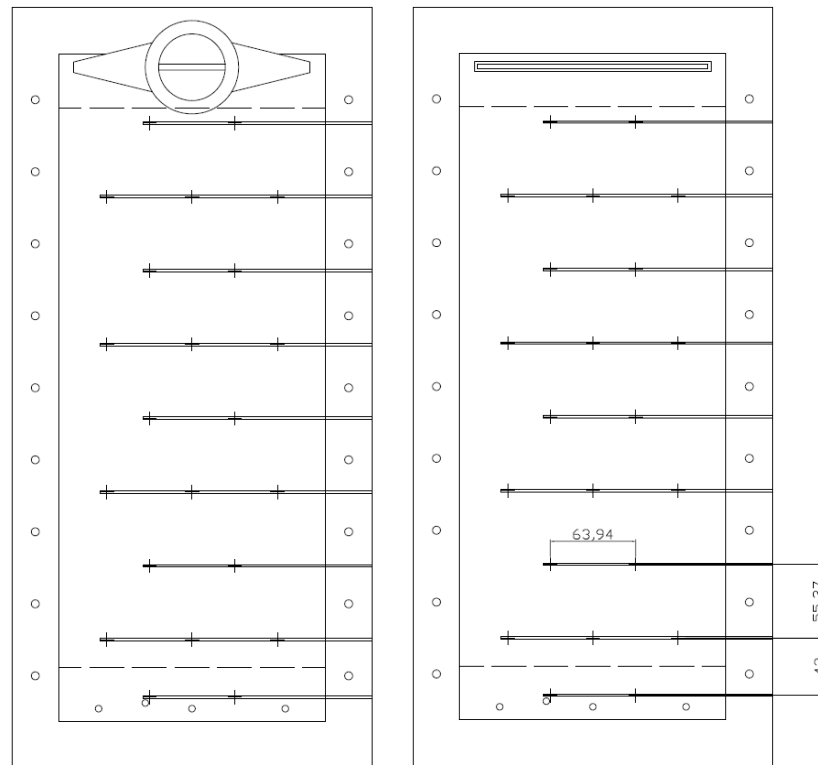


Figure 4.3: Location of thermocouples inside the central plate from the front view (left) and from the back view

The inlet temperature of the secondary fluid can vary from 10 °C to 25 °C. In order to promote nucleate boiling, the parallel flow configuration was chosen in agreement with the results obtained by Clausee *et al.* (2011) for a heat exchanger of similar size. The coolant mass flow rate is adjustable by manipulating the valve noted V8 on Fig. 4.1.

4.1.1.3 Instrumentation

Several types of instruments are implemented on the liquid and vapor lines as well as on the secondary fluid lines to measure temperatures, pressures and flow rates.

The secondary fluid flow rate at the evaporator is measured using an electromagnetic flow meter (F2) in a range of 1-2 dm³.min⁻¹ and with an accuracy of ± 0.5% of the flow rate measured. The liquid mass flow meter is made of a stainless steel tube without any moving parts or obstructions.

T-type thermocouples are inserted at different points of the test facility using compression fittings. They allow to measure the temperatures at the inlet and outlet of the secondary fluid on the condenser side (thermocouples named T9 and T10); at the inlet and outlet of the secondary fluid on the evaporator side (T7 and T8); in the liquid line (T1, T2, T3); and the vapor line (T4). Four contact thermocouples (not represented on the Fig. 4.1) were inserted in the feeding distributor. Three of them are located on the feeding tubes, one for each tube, at equal distance of the evaporator inlet and the throttling valve. The fourth thermocouple is located in one of these tubes, close to the evaporator in order to observe if any heat conduction is likely to disturb the measurements. Water flow temperatures are measured using thermocouples of 1.0 mm diameter. Due to width constraint, the embedded thermocouples used to measure evaporator wall temperature are of 0.5 mm in diameter.

All the thermocouples, including the 44 thermocouples located in the central plate of the evaporator, have been calibrated by means of a precision thermostatic bath and a reference Platinum Resistance

thermometer (Pt100) in the range 0.5 °C - 95 °C. After calibration, the maximum deviation observed from the mean temperature is lower than 0.1 K. The 44 thermocouples located in the central plate of the evaporator have been calibrated prior to be placed in the central plate.

Five pressure transducers are also used. They measure the absolute pressure at different points of the test rig with an accuracy of $\pm 0.075\%$. The transducer P1 placed just before the thermostatic bath B3 has a pressure range of 0–200 mbar. The three other pressure transducers (denoted P2 to P4, P11) have a pressure range of 0-50 mbar. They allow to measure the pressure at the inlet of the channel, at the outlet of the channel and at the inlet of the condenser respectively.

The T-type thermocouple T2 and the pressure transducer P2 are used to measure the temperature and the pressure at the channel inlet respectively. They are situated at the middle of two feeding orifices, one millimeter below their location.

All measurements are controlled by a Labview program that allows their recording.

Table 4.1 summarizes the measuring devices used in this test bench and their main characteristics.

Table 4.1: Specification of the different measuring devices

Devices	Type	Accuracy	Range
Thermometer	T-type thermocouple	0.1 °K	-10 to 85 °C
Refrigerant flow meter	Thermal mass flow meter	$\pm 1\%$ of full scale.	0.04 to 2 kg.h ⁻¹
Coolant flow meter	Electromagnetic flow meter	$\pm 0.5\%$ of reading	1 to 2 l.min ⁻¹
Pressure measurement	Pressure transmitter with ceramic sensor	$\pm 0.075\%$ of reading	5 x 0-50 mbar 1 x 0-200 mbar

4.1.1.4 The visualization test facility

A high-speed camera Genie HM1024 with the ability to take pictures at a frequency of 100 frames per second while maintaining a high image resolution (1024 x 768) is used in order to perform visualization. A zoom lens with a focal length range from 12.5 mm to 75 mm has been chosen to make observations of flow regimes on a macroscopic level. The camera is placed at a certain distance of the PMMA plate and in a manner to be located at the middle height of the plate. The light is situated above the high-speed camera (Fig. 4.4).

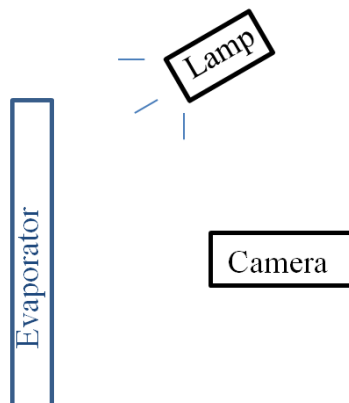


Figure 4.4: Schematic of the visualization test facility

4.1.2 Experimental procedure

4.1.2.1 Preparation and commissioning

Before filling the condenser with water, the entire experimental setup is vacuumed during at least 12 hours. The condenser is then filled with an amount of water that was previously boiled to decrease its gas content. The condenser and then the entire experimental setup are expunged of a part of the vapor phase once again, until the pressure measured is equal to the water saturation pressure at the measured temperature (i.e. $P_{11} = P_{\text{sat}}(T_{11})$) – The index is shown on Fig. 4.1).

The secondary fluid inlet temperatures at the evaporator and condenser are set to 17.5 °C and 8.5 °C. The temperature of the thermostatic bath B3 is set to 37.5 °C. The secondary fluid flow rate at the evaporator is set at 1 dm³.min⁻¹ and the refrigerant flow rate is controlled manually to reach a liquid height of 15 cm in the channel of the evaporator (filling ratio of 3/10). To maintain this desired height of the liquid level, the refrigerant mass flow rate is controlled automatically by means of a PID controller once the desired height is reached. The control parameter is the cooling capacity. It is evaluated from an energy balance on the secondary fluid side (\dot{Q}_{cool} , Eq. 4.1) and on the refrigerant side assuming that the cooling effect is only due to phase-change ($\dot{Q}_{\text{cool,refr}}$, Eq. 4.2).

$$\dot{Q}_{\text{cool}} = Cp_1 \cdot \dot{m}_{\text{fs}} \cdot (T_{\text{in}} - T_{\text{out}}) \quad (4.1)$$

$$\dot{Q}_{\text{cool,refr}} = \dot{m}_{\text{refr}} \cdot \Delta h_{\text{lv}} \quad (4.2)$$

Once steady state obtained, the prototype runs with these operating condition during 7 days. During this week, a part of the vapor trapped is periodically expunged. After 7 days, experiments could start up. As the prototype ensures high gas tightness, this procedure is not repeated again during the test campaign. One test campaign (i.e. 28 tests realized) lasts around two weeks.

4.1.2.2 Test campaign

To perform these tests, all the thermostatic baths are turned on. Once the prototype is fully thermalized at the desired temperatures, the channel is filled with refrigerant at the desired height of the liquid level that is primary parameter of the set of operating conditions. The PID controller is then activated. Once steady state is obtained data are collected each 1 s during 20 min or 30 min depending on the test campaign. Between two tests, the height of the liquid level and all the set point temperatures are changed in order to avoid systematic errors.

4.2 Overall approach by the method of experiments (DOE)

As nearly no compact heat exchangers have been tested for low-pressure evaporation this far, the behavior of plate-type heat exchangers in this pressure range is difficult to understand. It is thus difficult to anticipate the operating conditions for which an evaporation failure would occur or, on the contrary, for which the best cooling capacity would be obtained. Hence, the aim is to characterize the behavior of the evaporator at various operating conditions: secondary fluid inlet temperature, operating pressure, etc. For this purpose and in order to reduce the number of runs, an experimental campaign was defined using the methodology of design of experiments (DOE) (Goupy, 2000). The objective of the chosen design of experiments is to determine the operating conditions that will yield the highest cooling capacity in the selected experimental field. The establishment of a design of experiments is also a first step to apprehend the interactions between different experimental factors.

After a general introduction on this methodology, the chosen design of experiments is developed. Then, in order to validate the operating conditions covered by the experimental field, we have compared them with the operating conditions usually encountered in an absorption chiller.

4.2.1 Methodology

By means of a statistical analysis, it is possible to create a mathematical model which allows calculating a value of a certain physical parameter (the “response”, in the present case: the cooling capacity) as a function of the experimental factors of the established design of experiments. This theoretical response is calculated by means of a Taylor series of the relationship between the response and the factors of influence. The theoretical response is calculated as follows:

$$Y = b_0 + \sum_{i=1}^4 b_i X_i + \sum_{i=1}^4 b_{ii} X_i^2 + \sum X_i X_j + \dots \quad (4.3)$$

With Y the response in its unit (in the present case: watts) and X_i the centered data to range from -1 for the lowest level of the factor i to 1 for the highest level of the same factor i, i corresponding to the number of the factor studied.

As the model is based on a mathematical approach, the theoretical response should not be used for physical explanations of the phenomena.

The mathematical model then obtained (and checked) allows plotting the response surface and classifying the factors according to their impact on the response.

4.2.2 Presentation of the design of experiments

As the objective of this study is to evaluate the maximum cooling capacity with factor constraints, a design of experiments of “Doelhart” type was chosen. This design can be used for any number of factors and allows to add or remove easily one factor (on the condition that the factor to add or remove is set on the middle value of its experimental field, that corresponding to $X_i = 0$). Like for any type of design, each test to run is determined precisely by the design. The number of levels to set for each factors is imposed. However, the operator can chose which experimental factor will vary as the factor 1, etc. Due to this difference in levels to be imposed depending on the design of experiments, the choice for which factor should be chosen as factor 1, factor 2, etc. is thus of importance. In a Doelhart type design, higher steps are required for the first and the last factors. This means that the two factors chosen as the first and the last factor should have either level difficult to impose and/or have a linear effect on the response. As none of the factors can have only two levels with this design, two designs of experiments should be realized. Another disadvantage of this design is that third or upper-order interactions are not taken into account.

According to the current knowledge on phenomena that might occur in low-pressure compact evaporators based on plate-type heat exchanger geometry, the factors which could have an influence on the achieved cooling capacity are:

- The liquid column height
- The feeding mass-flow rate
- The secondary fluid temperature
- The secondary fluid mass flow rate
- The operating pressure
- The thickness of the channel

- The vapor quality at the entrance of the channel

In order to limit the number of tests, the secondary fluid mass flow rate is set to $1 \text{ dm}^3 \cdot \text{min}^{-1}$. This mass flow rate should allow obtaining a temperature difference of 5 K between the inlet and the outlet of the secondary fluid in operating conditions for which the vaporization of the refrigerant is fostered. The refrigerant mass flow rate is related to other factors (height of the liquid level, secondary fluid temperature, operating pressure) and cannot be imposed without having a risk of emptying or filling the channel with refrigerant. Thus, this one is controlled as explained in section 4.1.2 and is not set by the user. It is not considered as a factor. As explained above, the experimental setup works as a pump-assisted thermosyphon. The operating pressure is set by the secondary fluid temperature at the condenser. The controlling parameter is thus, in this case, the secondary fluid temperature set point at the condenser ($T_{\text{cond}}^{\text{c,fs}}$). Moreover, as the refrigerant should circulate from the evaporator to the condenser, it is necessary that the temperature at the evaporator is higher than the temperature at the condenser ($T_{\text{ev}}^{\text{c,fs}} > T_{\text{cond}}^{\text{c,fs}}$). For this reason, substituting the secondary fluid temperature set point of the evaporator ($T_{\text{ev}}^{\text{c,fs}}$), the factor studied is $\Delta T = T_{\text{ev}}^{\text{c,fs}} - T_{\text{cond}}^{\text{c,fs}}$. Lastly, because the vapor quality at the inlet of the channel results from the isenthalpic expansion of a subcooled liquid, the controlled factor associated to the vapor quality is the temperature of this liquid (namely $T_{B3}^{\text{c,fs}}$).

Fig. 4.5 shows on the drawing of the experimental setup the factors chosen to realize the design of experiments.

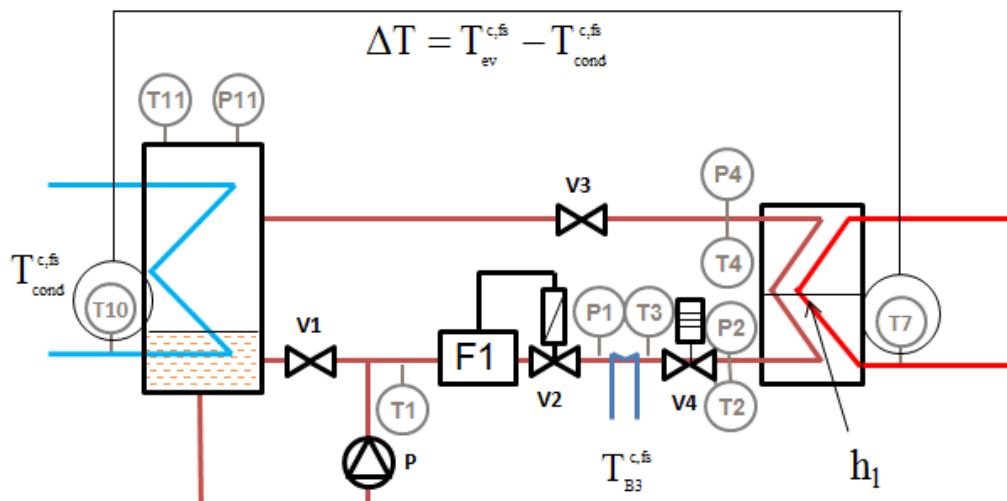


Figure 4.5: Factors of the design of experiments on the drawing of the experimental test setup

Table 4.2 gathers these factors and the chosen experimental field.

Table 4.2: Analysis of factors influencing the cooling capacity

	Factors	Field	Constraints
1	h_l	[5 to 25 cm]	Max 25 cm (water losses due to the vapor flow rate)
2	$T_{cond}^{c,fs}$	[2 °C to 15 °C]	Min: 0 °C
3	$T_{B3}^{c,fs}$	[30 °C to 45 °C]	
4	ΔT	[3 K – 15 K]	$T_{ev}^{c,fs} \subset [10 °C – 25 °C]$
	Thickness of the channel	2 mm / 4 mm	

As the height of the liquid level (h_l) – which is also the image of the filling ratio - cannot be imposed easily, it was chosen as the first factor. As the response is believed to vary rather linearly with the secondary fluid temperature, the factor $T_{ev}^{c,fs}$ was chosen as the fourth one. The two others factors $T_{cond}^{c,fs}$ and $T_{B3}^{c,fs}$ are arbitrarily chosen as respectively the second and third factor. Regarding the confined space, only two levels could be set (2 mm and 4 mm). It was thus decided to establish a design of experiments for each confined space investigated.

According to the design of experiments chosen, the factors studied and the experimental field, the tests to run are listed on Table 4.3. The associated secondary temperature set point at the evaporator and the associated driving pressure calculated as (4.4) are also displayed in Table 4.3.

$$\Delta P = P_{sat}(T_{ev}^{c,fs}) - P_{sat}(T_{cond}^{c,fs}) \quad (4.4)$$

Table 4.3: Experimental tests for $e = 4$ mm with associated driving pressure

Test n°	h_l (cm)	$T_{cond}^{c,fs}$ (°C)	$T_{B3}^{c,fs}$ (°C)	ΔT	$T_{ev}^{c,fs}$ (°C)	ΔP (kPa)
1	15	8.5	37.5	9.0	17.5	0.89
2	25	8.5	37.5	9.0	17.5	0.89
3	20	14.1	37.5	9.0	23.1	1.22
4	10	14.1	37.5	9.0	23.1	1.22
5	5	8.5	37.5	9.0	17.5	0.89
6	10	2.9	37.5	9.0	11.9	0.64
7	20	2.9	37.5	9.0	11.9	0.64
8	20	10.4	43.62	9.0	19.4	0.99
9	10	10.4	43.62	9.0	19.4	0.99
10	15	4.7	43.62	9.0	13.7	0.72
11	20	6.6	31.38	9.0	15.6	0.80
12	10	6.6	31.38	9.0	15.6	0.80
13	15	12.3	31.38	9.0	21.3	1.10
14	20	10.4	39.03	13.7	24.1	1.75
15	10	10.4	39.03	13.7	24.1	1.75
16	15	4.7	39.03	13.7	18.5	1.27
17	15	8.5	32.91	13.7	22.2	1.58
18	20	6.6	35.97	4.3	10.9	0.33
19	10	6.6	35.97	4.3	10.9	0.33
20	15	12.3	35.97	4.3	16.5	0.45
21	15	8.5	42.09	4.3	12.8	0.36

4.2.2 Comparison of the experimental domain with the operating conditions in an absorption chiller

As the experimental setup does not operate like an absorption chiller, it is necessary to transpose experimental operating conditions to operating conditions that could occur in an absorption chiller. In this goal, a MATLAB® program was developed. In order to simplify the thermodynamic model, an ideal absorption chiller (i.e. with an infinite solution mass flow rate and without any heat or mass transfer resistance) is considered. Each experimental point (or more precisely each $T_{ev}^{c,fs} / T_{cond}^{c,fs}$ pair) is considered and transposed in the absorber temperature and mass fraction of a Lithium-Bromide solution occurring in an ideal absorption chiller. To do so, the experimental condenser is assumed to be a vessel at P_{cond} and $T_{cond}^{c,fs}$ in which the liquid phase and the vapor phase are at equilibrium (Fig. 4.6). Free enthalpies are thus equal:

$$g_{cond,l}(P_{cond}, T_{cond}^{c,fs}) = g_{cond,v}(P_{cond}, T_{cond}^{c,fs}) \quad (4.5)$$

Then, a vessel at P_{ev} and T_{abs} , representing the absorber of an ideal machine is considered (Fig. 4.5). Here also, liquid and vapor phases are assumed to be in equilibrium. Thus:

$$g_{sol}(P_{ev}, T_{abs}, X_{LiBr}) = g_{abs,v}(P_{ev}, T_{abs}) \quad (4.6)$$

For the two systems to be equivalent the equality $\Delta g_{cond} = \Delta g_{abs}$ is mandatory. As vapor comes from the evaporator in both cases, the relation becomes:

$$g_{cond,v}(P_{cond}, T_{cond}^{c,fs}) = g_{abs,v}(P_{ev}, T_{abs}) \quad (4.7)$$

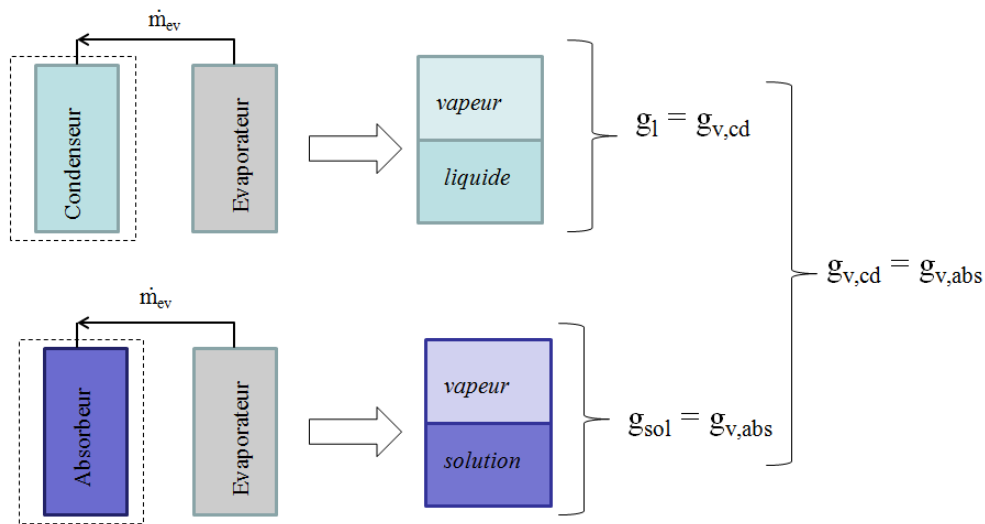


Figure 4.6: Schematic of principle of the thermodynamical model developed

For given P_{cond} , $T_{cond}^{c,fs}$ and P_{ev} , it is possible to calculate the temperature of the absorber and the mass fraction of a lithium-bromide solution corresponding to the experimental conditions. Table 4.4 shows results obtained for the investigated experimental points. Free enthalpies are calculated according to relations used by Kim and Infante Ferreira (2006).

Table 4.4: Corresponding absorber operating conditions (Abs) for given experimental operating conditions (Exp)

Exp	$T_{cond}^{c,fs}$ (°C)	8.5	2.87	10.38	4.74	6.62	4.74	6.62	12.26	8.5
Exp/Abs	$T_{ev}^{c,fs}$ (°C)	17.5	11.87	19.38	13.74	15.62	18.49	10.88	16.51	12.75
Abs	T_{abs} (°C)	42.29	35.47	44.56	37.75	40.02	43.73	34.1	40.77	36.33
	X_{LiBr} (-)	0.5146	0.5115	0.5155	0.5126	0.5136	0.5165	0.5099	0.5121	0.5107

As shown in this table and as represented on Fig.4.7, experimental operating conditions are similar to those obtained in an absorption chiller. Indeed, according to the literature (Henning, 2007; Goulet, 2011) and according to manufacturers' data (Trane, Voltas, EAW), typical operating conditions in a sorption chiller are a chilled water at a temperature greater than 5 °C, a cooling water temperature to range mainly from 20 °C to 35 °C and a driving temperature to range from 80 °C to 110 °C. In these conditions, the mass fraction of lithium bromide in the aqueous solution ranges from 45 % to 55 % at the outlet of the absorber. Despite the fact that the corresponding temperature at the absorber is slightly higher than temperatures usually encountered in absorption chillers for most of the points, the difference remains all the more acceptable that this temperature corresponds to the solution temperature at the inlet of the absorber. Moreover, the mass fraction of the lithium-bromide solution, from which derives the driving force, agrees well with the mass fraction of the lithium-bromide solution encountered in these industrial processes.

-  : usual absorption machines operating conditions for the points of the cycle represented by ★
-  : location of points obtained by the model
-  : example of an absorption cycle point given by the model
-  : absorption cycle reconstruction knowing Lithium-bromide solution mass flow rate and evaporation mass flow rate

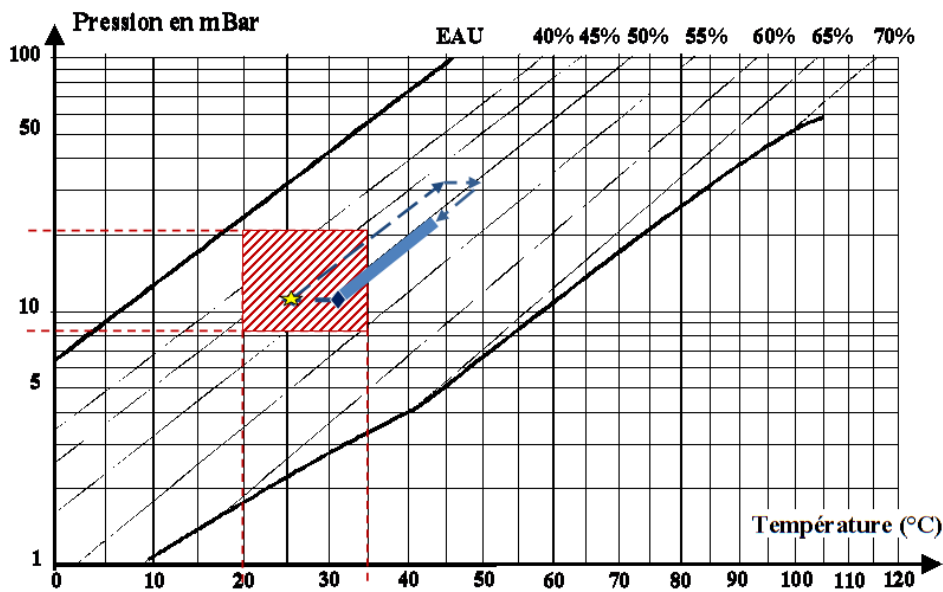


Figure 4.7: Usual absorption chillers operating conditions at the absorber outlet and schematic of a given cycle obtained by the thermodynamical model on Dühring diagram.

4.3 Design of experiments results

4.3.1 Flow regimes

Two versions of the central plate of the evaporator exist. The only difference between these two lies in the implementation of the thermocouples inside the plate and thus in the presence of bands of tin on the vaporization surface. Two examples of bubble obtained for a same test but with the two versions of the plate are shown on Fig. 4.8. On these pictures, notations used thereafter are also referred.

As nearly no difference of boiling behavior could be observed between the tests with both plates, and although all the results shown thereafter were obtained with the instrumented plate, the shown pictures could be those recorded with the plate without thermocouples. This choice was made when vaporization phenomena observed were similar for both plates as the visualization is less disturbed by the polished surface.

All the results shown in this section were obtained for a thickness of the channel of 4 mm.

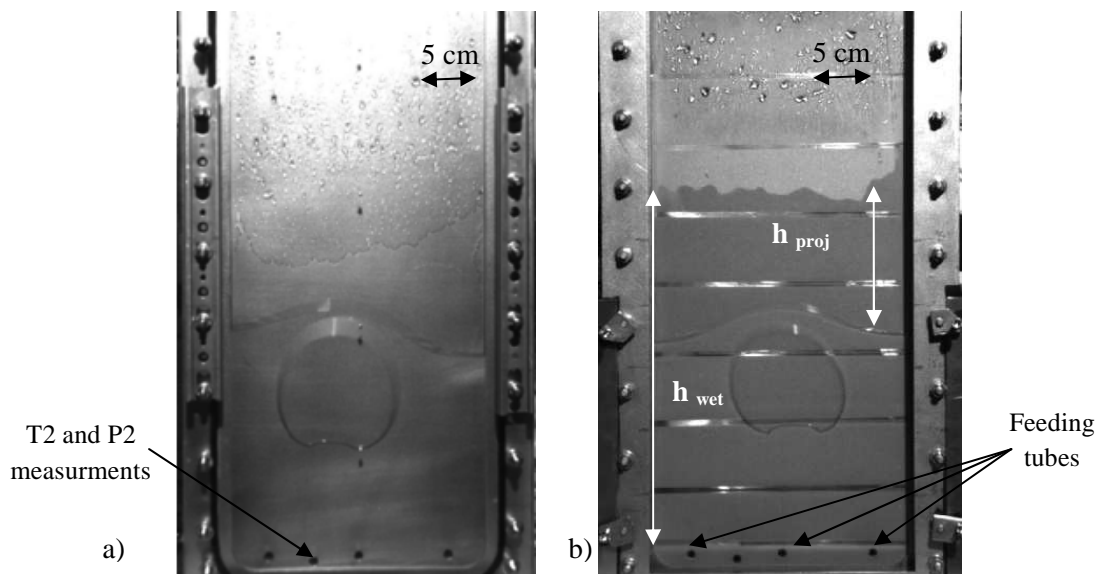


Figure 4.8: Bubble growth inside the channel of the evaporator a) with the central plate without thermocouples
 b) with the central plate instrumented ($h_l = 15$ cm, $T_{\text{cond}}^{\text{c,fs}} = 12.5$ °C, $T_{\text{ev}}^{\text{c,fs}} = 21.3$ °C, $x = 2.5$ %)

4.3.1.1 Flow observed

During the experiments, different flow regimes were observed. Three of them occurred particularly often. These three regimes are described thereafter. On the following description, a letter A noted on Fig. 4.11 and 4.12 refers to a bubble which collapses, letter B to a bubble which grows and will then splash on the surface, letter C to the evaporation of a film and/or to dry patch. An arrow points an interesting element. The bright part of the picture is due to the light. Dots seen along the symmetry axis of the plate are located on the exterior of the channel and do not disturb the flow.

- **Flow regime R1:** Appearance and quick collapse of bubbles of millimeter sizes or few centimeters sizes located at the end of the feeding tubes at the bottom of the channel (Fig. 4.9).

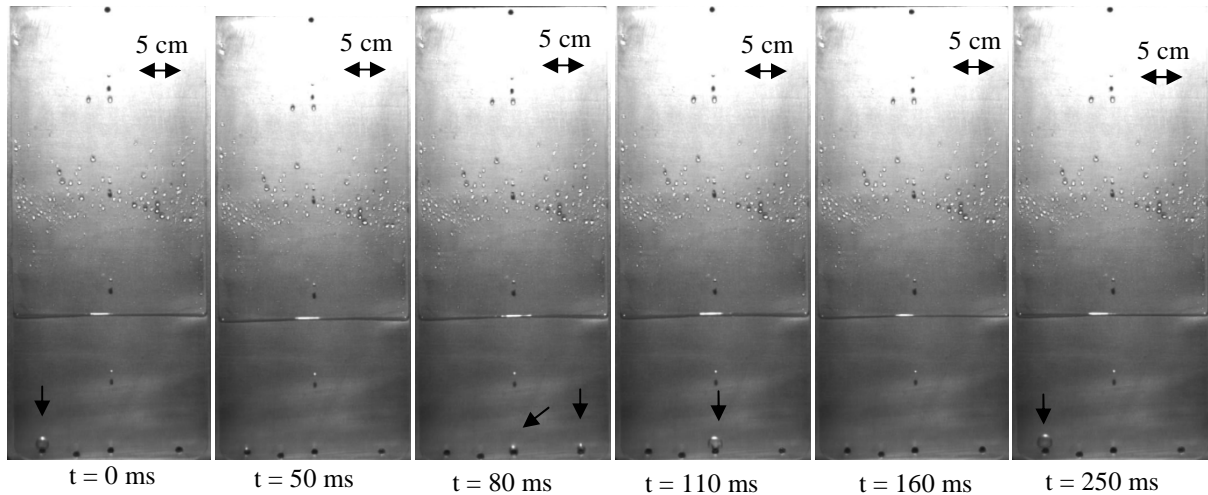


Figure 4.9: Video sequence of the flow regime R1 ($h_1 = 15$ cm, $T_{\text{cond}}^{\text{c,fs}} = 8.5$ °C, $T_{\text{ev}}^{\text{c,fs}} = 12.8$ °C)

Fig. 4.10 shows a zoom on a bubble during its growth, which also reveals its change of shape.

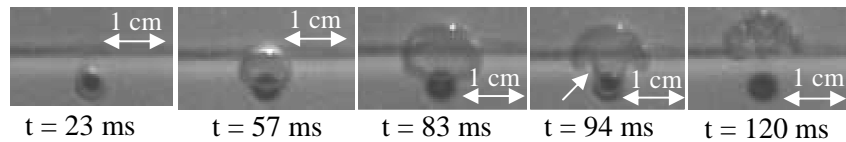


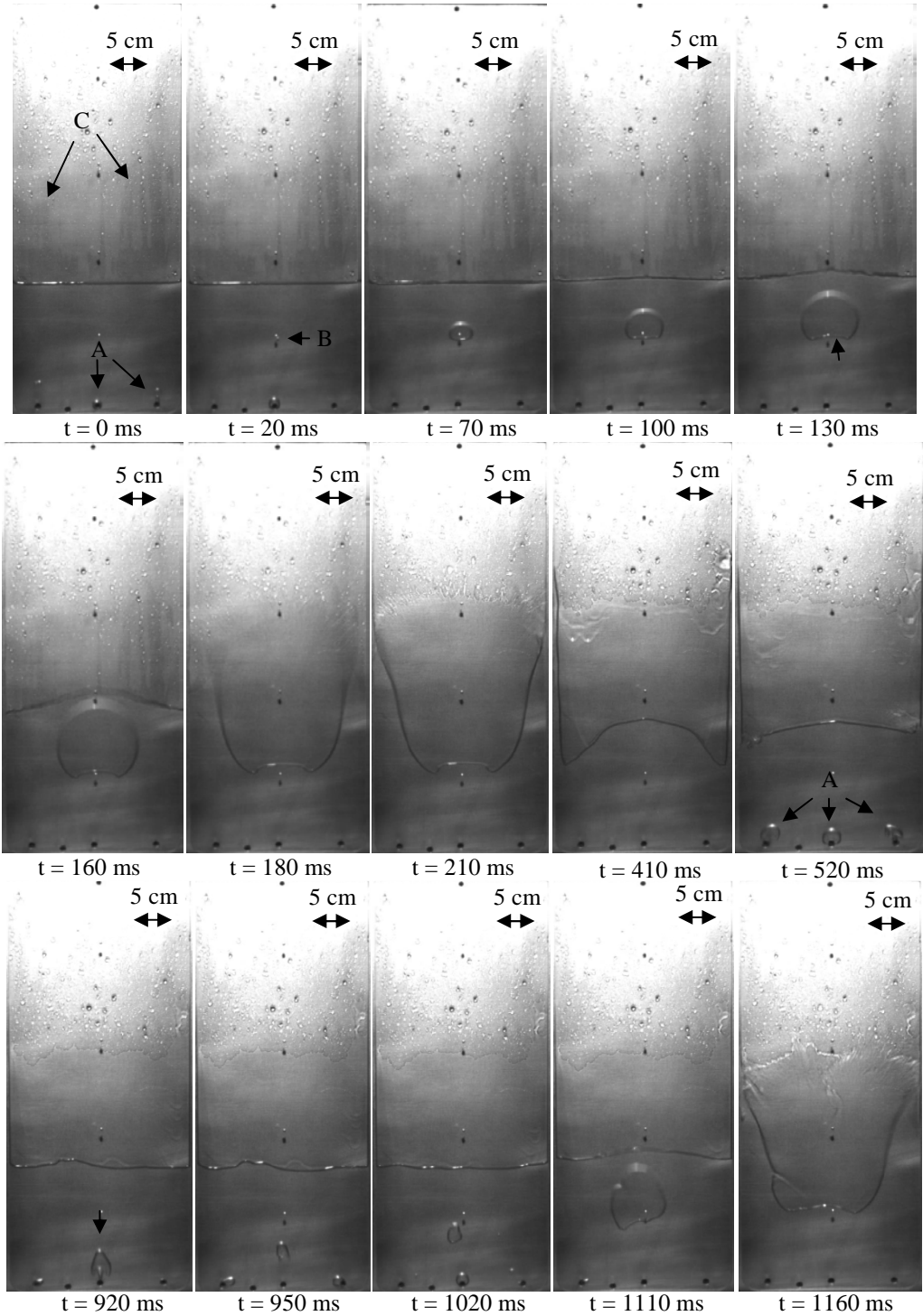
Figure 4.10: Bubble growth and collapse at the outlet of the feeding pipe ($h_1 = 10$ cm, $T_{\text{cond}}^{\text{c,fs}} = 10.4$ °C, $T_{\text{ev}}^{\text{c,fs}} = 19.4$ °C).

The bubble rapidly collapses ($t = 120$ ms). It has first a spherical shape at the beginning of the growth due to its small diameter (around 5 mm to 1 cm) and thus to the predominance of surface tension forces ($t = 57$ ms). It then evolves to a shape of a mushroom with a particular bubble curvature at the base of the mushroom head ($t = 94$ ms). This shape is probably due to the buoyancy force and to fluid recirculation around the bubble (Katto *et al.*, 1970; McGillis *et al.*, 1991a).

As bubbles observed during this regime collapse, damage on the wall at this location could be observed after several hours of experiments

- **Flow regime R2:** Bubbles still collapse at the inlet of the channel but from time to time a bubble of several centimeters appears about 5 cm below the free surface (Fig. 4.11). A film is created on the surface above the free interface since the bubble pushes the free surface up and the double vapor-liquid-vapor interface breaks. Since the interface of the bubble breaks, droplets are projected on the surface and a falling film is created. Evaporation then immediately takes place. The departure of the large bubble can be followed by the departure of several other bubbles with a diameter smaller than that of the first large bubble. The frequency of appearance of the first large bubble depends on running conditions. For some tests, such large bubbles could be observed almost permanently.

During this regime, three main periods could be observed: a period of growth and then break up of a large bubble, a period where many bubbles chaotically grow and collapse in the vicinity of the wall (referred thereafter as “bubble crisis”) and a period of flow similar to the flow regime named R1 where simultaneously, on the upper part of the channel (above the free surface), evaporation of a liquid film takes place. These three periods are described thereafter.



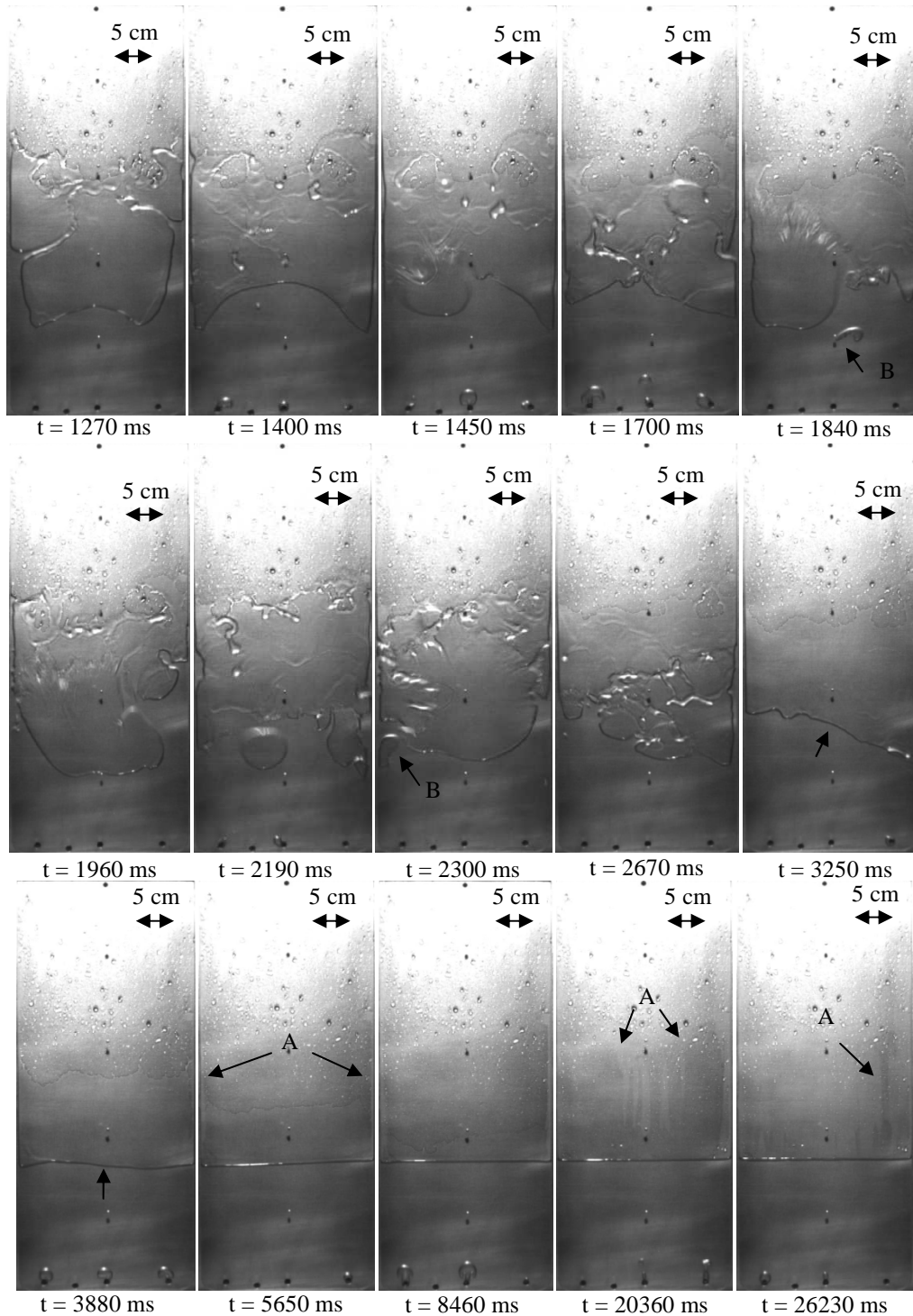


Figure 4.11: Video sequence of the flow regime R2 ($h_1 = 15$ cm, $T_{\text{cond}}^{\text{c,fs}} = 8.5$ °C, $T_{\text{ev}}^{\text{c,fs}} = 17.5$ °C)

Let us start the description of the cycle when a bubble of several centimeters of diameter grows spontaneously few centimeters below the free surface ($0 \text{ ms} < t < 520 \text{ ms}$). Its shape and growth are similar to those of bubbles described in Chap 3. At the beginning of the growth, the bubble has a spherical shape ($t < 50 \text{ ms}$) and then a hemispherical shape ($t = 70 \text{ ms}$). As the bubble keeps growing, due to the buoyancy force, a flattening of its shape is observed at its base ($t = 100 \text{ ms}$). At $t = 130 \text{ ms}$, the bubble of several centimeters pushes the free surface up. A concave curvature is observed at its base but the foot of the bubble remains at the same location than at the beginning. During all this time, above the free surface, the evaporation of a previously formed liquid film is observed ($0 < t < 160 \text{ ms}$). During this period of time, no bubble enters into the lower part of the channel through the feeding port ($t \geq 70 \text{ ms}$). Then, between $t = 170 \text{ ms}$ and $t = 200 \text{ ms}$, as the bubble reaches an equivalent radius (radius in the plane of observation calculated from the projected area of the actual vapor mass) estimated to 12 cm, the double vapor-liquid-vapor interface breaks. Droplets are splashed on the heated wall and on the Plexiglas® wall. A new liquid film is formed and flows down along both walls ($t = 410 \text{ ms}$). Evaporation immediately takes place. At $t = 520 \text{ ms}$, once the newly formed liquid-vapor interface tends to stabilize, collapsing bubbles are observed again at the bottom entrance of the channel.

From **920 ms to 3250 ms**, as observed in subatmospheric pressure boiling at the scale of a bubble, the departure of the large bubble is followed by a “bubble crisis”. A bubble coming from one of the three feeding ports seems to be lifted or sucked probably by the bubble motion induced by the growth of the first bubble ($t = 920 \text{ ms}$). This bubble rises, grows and reaches the free surface ($t = 1160 \text{ ms}$). As it reaches the free surface, the bubble erupts like the previous bubble, but the liquid splashed on the wall is projected to a lower location on the wall than for the first bubble formed. This bubble is then followed by many other bubbles growing homogeneously on the width of the channel but growing mainly in the area of water defined between the free surface and around 5 cm below ($1270 \text{ ms} < t < 3250 \text{ ms}$). As observed during experiments reported in the two previous chapters, the shape and growth of bubbles formed depend on the history of the bubbles, i.e. on the size and frequency of preceding bubbles and on the movements of the free surface interface. During this period of time, the free surface interface moves a lot and intense liquid motion is observed impacting the secondary bubbles growth and the shape of the collapsing bubbles at the bottom entrance of the channel. Indeed, at this location, some bubbles observed can be lifted from the bottom of the plate before collapsing ($t = 1400 \text{ ms}$). The motion of the interface also disturbs the evaporation and the flow of the liquid film situated close to the free surface. Due to this motion and to the projection of droplets, occurrence of downward and upward flowing liquid films is observed ($1160 \text{ ms} < t < 3880 \text{ ms}$).

At the end of the bubble crisis (**3880 ms < t < 26230 ms**), the newly formed interface is stabilized. Regime similar to the regime R1 occurs in the lower part of the channel (i.e. the part filled with liquid) whereas above the free surface, evaporation of a liquid film is observed again. From $t = 3880 \text{ ms}$, the liquid film only flows downwards. This liquid film is first evaporated on the top and at the edge of the rivulet ($t = 5650 \text{ ms}$). Then dry patches appear and vertical dry lines are observed ($t = 20360 \text{ ms}$). All the liquid could then be evaporated (or not) this way before the occurrence of the new boiling cycle.

Since the boundary of the liquid film is situated on each edge of the plate and on the top of the liquid rivulet, the liquid film is thinner at these spots and thus, according to the literature, heat transfer is better. As the heat transfer is better, these spots are evaporated quicker than the other spots. This is what one could observe during these experiments. The occurrence of dry patches is also not surprising as liquid falls due to the gravity force. Thus, the mass flow rate must be low and unfavorable to film stabilization. Moreover as there is a liquid-vapor contact and as the two fluids flow in opposite

directions, the vapor flow could be a source of perturbation and thus contribute to breakup of the liquid rivulet.

The absence of collapsing bubbles at the bottom of the channel during the growth of the first large bubble is probably due to the stop of the upward liquid flow as the bubble grows. Indeed, as the bubble becomes larger, liquid is pushed in all directions. Although the bubble mostly expands upward, the bubble foot remains at the same location for the main part of the growth. This means that it could not expand downward but it creates a sufficient pressure to stop the liquid flow below the bubble. As this pressure stops the liquid flow, bubble leaving the feeding port cannot expand and thus cannot be formed.

- **Flow regime R3:** The bubbles entering the channel grow and splash liquid over the surface without experimenting any collapse like it could be the case in the previous regimes (Fig 4.12).

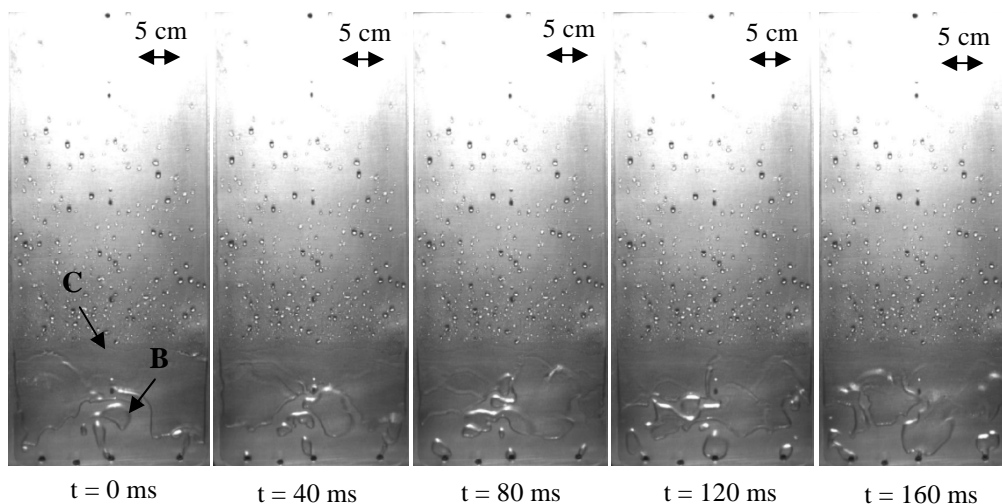


Figure 4.12: Video sequence of the flow regime R3 ($h_l = 5$ cm, $T_{\text{cond}}^{\text{c,fs}} = 8.5$ °C, $T_{\text{ev}}^{\text{c,fs}} = 17.5$ °C)

This regime occurs for a low height of the liquid level and/or for a high temperature difference between the temperature at the condenser and at the evaporator (ΔT). During this regime, the motion of the free interface strongly impacts the shape of the bubbles. The vapors masses do not exhibit any remarkable or regular shape. Bubbles are generally smaller than bubbles observed in boiling regime R2 and are formed almost permanently. The amount of liquid splashed on the plate is lower than the amount of liquid splashed on Fig. 4.11 but the few centimeters situated above the free surface are always wet due to the high bubble frequency of appearance and breaking. No breaking of the liquid falling film is observed during this regime.

The occurrence of these various regimes and the appearance (or not) of a bubble can be linked to the conditions of pressure and temperature on the refrigerant side. Different cases corresponding to different kinds of temperature profiles are presented on Fig. 4.13. Due to the mass flow difference between the secondary fluid and the refrigerant, if no phase-change occurs in the channel, the secondary fluid imposes the temperature to the refrigerant inside the channel. Due to the influence of the hydrostatic pressure on the local pressure, this results in a non-homogeneity of the boiling environment, especially in terms of subcooling degree. Depending on the given height of the liquid level and on the vapor pressure, the boiling could be highly subcooled for a large area of the plate (Fig. 4.13a). In such case, a cooling capacity close to 0 W is measured (regime R1). As the

environment is highly subcooled, the heat released by the collapse of the entering bubble is not sufficient to heat up the liquid. As no bubble appears, no heat transfer by evaporation is possible. For a same vapor pressure, reducing the liquid height allows to reduce the subcooling degree and thus fosters the growing of a bubble (Fig. 4.13b). This bubble will then appear in the favorable part of the plate, i.e. above the subcooled area.

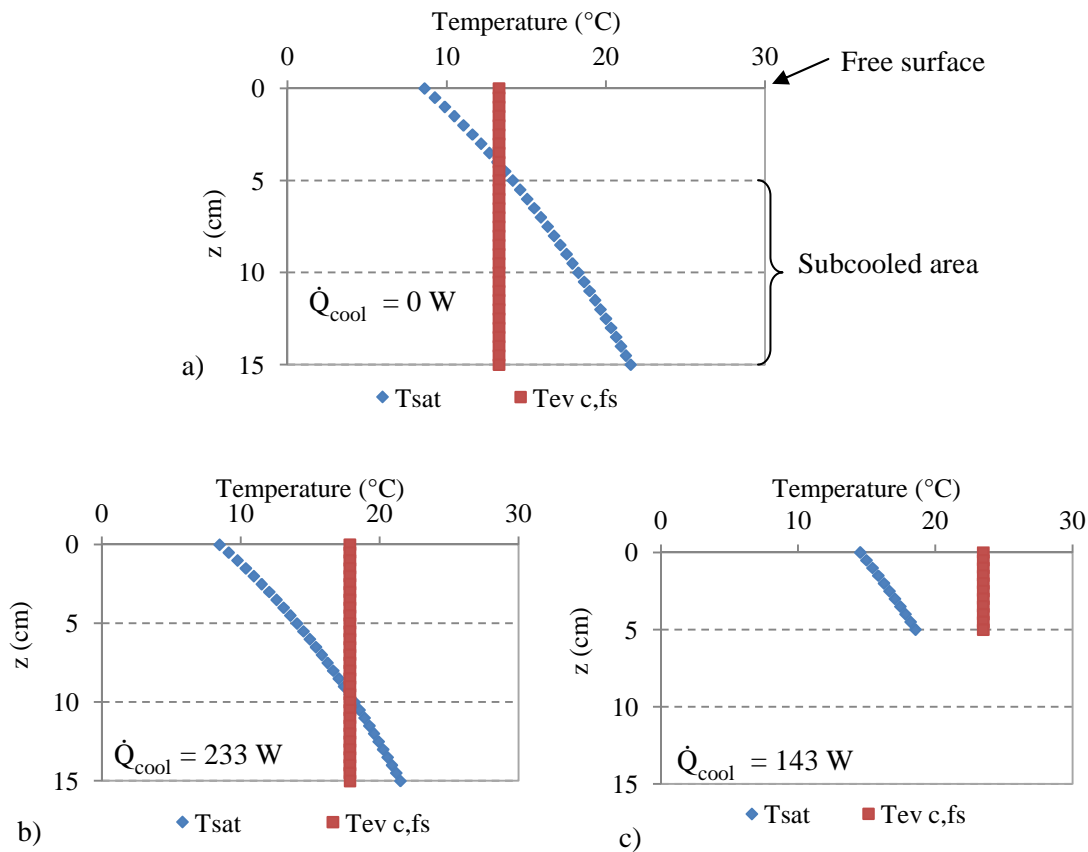


Figure 4.13: Evolution of the saturation temperature in the liquid part of the plate for different operating conditions without any phase-change occurring at $T_{cond}^{c,fs} = 8.5$ $^{\circ}C$ and a) $h_1 = 15$ cm, $T_{ev}^{c,fs} = 12.8$ $^{\circ}C$; b) $h_1 = 15$ cm, $T_{ev}^{c,fs} = 17.5$ $^{\circ}C$; c) $h_1 = 5$ cm, $T_{ev}^{c,fs} = 17.5$ $^{\circ}C$

The cooling capacities indicated on Fig. 4.13 were obtained for the tests as shown on Fig. 4.9, Fig.4.11 and Fig. 4.12. This cooling capacity is calculated by using Eq. 4.1.

4.3.1.2 Influence of the flow patterns on heat transfer

During the experiments, it was observed that the overall heat flux exchanged between the secondary fluid and the refrigerant depends on the growth of bubbles and thus, on the boiling regime. However, the cooling capacity is mainly due to the film evaporation and not to bubble growth. Even though the bubbles are large, their frequency of appearance is low (less than 1 bubble per second for almost all the tests covering the experimental field). Thus, the amount of vapor produced under the form of bubble is negligible. As an example, during the test n $^{\circ}$ 1 ($T_{cond}^{c,fs} = 8.5$ $^{\circ}C$, $T_{ev}^{c,fs} = 17.5$ $^{\circ}C$, $x = 2.5$ %), the feeding mass flow rate was recorded at 312 g/h to maintain a liquid level of 15 cm. During this test, a cooling capacity of 225 W was recorded and the observed bubble frequency 0.2 Hz. The cooling capacity due to boiling was estimated at 1 W which represents less than 0.5 % of heat flux transferred.

To illustrate this statement (i.e. the fact that the cooling capacity achieved is mainly due to the falling film evaporation rather than the growth of a bubble), Fig. 4.14 shows an example of local heat fluxes estimated from the secondary fluid to the refrigerant. These heat fluxes are determined by means of the Fourier's law from temperatures measured at each thermocouple pair (inserted on both sides of the central plate of the evaporator).

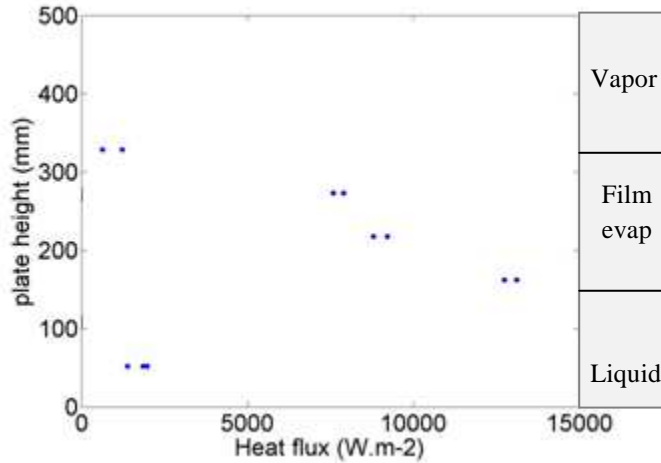


Figure 4.14: Heat flux estimated along the evaporator height by means of thermocouples inserted inside the central plate of the evaporator ($T_{\text{cond}}^{\text{c,fs}} = 8.5 \text{ }^\circ\text{C}$, $T_{\text{ev}}^{\text{c,fs}} = 17.5 \text{ }^\circ\text{C}$, $T_{\text{B3}}^{\text{c,fs}} = 37.5 \text{ }^\circ\text{C}$, $h_1 = 15 \text{ cm}$)

In this example ($T_{\text{cond}}^{\text{c,fs}} = 8.5 \text{ }^\circ\text{C}$, $T_{\text{ev}}^{\text{c,fs}} = 17.5 \text{ }^\circ\text{C}$, $T_{\text{B3}}^{\text{c,fs}} = 37.5 \text{ }^\circ\text{C}$, $h_1 = 15 \text{ cm}$), the heat flux transferred was estimated to range from about 7 kW.m^{-2} to 14 kW.m^{-2} in the portion of the channel where evaporation takes place whereas it was estimated to range from 0 kW.m^{-2} to 2 kW.m^{-2} in the vapor and liquid part. In the liquid part, the heat must be transferred mainly by convection due to the liquid motion, as large bubbles grow and break. Close to the bottom entrance, the convection phenomena must be enhanced by the re-condensation of the bubbles at the end of the feeding pipe. In the vapor part, even if the flow velocity is high (estimated at 12.7 m.s^{-1} for this test) the flow remains laminar and the vapor at such low pressure is a highly isolating fluid. The occurrence of such a high heat transfer at $t = 32.8 \text{ cm}$ is thus probably due to the presence of disparate droplets wetting locally the wall and being evaporated. A part of the heat transfer calculated could also be overestimated due to local diversions of the heat flux (“heat pumping effect”). Indeed, conduction inside the central plate might not be perfectly 1D as assumed and as obtained with the Star-CCM+® simulation but rather more 2 or 3D because of the intense evaporation of the falling film (cf. Appendix I, Fig. I.2).

Nevertheless, Fig. 4.14 shows that heat transfer obtained in the vapor and liquid parts are around three times lower than heat transferred by evaporation. Thus, the film evaporation should be promoted in order to obtain a significant heat transfer. This conclusion is in agreement with results obtained for other tests ran: the larger the film evaporation area, the higher the cooling capacity (Fig. 4.15).

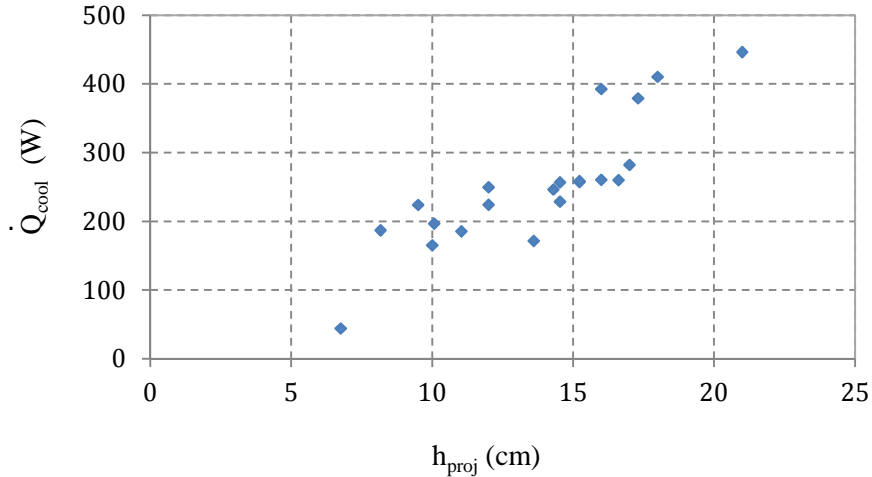


Figure 4.15: Evolution of the cooling capacity obtained during test run with the height of liquid level projected, i.e. with the distance from the newly formed free surface and the top of the liquid rivulet

4.3.2 Results' analysis for a thickness of the channel of 4 mm

Since different regimes occur and the height at which the liquid is splashed depends on the operating conditions, cooling capacities ranging from 0 to 458 W were measured at the secondary fluid. Table 4.5 gathers the cooling capacities obtained during the tests, the corresponding theoretical cooling capacities given by the design of experiments model and the thermodynamic vapor qualities calculated by assuming that both phases are saturated at the inlet of the channel (Eq. 4.8).

$$x = \frac{(h_{in\ V4} - h_{out\ V4-l,sat})}{(h_{out\ V4-v,sat} - h_{out\ V4-l,sat})} \quad (4.8)$$

The latter assumption was validated by the temperatures measured by the four thermocouples located in the feeding channels. The subscripts “in V4” and “out V4” refer to the inlet and outlet of the valve V4. The location of this valve is shown on Fig. 4.1.

For each line of Table 4.5, the cooling capacity (\dot{Q}_{cool}) is an average of the cooling capacity calculated by averaging during 30 min the instantaneous cooling capacity estimated thanks to Eq. 4.1. The same procedure is used for the calculation of the vapor quality. The test n°13 of the design of experiments is repeated four times (Tests n° 22 to 24) in order to estimate the experimental error. This choice was made because of the difficulty to get repeatable values for this point. The theoretical cooling capacity ($\dot{Q}_{cool,th}$) is evaluated thanks to the mathematical model obtained by the design of experiments. The model coefficients of this mathematical model are shown in Table 4.6.

The experimental error (calculated from tests of repeatability) is 9 W. The standard error of the estimate of the model is 14.7 W and the mean absolute error is 8 W. The coefficient b_0 represents the value of the cooling capacity obtained for the central point of the design i.e. for $h_1 = 15$ cm, $T_{cond}^{c,fs} = 8.5^\circ\text{C}$, $T_{B3}^{c,fs} = 37.5^\circ\text{C}$ ($x = 2.5\%$) and $\Delta T = 9$ K. The theoretical driving force calculated for this point (Eq. 4.4) is 8.9 mbar. The values of all the coefficients b_i and b_{ii} are related to the weight of each factor.

Table 4.5: Tests realized and response obtained

Test n°	h_1 (cm)	$T_{cond}^{c,fs}$ (°C)	$T_{ev}^{c,fs}$ (K)	ΔP (kPa)	x (%)	\dot{m}_{refr} (g.h ⁻¹)	\dot{Q}_{cool} (W)	$\dot{Q}_{cool, th}$ (W)	Residual (W)
1	15	8.5	17.5	0.89	2.5	312	225	225	0
2	25	8.5	17.5	0.89	1.8	351	261	248	-13
3	20	14.1	23.1	1.22	1.8	409	283	286	4
4	10	14.1	23.1	1.22	2.5	330	247	246	0
5	5	8.5	17.5	0.89	3.6	230	166	178	7
6	10	2.9	11.9	0.64	3.6	236	172	168	-29
7	20	2.9	11.9	0.64	2.6	285	197	197	0
8	20	10.4	19.4	0.99	3.1	325	250	244	-6
9	10	10.4	19.4	0.99	3.9	300	224	218	-7
10	15	4.7	13.7	0.72	3.8	251	186	190	4
11	20	6.6	15.6	0.80	1.3	342	229	236	7
12	10	6.6	15.6	0.80	2.1	260	187	193	6
13	15	12.3	21.3	1.10	1.2	350	260	257	-3
14	20	10.4	24.1	1.75	2.6	625	447	461	15
15	10	10.4	24.1	1.75	3.2	550	393	387	-6
16	15	4.7	18.5	1.27	3.2	550	379	379	-1
17	15	8.5	22.2	1.58	1.8	550	411	403	-8
18	20	6.6	10.9	0.33	2.1	0	-2	4	6
19	10	6.6	10.9	0.33	3.0	84	24	9	-15
20	15	12.3	16.5	0.45	2.0	57	44	45	1
21	15	8.5	12.8	0.36	3.3	0	-5	2	8
22	15	12.26	21.26	1.10	2.5	365	257	257	0
23	15	12.26	21.26	1.10	1.8	350	257	257	0
24	15	12.26	21.26	1.10	1.8	350	259	257	-2

Table 4.6: Coefficients of the mathematical model (Eq. 4.3) obtained by the design of experiments

b_0	b_1	b_2	b_3	b_4	b_{11}	b_{22}	b_{33}
$\dot{Q}_{cool, th} _0$	H_1^*	$T_{cond}^{c,fs} *$	$T_{B3}^{c,fs} *$	ΔT^*	H_1^{*2}	$T_{cond}^{c,fs} *^2$	$T_{B3}^{c,fs} *^2$
224.59	34.73	48.36	-6.90	247.84	-11.37	3.74	-0.45

b_{44}	b_{12}	b_{13}	b_{14}	b_{23}	b_{24}	b_{34}
ΔT^{*2}	$H_1^* T_{cond}^{c,fs} *$	$H_1^* \Delta T^*$	$H_1^* T_{B3}^{c,fs} *$	$T_{cond}^{c,fs} * T_{B3}^{c,fs} *$	$T_{cond}^{c,fs} * \Delta T^*$	$T_{B3}^{c,fs} * \Delta T^*$
-19.57	6.13	-11.91	50.90	3.70	9.57	19.62

In order to check the consistency of the model, different tests were run. As the objective is to identify the best operating conditions, these tests correspond to the maximal cooling capacity achievable according to the model for the entire plate in the entire experimental field (denoted Tests Verif_1 in Table 4.7) and under constraints (Tests Verif_2 to Verif_4). The constraints chosen are constraints of driving pressure and constraints of secondary fluid temperature at the evaporator. Indeed, the experimental range allows theoretical driving pressure differences from 3.3 to 22 mbar, which is representative of operating conditions occurring in a LiBr/H₂O absorption chiller. However some of

them were obtained for evaporation temperature higher than 20 °C. In this case they are not taken into account. Moreover, as for driving pressure difference below 4 mbar the cooling capacity measured is low, only driving pressure differences ranging from 6 to 9 mbar are reported. The temperature set-point $T_{B3}^{c,fs}$ and the ΔT are arbitrary given at 37.5 °C and at 9 K respectively. Results of these tests are shown on Table 4.7.

Table 4.7: Model verification tests

Test n°	h_l (cm)	$T_{cond}^{c,fs}$ (°C)	$T_{ev}^{c,fs}$ (°C)	ΔP (kPa)	x (%)	\dot{m}_{refr} (g.h ⁻¹)	\dot{Q}_{cool} (W)	$\dot{Q}_{cool,th}$ (W)	Residual
Verif_1	25	14.16	27.90	2.14	0.8	1100	481	528	-47
Verif_2	25	2.87	11.87	0.64	2.0	297	207	204	3
Verif_3	25	4.74	13.74	0.72	2.0	299	222	218	4
Verif_4	25	6.66	15.66	0.80	1.9	320	240	233	7

According to Tables 4.5 and 4.7, the mathematical model obtained follows the cooling power trend satisfactorily. The model is thus validated and the factors could be classified according to their impact on the response.

According to the coefficient of the mathematical model obtained (Table 4.6), the weightiest factor between all the factors is ΔT (value of 247.84). The higher the ΔT , the higher the cooling capacity obtained. This could seem not surprising but the ΔT is not directly proportional to the driving pressure ΔP . Indeed, regarding saturation curves, for a given ΔT but for two different $T_{cond}^{c,fs}$, one smaller than the other, the ΔP will be smaller for the lower $T_{cond}^{c,fs}$ (Fig. 4.16).

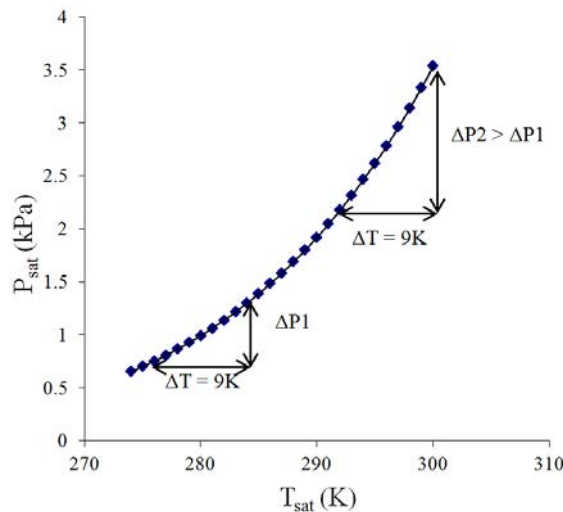


Figure 4.16: Evolution of the saturation pressure according to the saturation pressure and driving pressure associated to a given ΔT

This explained the value of the coefficient b_2 . For a given ΔT , the higher the $T_{cond}^{c,fs}$, the larger the ΔP and thus the higher the cooling capacity obtained.

The weight of the factor ΔT could however be better explained by studying conditions of pressure and temperature occurring inside the evaporator. Indeed, it is fed with a liquid at temperature close to the

saturation temperature i.e. close to $T_{\text{sat}}(P_{\text{cond}} + \rho gh_1)$. For some experimental conditions, the temperature at the inlet of the plate is thus higher than the temperature of the secondary fluid (Fig. 4.13a and 4.13b). This configuration becomes less and less predominant when the ΔT is high or when the height of the liquid level is low. Thus, for a given height of the liquid level and a given $T_{\text{cond}}^{\text{c,fs}}$, increasing the ΔT means decreasing the probability of the liquid to be in subcooled conditions and/or to limit the subcooled fraction of the plate.

The second weightiest coefficient is b_{14} . This coefficient is linked to the impact of the interaction of h_1 and ΔT on the cooling capacity achieved. This influence of the interaction of these two factors could be due to the fact that a low height of liquid level or a high ΔT results in a low subcooling degree at the bottom of the plate. On contrary, a high height of the liquid level or a low ΔT results in a high subcooling degree at the bottom of the plate. These two effects could be balanced one with another. Indeed, by varying the height of the liquid level and the ΔT between secondary fluid temperature set-point at the condenser and at the evaporator, a given subcooling degree will be given. But, by doing so, the subcooling gradient will be different (cf. Chap 2 section 2.2). Moreover, for a low height of liquid, the height up to which the liquid is splashed is low and thus the cooling capacity achieved is low. Thus, there should be an optimal height of the liquid level for a given ΔT . Fig. 4.17a shows the influence of the ΔP (and thus of the ΔT as $T_{\text{cond}}^{\text{c,fs}}$ is given at 8.5 °C) for a given h_1 of 5 cm, 15 cm and 25 cm. Fig. 4.17b shows the influence of the liquid height for a given $T_{\text{cond}}^{\text{c,fs}}$ of 8.5 °C and four different ΔP .

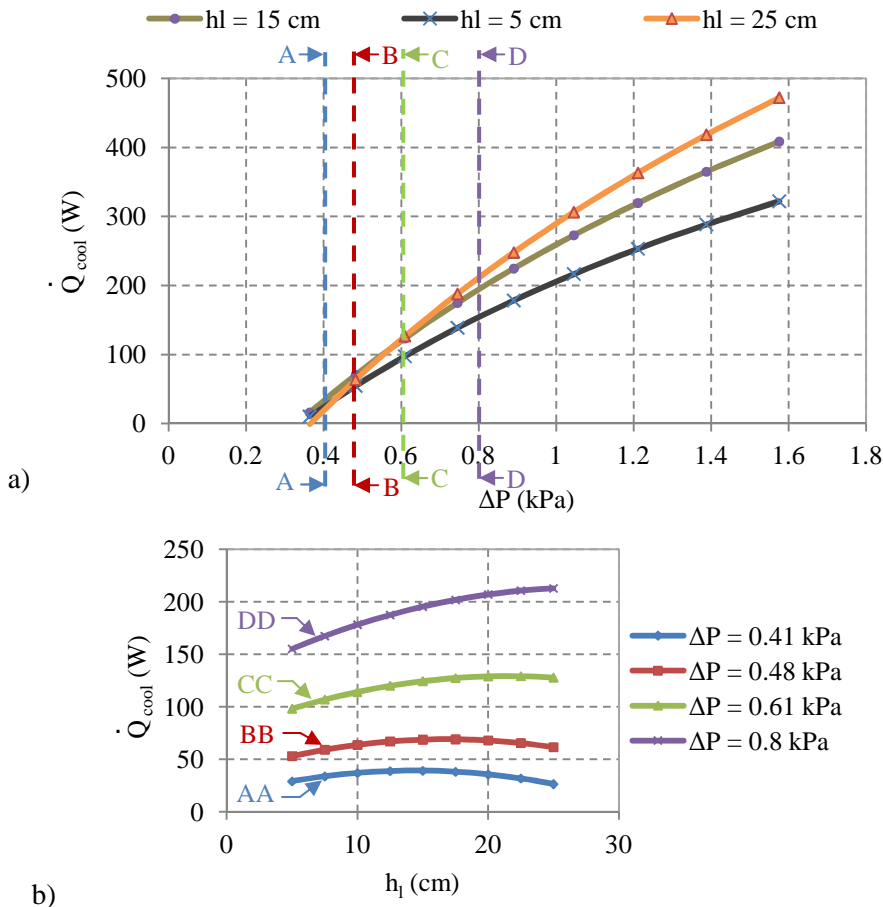


Figure 4.17: Evolution of cooling capacity achieved with a) the driving pressures for 3 different heights of the liquid level; b) the height of the liquid level for 4 different driving pressures ($T_{\text{cond}}^{\text{c,fs}} = 8.5$ °C; $T_{\text{B3}}^{\text{c,fs}} = 37.5$ °C)

As indicated by the coefficient b_1 and b_4 , the higher the h_1 and ΔT (and thus the ΔP for a given $T_{\text{cond}}^{\text{c,fs}}$), the higher the cooling capacity. However, as observed on Fig. 4.15 and as expected, for low ΔP (and thus low ΔT for a given $T_{\text{cond}}^{\text{c,fs}}$), an optimal height of the liquid level exists. This optimal height of the liquid level increases with the driving pressure ΔP and thus with the increase of ΔT for a given $T_{\text{cond}}^{\text{c,fs}}$. For driving pressure of 0.6 (i.e. for a ΔT given at 6.65 °C and a $T_{\text{cond}}^{\text{c,fs}}$ given at 8.5 °C), this optimal height of the liquid level may be located outside the experimental field. This means that for a driving pressure higher than 0.6 kPa and for a given $T_{\text{cond}}^{\text{c,fs}}$ of 8.5 °C, the height of the liquid level for which the highest cooling capacity is achieved is higher than 25 cm, i.e. the filling ratio should be higher than 0.5 to achieve the best cooling capacity. However, this result should be used with caution as it is obtained by an analysis of the mathematical model. Moreover, although the theoretical model indicates that the filling ratio should be higher than 0.5, for a given ΔP , the height up to which the liquid is splashed should be high enough to project liquid outward the evaporator without being evaporated. This phenomenon, prejudicial for the cooling capacity achievable, is for example observed for the test n°14, i.e. for a height of the liquid level of 20 cm and a ΔP of 1.75 kPa.

Another interesting result to notice on Fig. 4.17 is that the influence of the height of the liquid level on the achieved cooling capacity becomes more significant when increasing the driving pressure. A degradation of the evaporator performance up to 30 % could be for example observed by setting a height of the liquid level lower than 25 cm (which is lower than the optimal length) at 0.9 kPa.

As for low driving pressure, an optimal height of the liquid level exists in the experimental field, a first approach would consist in considering that the optimal height of the liquid level is the height for which the subcooling is null, i.e. the height for which the evaporator is fed with saturated liquid at the same temperature as the secondary fluid as long as this height of the liquid level remains sufficient. Experiments were thus conducted to compare the cooling capacity obtained for the design of experiments points with the height of the liquid level h_1 and for the same points but with this “favorable liquid column height”. The results show that for the major part of the design of experiments points, the cooling capacity obtained decreases with the decrease of the liquid column height. For example 26 W (i.e. 11.6 %) are lost for the central point by varying the height of the liquid level from 15 cm to 9 cm. The mathematical model is in agreement with this observation. This shows that a certain amount of liquid is required to obtain the best cooling capacity possible for given operating conditions even if this means that at the bottom of the plate, the liquid is subcooled.

4.3.3 Impact of the channel thickness

The channel thickness was decreased to 2 mm. For a same evaporative mass flow rate than that achieved at 4 mm, the vapor velocity is hence doubled. As the vapor velocity is doubled, phenomena observed should be different especially in the film evaporation area. Indeed, the vapor velocity should impact the falling film stability and the cooling capacity. Moreover, as mentioned in the literature and as observed in Chap. 3, the heat transfer coefficient should be also impacted by the decrease of the channel thicknesses at the bottom of the channel, i.e. at the part of the channel filled with liquid (configuration close to pool boiling). Indeed, decreasing the thickness has an influence on the deformation of the bubble. Decreasing the thickness also leads to increase convective effects induced by the bubbles growth and rise and it modifies the boiling regime obtained. Thus, one should expect to observe differences in the regime flow observed and in the cooling capacity achieved between these two thicknesses. The first part of this section is thus dedicated to the flow visualization at $e = 2$ mm and then to the results of the design of experiments.

4.3.3.1 Visualization

Same three main flow regimes as observed for $e = 4$ mm were observed at $e = 2$ mm. However, these regimes did not always occur for the same operating conditions as for $e = 4$ mm (cf. Appendix J). For some operating conditions another regime flow was even observed. This regime flow is described thereafter:

- **Flow regime R4:** As a bubble grows and splashes liquid on the wall, the liquid is dragged by the vapor and evacuated forming an upward liquid flow (Fig. 4.18). The plate is wetted up to a higher location than with flow regime introduced previously. As observed for film flow, dry paths are created and liquid is evacuated from the evaporator following a preferential path. Droplets created by the break of the interface of the bubble flow at first upward and then can either coalesce and flow downward, be dragged by the vapor flow or be evaporated slowly. Their shape and volume vary with the time (droplets referred as 1, 2 and 3 on Fig. 4.18).

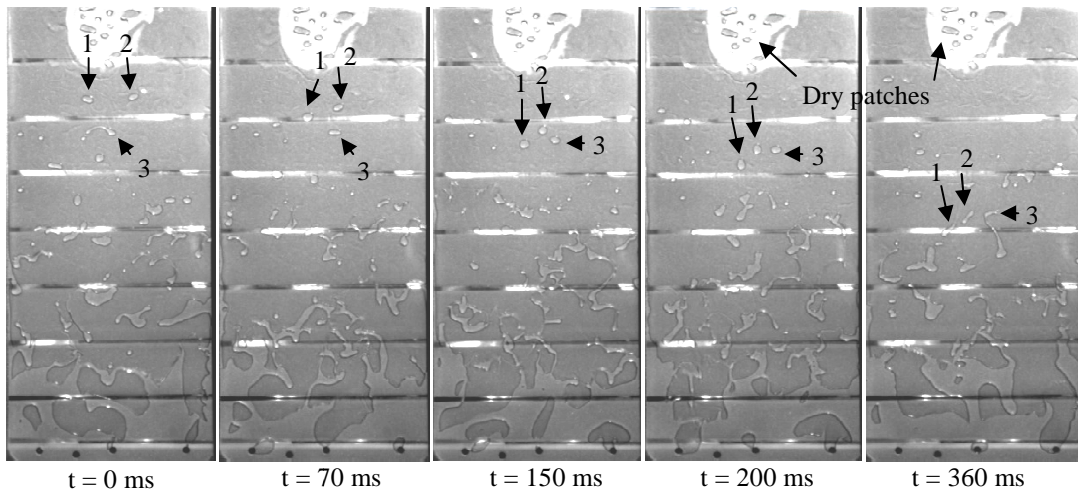


Figure 4.18: Video sequence of the flow regime R4 ($h_1 = 25$ cm, $T_{\text{cond}}^{\text{c,fs}} = 14.2$ °C, $T_{\text{ev}}^{\text{c,fs}} = 27.9$ °C)

This regime is observed for the tests n°14, 15 and 17. During this regime, an almost horizontal free surface could be sometimes observed as for the flow regime R2 (Test n°15 and 17). But as for the test n° 14 and the test shown on Fig. 4.18, the free surface could be highly disturbed. In this last case, the mass flow rate of vapor evaporated is high compared to the mass flow rate obtained for other regimes. As no liquid column is observed, bubbles feeding the evaporator immediately grow and droplets created by the breaking of these bubbles are dragged by the vapor flow. In all cases, during this regime a considerable amount of water leaves the evaporator without being evaporated.

For some tests (Test n° 8 and 16), both regimes R2 and R4 coexist: as bubbles grow and break, liquid is splashed on the wall above the free surface. But, instead of observing a downward liquid flow like for the flow regime R2, an upward liquid flow is observed before the evaporation of the liquid film takes place (Fig. 4.19).

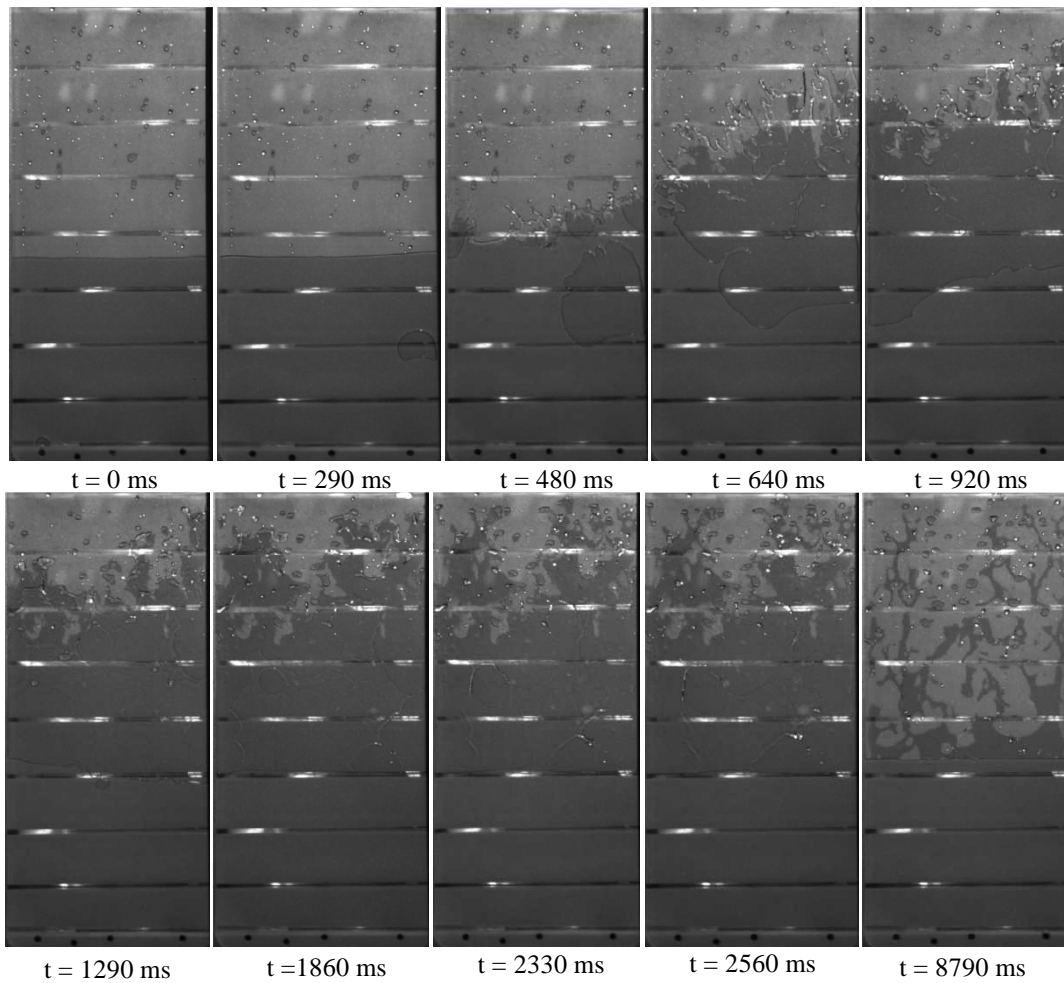


Figure 4.19: Video sequence of the upward flow observed ($h_1 = 20$ cm, $T_{\text{cond}}^{\text{c,fs}} = 10.4$ °C, $T_{\text{ev}}^{\text{c,fs}} = 19.4$ °C)

As observed on Fig. 4.19, the occurrence of these flow regimes are not the only difference observed between $e = 4$ mm and $e = 2$ mm. Indeed, at $e = 2$ mm, droplets trapped between the two walls of the evaporator are observed⁶. These droplets could remain trapped during several minutes before coalescing and flowing down, being dragged by the vapor flow or being evaporated. The presence of these droplets is probably due to the predominance of the capillary forces as the thickness of the channel is narrower than the capillary length calculated for water at the same operating conditions (around 2.7 mm). Another difference observed is that during the growth of the large bubbles, waves appear at the top of the bubbles (Fig.4.20). This effect may exist for a thickness of the channel of 4 mm but was not as significantly observed.

⁶ For $e = 4$ mm, droplets sometimes observed were attached to the adiabatic wall only.

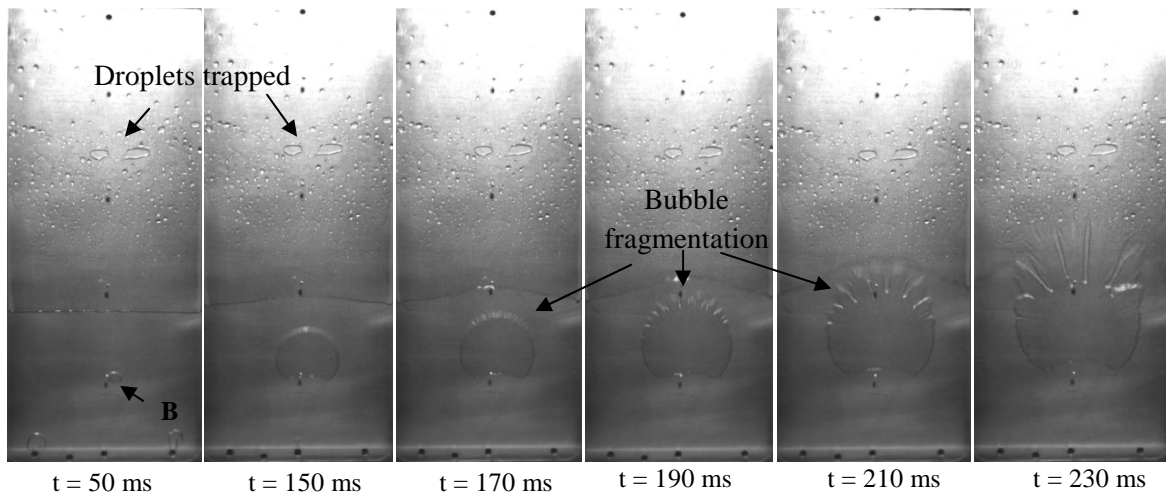


Figure 4.20: Bubble fragmentation and droplets trapped ($h_1 = 15$ cm, $T_{\text{cond}}^{\text{c,fs}} = 10$ °C, $\Delta T = 9$ K, $\dot{Q}_{\text{cool}} = 247$ W)

4.3.3.2 Design of Experiments

Some differences were also observed regarding the cooling power achieved and the behavior of the prototype for the two thicknesses investigated. Table 4.8 shows cooling capacity obtained for experiments conducted for a thickness of the channel of 2 mm.

As a result of the design of experiments realized, Table 4.9 shows the coefficients of the mathematical model obtained by the exploitation of this design for the two thicknesses.

In both cases the weightiest factors on the cooling capacity achieved are ΔT and $T_{\text{cond}}^{\text{c,fs}}$. This is due, as for $e = 4$ mm, to the fact that an increase in ΔT means, depending on the $T_{\text{cond}}^{\text{c,fs}}$, an increase in the driving pressure but also a decrease of the subcooled area at the inlet of the channel. The influence of $T_{\text{cond}}^{\text{c,fs}}$ on the cooling power achieved seems however more significant for $e = 2$ mm than for $e = 4$ mm. This is probably due to the fact that the higher the evaporation mass flow rate and thus the driving pressure, the better the wetting of the wall due to the drag of liquid by the high velocity vapor flow.

As indicated by the coefficient b_1 of the mathematical model, the decrease/increase of the cooling power with the height of the liquid level is nearly inexistent for $e = 2$ mm. This could be probably explained by a change in factors impacting the film evaporation. For $e = 4$ mm, the velocity and the frequency of the bubble control the evaporation of the water on the wall (alternating of wet and dry surface) whereas for $e = 2$ mm, this evaporation is controlled by the vapor flow velocity (surface almost wet at all times - wet area linked to the amount of water dragged by the vapor up to a certain distance). However, this influence of the height of the liquid level on the cooling power achieved is significant by its interaction with the factor $T_{B3}^{\text{c,fs}*}$, hence the vapor quality at the entrance of the channel (coeff. b_{13}). This means that an optimal height of the liquid level for a given $T_{B3}^{\text{c,fs}}$ exists. The existence of this optimal length for a given $T_{B3}^{\text{c,fs}}$ is well observed on Fig. 4.21.

Table 4.8: Tests realized and response obtained for $e = 2 \text{ mm}$

Test n°	h_l (cm)	$T_{\text{cond}}^{\text{c,fs}}$ (°C)	$T_{B3}^{\text{c,fs}}$ (°C)	ΔT (K)	$T_{\text{ev}}^{\text{c,fs}}$ (°C)	ΔP (kPa)	x (%)	\dot{m}_{refr} (g.h ⁻¹)	\dot{Q}_{cool} (W)	$\dot{Q}_{\text{cool, th}}$ (W)
1	15	8.50	37.5	9.0	17.50	0.89	2.3	229	170	165
2	25	8.50	37.5	9.0	17.50	0.89	1.7	220	173	148
3	20	14.13	37.5	9.0	23.13	1.22	1.8	320	237	245
4	10	14.13	37.5	9.0	23.13	1.22	2.4	309	221	215
5	5	8.50	37.5	9.0	17.50	0.89	3.7	185	123	148
6	10	2.87	37.5	9.0	11.87	0.64	3.4	136	93	85
7	20	2.87	37.5	9.0	11.87	0.64	2.4	98	49	55
8	20	10.38	43.62	9.0	19.38	0.99	3.1	130	87	111
9	10	10.38	43.62	9.0	19.38	0.99	3.7	275	190	160
10	15	4.74	43.62	9.0	13.74	0.72	3.8	7	-4	15
11	20	6.62	31.38	9.0	15.62	0.80	1.2	200	138	168
12	10	6.62	31.38	9.0	15.62	0.80	2.0	190	143	119
13	15	12.26	31.38	9.0	21.26	1.10	1.1	259	201	182
14	20	10.38	39.03	13.7	24.12	1.75	2.8	1839	433	426
15	10	10.38	39.03	13.7	24.12	1.75	2.8	750	398	409
16	15	4.74	39.03	13.7	18.49	1.27	2.6	406	305	287
17	15	8.50	32.91	13.7	22.25	1.58	1.5	979	398	411
18	20	6.62	35.97	4.3	10.88	0.33	2.1	0	-10	-21
19	10	6.62	35.97	4.3	10.88	0.33	3.0	0	-11	-4
20	15	12.26	35.97	4.3	16.51	0.45	2.1	0	-1	17
21	15	8.50	42.09	4.3	12.75	0.36	3.3	0	-15	-27
22	15	8.50	37.5	9.0	17.50	0.89	2.3	219	152	165
23	15	8.50	37.5	9.0	17.50	0.89	2.5	245	189	165
24	15	8.50	37.5	9.0	17.50	0.89	2.4	200	147	165
Verif_1	25	14.16	36.0	13.7	27.90	2.14	2.1	1991	503	553
Verif_2	6	2.87	37.5	9.0	11.87	0.64	3.8	150	95	88
Verif_3	10	4.74	37.5	9.0	13.74	0.72	3.1	161	111	113
Verif_4	12.5	6.66	37.5	9.0	15.66	0.80	2.8	211	145	139

Table 4.9: Coefficients of the mathematical model obtained by the design of experiments for $e = 2$ mm and $e = 4$ mm

Coefficients	Centered Factors	$e = 2$ mm	$e = 4$ mm
b_0	$\dot{Q}_{cool, th} \Big _0$	164.52	221,67
b_1	h_1^*	0.04	48,33
b_2	$T_{cond}^{c,fs}$	92.17	53,33
b_3	$T_{B3}^{c,fs}$	-37.52	-15,92
b_4	ΔT^*	248.10	238,69
b_{11}	h_1^{*2}	-16.84	-19,21
b_{22}	$T_{cond}^{c,fs}{}^2$	-13.52	-11,71
b_{33}	$T_{B3}^{c,fs}{}^2$	-50.44	-23,11
b_{44}	ΔT^{*2}	52.40	-14,43
b_{12}	$h_1^* T_{cond}^{c,fs}$	35.15	1,40
b_{13}	$h_1^* T_{B3}^{c,fs}$	-71.87	2,49
b_{14}	$h_1^* \Delta T^*$	27.13	18,62
b_{23}	$T_{cond}^{c,fs} * T_{B3}^{c,fs}$	59.28	36,69
b_{24}	$T_{cond}^{c,fs} * \Delta T^*$	59.51	47,57
b_{34}	$T_{B3}^{c,fs} * \Delta T^*$	-27.71	8,68

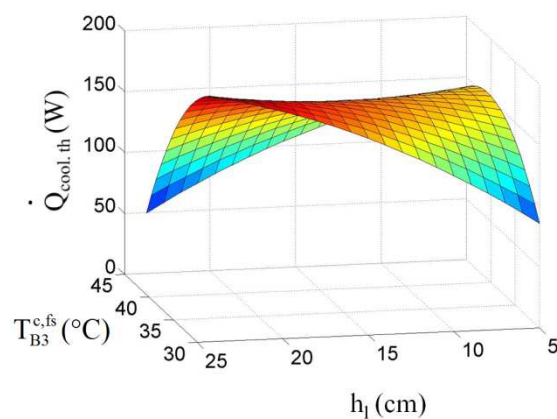


Figure 4.21: Response surface for $e = 2$ mm and for $\Delta T = 9$ K, $T_{cond}^{c,fs} = 8.5$ °C

4.3.4 Comparison of results obtained for $e = 4$ mm and $e = 2$ mm

As the phenomena observed for the two thicknesses of the channel are different for given operating conditions, the cooling capacity obtained is also different. Generally, the cooling power achieved for $e = 2$ mm is lower than the cooling capacity achieved for $e = 4$ mm. This could be in agreement with the statement of Golobic and Gaspersic (1997) who predicted, with a method based on thermodynamical corresponding states principle, that if flow instabilities are generated, the heat transfer performance could be degraded. Indeed, visualizations show that for a thickness of the channel of 4 mm, the liquid is splashed on the wall, a downward flow is observed and evaporation immediately takes places. For a thickness of the channel of 2 mm, the liquid is splashed on the wall but an upward flow is observed and droplets are dragged by the vapor flow or trapped between the two surfaces disturbing the flow. Areas of fluid recirculation were observed around the droplets trapped between the two walls.

Fig. 4.22 shows the evolution of the cooling capacity with the height of the liquid level for the two thicknesses and for four driving pressures ($T_{B3}^{c,fs} = 37.5$ °C, $\Delta T = 9$ K). The experimental results obtained for the theoretical highest cooling capacity for these four driving pressures are also referred in Table 4.10.

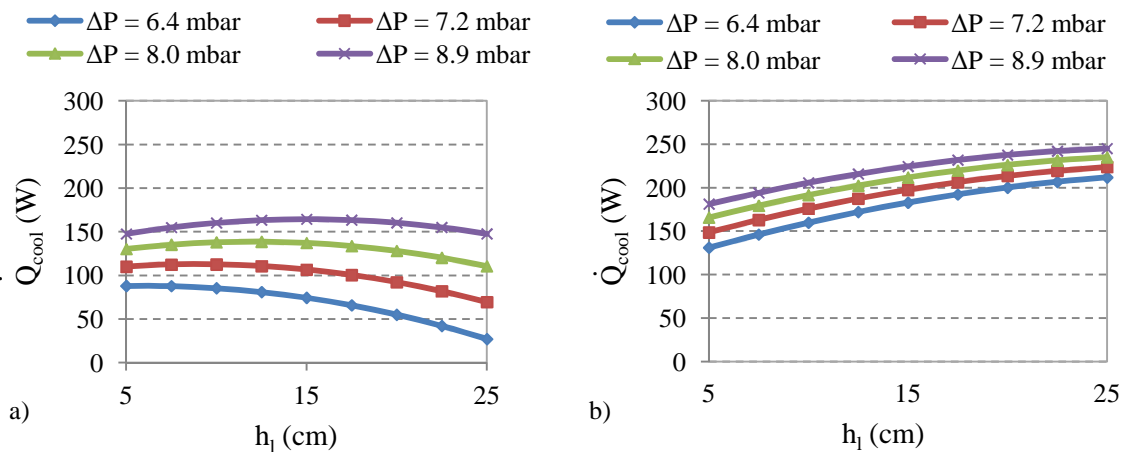


Figure 4.22: Evolution of the cooling capacity with the liquid height for four different driving pressures and for a) $e = 2$ mm and b) $e = 4$ mm ($T_{B3}^{c,fs} = 37.5$ °C, $\Delta T = 9$ K)

In these restricted experimental field, the cooling capacity obtained for $e = 2$ mm is always lower than the cooling capacity obtained for $e = 4$ mm for same operating conditions. A difference of twice the cooling capacity achieved for $e = 2$ mm could be experimentally measured for these tests (Table 4.10). In order to understand which phenomena are linked to this difference, heat fluxes estimated from thermocouples inserted inside the central plate for the both thicknesses and for the fourth test of Table 4.10 are shown on Fig. 4.23.

Table 4.10: Experimental results of the highest theoretical cooling capacity achievable for the four driving pressures investigated

				e = 4 mm				e = 2 mm				Comparison \dot{Q}_{cool} (%)
	$T_{cond}^{c,fs}$ (°C)	$T_{B3}^{c,fs}$ (°C)	$T_{ev}^{c,fs}$ (°C)	h_1 (cm)	x (%)	\dot{Q}_{cool} (W)	$\dot{Q}_{cool,th}$ (W)	h_1 (cm)	x (%)	\dot{Q}_{cool} (W)	$\dot{Q}_{cool,th}$ (W)	
$\Delta P = 6.4$ mbar	2.87	37.5	11.87	25	2.0	207	212	6	3.8	95	88	45
$\Delta P = 7.2$ mbar	4.74	37.5	13.74	25	2.0	222	224	10	3.1	111	113	50
$\Delta P = 8.0$ mbar	6.66	37.5	15.66	25	1.9	240	235	12.5	2.8	145	139	60
$\Delta P = 8.9$ mbar	8.50	37.5	17.50	25	1.8	261	245	25	1.7	173	148	66

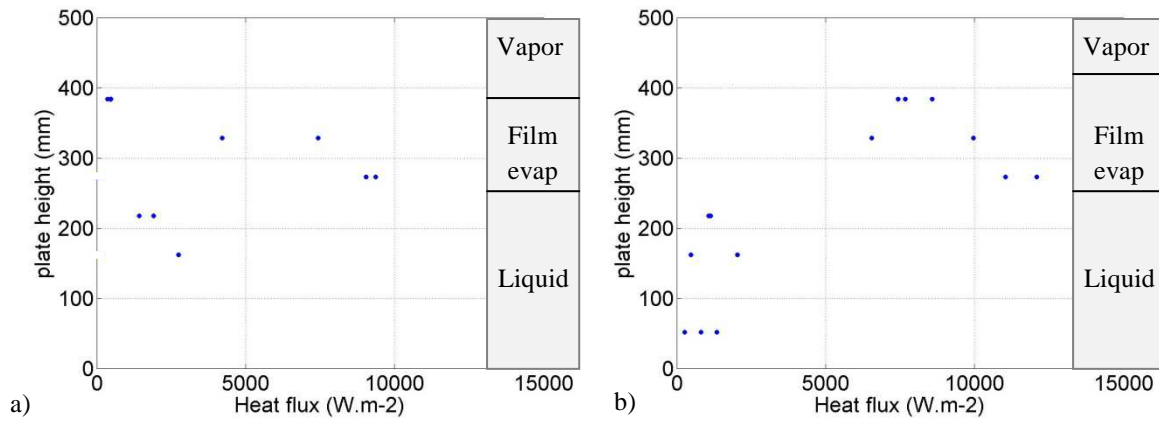


Figure 4.23: Heat flux calculated from thermocouples inserted inside the central plate for a) e = 2 mm and b) e = 4 mm (Test n°2- $\Delta P = 8.9$ mbar)

As observed from the Fig. 4.23, at 5.2 cm, no heat flux is measured for e = 2 mm whereas a mean heat flux of 1600 W.m^{-2} is estimated for e = 4 mm. Similar heat fluxes are estimated at a location of 16.2 cm and 21.8 cm for the both thicknesses. Then, at a location of 27.3 cm, the heat transfer is significantly improved and a mean heat flux of 9700 W.m^{-2} is estimated for a thickness of 2 mm whereas a mean heat flux of 12200 W.m^{-2} could be estimated for e = 4 mm. At location of 32.8 and 38.4 cm, the heat transfer decreases for both thicknesses, down to 7500 W.m^{-2} for e = 4 mm and down to 800 W.m^{-2} for e = 2 mm.

The difference of heat flux measured for the both thicknesses especially at a location of 5.2 cm is due to presence or not of heat transferred by convection. Indeed, visualization shows that the free interface is always moving for a thickness of 4 mm. On the contrary, for e = 2 mm, the movement of the free interface rapidly vanishes after the growth and the breaking of large bubbles. Moreover, for e = 2 mm, bubbles are smaller than bubbles observed for a thickness of 4 mm and start their growth at a location that ranges from 20 cm to 25 cm from the bottom of the channel. For e = 4 mm, periodical appearance of large bubble at a location ranging from 15 cm to 20 cm from the bottom of the channel is observed. Regarding the heat transferred by evaporation, the difference of heat flux estimated could be due to the difference of phenomena occurring inside the channel for the two thicknesses, i.e., the presence of higher vapor velocity flow for e = 2 mm as well as the presence of droplets or rivulets trapped between the two walls. Another explanation could be that, as the bubbles are smaller at 2 mm than at 4 mm and as the growth is different at these two thicknesses, the amount of liquid splashed on the wall is

different. Visualization shows that the liquid is splashed at a slightly higher distance from the free surface for $e = 4$ mm than for $e = 2$ mm.

As shown on Fig. 4.23, the difference in cooling power achieved for the both thicknesses is mainly due to the difference of amount of heat transferred by evaporation and thus to the difference between falling film evaporation and boiling phenomena. However, as the ΔT and the $T_{\text{cond}}^{\text{c,fs}}$ increase, the opposite trend is observed, i.e the theoretical cooling capacity achieved for $e = 2$ mm is higher than the theoretical cooling capacity achieved for $e = 4$ mm (Fig. 4.24). The highest cooling capacity achievable in the experimental field is thus obtained for a thickness of the narrow channel of $e = 2$ mm. This trend is confirmed by experimental results. Tests for which the maximal theoretical cooling capacity is achieved were run and results are gathered on Table 4.11.

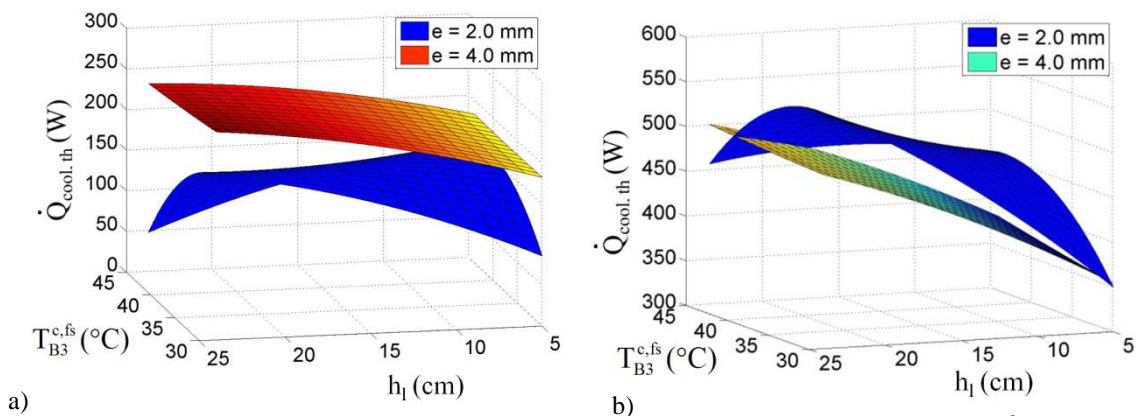


Figure 4.24: Response surfaces for the two thicknesses investigated and for a) $\Delta T = 9$ K, $T_{\text{cond}}^{\text{c,fs}} = 8.5$ °C and b) $\Delta T = 13.7$ K, $T_{\text{cond}}^{\text{c,fs}} = 14.2$ °C

Table 4.11: Experimental results of the highest theoretical cooling capacity achievable in the experimental field for $e = 2$ mm and $e = 4$ mm

	h_1 (cm)	$T_{\text{cond}}^{\text{c,fs}}$ (°C)	$T_{B3}^{\text{c,fs}}$ (°C)	$T_{\text{ev}}^{\text{c,fs}}$ (°C)	ΔP (kPa)	x (%)	\dot{Q}_{cool} (W)	$\dot{Q}_{\text{cool,th}}$ (W)
Max 4 mm	25	14.16	34.0	27.90	2.14	0.8	481	500
Max 2 mm	25	14.16	36.0	27.90	2.14	2.1	503	553

For $e = 4$ mm, a height of the liquid level could be maintained, which is not the case with a thickness of 2 mm (Fig. 4.25). This could explain the difference in cooling capacity achieved for the two thicknesses. Thus, for $e = 4$ mm, from a location of 5.2 cm to 21.8 cm, heat is transferred by convection induced by the growth of large bubbles. As the frequency of bubble growth is relatively high (1.44 bubbles per second), the fluid motion inside the channel is fostered and the resulting heat transfer is higher than for the other tests. For $e = 2$ mm, as a liquid height could not be maintained, heat is mainly transferred by evaporation. The resulting heat flux is higher than for a heat transfer by convection but is degraded compared to heat flux obtained for evaporation at a thickness of 4 mm (Fig. 4.26).

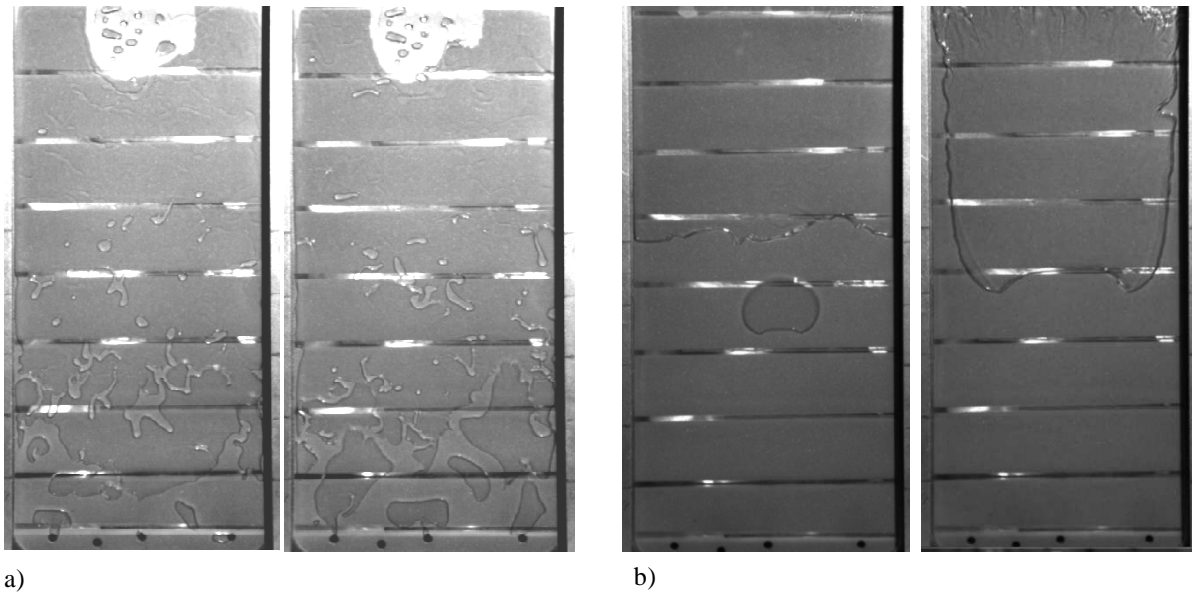


Figure 4.25: Pictures of the flow regime observed for the test of maximal cooling capacity in the experimental field for a) $e = 2$ mm and for b) $e = 4$ mm.

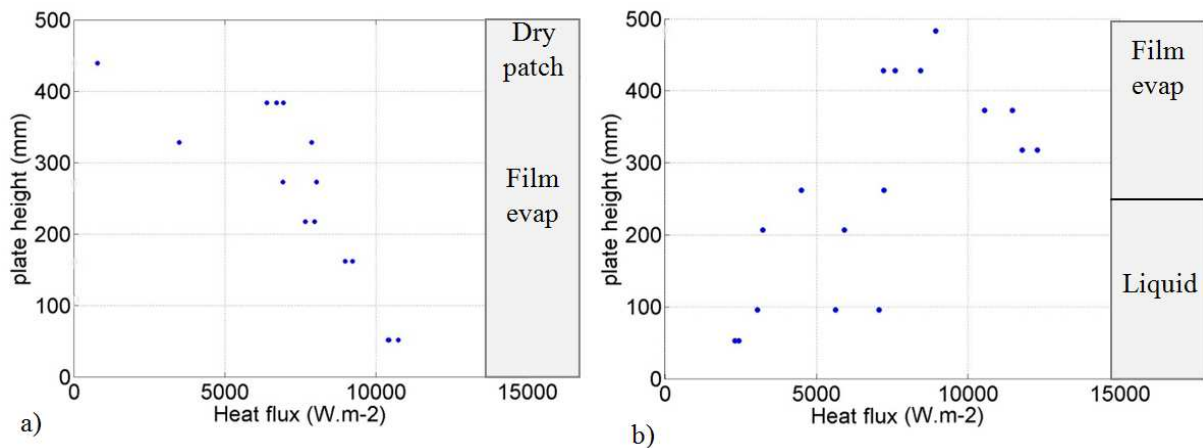


Figure 4.26: Heat flux calculated from thermocouples inserted inside the central plate for the test of maximal cooling capacity in the experimental field and for a) $e = 2$ mm and b) $e = 4$ mm

Although a cooling capacity of 500 W could be achieved for $e = 2$ mm, these operating conditions should not be favored as a lot of liquid refrigerant is evacuated off the evaporator by the vapor flow. Moreover, as the difference in cooling capacities obtained for the two thicknesses in the experimental field (where the cooling capacity is higher for $e = 2$ mm than for $e = 4$ mm) is not significant and as, generally, for $e = 2$ mm:

- the evacuation of liquid refrigerant by the vapor flow is observed for several tests
- the cooling capacity difference achieved for $e = 2$ mm and $e = 4$ mm at $h_1 = 25$ cm is only of 4 % of the maximal cooling capacity
- the experimental field where the theoretical cooling capacity is higher for $e = 2$ mm than for $e = 4$ mm is limited (Fig. 4.27)

a thickness of the channel of 4 mm should generally be preferable.

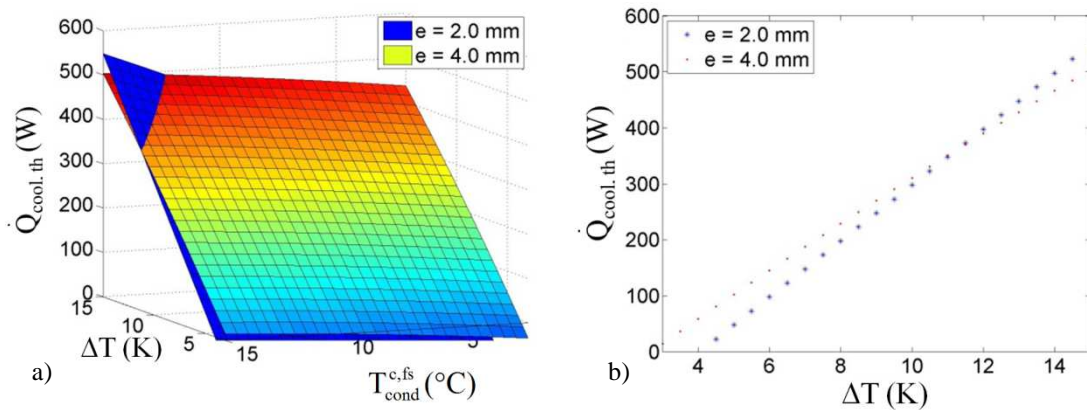


Figure 4.27: Response surfaces for a) $e = 2$ mm and $e = 4$ mm and b) evolution of the cooling capacity achieved depending on the ΔT for $T_{cond}^{c,fs} = 14.2$ °C ($h_1 = 25$ cm, $T_{B3}^{c,fs} = 37.5$ °C)

4.4 Discussion

As, according to the results presented in the previous section, a thickness of the channel of 4 mm should be preferred rather than a thickness of 2 mm, the following sections are focused on results obtained for a thickness of the channel of 4 mm.

4.4.1 Simplified temperatures profile inside the evaporator

Owing to the thermocouples implemented inside the central plate of the evaporator, heat fluxes were estimated. These thermocouples allowed also determining the temperature inside the plate. An example of temperature measured by these thermocouples is shown on Fig. 4.28.

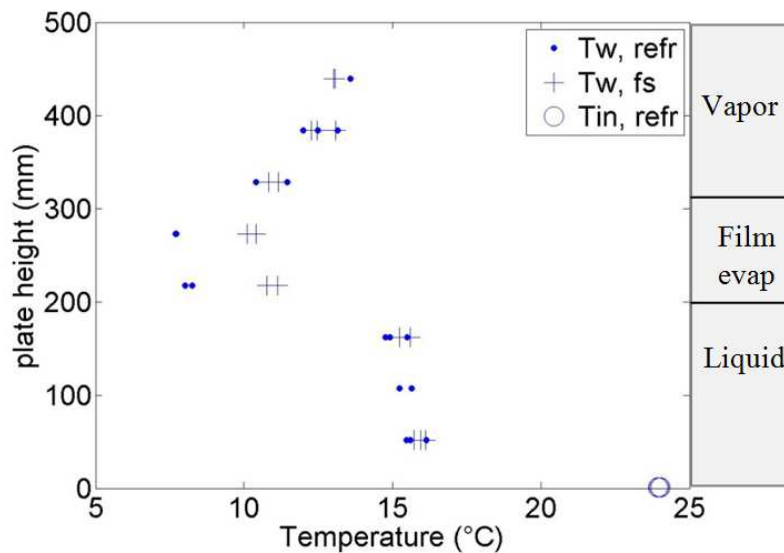


Figure 4.28: Temperature measured by thermocouples located inside the central plate of the evaporator on the refrigerant side (.), on the secondary fluid side (+) and by the four thermocouples located inside the feeding channels (o)

From these temperature profiles and based on our current knowledge on phenomena occurring inside the evaporator, for almost all the tests run, the evolution of the refrigerant and secondary fluid temperature inside the channel could be roughly schematized as on Fig. 4.29:

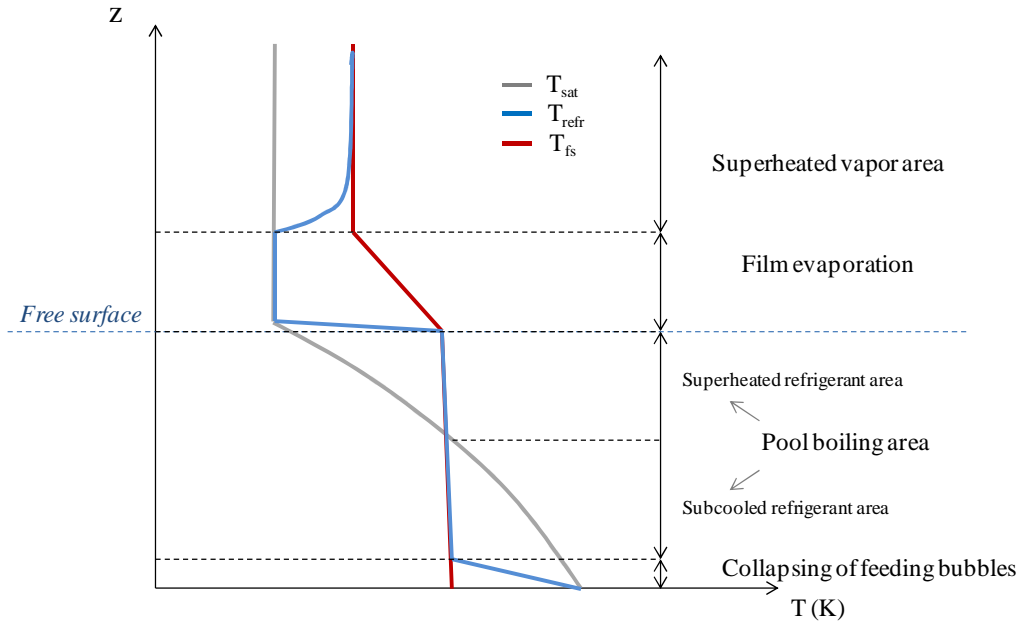


Figure 4.29: Schematic of the evolution of the secondary fluid and refrigerant temperature depending on the evaporator height

Let us follow a group of particles of refrigerant from the inlet of the evaporator to the outlet. Inside the feeding pipe, the refrigerant is at its saturation temperature. Liquid and vapor coexist. At the bottom of the channel, thermodynamic equilibrium is reached with the secondary fluid. The temperature of the tracked particles is imposed by the secondary fluid temperature. Due to the hydrostatic pressure, the tracked particles are thus either subcooled or either superheated depending on the secondary fluid temperature and on their location inside the channel. At the free surface and above the free surface, phase-change occurs and the tracked particles have a temperature close to the saturation temperature of the free surface. The temperature of the vapor is then here again imposed by the secondary fluid temperature.

Regarding the secondary fluid temperature, at the bottom of the channel, due to the difference between the two mass flow rates, the secondary fluid temperature is not significantly affected by the arrival of a warmer fluid on the refrigerant side of the evaporator neither by the release of energy due to the collapse of bubbles. As the frequency of the bubbles that may appear on the refrigerant side in the boiling area is low, and, the heat absorbed by the growth of these bubbles is negligible (around 5 J for a bubble of equivalent radius of 12 cm), the secondary fluid has almost a constant temperature in the whole pool boiling area. Then, where phase change of the refrigerant occurs by evaporation, the secondary fluid temperature is significantly decreased depending on the operating conditions.

4.4.2 Overall heat transfer coefficient

In order to determine the overall heat transfer coefficient of the evaporator, as first approach could consist in defining the mean heat transfer coefficient at the refrigerant side as follows:

$$h_{\text{refr}} = \frac{1}{H} \int_0^H \frac{\dot{q}(z)}{T_w(z) - T_1(z)} dz \quad (4.9)$$

Where H is the total height of the evaporator. Then the following equation could be used:

$$\frac{1}{KS} = \frac{1}{h_{\text{refr}}S_{\text{refr}}} + \frac{1}{h_{\text{fs}}S_{\text{fs}}} + \frac{e}{\lambda S} \quad (4.10)$$

However, by this methodology, the refrigerant temperature inside the channel needs to be known. Besides, if the temperature of the wall and the temperature of the fluid are close (which is probably the case) the heat transfer coefficient will be artificially high and subject to very strong uncertainties.

Since four areas with apparently different heat transfer coefficients could be observed inside the evaporator (the area at the inlet of the channel where thermal equilibrium is reached between the refrigerant and the secondary fluid and where the entering bubbles collapse, the pool boiling area, the film evaporation area and the vapor area), another approach could consist in considering that the evaporator is composed of four different heat exchangers (numbered thereafter from 1 for the collapsing area to 4 for the vapor part) placed in series. This methodology is used thereafter.

In the apparent heat exchanger 4 (vapor area), correlations based on the Nusselt number could be used. According to the table of Kays and Crawford cited in Bergam *et al.* (2011), for flow in rectangular tube where the width of the channel could be considered as infinite with respect to the thickness of this one, in which only one side of the channel is heated and for which the wall temperature is constant, the value of the Nusselt number defined by the Equation (4.11) is equal to 4.86.

$$\text{Nu} = \frac{hD_h}{\lambda} = 4.86 \quad (4.11)$$

Although the wall temperature is not strictly speaking constant, but since thermodynamic equilibrium seems to be reached between the refrigerant and the secondary fluid in the vapor area once the flow is established, this configuration was chosen with respect to the constant heat flux configuration. Thus, using the equation 4.11 to estimate heat transfer coefficients on both sides of the evaporator and then 4.10 to estimate the overall heat transfer coefficient for the apparent evaporator located at the vapor area, the overall heat transfer coefficient K could be estimated to range from $10.6 \text{ W.m}^{-2}.\text{K}^{-1}$ to $11.0 \text{ W.m}^{-2}.\text{K}^{-1}$ depending on the operating conditions.

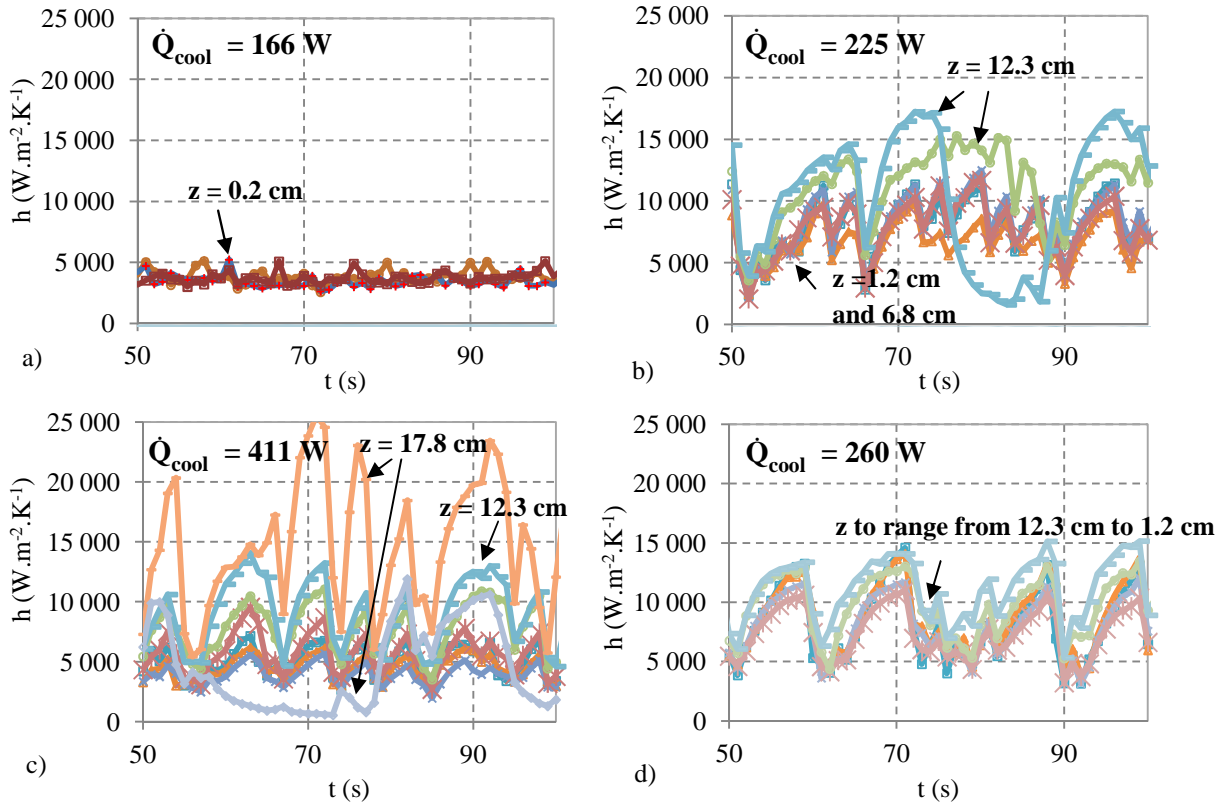
For the apparent heat exchangers 1 and 2 (liquid area constituted by the collapsing area and the pool boiling area), the temperature on both side of the apparent evaporators need to be known at each outlet and at each inlet of the heat exchangers considered in order to estimated the overall heat transfer coefficient K for each of them. With information available, one could think to gather the pool-boiling area and the collapsing area. However, heat transfer coefficients are not constant along these two areas and an inversion of the temperature is observed between the inlet and the outlet of these areas.

In the apparent heat exchanger 3, heat transfer coefficients depend on the thickness of the falling film. Heat transfer coefficients thus depend on the location along the plate and on the bubble frequency. The height of the heat exchanger depends on the height up to which the liquid is splashed for each bubble. All these parameters are linked to the operating conditions. Fig. 4.30 shows the evolution in time of heat transfer coefficients estimated for each thermocouple and for same running conditions but with different height of the liquid level (Fig. 4.30 a-b), same height of liquid level but with different inlet temperature of the secondary fluid (Fig. 4.30 b-c), and same height of the liquid level but with different operating pressure (Fig. 4.30 b-d). In this last case, the difference between the temperature set-point at the condenser ($T_{\text{cond}}^{\text{c,fs}}$) and the temperature set-point at the evaporator ($T_{\text{ev}}^{\text{c,fs}}$) is given at

9 K. The local heat transfer coefficients were calculated in the same manner as Chang *et al.* (2012), i.e. by using the following relation:

$$h = \frac{\dot{q}}{T_w - T_{sat}} \quad (4.12)$$

Where T_{sat} stands for the saturation temperature corresponding to the pressure detected at the outlet of the evaporator and \dot{q} is the heat flux estimated by means of the Fourier's law.



Location of the thermocouples (cm)

from the bottom:	from the free surface (z) for a)	from the free surface (z) for b), c), d)
5.2	0.2	-9.8
5.2	0.2	-9.8
5.2	5.7	-4.3
10.7	5.7	1.2
16.2	11.2	1.2
16.2	11.2	6.8
21.8	16.8	6.8
21.8	16.8	12.3
27.3	22.3	12.3
27.3	22.3	17.8
32.8	27.8	17.8
32.8	27.8	

Figure 4.30: Evolution in time of the heat transfer coefficients estimated for $T_{cond}^{c,fs} = 8.5\text{ }^\circ\text{C}$, $T_{ev}^{c,fs} = 17.5\text{ }^\circ\text{C}$ and
 a) $h_1 = 5\text{ cm}$; b) $h_1 = 15\text{ cm}$; for $h_1 = 15\text{ cm}$ and c) $T_{cond}^{c,fs} = 8.5\text{ }^\circ\text{C}$, $T_{ev}^{c,fs} = 22.3\text{ }^\circ\text{C}$; d) $T_{cond}^{c,fs} = 12.3\text{ }^\circ\text{C}$,
 $T_{ev}^{c,fs} = 21.3\text{ }^\circ\text{C}$

In the following section and on Fig. 4.30, distance noted z refers to the distance from the thermocouple to the free surface: $z < 0$ corresponds to a location below the free interface and $z > 0$ above it. The corresponding distances from the thermocouple to the bottom inlet of the channel are given on Fig. 4.30.

For the main part of the tests run, heat transfer coefficients estimated from the thermocouples in the film evaporation area increase when increasing the distance from the free interface. For example, on Fig. 4.30b, the highest heat transfer coefficient recorded is obtained for thermocouples located at $z = 12.3$ cm. This evolution of the heat transfer coefficients with the distance from the free surface is observed for each time step although at a certain time, the heat flux estimated at one of the two measurement areas located at $z = 12.3$ cm decreases significantly (the explanation of this phenomenon will be given thereafter). But heat transfer coefficients do not only vary with the distance from the free surface, they also vary with the time along a certain cycle. The heat transfer coefficients estimated at each thermocouple increase with the time until a time at which they suddenly decrease in less than 1 s. This cycle is repeated in an almost periodical manner depending on the location of the measurement and on the operating conditions.

Fig. 4.30a and b show that, as the height of the liquid level increases from $h_1 = 5$ cm to $h_1 = 15$ cm, both the maximal heat transfer coefficient estimated and the cooling capacity achieved increase. At the top of the liquid rivulet, the heat transfer coefficients vary from $5000 \text{ W.m}^{-2}.\text{K}^{-1}$ to $3200 \text{ W.m}^{-2}.\text{K}^{-1}$ for $h_1 = 5$ cm, and from $16800 \text{ W.m}^{-2}.\text{K}^{-1}$ to $1800 \text{ W.m}^{-2}.\text{K}^{-1}$ for $h_1 = 15$ cm. The difference between heat transfer coefficients obtained during these two tests is related to the thickness of the liquid film, hence on the frequency of bubbles and on the height up to which the liquid is splashed on the wall. Indeed, for $h_1 = 15$ cm, the height up to which the liquid is splashed is at least 13 cm and the bubble frequency 0.2 Hz. The liquid film could be partially evaporated and high heat transfer coefficients could be obtained. On the contrary for $h_1 = 5$ cm, at least 30 bubbles were observed in 8 s (3.75 Hz). The frequency of appearance of bubble is high and the area the film develops is often rewetted. Hence the thickness of the falling film remains relatively constant and thick. The heat transfer coefficients estimated for $h_1 = 5$ cm are thus lower than the heat transfer coefficients estimated for $h_1 = 15$ cm and vary slightly with time.

Same conclusion could be drawn for the other test runs: the overall cooling capacity achieved by film evaporation depends on the bubble frequency of appearance and on the distance between the top of the liquid rivulet and the free surface. However two others observations could be done:

- For a same location of thermocouples, various heat transfer coefficients could be estimated (Fig. 4.30c for $z = 17.8$ cm). This shows that the top of the liquid rivulet is probably located close to the location of these thermocouples. As the boundary of this rivulet is not a horizontal line and as the film begins to be evaporated on the edge of the rivulet, the thickness of the liquid film is not the same at the two locations of the thermocouples and thus, the heat transfer coefficients estimated is different. This figure also allows observing that, when the liquid film is fully evaporated, the heat transfer coefficients significantly decrease and reach a value similar to heat transfer coefficients calculated in the vapor part.
- Fig. 4.30d shows that the heat transfer coefficients achieved at the locations $z = 12.3$ cm and $z = 6.8$ mm are of the same order of magnitude and vary similarly. Visualization shows that during this test, the top of the rivulet is always situated between 1 cm and 4 cm above the

location of the thermocouples and that the liquid film never breaks. The wall is rewetted roughly every 5 s.

Contrary to what happens in falling film evaporator, the falling mass flow rate, and the distribution of liquid is not controlled. However by affecting the local value of heat transfer coefficient at the measurement spot to a certain area of the wall around this spot, space and time averaged heat transfer coefficients could be determined. From these estimated mean heat transfer coefficients and based on the Nusselt theory (cf. Chap. 1, section 1.6.1), a mean liquid film thickness δ could be evaluated. Table 4.12 gathers averaged values of the mean film thickness calculated, the mean heat transfer coefficients obtained during test shown on Fig. 4.30 as well as the K_3 obtained with Eq. 4.10. The cooling power obtained with these coefficients and using the ΔT_{LM} method is calculated. The cooling power achieved during the tests is shown as well as heat transfer coefficient calculated using Chang *et al.* (2012) correlation available for what the authors called “the intermittent region” (Table 4.12b).

Table 4.12: Cooling capacity obtained in the apparent evaporator 3 with a) the ΔT_{LM} method assuming an overall falling film heat transfer coefficient (h_3) b) using Chang *et al.* (2012) correlation (h_{Chang})

Test n°	h_3	δ	K_3	S_3	$K_3 S_3$	$\dot{Q}_{3,calc}$	\dot{Q}_{cool}	Relative difference
	(W.m ⁻² .K ⁻¹)	(μ m)	(W.m ⁻² .K ⁻¹)	(m ²)	(W.K ⁻¹)	(W)	(W)	(%)
1	6526	88	801	0.0334	26.8	213	225	5.5
2	5690	101	787	0.0312	24.6	226	261	13.3
3	7851	75	818	0.0340	27.8	201	283	29.0
5	3720	155	733	0.0200	14.7	124	166	25.1
8	6361	91	799	0.0300	24.0	186	244	24.0
9	6465	90	800	0.0260	20.8	166	218	23.9
10	4314	132	754	0.0245	18.5	155	186	16.8
13	8826	66	828	0.0355	29.4	223	260	14.1
15	6185	94	796	0.0320	25.5	333	393	15.3
17	7087	81	809	0.0470	38.0	403	411	1.9

a)

Test n°	h_{Chang}	KS_{Chang}	$\dot{Q}_{3,Chang}$	Relative difference
	(W.m ⁻² .K ⁻¹)	(W.K ⁻¹)	(W)	(%)
1	2656	680	180	19.9
2	2276	652	187	28.2
3	2550	672	165	41.6
5	2491	668	113	31.8
8	2420	663	158	35.2
9	2309	654	135	37.8
10	2345	657	135	27.5
13	2609	676	183	29.8
15	2641	679	168	57.2
17	2455	666	332	19.3

b)

The cooling power was calculated assuming that the refrigerant is at its saturation temperature at the inlet and outlet of the apparent heat exchanger 3. It is also assumed that the secondary fluid temperature at the inlet of the apparent heat exchanger 3 is almost the same as the temperature given at the inlet of the whole evaporator and that the temperature at the outlet of the heat exchanger 3 is close to the one measured at the outlet of the whole evaporator.

By this method, the overall heat transfer coefficient K_3 ranges from $733 \text{ W.m}^{-2}.\text{K}^{-1}$ to $828 \text{ W.m}^{-2}.\text{K}^{-1}$. With these coefficients, the cooling capacity achieved for the whole evaporator is predicted with an error of less than 30 %. Correlation developed by Chang *et al.* predicts lower and almost constant heat transfer coefficients for the film evaporation area (h_{Chang}). This induces a higher discrepancy between the measured cooling capacity and the cooling capacity calculated ($\dot{Q}_{3,\text{Chang}}$). However, this correlation was developed for an evaporator much smaller than the evaporator studied in the present study and phenomena must be quite different, especially regarding the thickness of the film. Moreover, in their study, the heat flux is imposed.

Whatever the studied case, the calculated cooling capacity depends significantly on the estimated height up to which the liquid is splashed. This height is to date determined experimentally. The next step is thus to understand driving phenomena resulting in a high projection of liquid above the free surface in order to be able to predict this height.

4.4.3 Dimensionless numbers

Previous sections show that the achieved cooling capacities depend mainly on the height at which the liquid is splashed above the free surface. In order to provide some first tools or guidelines for the design of low pressure evaporators, reflexions based on dimensionless numbers are proposed. The analysis is based only on results related to a channel thickness of 4 mm. This discussion is also helpful in order to find driving phenomena.

In order to have a significant amount of water splashed on the wall, a bubble needs to be generated. The influence of the boiling environment and of the operating conditions on the cooling capacity achieved must thus be taken into account with usual dimensionless number used to characterize the boiling environment such as the Jacob number:

$$\text{Ja} = \frac{\rho_1 C_p (T_{\text{ev}}^{\text{c,fs}} - T_{\text{sat}})}{\rho_v \Delta h_{\text{lv}}} \quad (4.13)$$

the Prandtl number :

$$\text{Pr} = \frac{\mu_1}{\rho_1 \alpha_1} \quad (4.14)$$

the Grashof number:

$$\text{Gr} = \frac{g \beta (T_{\text{ev}}^{\text{c,fs}} - T_{\text{sat}}) h_1^3 \rho_1^2}{\mu_1^2} \quad (4.15)$$

the Rayleigh number:

$$\text{Ra} = \text{Gr.Pr} \quad (4.16)$$

Or the Weber number:

$$We = \frac{\rho_l V_b [dR/dt]^2}{\sigma} \quad (4.17)$$

The Jacob number, often used when boiling heat transfer comes into play, is a number used to compare the amount of energy transferred by sensible heat and the amount of energy transferred by phase-change. Results obtained for this number are plotted on Fig. 4.31. The specific cooling capacity is defined as the ratio of the cooling capacity and the height of the surface wetted (pool boiling area + falling film area) named thereafter h_{wet} .

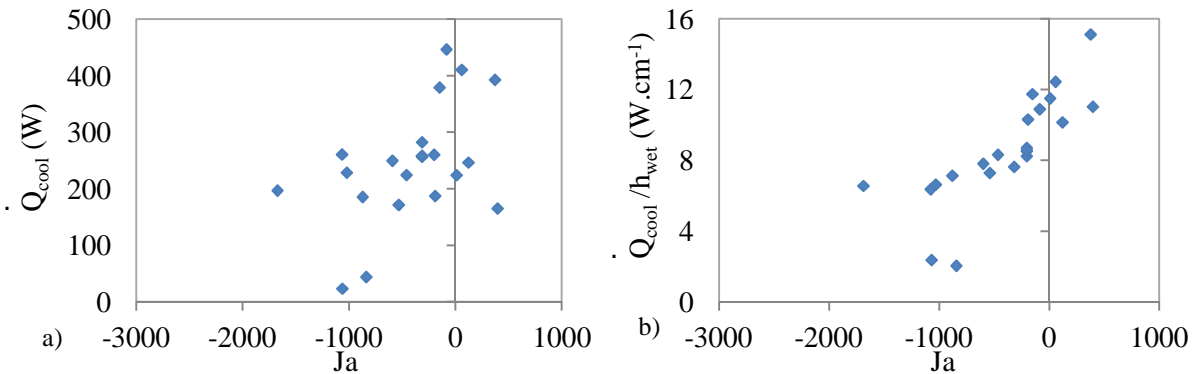


Figure 4.31: Evolution of a) the cooling capacity achieved and b) the specific cooling capacity achieved with the Jacob number

Properties of the water at its saturation temperature are taken at the bottom of the channel. The negative Jacob number is thus due to the fact that at the bottom of the channel, the liquid refrigerant is subcooled since thermal equilibrium is reached with the secondary fluid. The lower the Jacob number, the more subcooled the environment. For negative Jacob number on Fig. 4.31a and for all Jacob number investigated on Fig. 4.31b, the decrease of the cooling capacity with the decrease of the Jacob number thus means that in order to obtain the best cooling capacity/specific cooling capacity the liquid should not be significantly subcooled at the inlet of the channel. However, as observed on Fig. 4.31a, for a positive Jacob Number, the cooling capacity could be lower than the cooling capacity obtained for a Jacob number close to -300. This observation is in agreement with the conclusion made in section 4.3.2 which stipulates that the liquid should be slightly subcooled in order to obtain the best cooling capacity.

The Prandlt number is often used for studies involving boiling at low pressure. Indeed, literature shows that at subatmospheric pressure, hydrodynamic phenomenon are preponderant compared to thermal diffusion phenomena. This ratio is reflected by the Prandlt number (Fig. 4.32).

A slight decrease of the specific cooling capacity and of the cooling capacity with the Prandlt number is observed. This evolution of the (specific) cooling capacity with the Prandlt number means that the dynamic viscosity of the fluid shall not be too high compared to its thermal diffusivity. This means that the bubble growth should be mostly inertial rather than thermally-controlled, i.e. that the bubble growth should be rapid. The rapid growth of the bubble should result in a high height up to which the liquid is splashed. Indeed, as the height up to which the liquid splashed is induced by the splash of droplets due to the growth and the break of the interface of a large bubble, the amount of liquid splashed on the wall (and thus the cooling capacity achieved) should be linked to the kinetic energy of

the bubble growth transmitted to the droplets. The amount of liquid displaced by the bubble should also have an influence of the wetted area.

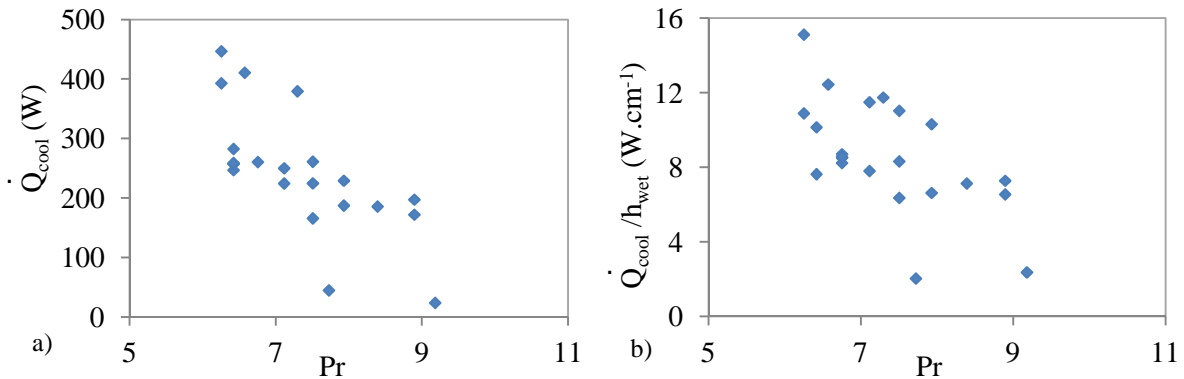


Figure 4.32: Evolution of a) the cooling capacity achieved and b) the specific cooling capacity achieved with the Prandtl number

Based on this analysis, the upward velocity of the bubble growth (dN/dt), the equivalent radius velocity (dR/dt – Fig. 4.33) and the bubble diameter just before its breaking for each test are studied. These three experimental characteristics of the bubble growth were estimated using a home-made image processing code developed under MATLAB® environment and inspired by the image processing code described in Chap 2, section 2.1.3.2.

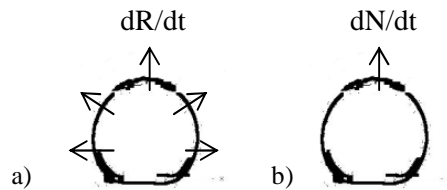


Figure 4.33: Schematic of the meaning of a) the equivalent radius velocity and b) the bubble growth upward velocity

No general trend of evolution of the cooling capacity with the bubble diameter or bubble growth velocity could be observed. The cooling capacity achieved or the specific cooling capacity achieved does not seem to be related to these parameters. These bubble dynamics characteristics were also inserted in Grashof, Rayleigh, Weber and Froude numbers but none of these numbers gave satisfactory results (cf. Appendix K).

The cooling capacity should nevertheless be linked to the bubble dynamics, that can sometimes be characterized by the product of the bubble frequency and the bubble equivalent radius. In that way, a slight trend of evolution of the cooling capacity and of the specific cooling capacity achieved with this product could be observed (Fig. 4.34).

If this product is inserted in the Froude number, a slight increase of the specific cooling capacity with the Froude number can be observed (Fig. 4.35).

Defined as Eq. 4.18, this number of Froude is linked to the ability of the fluid to wet the surface. The higher the Froude number, up to a higher location the evaporator is wetted and thus the better the specific cooling capacity achieved. When the Froude number increases, the wall is wetted to a higher location which should results in a higher cooling capacity. This effect is however not really significant in Fig. 4.35a.

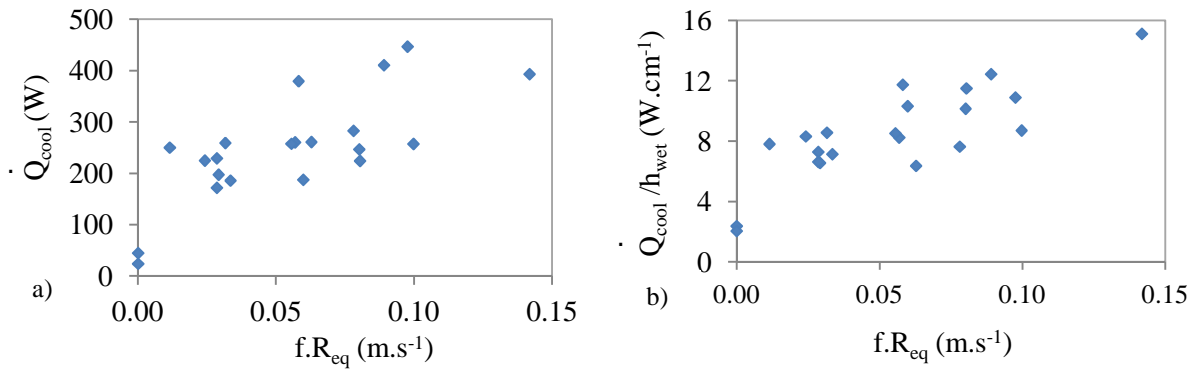


Figure 4.34: Evolution of a) the cooling capacity achieved and b) the specific cooling capacity achieved with the product bubble frequency by the bubble equivalent radius

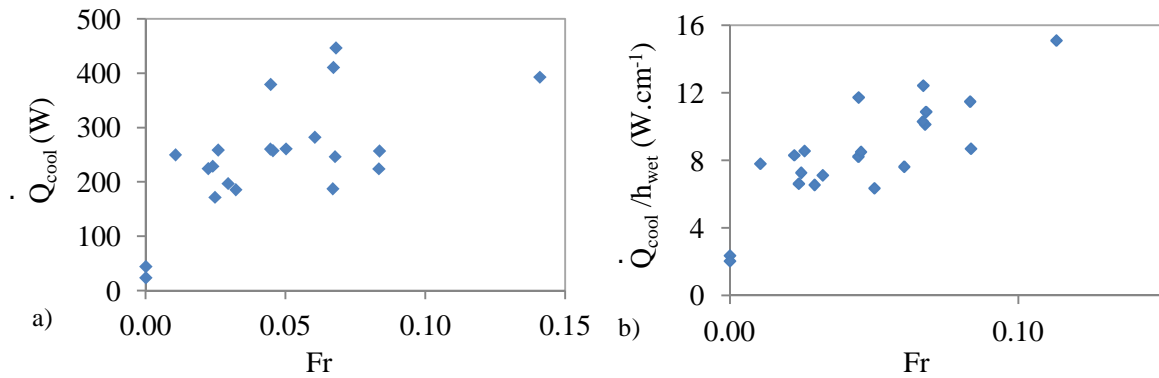


Figure 4.35: Evolution of a) the cooling capacity achieved and b) the specific cooling capacity achieved with the Froude number

$$Fr = \frac{f \cdot R_{eq}}{\sqrt{g \cdot h_{proj}}} \quad (4.18)$$

Beyond the dimensionless number studied above that give information on the evolution of the cooling capacity with thermophysical properties of water (Pr), boiling environment (Ja) and bubble growth characteristics (Fr), information regarding operating conditions should also be introduced. For that purpose, a new dimensionless number was developed:

$$P_{adim} = \frac{\rho_l g h_1}{P_{sat} + \rho_l g h_1} \frac{P_{sat}}{P_{triple}} \quad (4.19)$$

This dimensionless number is a product of two other dimensionless numbers. The first one gives the ratio of the hydrostatic pressure compared to the pressure at the inlet of the channel. It is linked to the subcooling degree of the environment at the refrigerant inlet. The second one compares how the operating pressure is far away from the triple point. The triple point is used as reference instead of the more common use of the critical pressure because the critical pressure is very far from the operating pressure which results in very small and not well significant values of P/P_{ref} . In addition, from a practical point of view, the triple point determines the limit of the operating pressure of the evaporator.

The combination of these two numbers ensures that one value of the combined number P_{adim} refers to one specific operating condition. Nevertheless, no trend is observed regarding the evolution of this number with the specific cooling capacity. It is however different when analyzing the evolution of the cooling capacity with this number (Fig. 4.36a).

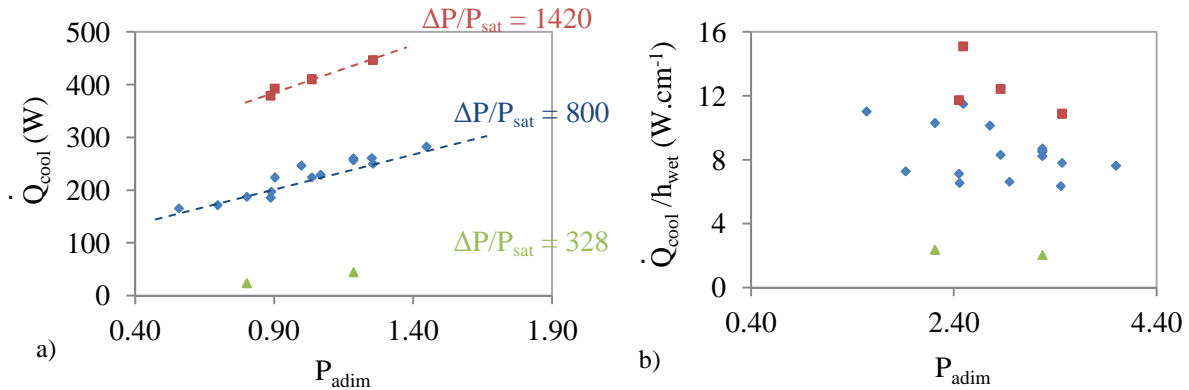


Figure 4.36: Evolution of a) the cooling capacity achieved and b) the specific cooling capacity achieved with the dimensionless pressure

The cooling capacity increases linearly with the increase of P_{adim} but three distinct y-intercepts are observed depending on the ratio $\Delta P/P_{sat}$. The higher the ratio, the higher the cooling capacity obtained for a given P_{adim} . Based on this result, the influence of ΔP and P_{sat} on the cooling capacity are analyzed separately (Fig. 4.37). As expected, the higher the driving pressure difference the higher the cooling capacity achieved (Fig. 4.37a) and generally, for a given $\Delta P/P_{sat}$, the higher the operating pressure the higher the cooling capacity achieved (Fig. 4.37b).

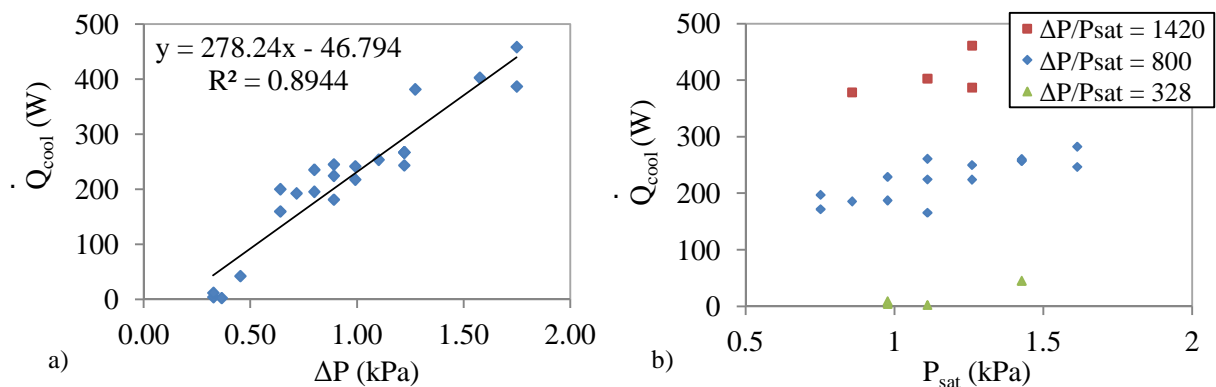


Figure 4.37: Evolution of the cooling capacity with a) the driving pressure and b) the operating pressure

As it was observed experimentally that the amount of water situated above the location of the large growing bubble impacts the height up to which the liquid is splashed, the evolution of the cooling capacity with a Bond number is also studied (Fig. 4.38). The Bond number used thereafter is defined as the ratio of height of the liquid level compared to the bubble diameter. As the bubble growth velocity must have an influence on the projection height it was chosen to use the length developed in Chap. 3 section 3.2.2 as the characteristic length. Thus, the Bond number used is defined as follows:

$$Bo = \frac{h_l}{\frac{u^2}{2g} + \sqrt{\left(\frac{u^2}{2g}\right)^2 + LC^2} + \frac{\mu u}{[(\rho_l - \rho_v)g]}} \quad (4.20)$$

With u a scaling velocity. This scaling velocity was chosen as the inertial velocity developed by Judd *et al.* (2004) and defined as Eq. 4.21.

$$u_i = \sqrt{\frac{4\sigma}{3\rho_l R_{cav}}} \quad (4.21)$$

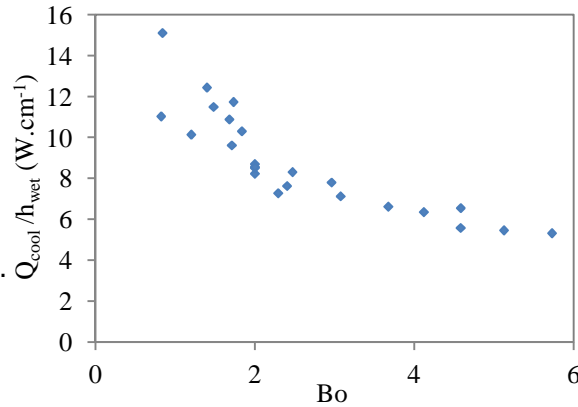


Figure 4.38: Evolution of the specific cooling capacity achieved with the Bond number

The general trend thus observed is a decrease of the specific cooling capacity with the increase of the Bond number. A change in the slope is observed for a Bond number of 2. This might suggest that there are two areas governed by different mechanisms. Further investigations must be done in order to validate or not this assumption.

Lastly, in an attempt to develop dimensionless correlations, the Vaschy-Buckingham theorem was used. Thanks to this theorem, two dimensionless cooling capacities were defined. The first one is based on a number close to the Figure of Merit ($Me = \frac{\rho_l \sigma \Delta h_{lv}}{\mu_l}$) proposed by Chi (1976) in the context of capillary heat pipes.

$$\dot{Q}_{cool,adimv} = \frac{\dot{Q}_{cool}}{h_{wet} W_{ev}} \frac{\mu_l}{\rho_v \sigma \Delta h_{lv}} \quad (4.22)$$

Fig. 4.39 shows the evolution of this dimensionless cooling capacity with the ratio of the operating pressure by the pressure at the triple point. A decrease of the dimensionless cooling capacity with the working pressure is observed for the main part of the experimental points.

The second dimensionless number is defined as follows:

$$\dot{Q}_{adim} = \dot{Q}_{cool} \frac{\rho_v}{\mu_l \sigma} \quad (4.23)$$

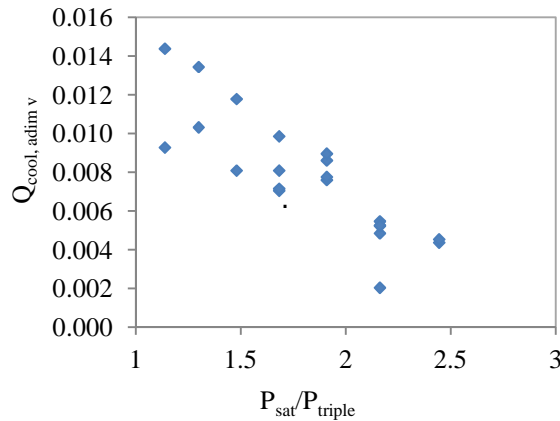


Figure 4.39: Evolution of dimensionless cooling capacity achieved with the ratio P_{sat}/P_{triple}

These properties were chosen to develop this number because the lower the vapor density, the larger the bubble and the higher the liquid film area. But this growth will be refrained by the surface tension and the liquid viscosity.

The evolution of this dimensionless capacity with the modified Jacob number per the ratio P_{sat}/P_{triple} is shown on the Fig. 4.40 for a thickness of the channel of 2 mm and 4 mm.

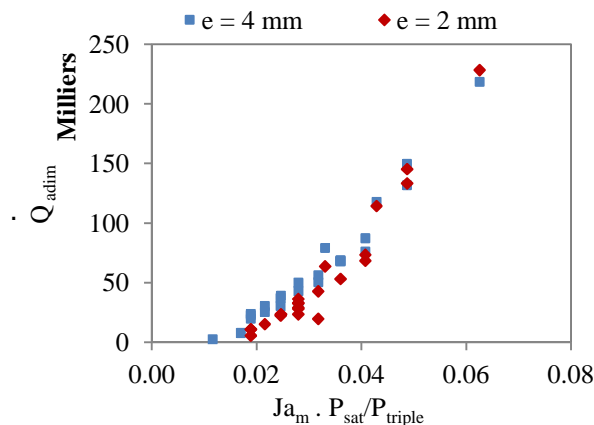


Figure 4.40: Evolution of dimensionless cooling capacity achieved with the modified Jacob number per the ratio P_{sat}/P_{triple}

The modified Jacob number being defined as follows:

$$Ja_m = \frac{C_{p_l} (T_w - T_{sat})}{\Delta h_{lv}} \quad (4.24)$$

A significant increase of this second dimensionless cooling capacity with the modified Jacob number per the working pressure is observed both for $e = 4$ mm and for $e = 2$ mm.

To continue these reflexions, experiments must be done with different working fluids. Indeed, by changing the working fluid, the thermophysical properties of the refrigerant will change, therefore impacting the value and the evolution of the dimensionless numbers studied.

Conclusion

An experimental setup working as a pump-assisted closed-loop thermosyphon was designed and built. It allows the observation of the water vaporization inside a channel of a smooth plate-type heat exchanger (0.2m width x 0.5 m height) in conditions that might occur in sorption chillers. During the experiments conducted, three main flow regimes were observed:

- a first regime characterized by the appearance and quick collapse of bubbles of few centimeters size at the inlet of the channel;
- a second boiling regime characterized by the periodic appearance of a large bubbles of several centimeters. When these bubbles surge out, droplets are splashed on the wall and a liquid film is created. Evaporation immediately takes place.
- a third regime during which boiling takes place almost continuously: the small bubbles observed at the bottom do not collapse but continue growing and splash liquid on the wall.

During the first flow regime, the cooling capacity measured was almost null. For the two latter regimes, different working areas were identified: a pool boiling area, a film evaporation area and a vapor area. The cooling capacity achieved is mainly due to the evaporation of the liquid film formed by the splashing of droplets in the film evaporation area. The higher and thinner the liquid film created, the higher the cooling capacity achieved (up to $25 \text{ kW}\cdot\text{m}^{-2}\cdot\text{K}^{-1}$). It was shown that the overall heat transfer coefficients obtained in this part allows to predict the overall cooling capacity achieved with a maximum relative difference of 30 %.

A design of experiments (DOE) has been established and checked. With the experimental setup employed, cooling capacities from 0 to 503 W were measured for a thickness of the channel of 2 mm and 4 mm. Thanks to the exploitation of the mathematical model obtained, optimal points under different constraints were found. A maximum cooling capacity of $553 \pm 30 \text{ W}$ in the entire experimental field was predicted. Factors impacting the cooling capacity were also identified: the weightiest factors are the temperature difference between the evaporator and the condenser and the operating pressure (temperature set at the condenser). These two parameters are linked to the driving pressure difference. The existence of an optimal height of the liquid level depending on the operating conditions was also shown.

The evolution of the cooling capacity achieved for $e = 4 \text{ mm}$ with several dimensionless numbers was also analyzed in order to find driving phenomena and, in the end, to be able to design properly low pressure heat exchangers. This analysis was particularly useful to complete the conclusions drawn from visualization and from the use of the mathematical model. It has been shown that the cooling capacity depends slightly on the Prandtl number, on the Jacob number, on the Froude number and on a Bond number. A dimensionless number linked to the ratio of the hydrostatic pressure and the pressure at the inlet of the channel was developed in order to take into account the evaporator operating conditions. This number allows to indicate how far the operating pressure is from the triple point and thus the limit of the evaporator operating conditions. The ratio of the driving pressure to the operating pressure and this dimensionless number have a significant influence on the cooling capacity achieved. The evolution of two dimensionless cooling capacities with for the first one the ratio $P_{\text{sat}}/P_{\text{triple}}$, and for the second one a modified Jacob number were also plotted. Further investigations should be done in order to find other relevant dimensionless numbers and, in order to to this, experiments should be realized with different working fluids.

5 PRELIMINARY EXPERIMENTAL INVESTIGATION OF WATER BOILING PHENOMENA IN A THIN LIQUID LAYER

As exposed in the previous chapter, a major part of the cooling capacity obtained in the channel of the evaporator is due to the evaporation of a liquid film due to the splashing of droplets on the evaporator wall. A bubble surges out of the free interface and the double vapor-liquid-vapor interface of the bubble breaks, forming these droplets.

The objective of this chapter is to observe the breaking of the bubble and the formation or not of droplets from a more fundamental point of view. Thus, the boiling phenomenon in a liquid layer of thickness ranging from 3 mm to 200 mm at subatmospheric pressure which can typically occur in evaporators of absorption or adsorption systems using water as refrigerant is studied. The liquid height chosen for this study can be lower than the diameter of the bubble, which allows the bubble to surge out of the interface. This configuration could be also representative of flooded evaporators. A high-speed camera is used to study the bubbles dynamics (section 5.1). A breaking of the bubble at the vapor-liquid-vapor interface can be observed or not. In the latter case the bubble keeps growing until having a diameter up to 150 mm. Boiling curves at 1.2 kPa for different liquid layer thicknesses are also presented in order to study the influence of experimental conditions on the heat transfer (section 5.2).

5.1 Visualization: the occurrence of two typical behaviors

All the results shown and discussed thereafter were obtained with the experimental setup introduced in section 2.1. The boiling thus takes place on a horizontal plane surface.

Visualization and experiments were conducted at a vapor pressure of 1.2 kPa and 3 kPa for a height of the liquid level above the heated surface varying from 3 to 200 mm. During these experiments, two main different behaviors were observed: a breaking of the double vapor-liquid-vapor interface during the growth of the bubble or the creation of a vortex at the top of the bubble. Fig. 5.1 shows a typical bubble growth dynamics in this first case; Fig. 5.2 is for the second case.

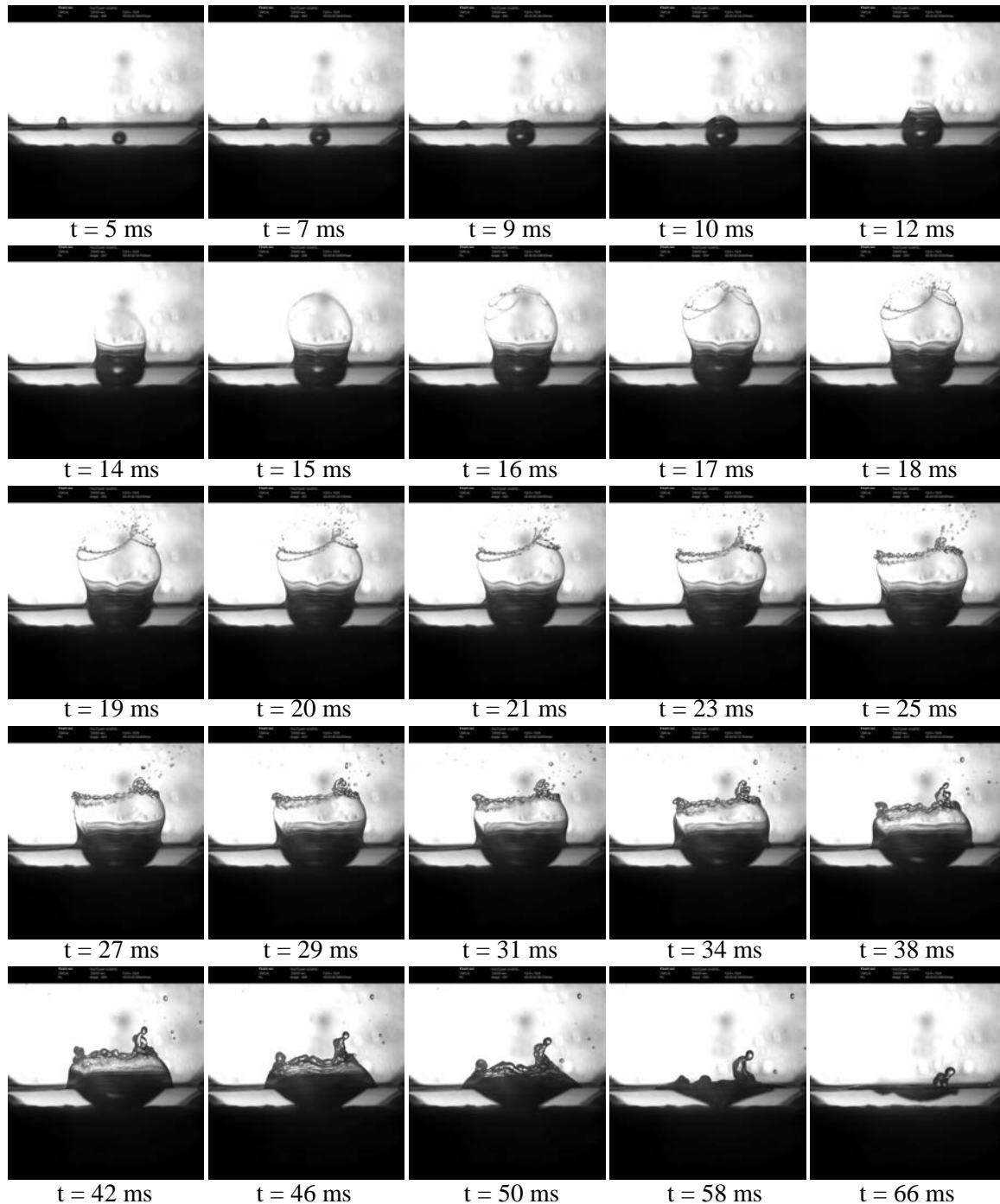


Figure 5.1: Bubble growth in a liquid layer of 3 mm with a breaking of the bubble at the interface liquid/vapor ($P_v = 3 \text{ kPa}$, $T_1 = 24 \text{ }^\circ\text{C}$, $h_1 = 3 \text{ mm}$, $\dot{q} = 1.6 \text{ W.cm}^{-2}$)

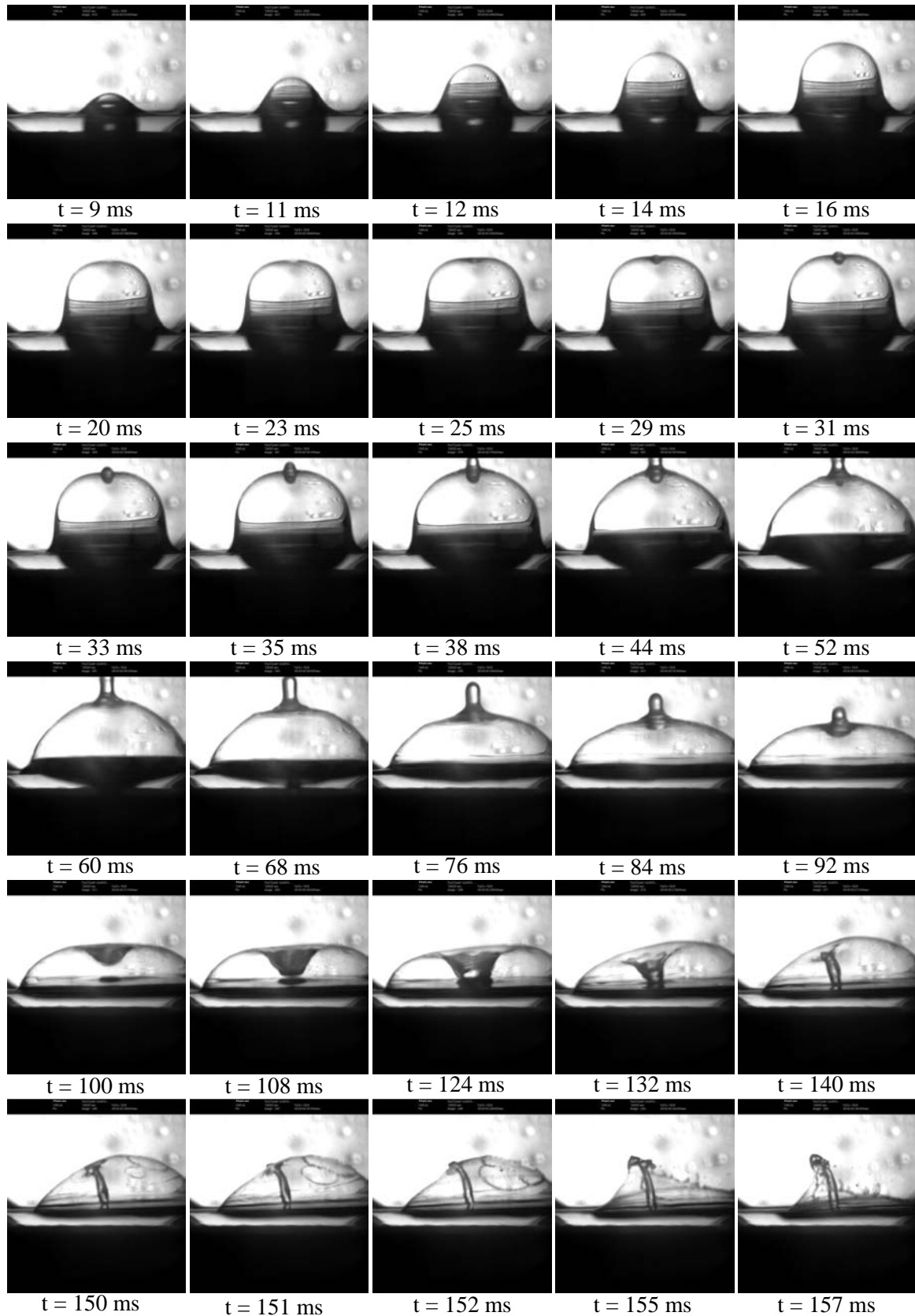


Figure 5.2: Bubble growth in a liquid layer of 3 mm with thick top of the bubble falling down its center ($P_v = 3 \text{ kPa}$, $T_l = 24 \text{ }^\circ\text{C}$, $h_l = 3 \text{ mm}$, $\dot{q} = 1.6 \text{ W.cm}^{-2}$)

In the first case, the bubble starts growing until reaching the free surface 9 ms after the beginning of its growth. As the free surface is reached, the bubble keeps growing, which forms a double vapor-liquid-vapor interface. This double interface is elongated until its breaking at different spots at the same time ($t = 16$ ms). Even when and after the double interface breaks, the bubble keeps on growing.

The bubble grows faster in the vapor than in the liquid part. This confers to the bubble a particular shape with a restricted horizontal radius at the free surface from 14 ms to 25 ms. The kinetics of the bubble growth seems to be faster than the kinetics of the thermocapillary effect, which confers this particular shape to the bubble and which leads to the breaking of the double interface.

Gong *et al.* (2013), studying the boiling phenomenon in similar configuration (on a heater surface with an artificial cavity and using water as working fluid) observed that the bubble sticks the heater surface for a relatively long period with respect to what is observed during boiling in a layer of thickness larger than the bubble departure diameter. The authors explained this behavior by the fact that, as the water layer thickness is smaller than the bubble diameter, the buoyancy force which helps to lift the bubble is decreased. Despite the fact that in this study the bubble diameter is larger than the water layer thickness, not such phenomenon was observed: the bubble foot remains attached to the heated surface during a similar or even shorter period than observed in the Chap. 2. This could be due to the force balance at subatmospheric pressure: the decrease of the buoyancy force could not have an influence as significant as at atmospheric pressure. Further investigation must be done in order to understand the influence on each force on the bubble growth at subatmospheric pressure and validate or not this assumption.

As indicated previously, another behavior of the bubble dynamics under exactly same running conditions can be observed (Fig. 5.2). During the 16 first milliseconds of the growth, the bubble behavior is the same as in the previous case. The bubble first exhibits a hemispherical shape and then, after 8 ms, as the bubble reaches the free surface, the vertical diameter of the bubble becomes larger than the horizontal one. However, at 16 ms no breaking of the double vapor-liquid-vapor interface is observed. The bubble keeps growing until its top starts to be flattened ($t = 20$ ms). The aspect ratio (ratio of bubble height to bubble horizontal diameter) is close to 1.33. Within the next 5 ms, the bubble height remains constant while the horizontal diameter is getting larger and larger, so that the aspect ratio decreases from 1.33 to 0.9. Meanwhile, a volume of liquid is formed at the top of the bubble. This "pocket" of liquid grows symmetrically on both sides of the double interface, i.e. on the vessel vapor side and on the bubble vapor side. Then, the pocket grows upwards and only on the vessel vapor side (33 ms to 60 ms). At 60 ms, the bubble detaches, the horizontal diameter of the bubble is maximal and the liquid pocket reaches its highest level. As the double interface cannot be fed with liquid anymore, the pocket stops its growth. Then, the liquid contained in the pocket falls down due to the gravity and, simultaneously, the bubble condenses. At 148 ms, a breaking at the double vapor-liquid-vapor interface of the bubble is observed. Then, the interface breaks at different other spots. The fluid remained in the liquid state falls into the liquid pool.

The flattened shape observed at 20 ms could be explained as the coldest area is situated at the top of the bubble. A balance is reached between the growth of the bubble and its condensation. Other phenomena like the growth of the bubble without a breaking in its interface and the appearance of the pillar of liquid at the top of the bubble could be due, for the main part, to the Marangoni effect. Indeed, due to the difference of liquid conditions between the liquid close to the boiling surface and the liquid close to the free surface, the Marangoni effect is enhanced. The change in the surface tension around the bubble curvature has as a consequence a pumping of the liquid from the base to the top of the bubble. The evaporation of the vapor/liquid interface of the bubble could be balanced by the

condensation and the feed of liquid due to the thermocapillary effect. As liquid moves from the base to the top of the bubble, the top is the place where the liquid converges. Due to the motion of liquid and its jointure at the top, a vortex is created explaining the singularity observed.

A surprising bubble curvature can be observed at the free interface during the growth of the bubble (mainly from 11 to 35 ms). This discontinuity of bubble curvature is however probably due to a mirage effect (strong changes in refraction index induced by temperature gradients and by the liquid-vapor discontinuity).

Fig. 5.3 shows the growth of a bubble in a liquid layer of 7 mm. The heat flux imposed is much greater (17.8 W.cm^{-2} vs. 1.6 W.cm^{-2}) and the vapor pressure is more than twice lower than for Figs. 5.1 and 5.2. Due to the difference in the liquid height, the difference in the pressure conducting to a difference in the surface tension, and the difference in the imposed heat flux between the two cases, the Marangoni effect is more significant in this latter case. As a matter of fact, the double interface is thicker and it is more visible that the top of the bubble is fed with liquid. The growth velocity of the liquid pocket is slower than previously and the top of the pocket reaches a lower height before falling down. This is probably due to a balance between the weight of the liquid and the kinetic energy inducing the vortex. The growth of the bubble along the horizontal axis is also limited, so that the minimum aspect ratio estimated before the bubble condenses is 0.95. Nevertheless, the global shape remains similar to the one observed in Fig. 5.2.

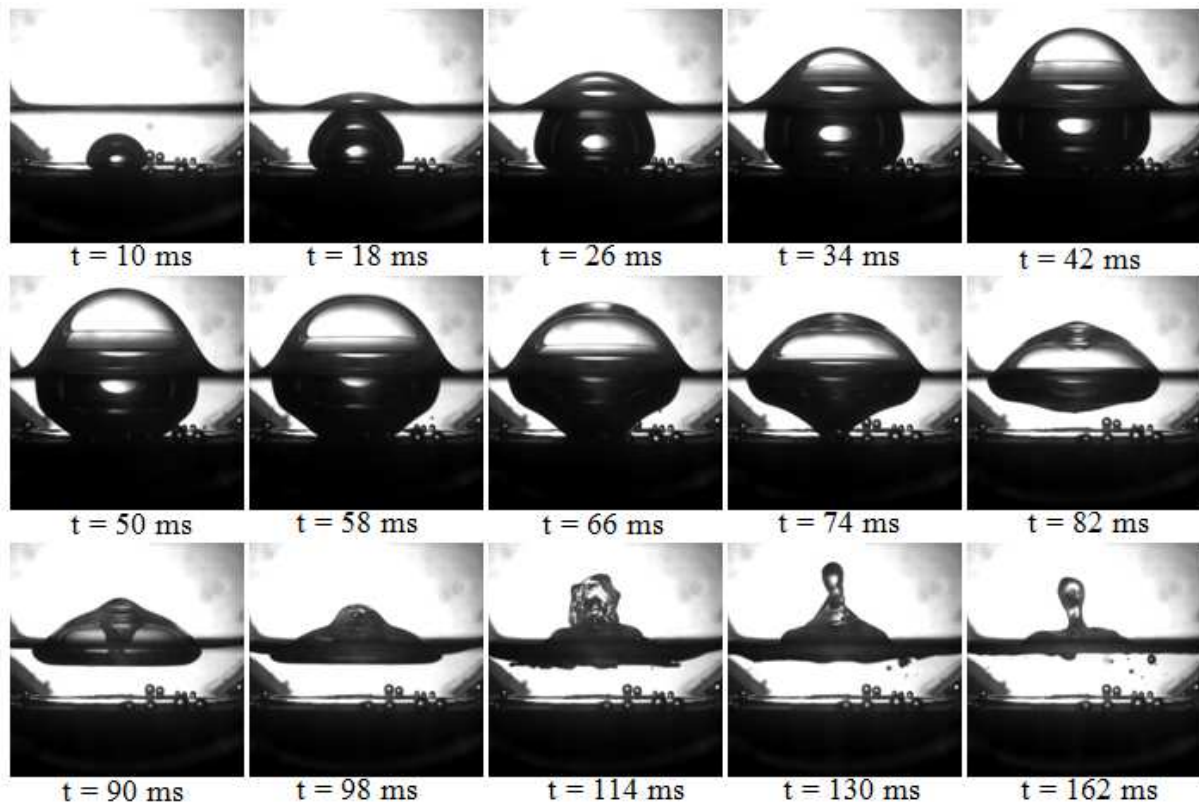


Figure 5.3: Bubble growth in a liquid layer of 7 mm without breaking of the bubble ($P_v = 1.25 \text{ kPa}$, $T_l = 10 \text{ }^\circ\text{C}$, $h_l = 7 \text{ mm}$, $\dot{q} = 17.8 \text{ W.cm}^{-2}$)

5.2 Experimental boiling curves

Boiling curves for different heights of the liquid level ranging from 3 mm to 200 mm are plotted in Fig. 5.4. These boiling curves are plotted as the evolution of the instantaneous heat flux vs. instantaneous wall superheated. Each points is monitored every 3 s during 10 min once an overall steady-state inside the vessel is obtained.

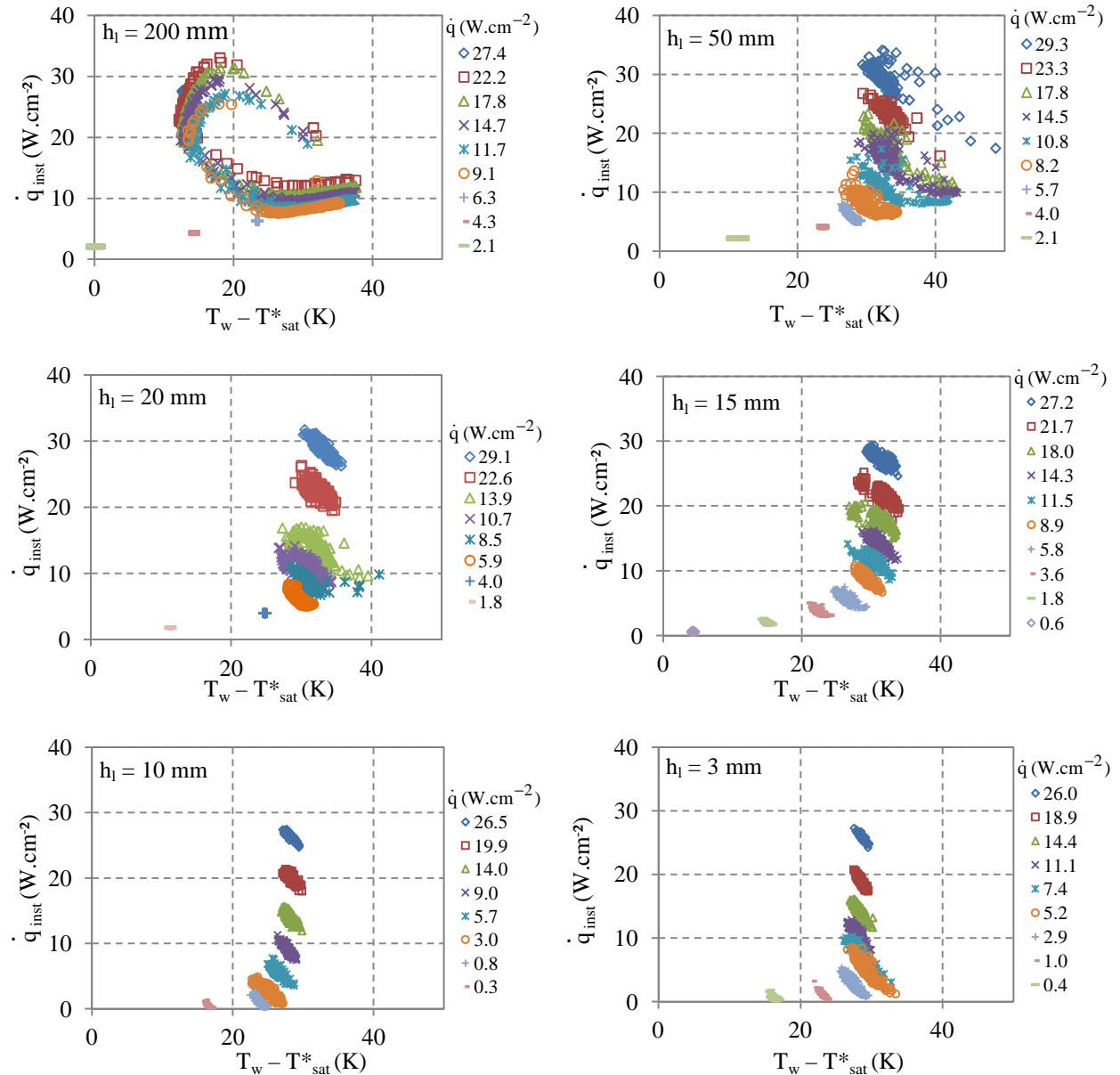


Figure 5.4: Boiling curves for $P_v = 1.2$ kPa and a) $h_l = 200$ mm, b) $h_l = 50$ mm, c) $h_l = 20$ mm, d) $h_l = 15$ mm, e) $h_l = 10$ mm, f) $h_l = 3$ mm

At 200 mm, for each imposed heat flux, the boiling regime observed is either natural convection, fully developed boiling or the specific regime named "cyclic boiling" that was described in Chap. 2. However, as the water liquid layer diminishes, the cyclic boiling regime is less and less pronounced. The amplitude of wall temperature fluctuation is smaller. As explained in Chap. 2, this is probably due to the fact that the far field liquid bulk cannot circulate as easily as it could with higher water level and thus the heating surface cannot be rewetted by cold liquid (McGillis *et al*, 1991a). Another explanation

is that, as the liquid height decreases, the difference between the vapor pressure and the pressure at the surface level decreases as well. Thus, the liquid in the pool is less and less subcooled compared to the saturation temperature at the surface level.

As this boiling regime is less apparent, periods of high and low heat transfer coefficient are less and less observed. The instantaneous value of the heat transfer coefficient (for a given imposed heat flux) is more and more constant along the time as the liquid height diminishes.

Conclusion

Experiments of pool boiling in a liquid layer of limited thickness were conducted for a vapor pressure of 1.2 kPa and 3 kPa and for a liquid height ranging from 3 mm to 200 mm. During the growth of the bubble, a breaking of the double vapor-liquid-vapor interface could be observed. If the bubble has time to grow without any breaking, the liquid/vapor interface of the bubble becomes thicker at the top due to the thermocapillary motion. As the liquid arrives from the base to the top of the bubble by every way possible and with a sufficient velocity, a vortex is formed. When the amount of liquid becomes too heavy, the liquid falls down at the center of the bubble. By increasing the thickness of the water layer, the thermocapillary effect is enhanced and the double interface becomes thicker. The vortex has less time to be formed and thus, the singularity at the top of the bubble is less pronounced.

Boiling curves were also plotted to analyze the heat transfer in such conditions. As the layer thickness decreases, the so-called "cyclic boiling" regime that is well observed at 200 mm is less and less likely to occur: as a matter of fact, it is more and more difficult for the far field liquid to move to the surface and rewet it; in addition, the bulk surrounding liquid is less subcooled. Lastly, when reducing the liquid layer thickness, the instantaneous value of the heat transfer coefficient (for a given imposed heat flux) is more and more constant along the time.

CONCLUSION AND PERSPECTIVES

Synthesis

Knowledge on water vaporization under conditions that might occur in evaporators used in sorption chillers using water as refrigerant is of fundamental importance in order to be able to design properly compact low pressure evaporator and to make competitive this environmentally-friendly technique. Water boiling and more generally water vaporization at low pressure was studied in the present thesis both from a fundamental point of view (experiments conducted at the bubble scale) and from a more applicative point of view (experiments conducted at the scale of the plates of a plate-type evaporator). The following conclusion could be drawn:

A first experimental setup has been designed and built in order to observe pool-boiling water behavior at a pressure down to 0.8 kPa. As the specificity of low pressure pool boiling lies in the non homogeneity of the boiling environment, the influence of the hydrostatic pressure on the boiling environment was discussed. Since the hydrostatic pressure is of the same order of magnitude as the vapor pressure, the boiling environment is highly subcooled. Varying the height of the liquid level and/or the vapor pressure allow to vary the local saturation pressure, the maximal subcooling degree and the subcooling gradient. All these parameters are mutually dependent. This unusual environment has noticeable influence on the bubble size and on the bubble growth.

First, water pool boiling in horizontal orientation was studied. Bubbles with centimeter size and particular shape of mushroom were observed. As mentioned in the literature, the size of these bubbles increases when decreasing the pressure. However, it was shown that this increase in the bubble detachment diameter holds only down a pressure of about 1.8 kPa. Below that pressure, the effect of the large subcooling degrees that are encountered in such conditions is no more counterbalanced by the evolution of the thermophysical properties (especially the decrease of the vapor density).

Boiling curves for pressures ranging from 0.8 kPa to 100 kPa were also plotted. Since significant fluctuations of the wall superheated in certain conditions of imposed heat flux were observed, these curves were plotted as the instantaneous heat flux vs. the instantaneous wall superheat for a given heat flux imposed at the heater. Same kind of boiling curves were plotted for a vapor pressure of 1.2 kPa and height of the liquid level of 200 mm, 150 mm and 100 mm. By analyzing these curves, the occurrence of a boiling regime specific to the subatmospheric pool boiling was highlighted. This regime was named "cyclic boiling regime". During this regime, fluctuations of the wall temperature can reach 20 K. The heat transfer coefficient is thus severely affected with respect to the usual fully-developed nucleate boiling. This regime is less and less pronounced as the height of the liquid level diminishes, probably because of the decrease of the subcooling degree when decreasing the height of the liquid level.

Then, in order to be closer to a plate-type heat exchanger configuration, water pool boiling in vertical configuration first without and then with confinement was studied. In free boiling, boiling curves for different vapor pressures and heights of the liquid level were plotted and compared with those obtained in horizontal configuration. The cyclic boiling regime observed in horizontal orientation was also observed during visualization but the boiling curve shape characteristics of this regime was less significantly observed. It was also shown that the vapor pressure has a negligible influence on the heat transfer whereas a decrease of the height of the liquid level for a given pressure significantly improves

Conclusion

heat transfer. This is due to the balance between heat transfer mechanisms in vertical orientation and phenomena due to subcooling of the environment. As the pressure decreases, the boiling environment is more subcooled but bubbles formed are larger. The evaporation of the microlayer is fostered and the convective effects due to the wake-induced flow are higher. Phenomena due to the subcooling degree of the environment and phenomena due to the bubble shape and growth are balanced. On contrary, for a given vapor pressure, when the height of the liquid decreases, the local pressure decreases as well as the subcooling degree of the boiling environment. Bubbles are larger and the subcooling is lower. Both phenomena induce a decrease of wall superheat required to set boiling on.

During the study of boiling in vertical orientation with confinement, boiling curves for different channel thicknesses and for a pressure ranging from 1.2 kPa to 5 kPa were plotted and analyzed. As the pressure and the channel thickness decrease, the occurrence of the cyclic boiling regime was observed. The same characteristic shapes of the boiling curves like the ones obtained in horizontal orientation were obtained and the same conclusion could be drawn: the cyclic boiling regime is responsible for a degradation of the heat transfer. It was shown that the influence of the pressure on the heat transfer is not significant when this regime is not set on. Beyond the effect of the boiling regime, experiments with high speed PIV were conducted in order to highlight the influence of the wake-induced flow for very narrow channels. An increase of the velocity of the liquid feeding the channel was shown when decreasing the thickness from $e = 4.44$ mm to $e = 2.24$ mm and for a vapor pressure of 1.8 kPa. The significance of the Bond number, often used in studies of boiling in confined space, was also discussed since in the present operating conditions the capillary length and the channel thickness were of a few millimeters while the bubble diameter could reach up to 15 cm.

The second experimental setup allows the observation of the water vaporization inside a channel of a smooth plate-type heat exchanger (0.2m width x 0.5 m height) in conditions that might occur in sorption chillers (working pressure ranging from 16 kPa to 0.85 kPa, secondary fluid temperature ranging from 10.9 to 23.1 °C, filling ratio ranging from 1/2 to 1/10 of the whole channel height). The methodology of the design of experiments was followed in order to find conditions which yield the maximal cooling capacity under a given set of constraints. This methodology was followed for a thickness of the channel equal to 2 mm and 4 mm. During these experiments three main flow regimes were observed:

- a first regime characterized by the appearance and quick collapse of bubbles of few centimeters size at the inlet of the channel;
- a second boiling regime characterized by the periodic appearance of a large bubbles of several centimeters which, while they grow, push the surface up and are responsible for splashing droplets on the wall. A liquid film is thus created and evaporation immediately takes place. Appearance and quick collapse of smaller bubbles are still observed at the bottom of the channel;
- a third regime during which boiling takes place almost continuously: the small bubbles observed at the bottom do not collapse but continue growing and splash liquid on the wall.

During the first flow regime, the cooling capacity measured was almost null. For the two latter regimes, different working areas were identified: a pool boiling area, a film evaporation area and a vapor area. It was shown that the cooling capacity achieved is mainly due to the evaporation of the liquid film formed by the splashing of droplets in the film evaporation area. The higher and thinner the liquid film created, the higher the cooling capacity achieved. Cooling capacity ranging from 0 to 503 W were measured and conditions to obtain the best cooling capacity were determined. Experimental factors having a significant influence on the cooling capacity were identified. It was

shown that the factor that links to the operating pressure and the driving pressure is the weightiest factor. It was also shown that an optimal filling ratio exists and that a thickness of a channel of 4 mm should be favored.

Finally, an overall heat transfer coefficient was estimated. Because film evaporation is the predominant phenomenon for heat transfer, considering solely the fraction of the plate where film evaporation takes place for the calculation of the overall heat transfer coefficient allows to predict the overall cooling capacity with a maximal relative difference of 30 %. In order to provide some first tools or guidelines for the design of low-pressure evaporators, reflexions based on dimensionless numbers were also proposed. It was shown that the cooling capacity depends slightly on the Prandtl number, on the Jacob number, on the Froude number and on a Bond number. A dimensionless number based on the ratio of the hydrostatic pressure and the pressure at the entrance of the channel was developed in order to take into account the evaporator operating conditions. The ratio of the driving pressure to the operating pressure and this dimensionless number have a significant influence on the cooling capacity achieved.

Lastly, since it was shown that the cooling capacity achieved is to a major extent linked to the height up to which the liquid is splashed, a fundamental study about water boiling phenomena in a liquid layer was started. Such a configuration gives birth to bubbles with a membrane-type boundary (i.e. a double vapor-liquid-vapor interface). This preliminary study highlighted two mains different behavior likely to occur (with a certain stochastic character) in such operating conditions. On the one hand, while the bubbles grow, a breaking of the double vapor-liquid-vapor interface could be observed or not. If the bubble has time to grow without any breaking, the liquid/vapor interface of the bubble becomes thicker at the top due to the thermocapillary motion. Since the liquid arrives from the base to the top of the bubble by every way possible and with a sufficient velocity, a vortex is formed. The formation of this vortex could be more or less pronounced depending on the layer thickness.

Perspectives

In order to continue the present work and have a better understanding of low pressure vaporization phenomena, several actions could be taken. They are suggested below:

- Same experiments could be realized with other working fluids. At the bubble scale, changing the working fluid should allow to understand and highlight the role of dynamic forces in the bubble growth and detachment process. As, to the author knowledge, nearly no correlation is available in the literature for such pressures range, these experiments could help in the development of such correlations (either for the bubble growth, the bubble departure diameter or heat transfer correlations). Vaporization of different fluids inside the channel of the evaporator should also allow highlighting driving phenomena and help go further in our attempts to develop correlations to design properly low pressure evaporators since the fluid nature obviously influences the value and the evolution of dimensionless numbers with operating conditions.
- Still using water as working fluid, efforts could be done to develop flow patterns maps. In the pool boiling configuration, these map could help understand and apprehend when the cyclic boiling regime would occur. As similar cyclic boiling regime was observed during experiments conducted in the channel of the plate-type heat exchanger, this knowledge could be also really helpful in the determination of the range of operating conditions for low-pressures evaporators. A flow pattern map specific to the vaporization of water inside the

channel could be also drawn in that purpose. Indeed, the operating conditions should favor the creation of the liquid film but the refrigerant should not leave the evaporator without being evaporated. The height of the evaporator should thus be a parameter of the map to give information on the entrainment of droplets.

- To pursue the reach for optimal operating conditions, a third parameter to apprehend is the waiting time between successive bubbles. Predicting this waiting time could be of fundamental importance as, like observed in our experiments, a too high bubble frequency leads to a thick film and thus to a medium heat transfer coefficient whereas a too low bubbles frequency leads to a noticeable decrease of the heat transfer coefficients. McGillis *et al.* (1991a) already proposed a correlation. Further investigation could be done in order to validate or not results obtained with this correlation and proposed correlation available for plate-type heat exchanger.
- The influence of the channel geometry and of the surface could be also analyzed. A first idea could be to study the influence on the cooling capacity (and more specifically on the film evaporation) of a surface where vertical and/or horizontal bends would be disposed. Since there is a change in curvature between two bends, the resulting capillary pressure could be high and thus a motion of the fluid by capillarity should be observed. Since the film could be thinner in some spot, the heat transfer coefficient could be enhanced.
- Lastly, it could be of interest to study the dynamics of water bubble at the bubble scale, but with a secondary fluid as the thermal load. As a matter of fact, using a secondary fluid as the heat source would better represent the actual thermal conditions prevailing in evaporator: these conditions are neither imposed heat flux nor imposed temperature. The impact of the conditions for the onset of boiling should be investigated: for instance, one expects a lower wall superheat required to generate a bubble and to a more accurate determination of the optimal operating conditions to run compact low pressures evaporators.

References

- Ait Ameer M., 2006. Etude expérimentale de l'ébullition naturelle confinée: analyse des instabilités et des transferts thermiques. Ph.D. Thesis, Insa de Lyon. France.
- Aoki S., Inoue A., Aritomi M., Sakamoto Y., 1982. Experimental study on the boiling phenomena within a narrow gap. *Int. J. Heat Mass Transfer*. Vol. 25, n° 7, p. 985-990.
- Bankoff S.G, 1957. Ebullition from solid surfaces ion the absence of a pre-existing gaseous phase. *Trans. Am. Soc. Mech Engrs*. vol. 79, p. 735-740.
- Bankoff S.G., 1958. Entrapment of gas in the spreading of a liquid over a rough surface. *AIChE Journal*. vol 4, p. 24–26.
- Barbusse S., Gagnepain L., 2003. La climatisation automobile : Impact énergétique et environnemental. ADEME 4183.
- Bell L.A, Al-Daini A.J., Al-Ali H., Abdel-Gayed R.G., Duckers L., 1996. The Design of an Evaporator/Absorber and Thermodynamic Analysis of a Vapor Absorption Chiller Driven by Solar Energy. *World Renewable Energy Congress*.
- Bergman T. L., Lavine A. S., Incropera F. P., Dewitt P. (2011). *Fundamentals of heat and mass transfer*. John Wiley & Sons.
- Bonjour J., 1996. Amélioration des transferts thermiques en ébullition naturelle convective par effet de confinement. Ph.D. Thesis, Insa de Lyon. France.
- Bonjour J., Boulanger F., Gentile D., Lallemand M., 1997. Etude phénoménologique de l'ébullition en espace confiné à partir d'un site de nucléation isolé. *Rev. Gén. Therm*. Vol. 36, p. 562-572.
- Bonjour J., Lallemand M., 1998. Flow patterns during boiling in a narrow space between two vertical surfaces. *International Journal of Multiphase Flow*. vol 24, p. 947-960.
- Borishanskiy V. M., Danilova G. N., Gotovskiyy M. A., Borishanskiy A. V., Danivola G. P., Kupriyanova A. V., 1981. Correlation of data on heat transfer, and elementary characteristics of the nucleate boiling mechanism. *Heat transfer Soviet Research*. Vol. 13, p. 100-116.
- Boudard E, Bruzzo V. Heat exchange and heat transfer device, in particular for a motor vehicle. *European Patent 1751477B1*; 2009.
- Bretherton F. P., 1961. The motion of long bubbles in tubes. *Journal of Fluid Mechanics*. vol. 10, p. 166- 188.
- Brown J.S., Domanski P.A., 2014. Review of alternative cooling technologies. *Applied Thermal Engineering*, doi: 10.1016/j.applthermaleng.2013.12.014.
- Buyevich Y.A., Webbon B.W., 1996. Dynamics of vapour bubbles in nucleate boiling. *International Journal of Heat and Mass Transfer*. vol 39, n°12, p. 2409–2426

References

- Carey V.P., 1992. Liquid-vapor phase-change Phenomena. Washington : Hemisphere Publishing Corporation, 645 p.
- Castro J., Oliva A., Perez-Segarra C.D., Oliet C., 2008. Modelling of the heat exchangers of a small capacity, hot water driven, air-cooled H₂O-LiBr absorption cooling machine. International Journal of Refrigeration. vol 31, p. 75-86.
- CENERG, 2002. Chiffres clés de la climatisation dans le monde, en Europe et en France, disponible sur le site du centre d'Energétique de l'Ecole des Mines de Paris : www.cenerg.ensmp.fr.
- Chan, M. A., Yap, C. R., Ng, K. C., 2010. Pool boiling heat transfer of water on finned surfaces at near vacuum pressures. Journal of Heat Transfer. vol. 132.
- Chang S.W., Lo D. C., Chiang K. F., Lin C. Y., 2012. Sub-atmospheric boiling heat transfer and thermal performance of two-phase loop thermosyphon. Experimental Thermal and Fluid Science. vol 39, p. 134-147.
- Charnay R., 2014. Experimental study of flow boiling in horizontal minichannels at high saturation temperature. Ph.D. Thesis, Insa de Lyon. France.
- Charnay R., Revellin R., Bonjour J., 2013. Flow pattern characterization for R-245fa in minichannels: optical measurement technique and experimental results. International Journal of Multiphase Flow. vol 57, p. 169 - 181.
- Chi S.W., 1976. Heat pipe theory and practice: a sourcebook. Hemisphere Pub. Corp.
- Chien L. H., Tsai Y. L., 2011. An experimental study of pool boiling and falling film vaporization on horizontal tubes in R-245fa. Applied Thermal Engineering. vol. 31, p. 4044-4054.
- Clark J. A., Merte H., 1973. Private communication with Van Stralen. University of Michigan.
- Clausse M., Leprieur J., Meunier F., 2011. Experimental test of plate evaporator for sorption refrigeration systems. ISHPC 11, Padova Italie, paper I-86.
- Clauzade B., 1996. Etude des échangeurs et évaporateurs à film ruisselant sur paroi en graphidite. Ph.D. Thesis, INPL. France.
- Cole R., 1974. Boiling nucleation. Advance Heat Transfer, New York : Academic Press, 85-167.
- Cole R., Rohsenow W. M., 1969. Correlation of bubble departure diameters for boiling of saturated liquids. Chem. Engineering Prog. Symposium Series, Heat Transfer. vol. 65, n°92, p. 211-213.
- Cole R., Shulman H.L., 1966. Bubble departure diameters at subatmospheric pressures. Chem. Eng. Progress Symp. Series, Heat Transfer. vol 64, n°64, p. 6-16.
- Collier J. G., Thome J. R., 1994. Convective boiling and condensation. Oxford Science Publication.
- Cooper M.G., Lloyd A.J.P., 1969. The microlayer in nucleate pool boiling. International Journal of Heat and Mass Transfer. vol 12, p. 915-933.
- Cusursuz A., Ginet N., Cioulachtjian S., Lallemand M., 2001. Durée d'attente, durée de grossissement d'une bulle isolée. Congrès français de Thermique, Nantes. p. 413-418.

- EAW: <http://www.eaw-energieanlagenbau.de/absorber-akm.html> viewed the 24/06/2015.
- Eddington R. I., Kenning D. B. R., Korneichev A. I., 1978. Comparison of gas and vapour bubble nucleation on a brass surface in water. *Int. J. Heat Mass Transfer*. vol 21, p. 855-862.
- El-Genk M. S., Saber H. H., 2001. Minimum thickness of a flowing down liquid film on a vertical surface. *International Journal of Heat and Mass Transfer*. vol 44, p. 2809-2825.
- Estiot E., Natzer S., Harm M., Kren C., Schweigler C., 2006. Heat exchanger development for compact water/LiBr sorption systems, *Proceedings of the ASME Advanced Energy Systems Division*.
- Fernandez-Seara J., Pardinas A.A, 2014. Refrigerant falling film evaporation review: Description, fluid dynamics and heat transfer. *Applied Thermal Engineering*. vol 64, p. 155-171.
- Flores C., 2014. Etude des transferts de masse et de chaleur au sein d'un absorbeur eau/bromure de lithium. Ph.D. Thesis, Université de Grenoble. France.
- Florides G.A., Kalogirou S.A., Tassou S.A., Wrobel L.C., 2003. Design and construction of a LiBr-water absorption machine. *Energy Conversion & Management*. vol 44, n°15, p. 2483-2508.
- Fritz W., 1935. Berechnung des Maximalvolumen von Dampfblasen. *Phys. Zeitung*. Vol. 36.
- Fujita Y., Bai Q., 1997. Critical heat flux of binary mixtures in pool boiling and its correlation in terms of Marangoni number. *International Journal of Refrigeration*. vol 20, p. 616-622.
- Fujita Y., Ohta H., Uchida S., Nishikawa K., 1988. Nucleate boiling heat transfer and critical heat flux in narrow space between rectangular surfaces. *International Journal of Heat and Mass Transfer*. vol 31, p. 229-239.
- Fujita Y., Uchida S., 1995. Enhanced nucleate boiling heat transfer in a narrow confined space between a heating surface and slitted plate. *Fuel and Energy Abstracts*, September. vol 36, p. 351-360.
- Ginet N., 1999. Analyse des mécanismes contrôlant la croissance et l'ascension d'une bulle isolée en ébullition nucléée. Ph.D. Thesis, Insa de Lyon. France.
- Golobic I., Gaspersic B., 1996. Corresponding states correlation for maximum heat flux in two-phase closed thermosyphon. *International Journal of Refrigeration*. vol 20, n°6, p. 403-410.
- Gong S., Ma W., Li L., 2013. An experimental study on the effect of liquid film thickness on bubble dynamics. *Applied Thermal Engineering*. vol 51, p. 459-467.
- Gorenflo D., Baumhögger E., Herres G., Kotthoff S., 2013. State-of-the-art of pool boiling prediction methods, 4th IIR Conference on Thermophysical Properties and Transfer Processes of Refrigerants, Delft, The Netherlands, paper TP-004.
- Goulet R., 2011. Development and analysis of an innovative evaporator/absorber for automotive absorption-based air conditioning systems: investigation on the simultaneous heat and mass transfer. Ph.D. Thesis, Insa de Lyon. France.
- Goupy J., 2000. Modélisation par les plans d'expériences. *Technique de l'ingénieur R 275*.
- Grignon-Massé L., 2010. Développement d'une méthodologie d'analyse coût-bénéfice en vue d'évaluer le potentiel de réduction des impacts environnementaux liés au confort d'été : cas des

References

climatiseurs individuels fixes en France métropolitaine. Ph.D. Thesis, École nationale supérieure des mines de Paris. France.

Groeneveld D.C., 1973. Post-dryout heat transfer at reactor operating conditions. ANS Conf. 730304, p. 321–350.

Groeneveld D.C., Delorme G.G.J., 1976. Prediction of thermal non-equilibrium in the post-dry out regime. Nuclear Engineering Design. vol. 36, p. 17–26.

Gross U., 1994. Falling film evaporation inside a closed thermosyphon. Institution of Chemical Engineers Symposium series. Hemisphere Publishing Corporation. p. 443-443.

Grossman G., 1986. Heat and mass transfer in film absorption. In Handbook of heat and mass transfer. p. 211-257. Houston: Gulf publishing.

Gungor K.E., Winterton R.H.S. 1986., A general correlation for flow boiling in tubes and annuli. International Journal of Heat and Mass Transfer. vol 29, p. 351–358.

Haberman W.L., Morton R.K., 1953. An experimental investigation of the drag and shape of air bubbles rising in various liquids. Navy Department, The David W. Taylor Model Basin. Report 802, NS 715-102, 47 p.

Héas S., 2001. Etude expérimentale des transferts thermiques en ébullition libre et régime transitoire. Ph.D. Thesis, Insa de Lyon. France.

Henning H.M., 2007. Solar assisted air conditioning of buildings – an overview. Applied Thermal Engineering. vol 27, p. 1734-1749.

Hsu Y. Y., 1962. On the size range of active nucleation cavities on a heating surface. Journal of Heat Transfer. p. 207-216.

INRETS, 2007. Climatisation et auxiliaires: comment réduire la surconsommation et la surémission de CO². Technical report.

Jensen M. K., Memmel G. J., 1986. Evaluation of bubble departure diameters correlations. 8th Int. Heat Transfer Conf. 4, p. 1907-1912.

Judd R.L. and Lavdas C. H., 1980. The nature of nucleation site interaction. J. Heat Transfer. vol 102, p. 461-464.

Kattan N., Thome J. R., Favrat D. 1998. Flow boiling in horizontal tubes: Part 1- development of a diabatic two-phase flow pattern map. Journal of Heat and Mass Transfer. vol. 147, p. 120-140.

Katto Y., Yokoya S., 1966. Experimental study of nucleate pool boiling in case of making interference-plate approach to the heating surface. 3rd International Heat Transfer Conference, Chicago. vol 33, p. 219-227.

Katto Y., Yokoya S. and Yasumaka M., 1970. Mechanism of boiling crisis and transition boiling in pool boiling. 4th Int. Heat Transfer Conf. 4, p. 119-123.

Kays W. M., Crawford M. E., 1993 Convection Heat and Mass Transfer, 3rd ed. McGraw-Hill, New York.

- Kim J., Cheol H., Kim M. H., 2007. On the growth behavior of bubbles during saturated nucleate pool boiling at sub-atmospheric pressure. *International Journal of Heat and Mass Transfer*. vol 50, p. 3695-3699.
- Kim D.S., Haslinger G., Lesko M., Penthor A., 2008. Thermodynamic behaviour of a small LiBr-water absorption chiller with stainless steel plate heat exchangers: preliminary results. ISHPC 08, Seoul, South Korea.
- Kim D. S., Infante Ferreira C. A., 2006. A Gibbs energy equation for LiBr aqueous solutions. *Int. J. of Refrig.* vol 29, p. 36-46.
- Kim D. S., Infante Ferreira C. A., 2008. Flow patterns and heat and mass transfer coefficients of low Reynolds number falling film flows on vertical plates: Effects of a wire screen and an additive. *International Journal of Refrigeration*. vol. 32, p. 139-149.
- Kim H. Y., Kang B. H., 2003. Effects of hydrophilic surface treatment on evaporation heat transfer at the outside wall of horizontal tubes. *Applied Thermal Engineering*. vol 23, p. 449-458.
- Klausner J., Mei R., Bernhard D., Zeng L., 1993. Lift, drag and added mass of hemispherical bubble sliding and growing on a wall in a viscous linear shear flow. *International Journal of Heat and Mass Transfer*. vol. 36, p. 651-662.
- Koffman N., 2014. Films liquides tombants avec ou sans contre-écoulement de gaz : application au problème de l'engorgement dans les colonnes de distillation. Ph.D. Thesis, UPMC. France.
- Labuntsov D. A., Jagov V. V., Gorodov A. K., 1978. Critical heat fluxes in boiling at low pressure region. *Proc. 6th Int. Heat Transfer Conf.* Vol 1, p 221-225.
- Lanzerath F., Erdogan M., Screiber H., Steinhilber M., Bardow A., 2014. Combinaison of finned tubes and thermal coating for high performance water evaporation in absorption heat pumps. ISHPC 14, Washington, USA, paper 19.
- Lee H.S., Merte H., 1996. Spherical vapor bubble in uniformly superheated liquids. *Int. J. Heat Mass Transfer*. Vol. 39, p. 2427-2447.
- Leprieur J., 2014. Développement d'une pompe à chaleur à absorption en vue de l'utilisation des rejets thermiques d'une pile à combustible embarquée. Mémoire Diplôme Ingénieur CNAM. France.
- Madjeski J., 1966. Activation of nucleation cavities on a heating surface with temperature gradient in superheated liquid. *Int. J. Heat Mass Transfer*. Vol. 9, p. 295-300.
- Makni F., 2012. Développement d'un outil de simulation 2D-3D pour l'amélioration de la conception des adsorbants dédiés aux systèmes de climatisation. Ph.D. Thesis, CNAM. France.
- McGillis R., Carey V. P., Fitch J. S., Hamburg W. R., 1991a. Pool boiling on a small heat dissipating element in water at low pressure. ASME/AIChE National Heat Transfer Conference, Minneapolis, Minnesota.
- McGillis R., Carey V. P., Fitch J. S., Hamburg W. R., 1991b. Pool boiling enhancement techniques for water at low pressure. *Proceedings of the Seventh IEEE Semiconductor Thermal Measurement and Management Symposium*. Phoenix, Arizona. P. 64-72.
- Miskimin M., Edberg B., 1998. Thermak System for a vehicle. Patent WO98 34807.

References

- Morison K. R., Worth Q. A. G., O'Dea N. P., 2006. Minimum wetting and distribution rate in falling film evaporators. *Food and Bioproducts Processing*. vol. 84, n°4, p. 302-310.
- Moriyama K., Inoue A., 1996. Thickness of the liquid film formed by a growing bubble in a narrow gap between two horizontal plates. *Journal of Heat Transfer*. vol 18, p. 132-139.
- Mukherjee A., Dhir V.K., 2004. Study of lateral merger of vapor bubbles during nucleate pool boiling, *Journal of Heat Transfer*. vol 126, p. 1023–1039.
- Niebergall W., 1959. Sorptionskältmaschinen. *Handbuch der Kältetechnik*. vol 7. Berlin: Springer.
- Nishikawa K., et al., 1976. *Japan Society of Mechanical Engineers*. Vol. 42.
- Nosoko T., Yoshimura P. N., Nagata T. et Oyakawa K., 1996. Characteristics of two-dimensional waves on a falling liquid film. *Chemical Engineering Science*. vol. 51, p. 725-732.
- Nukiyama S., 1934. The maximum and minimum values of heat transmitted from metal to boiling water under atmospheric pressure. *J. Soc. Mec. Eng. Jap.* vol 37, p. 367-374.
- Papon P., Leblond J., 1990. *Thermodynamique des matériaux*. Editions Hermann, Paris.
- Passos J. C., Hirata F. R., Possamai L. F. B., Balsamo M., Misale M., 2004. Confined boiling of FC72 and FC87 on a downward facing heating copper disk. *International Journal of Heat Fluid Flow*. vol 25, p. 313-319.
- Rahman H., Hawlader M.N.A., Malek A., 2003. An experiment with a single-effect submerged vertical tube evaporator in multi-effect desalination. *Desalination*. vol 156, p. 91-100.
- Rampisela P.F., 1993. Etude expérimentale de l'ébullition en espace confiné. Ph.D. Thesis, CENG, Grenoble. France.
- Revellin R., 2005. Experimental two-phase fluid flow in microchannel. Ph.D. Thesis, EPFL. France.
- Revellin R., Agostini B., Ursenbacher T., Thome J. R., 2008. Experimental investigation of velocity and length of elongated bubbles for flow of R-134a in a 0.5 mm microchannel. *Experimental Thermal and Fluid Science*. vol 32, n°3, p. 870 – 881.
- Robinson A. J., Judd R. L., 2004. The dynamics of spherical bubble growth. *International Journal of Heat and Mass Transfer*. vol 47, p. 5101-5113.
- Rohsenow W. M., Hartnett P., Cho Y. I., 1998. *Handbook of Heat Transfer*. McGraw Hill. US.
- Rullière R., Siedel B. and Haberschill P., 2012. Experimental evaluation of bubble growth of water at very low pressure. *ECI 8th Int. Conf. On Boiling and Condensation Heat Transfer*. Lausanne. Switzerland.
- Sabir H.M., Bwalya A.C. , 2002. Experimental study of capillary-assisted water evaporators for vapour-absorption systems. *Applied Energy*. vol 71, p. 45-57.
- Sabir H.M., ElHag Y.B.M., 2007. A study of capillary-assisted evaporators. *Applied Thermal Engineering*. vol 27, p. 1555-1564.
- Sakurai A., Mizukami K., Shiotsu M., 1970. Experimental studies on transient boiling heat transfer and burnout. 4th International Heat Transfer Conference, Versailles. France.

- Schnabel S., Witte C., Weber C., 2008. Water as refrigerant – experimental evaluation of boiling characteristics at low temperatures and pressures, ISHPC 08, Seoul, Korea, paper 26.
- Schnabel S., Scherr K. T., Kowol J., Schossig P., 2011. Evaluation of different evaporator concepts for thermally driven sorption heat pumps and chillers, ISHPC 11, Padua, Italy.
- Seiler M., Kühn A., Ziegler F., Wang X., 2013. Sustainable cooling strategies using new chemical system. *Industrial & Engineering Chemistry Research*. vol 52, p. 16519-16546.
- Shi M. H., Ji M. and Wang B. X., 1993. Analysis on hysteresis in nucleate pool boiling heat transfer. *Int. J. Heat Mass Transfer*. vol 36, n°18, p. 4461-4466.
- Siedel S., 2012. Bubble dynamics and boiling heat transfer: a study in the absence and in the presence of electric fields. Ph.D. Thesis, Insa de Lyon. France.
- Siedel S., Cioulachtjian S., Bonjour J., 2008. Experimental analysis of bubble growth, departure and interactions during pool boiling on artificial nucleation sites. *Experimental and Thermal Fluid Science*. vol 32, p. 1504–1511.
- Siedel S., Cioulachtjian S., Robinson A. J., Bonjour J., 2013. Integral momentum balance on a growing bubble. *Physics of Fluid*. vol 25, n° 12, p. 123301-123301-22.
- Son G., Dhir V. K., 1998. Numerical simulation of a single bubble during partial nucleate boiling on a horizontal surface. 11th International Heat Transfer Conference, Kyongju. Korea. vol 2, p. 533-538.
- Stutz B., Lallemand M., Raimbault F., Passos J., 2009. Nucleate and transition boiling in narrow horizontal spaces. *Heat Mass Transfer*. vol 45, p. 929–935.
- Thome J. R., 2004. Engineering data book III. Wolverine Tube Inc. <http://www.wlv.com/products/databook/db3/DataBookIII.pdf>.
- Trane: <http://www.trane.com> viewed the 24/06/2015.
- Van Leeuwen H. J. W., 1973. Private communication with Van Stralen. Eindhoven University of Technology.
- Van Stralen S. J. D., Cole R., Sluyter W. M., Sohal M. S., 1975. Bubble growth rates in nucleate boiling of water at subatmospheric pressures. *International Journal of Heat and Mass Transfer*. vol. 18, p. 655-669.
- Van Stralen S., 1979. Combined effect of relaxation and evaporation microlayers. *Boiling Phenomena*. vol 2, p. 467-501.
- Visentini R., 2012. Etude expérimentale des transferts thermiques en ébullition transitoire. Ph.D. Thesis, INP Toulouse. France.
- Voltas: <http://www.voltas.com/> viewed the 24/06/2015.
- Wojtan L., Ursenbacher T., Thome J. R., 2005. Investigation of flow boiling in horizontal tubes: Part I – A new diabatic two-phase flow pattern map. *International Journal of Heat and Mass Transfer*. vol. 48, p. 2955-2969.
- Wu W. G., Ma T. Z., Li H. Q., 1982. Experimental study of critical heat flux in pool boiling at low pressure. *Proc. 7th International Heat Transfer Conference*. vol. 4, p. 119-123.

References

- Xia Z. Z., Yang G. Z., Wang R. Z., 2008. Experimental investigation of capillary-assisted evaporation on the outside surface of horizontal tubes. *International Journal of Heat and Mass Transfer*. vol 51, p. 4047-4054.
- Yagov V. V., 2001. Bubble growth rate at pool boiling in wide range of reduced pressures. *Experimental Heat Transfer, Fluid Mechanics and Thermodynamics*. p. 331-336.
- Yao S.C., Chang, Y., 1983. Pool boiling heat transfer in a confined space. *International Journal of Heat and Mass Transfer*. vol 26, p. 841-848.
- Yuan D. W., Pan L. M., Chen D., Zhang H., Wei J. H., Huang Y. P., 2011. Bubble behavior of high subcooling flow boiling at different system pressure in vertical narrow channel. *Applied Thermal Engineering*. vol 31, p. 3512-3520.
- Zaitsev D.V., Kabov O.A., Cheverda V.V., Bufetov N.S., 2004. The effect of wave formation and wetting angle on the thermocapillary breakdown of a falling liquid film. *High. Temp.* vol. 42, p. 450-456.
- Zeng L.Z., Klausner J.F., Mei R., 1993. A unified model for the prediction of bubble detachment diameters in boiling systems. *International Journal of Heat and Mass Transfer*. vol 36, p. 2261–2270.
- Ziegler F., 2014. Options for new working pairs – perceptions and misperceptions. Keynote ISHPC 2014, USA.
- Zuber N., 1959. Hydrodynamic aspects of boiling heat transfer. Report AECU-4439, U. S. Atomic Energy Commission.
- Zuber N., Tribus M., Westwater J.W., 1961. The hydrodynamic crisis in pool boiling of saturated and subcooled liquids. *Int. Developments in Heat Transfer*, ASME, New York. p.230-236.
- Zur A., Shechtman I., 1995. Refrigeration, heating and Air Conditioning System for Vehicles. Patent US 5 383 341.

APPENDIX A: Boiling phenomena hysteresis on bubble size and boiling curves

In vertical and horizontal configurations, the size of the bubbles depends on the flow patterns but also on the initial conditions. Moreover, the size of the bubbles observed strongly depends on if boiling curves are obtained at increasing or decreasing heat flux. The size of bubbles formed is smaller in the former case than in the latter case. An example of boiling curve obtained with bubble observed for each area of the curve is shown in Fig. A.1. Each point placed on the graph is the time-averaged value of data recorded each 3 s during 10 min.

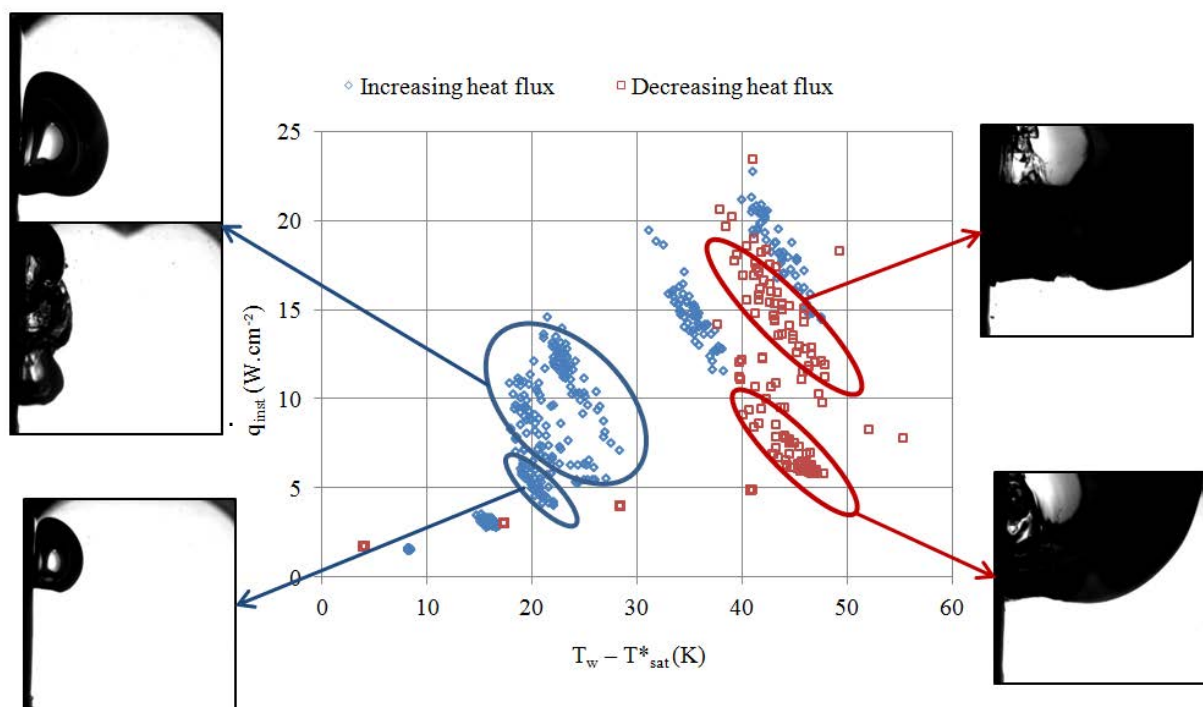


Figure A.1: Boiling curves at increasing \diamond and decreasing \square imposed heat flux and pictures of bubbles associated (vertical orientation, $P_v = 1.7$ kPa, $h_l = 167$ mm)

Even though water is a non-wetting fluid, a certain hysteresis of the boiling curve could be detected. In addition, the observed trend is against the intuition probably because of the dissolved gases trapped in the site. By increasing the heat flux and then decreasing this one, trapped gasses leave the nucleation site. The energy required to activate this site thus increase. If no leaks appear in the experimental vessel, this hysteresis effect disappears with the number of experiments conducted. An example of boiling curves obtained at increasing and decreasing heat fluxes with data recorded 24 hours after data represented on Fig. A.1 are shown on Fig. A.2.

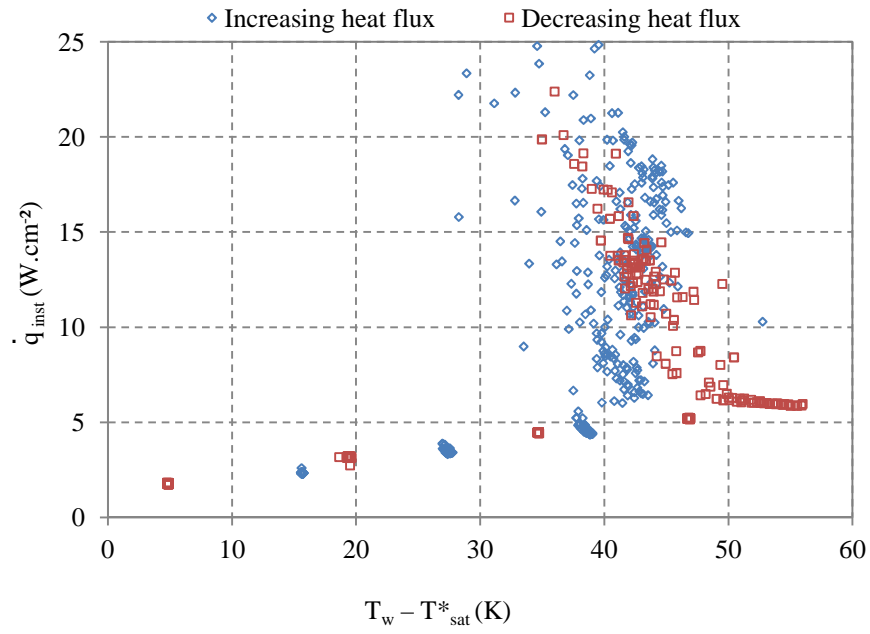


Figure A.2: Boiling curves at increasing \diamond and decreasing \square imposed heat flux (vertical orientation, $P_v = 1.2$ kPa, $h_l = 200$ mm)

APPENDIX B: Uncertainties on the calculation of heat fluxes and uncertainties associated with the heat storage term

Like shown in the main text, the heat flux dissipated to the fluid by the boiling surface can be calculated from the Fourier's law using rows of thermocouples along the copper block of the test sample. Knowing that the Fourier's law can be expressed as Eq. B.1 and using the logarithm method in order to calculate the experimental error, the experimental error can be expressed as Eq. B.2.

$$\dot{q}(z) = -\lambda_{Cu} \left. \frac{dT}{dz} \right|_{z=0} \quad (B.1)$$

$$\Delta\dot{q} = \dot{q} \left[\frac{\Delta(dT)}{dT} + \frac{\Delta(dz)}{dz} \right] \quad (B.2)$$

Since the respective uncertainties on the temperature and thermocouple position measurements are estimated to be ± 0.1 K and ± 0.4 mm, the heat flux uncertainty is estimated to be of 10 % for high heat flux and more than 50 % for very low heat flux. However, this method doesn't take into account the uncertainties associated with the heat storage term. These uncertainties are estimated from the first law. Based from the first law and still using the logarithm method, the experimental error due to the heat storage term could be calculated as follows:

$$\left[\frac{(\rho V)_{Cu} \cdot 2 \Delta T + \Delta \left(\frac{\Delta U}{U} + \frac{\Delta I}{I} \right) \dot{W}_{elec}}{\frac{(\rho V)_{Cu}}{dt} (T^t - T^{t-1}) - \dot{W}_{elec}^t} \right] \cdot \dot{q}_{storage} = \Delta \dot{q}_{storage} \quad (B.3)$$

An explicit method is used in order to determine these uncertainties. The uncertainties on the electric charge and on the voltage are estimated to be 0.005 A and 0.05 V respectively.

Since, based on a first law analysis, it could be shown that the heat stored into the wall at each time step is rather small (Fig. B.1), the uncertainties due to the storage term could be neglected.

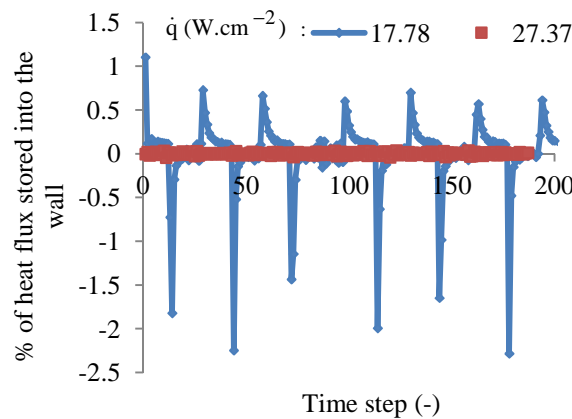


Figure B.1: Percentage of heat flux stored into the wall for two imposed heat fluxes (17.8 W.cm⁻²; 27.4 W.cm⁻²) – Figure associated with Fig. 2.19

APPENDIX C: Boiling curves obtained in horizontal orientation for $h_1 = 150$ mm and five different vapor pressures

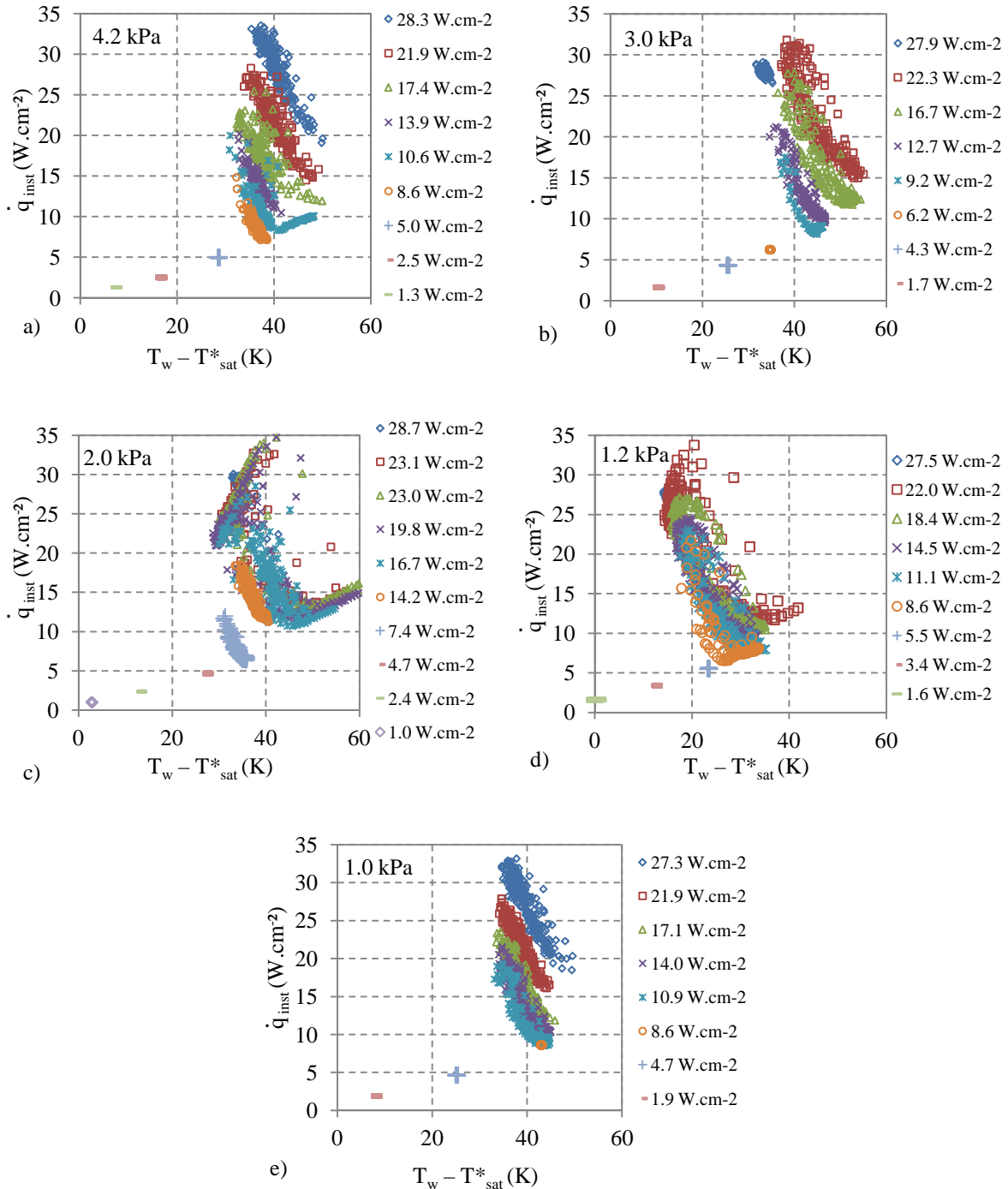


Figure C.1: Boiling curves for $h_1 = 150$ mm and a) $P_v = 4.2$ kPa; b) $P_v = 3$ kPa; c) $P_v = 1.8$ kPa; d) $P_v = 1.2$ kPa; e) $P_v = 0.8$ kPa

APPENDIX D: Boiling curves obtained in horizontal orientation for $h_l = 100$ mm and five different vapor pressures

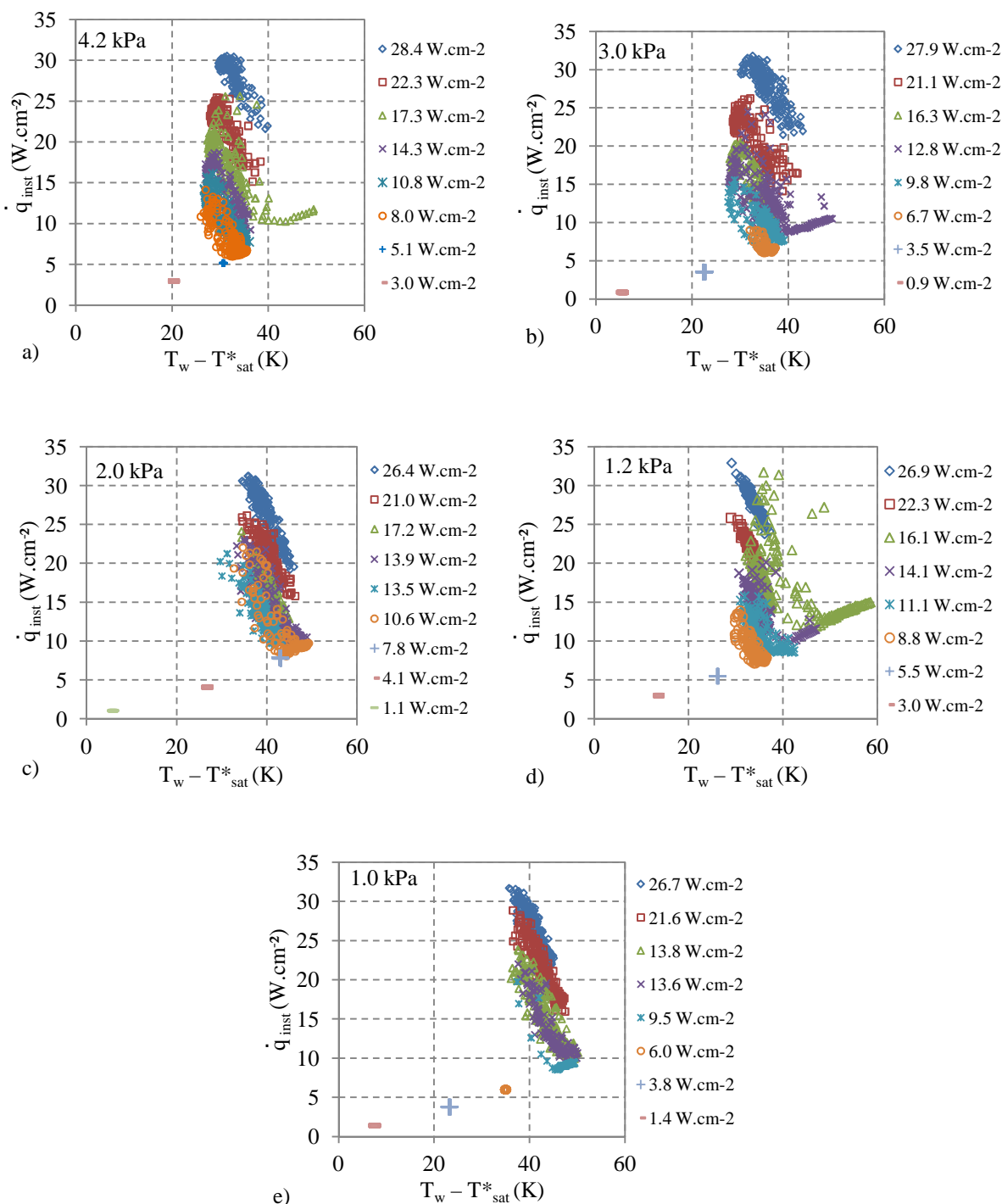


Figure D.1: Boiling curves for $h_l = 100$ mm and a) $P_v = 4.2$ kPa; b) $P_v = 3$ kPa; c) $P_v = 1.8$ kPa; d) $P_v = 1.2$ kPa; e) $P_v = 0.8$ kPa

APPENDIX E: Water vaporization inside a channel of a smooth plate- Results obtained with the first version of the plate and comparison with result introduced in the main text

E.1 First version of the experimental setup

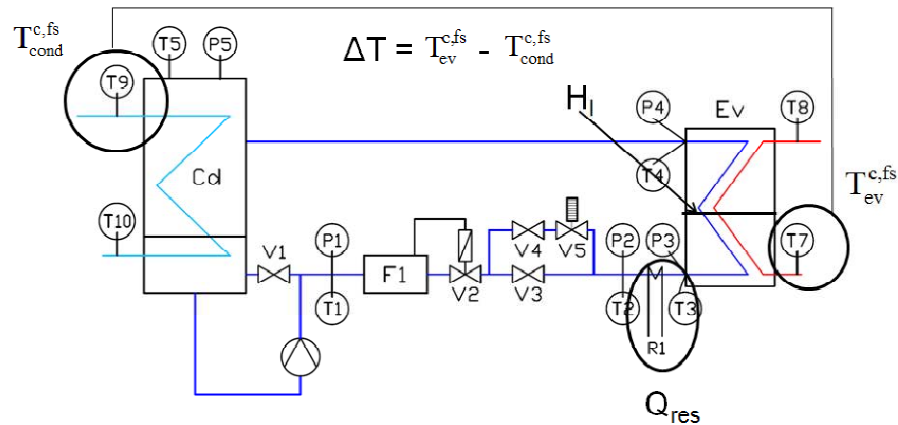


Figure E.1: Factors of the experimental design on the drawing of the experimental test setup.

The first version of the prototype is the same as used in Chap. 4, except that the central plate of the evaporator is not instrumented and that the liquid line is not exactly the same regarding the components implemented on it. In this version of the experimental setup, the refrigerant which circulates in the liquid line is expanded through the valve V3 and can then be heated or not before entering the plate thanks to the cartridge heater R1. This latter component allows setting the vapor quality at the inlet of the channel from 0 to 20 %.

With this version of the set up, several problems were observed:

- First, it was observed that the cooling power achieved was not always continuous even if steady state was obtained. These fluctuations of the cooling capacity could be related to the flow regime (evaporation or waiting time without any appearance of bubble or falling film evaporation-Fig. E.2a) or to the creation of a parasitic bubble in the feeding liquid line (Fig. E.2b). In the first case, one or several bubbles appear spontaneously few centimeters below the free surface. As liquid is splashed on the wall, a downward liquid flow is created. Evaporation immediately takes place leading to high heat transfer coefficient. Then, as all the liquid film is evaporated, the cooling capacity decreases rapidly until a second bubble or group of bubbles appear (a decrease of more than 150 W could be observed, cf. Fig. E.2a). This kind of behavior however remains in the field of likely representative behaviors of real plate heat exchanger. In the second case, the cooling capacity is first null or negative due to ambient heat losses. As the cooling power is null, the feeding mass flow rate is set to 0 g.h⁻¹ but as an electrical power is set at the cartridge heater, the pipe is heated. Thus, when the temperature inside the pipe is higher than the saturation temperature, a bubble is created. During this time, no large bubbles are observed inside the channel of the evaporator. As the feeding mass flow rate is null, thermal equilibrium is reached between the refrigerant and the secondary fluid temperature. A part of refrigerant is then superheated. Thus, when the bubble leaves the pipe, it disrupts the superheated liquid and a boiling crisis occurs close to the free interface. Evaporation immediately takes place and a cooling power of 80 W or more could be obtained (Fig. E.2b).

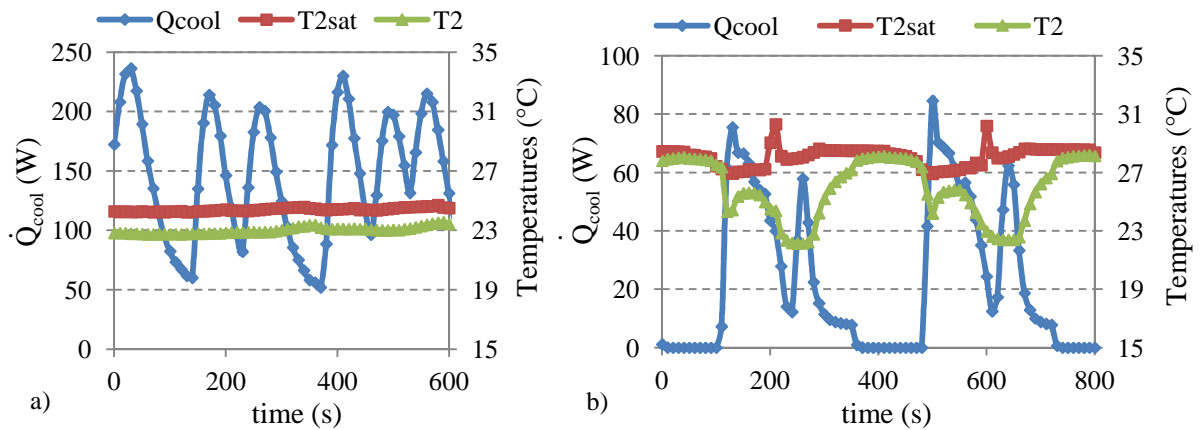


Figure E.2: Evolution in time of the cooling power achieved due to a) periodic and spontaneous growth of a bubble (test n°13 - 4 mm) b) the appearance of a parasitic bubble in the liquid line (test n°2 - 4 mm)

Strictly speaking, evaporation occurred at the free interface surface for probably all the tests realized. However, this evaporation was not as significant to affect the temperature of the secondary fluid. This is all the more difficult to observe as, even if all the pipe and evaporator were insulated, there are ambient heat losses. But, for test were the cooling capacity achieved were null and so the feeding mass flow rate, a decrease of the height of the liquid level was observed. In any case this kind of behavior is poorly controlled and repeatable and it is not likely to represent realistic operation of plate heat exchanger.

- Second, as show on Table E.1, the vapor mass quality could not be always calculated and the value calculated was not always repeatable (Tests n°22 and 23 in Table E.1). This deviation and impossibility to calculate the vapor quality is due to the presence of static vapor masses while a given electrical power is imposed at the cartridge heater during a certain time. Even if these differences on the mass vapor quality induce a small difference regarding the void fraction for all the tests run (c.f. Appendix K), the mass vapor quality should be better controlled for the neatness of the result.

From these observations, several changes were brought to the initial experimental setup. Thus, in order to avoid the parasitic boiling due on one hand, to an insufficient thermal insulation and, on the other hand, to the presence of cartridge heater and in order to better control the vapor quality, three major modifications were performed:

- The cartridge heater was removed and replaced by a thermostatic bath
- The fluid is expanded after being heated by the thermostatic bath
- All the lines and the secondary fluid side of the evaporator are drowned in beads of polystyrene

These changes also present the advantage to be closer to the operating conditions of a standard absorption chiller as the fluid is normally not heated after its expansion.

Once changes were made and once a new central plate was manufactured, several tests were run to compare the behavior between the previous version (tests referred thereafter with the mention V_1) and the new version of the setup (tests referred thereafter with the mention V_2). Results obtained with the first version of the experimental setup are described in the following part.

E.2. Experimental design results for e = 4 mm

Cooling capacities ranging from 0 to 461 W were measured at the secondary fluid. Table E.1 gathers the cooling capacities obtained during the tests, the theoretical cooling capacities given by the experimental design model and the thermodynamic vapor qualities calculated by assuming that both phases are saturated at the inlet of the channel (Eq. E.1).

$$x = \frac{\frac{\dot{W}_{elec}}{\dot{m}_{refr}} + (h_2 - h_{3-l,sat})}{(h_{3-v,sat} - h_{3-l,sat})} \quad (E.1)$$

The subscripts 1 2 3 referred to the location of thermocouples and pressure transducers used to calculate the enthalpies. These indexes are shown on Fig. E.1.

The cooling capacity shown in this table is an average of cooling capacity calculated every one second during half an hour after steady state is obtained. Same procedure is used for the calculation of the vapor quality. As for some tests, the cooling capacity calculated was most of the time null, the refrigerant mass flow rate was null and so that the vapor quality is meaningless. In this cell, the associated case is filled with an “X”.

Table E.1: Tests realized and response obtained

Test n°	h _l (cm)	T _{cond} ^{c.fs} (°C)	T _{ev} ^{c.fs} (°C)	ΔP (kPa)	x _w (%)	Q̇ _{cool} (W)	Q̇ _{cool,th} (W)	Residual (W)
1	15	8.5	17.5	0.89	9.7	231	232	1
2	25	8.5	17.5	0.89	X	41	59	18
3	20	14.1	23.1	1.22	7.8	279	268	-11
4	10	14.1	23.1	1.22	10.3	236	235	-1
5	5	8.5	17.5	0.89	15.7	144	126	-18
6	10	2.9	11.9	0.64	13.6	167	177	11
7	20	2.9	11.9	0.64	X	78	78	1
8	20	10.4	19.4	0.99	14.3	257	256	-1
9	10	10.4	19.4	0.99	18.2	213	186	-26
10	15	4.7	13.7	0.72	18.4	213	219	6
11	20	6.6	15.6	0.80	X	16	43	26
12	10	6.6	15.6	0.80	2.6	177	179	1
13	15	12.3	21.3	1.10	2	238	232	-6
14	20	10.4	24.1	1.75	3.3	461	455	-6
15	10	10.4	24.1	1.75	7.5	378	423	45
16	15	4.7	18.5	1.27	6.5	394	377	-17
17	15	8.5	22.2	1.58	1.9	421	399	-22
18	20	6.6	10.9	0.33	X	0	-45	-45
19	10	6.6	10.9	0.33	2.3	49	54	6
20	15	12.3	16.5	0.45	25	49	67	17
21	15	8.5	12.8	0.36	28.7	54	76	22
22	15	8.5	17.5	0.89	4.9	229	232	3
23	15	8.5	17.5	0.89	9.5	239	232	-6
24	15	8.5	17.5	0.89	9.8	230	232	2

The central point of the experimental design (Test n°1) is repeated three times (Tests n° 22 to 24) in order to estimate the experimental error.

The theoretical cooling capacity is evaluated thanks to the mathematical model obtained by the experimental design. The model coefficients are shown in Table E.2.

Table E.2: Coefficients of the mathematical model obtained by the experimental design

b₀	b₁	b₂	b₃	b₄	b₁₁	b₂₂	b₃₃
233.74	-40.4	62.36	53.68	232.32	-137.34	-39.83	-47.96
b₄₄	b₁₂	b₁₃	b₁₄	b₂₃	b₂₄	b₃₄	
38.68	76.98	98.55	14.59	7.49	33.87	9.22	

The standard deviation of the obtained model is 16.6 W and the confidence interval 37 W. The coefficient b_0 represents the value of the cooling capacity obtained for the central point of the design i.e. for $h_l = 15$ cm, $T_{cond}^{c,fs} = 8.5$ °C, $Q_{res} = 25$ W ($X \approx 9.5$ %) and $\Delta T = 9$ K. The theoretical driving force calculated for this point is 8.9 mbar. The values of the coefficients b_i and b_{ii} are related to the weight of each factor.

In order to check the consistency of the model, different tests were run. As the objective is to obtain the best operating conditions, these tests correspond to the maximal cooling capacity achievable according to the model for the entire plate at the driving pressures of 2.14 kPa and 1.22 kPa (Tests Verif_1 and Verif_2) and for the best specific cooling capacity at these same driving pressures (Tests Verif_3 and Verif_4). Results of these tests are shown on Table E.3.

Table E.3: Model's verification tests

Test n°	h_l (cm)	$T_{cond}^{c,fs}$ (°C)	$T_{ev}^{c,fs}$ (°C)	ΔP (kPa)	x_w (%)	\dot{Q}_{cool} (W)	$\dot{Q}_{cool,th}$ (W)	Residual
Verif_1	20	14.2	27.9	2.14	3.1	513	548	-35
Verif_2	19	14.2	23.2	1.22	11.9	312	296	16
Verif_3	5	14.2	27.7	2.09	11.7	294	269	25
Verif_4	5	14.2	23.2	1.22	10.3	167	134	33

The mathematical model obtained follows the actual cooling power trend satisfactorily. The model is thus validated and the factors could be classified according to their impact on the response:

Two coefficients have absolute values higher than the others: b_4 and b_{11} . As b_4 is higher than the other ones (except b_0), the weightiest factor of all is ΔT as for results presented in the main text. Explanations of the influence of this factor on the cooling capacity obtained are discussed in Chap. 4.

The second weightiest coefficient is b_{11} , i.e. h_l^2 . This means that the evolution of the cooling capacity with the height of the liquid level is non linear. As explained in the main text, a low height of liquid level results in low subcooling degree at the inlet of the plate but also in weak splashing of liquid on the plate. As it can be seen in Chap. 4, the splashing phenomenon tends to be intensified when increasing the height of the liquid level. However, increasing the height of the liquid level tends to limit the boiling phenomenon because of the induced increased of the subcooling degree.

According to this analysis on the influence of the factor h_l , a first approach would consist in considering that the optimal height of the liquid level is the height for which the subcooling is null, i.e. the height for which the evaporator is fed with liquid at the same temperature as the secondary fluid as long as this height of the liquid level remains sufficient. Experiments were thus conducted to compare the cooling capacity obtained for the experimental design points with the height of the liquid level h_l and for the same points but with this “favorable liquid column height” called thereafter h_{fav} . The results show that for the major part of the experimental design points, the cooling capacity obtained decreases when decreasing the liquid column height, i.e. when decreasing the subcooling. For example 26 W (i.e. 11 %) are lost for the central point by varying the height of the liquid level from 15 cm to 9 cm. The mathematical model is in agreement with this observation. Table E.4 gathers data regarding the favorable height of the liquid column and the theoretical optimal height of the liquid level (calculated by the model) depending on $T_{cond}^{c,fs}$ and the theoretical driving pressure. Except for two points for which the favorable liquid column height is higher than the mid-height of the plate, the theoretical optimal height is greater than the favorable height. This shows that a certain amount of liquid is required to obtain the highest possible cooling capacity for given operating conditions.

Table E.4: Favorable and theoretical liquid height for different $T_{cond}^{c,fs}$ and ΔP

$T_{cond}^{c,fs}$ (°C)	8.50	14.13	2.87	10.38	4.74	6.62	12.26	10.38	4.74	8.50	6.62	12.26	8.50
ΔP (kPa)	0.89	1.22	0.64	0.99	0.72	0.80	1.10	1.75	1.27	1.58	0.33	0.45	0.36
h_{fav} (cm)	9.09	12.48	6.52	10.12	7.30	8.15	11.25	17.87	12.99	16.09	3.32	4.62	3.71
h_{opt} (cm)	13.81	16.17	11.45	17.49	15.13	10.14	12.50	16.17	13.81	12.50	11.45	13.82	15.13

In order to highlight the influence of the height of the liquid on the theoretical cooling capacity, the variation of the cooling capacity with the liquid column height for four driving pressure differences is plotted on Fig. E. 3. The experimental range allows theoretical driving pressure differences from 3.3 to 22 mbar, which is representative of operating conditions occurring in a LiBr/H₂O absorption chiller. However some of them have been obtained for evaporation temperature higher than 20 °C, in such case they are not taken into account. Moreover, as for driving pressure difference below 6 mbar no cooling capacities are measured, only driving pressure differences ranging from 6 to 9 mbar are reported. As the coefficient related to \dot{W}_{elec} shows a weak influence of this factor, the electrical power is set at 25 W. The ΔT is arbitrary set at 9 K.

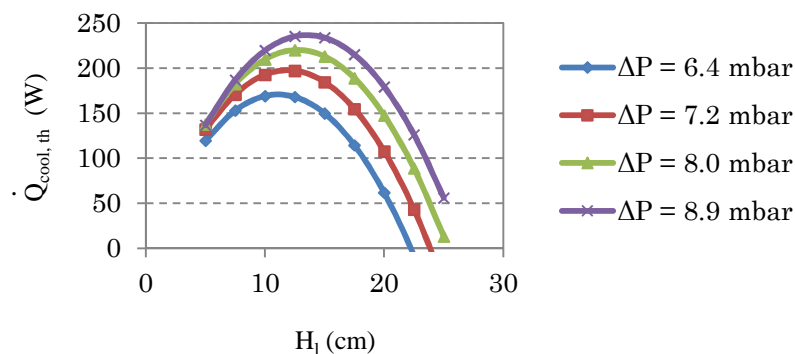


Figure E. 3: Evolution of the cooling capacity with the liquid height for four different driving pressures ($Q_{res} = 25$ W, $\Delta T = 9$ K)

For each ΔP , there exists an optimal height of the liquid level that allows to maximize the cooling capacity. Whatever the driving pressure, this optimal liquid height is ranging between 10 and 15 cm i.e. between 1/5 and 1/3 of the entire plate height which confirms the trends observed by Clausee *et al.* (2011). This could be due either to the huge amount of liquid located above the growing bubble or to the subcooled condition which permits to store the energy in the wall, which heat is then released during the bubble growth or to both phenomena.

Fig. E. 3 also shows that the influence of the driving pressure difference on the cooling capacity is negligible for a low liquid column height. Increasing the driving pressure difference for a height of the liquid level superior to 10 cm could allow to significantly increase the cooling capacity and to significantly change the optimal liquid height. However, in this restricted experimental field the maximal cooling capacity obtained is 233 W, i.e. half of the cooling capacity obtained for the entire experimental field (Test Verif_1). This is in agreement with the literature: increasing the working pressure at the evaporator allows to nearly double the cooling capacity achieved for the same ΔT as the both parameters have a significant influence on the driving pressure.

E.3 Comparison with results obtained for a thickness of the channel of 2 mm

Same tests were run for a thickness of the channel of 2 mm (Appendix F).

As some differences were noticed during the visualization (cf. Chap. 4), the cooling power achieved and the behavior of the prototype presented also some differences for the two thicknesses investigated. Table E. 5 shows the coefficients of the mathematical model obtained by the experimental design for the two thicknesses.

Table E. 5: Coefficients of the mathematical model obtained by the experimental design for $e = 2$ mm and $e = 4$ mm

Coefficients	Centered Factors	$e = 2$ mm	$e = 4$ mm
b_0	$\dot{Q}_{cool, th} _0$	165.39	233.74
b_1	H_1^*	-21.67	-40.40
b_2	$T_{cond}^{c,fs} *$	110.94	62.36
b_3	Q_{res}^*	15.44	53.68
b_4	ΔT^*	248.28	232.32
b_{11}	H_1^{*2}	-68.68	-137.34
b_{22}	$T_{cond}^{c,fs} *^2$	16.41	-39.83
b_{33}	Q_{res}^{*2}	0.74	-47.96
b_{44}	ΔT^{*2}	79.52	38.68
b_{12}	$H_1^* T_{cond}^{c,fs} *$	61.43	76.98
b_{13}	$H_1^* Q_{res}^*$	41.93	98.55
b_{14}	$H_1^* \Delta T^*$	24.98	14.59
b_{23}	$T_{cond}^{c,fs} * Q_{res}^*$	18.27	7.49
b_{24}	$T_{cond}^{c,fs} * \Delta T^*$	98.28	33.87
b_{34}	$Q_{res}^* \Delta T^*$	39.80	9.22

In both cases the weightiest factors on the cooling capacity achieved are ΔT and $T_{\text{cond}}^{\text{c,fs}}$. This is due, as for $e = 4$ mm, to the fact that an increase in ΔT means, depending on the $T_{\text{cond}}^{\text{c,fs}}$, an increase in the driving pressure but also a decrease of the subcooled area at the inlet of the channel. The influence of the $T_{\text{cond}}^{\text{c,fs}}$ on the cooling power achieved seems however more significant for $e = 2$ mm than for $e = 4$ mm. This is probably due to the fact that the higher the evaporation mass flow rate and thus the driving pressure, the more efficient the wetting of the wall due to the drag of liquid by the high velocity vapor flow.

The theoretical cooling powers achieved for same conditions as the Fig. E.3 are represented on Fig. E.4.

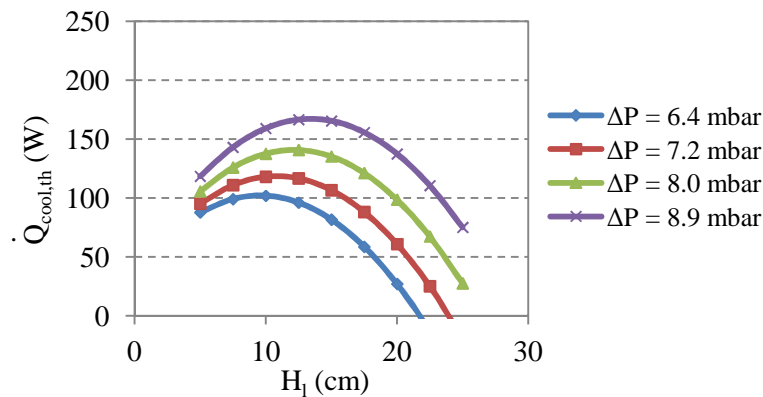


Figure E.4: Evolution of the cooling capacity with the liquid height for four different driving pressures ($Q_{\text{res}} = 25$ W, $\Delta T = 9$ K, $e = 2$ mm)

The decrease/increase of the cooling power with the height of the liquid level is less significant for $e = 2$ mm than for $e = 4$ mm. This could be probably explained since for $e = 4$ mm, the velocity and the frequency of the bubble controls the evaporation of the water on the wall (alternating of wet and dry surface) whereas for $e = 2$ mm, this evaporation is controlled by the vapor flow velocity (surface almost wet at all times - wet area linked to the amount of water dragged by the vapor up to a certain distance).

E.4 Comparison with results obtained with the two versions of the experimental setup

Tests for $e = 2$ mm and $e = 4$ mm were run with the both versions of the experimental setup. Coefficients of the experimental design obtained are gathered in Table E.6.

The theoretical cooling capacity obtained for the central test (Test n°1) is similar for the both version of the experimental setup even for $e = 2$ mm than for $e = 4$ mm. However, the influence of the height of the liquid level on the theoretical cooling capacity obtained is smooth ($e = 2$ mm) or even positive ($e = 4$ mm), i.e. that the higher the height of the liquid level, the greater the cooling capacity achieved. The non-linearity of this factor is also less significant.

Table E.6: Coefficients of the mathematical model obtained by the experimental design before (V_1) and after (V_2) experimental setup changes.

Coefficients	Centered Factors	e = 4 mm V_1	e = 4 mm V_2	e = 2mm V_1	e = 2 mm V_2
b_0	$\dot{Q}_{cool, th} _0$	233,74	221,67	165.39	164.52
b_1	H_1^*	-40,40	48,33	-21.67	0.04
b_2	$T_{cond}^{c,fs}$	62,36	53,33	110.94	92.17
b_3	Q_{res}^* (for V1) $T_{B3}^{c,fs}$ (for V2)	53,68	-15,92	15,44	-37,52
b_4	ΔT^*	232,32	238,69	248.28	248.10
b_{11}	H_1^{*2}	-137,34	-19,21	-68.68	-16.84
b_{22}	$T_{cond}^{c,fs}{}^2$	-39,83	-11,71	16.41	-13.52
b_{33}	Q_{res}^{*2} (for V1) $T_{cond}^{c,fs}{}^2 T_{B3}^{c,fs}{}^2$ (for V2)	-47,96	-23,11	0.74	-50.44
b_{44}	ΔT^{*2}	38,68	-14,43	79.52	52.40
b_{12}	$H_1^* T_{cond}^{c,fs}$	76,98	1,40	61.43	35.15
b_{13}	$H_1^* Q_{res}^*$ (for V1) $H_1^* T_{B3}^{c,fs}$ (for V2)	98,55	2,49	41.93	-71.87
b_{14}	$H_1^* \Delta T^*$	14,59	18,62	24.98	27.13
b_{23}	$T_{cond}^{c,fs} Q_{res}^*$ (for V1) $T_{cond}^{c,fs} T_{B3}^{c,fs}$ (for V2)	7,49	36,69	18.27	59.28
b_{24}	$T_{cond}^{c,fs} \Delta T^*$	33,87	47,57	98.28	59.51
b_{34}	$Q_{res}^* \Delta T^*$ (for V1) $T_{B3}^{c,fs} \Delta T^*$ (for V2)	9,22	8,68	39.80	-27.71

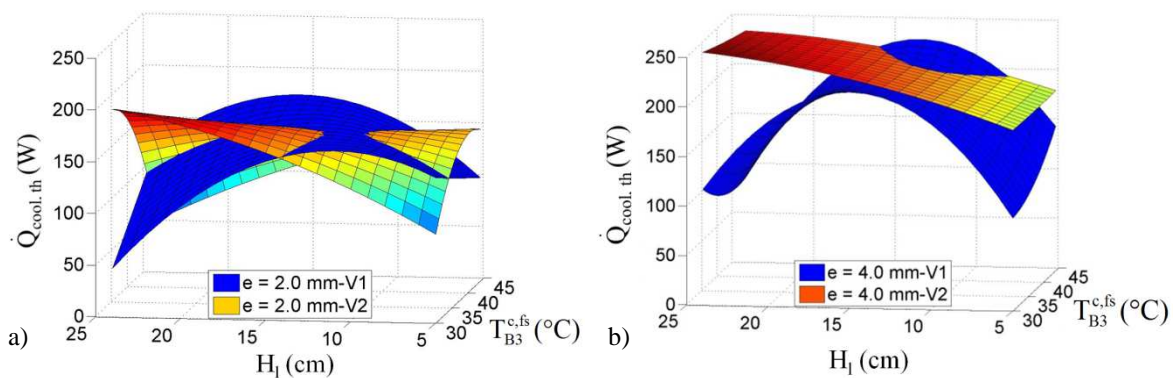


Figure E.5: Response surfaces for a) e = 2 mm and b) e = 4 mm before (V_1) and after (V_2) experimental setup changes ($\Delta T = 9$ K, $T_{cond}^{c,fs} = 8.5$ °C).

Even if the surface response is not exactly the same, the theoretical cooling power achieved for e = 2 mm lies in the same domain before and after experimental setup changes for $\Delta T = 9$ K and $T_{cond}^{c,fs} = 8.5$ °C. Same conclusion cannot be drawn for e = 4 mm. Indeed, the theoretical cooling power is generally higher with the new liquid line and the new plate than before, except for a small portion of

the experimental field. Moreover, as observed with the coefficient b_1 , the influence of the height of the liquid level is almost negligible and the higher the filling ratio, the greater the cooling capacity achieved. The response area where low cooling capacities are achieved are also not observed anymore for $\Delta T = 9$ K, $T_{\text{cond}}^{\text{c,fs}} = 8.5$ °C.

This difference in the response surface between both versions of the setup and for $e = 4$ mm is due to the apparition of bubbles of millimeter size coming from the distributor and disrupting the refrigerant superheated area. While a two-phase flow feeds the channel, the vapor phase rapidly collapses at the inlet of the channel. However, periodically, the vapor does not entirely collapse and a small fraction of vapor remains stable. The diameter of the bubble formed by this small vapor fraction remains constant as the bubble rise. As the bubble reaches the superheated area, it suddenly grows and in few milliseconds. A bubble of centimeter sizes is then formed, which splashes droplets on the wall above the free surface.

APPENDIX F: Responses to tests realized for the experimental design and error calculation

Table F.1: Results of the experimental design for $e = 2$ mm and the first version of the prototype (V1)

Test n°	h_l (cm)	$T_{cond}^{c,fs}$ (°C)	Q_{res} (W)	ΔT (K)	$T_{ev}^{c,fs}$ (°C)	ΔP (kPa)	x (%)	\dot{m}_{refr} (g.h ⁻¹)	\dot{Q}_{cool} (W)	$\dot{Q}_{cool,th}$ (W)
1	15	8.50	25	9.0	17.50	0.89	12.6	285	167	165
2	25	8.50	25	9.0	17.50	0.89	X	0	42	75
3	20	14.13	25	9.0	23.13	1.22	7.5	442	282	272
4	10	14.13	25	9.0	23.13	1.22	9.6	374	235	241
5	5	8.50	25	9.0	17.50	0.89	14.9	250	151	118
6	10	2.87	25	9.0	11.87	0.64	21.8	172	93	102
7	20	2.87	25	9.0	11.87	0.64	X	0	33	27
8	20	10.38	45.4	9.0	19.38	0.99	15.8	401	229	214
9	10	10.38	45.4	9.0	19.38	0.99	20.3	326	183	184
10	15	4.74	45.4	9.0	13.74	0.72	31.4	224	108	111
11	20	6.62	4.6	9.0	15.62	0.80	X	0	74	73
12	10	6.62	4.6	9.0	15.62	0.80	3.7	199	132	147
13	15	12.26	4.6	9.0	21.26	1.10	2.2	319	218	214
14	20	10.38	30.1	13.7	24.12	1.75	0.8	1930	482	473
15	10	10.38	30.1	13.7	24.12	1.75	6.1	652	423	449
16	15	4.74	30.1	13.7	18.49	1.27	8.0	502	322	315
17	15	8.50	9.7	13.7	22.25	1.58	1.8	585	393	383
18	20	6.62	19.9	4.3	10.88	0.33	X	0	-11	-36
19	10	6.62	19.9	4.3	10.88	0.33	50.7	58	23	32
20	15	12.26	19.9	4.3	16.51	0.45	X	0	38	45
21	15	8.50	40.3	4.3	12.75	0.36	X	0	-1	9
22	15	8.50	25	9.0	17.50	0.89	12.8	282	164	165
23	15	8.50	25	9.0	17.50	0.89	12.7	284	167	165
24	15	8.50	25	9.0	17.50	0.89	13.0	278	163	165

Table F.2: Results of the experimental design for $e = 4$ mm and the first version of the prototype (V1)

Test n°	h_l (cm)	$T_{cond}^{c,fs}$ (°C)	Q_{res} (W)	ΔT (K)	$T_{ev}^{c,fs}$ (°C)	ΔP (kPa)	x (%)	\dot{m}_{refr} (g.h ⁻¹)	\dot{Q}_{cool} (W)	$\dot{Q}_{cool,th}$ (W)
1	15	8.50	25	9.0	17.50	0.89	9.7	372	231	232
2	25	8.50	25	9.0	17.50	0.89	X	0	41	59
3	20	14.13	25	9.0	23.13	1.22	7.8	430	279	268
4	10	14.13	25	9.0	23.13	1.22	10.3	361	236	235
5	5	8.50	25	9.0	17.50	0.89	15.7	243	144	126
6	10	2.87	25	9.0	11.87	0.64	13.6	277	167	177
7	20	2.87	25	9.0	11.87	0.64	X	0	78	78
8	20	10.38	45.4	9.0	19.38	0.99	14.3	460	257	256
9	10	10.38	45.4	9.0	19.38	0.99	18.2	370	213	186
10	15	4.74	45.4	9.0	13.74	0.72	18.4	360	213	219
11	20	6.62	4.6	9.0	15.62	0.80	X	0	16	43
12	10	6.62	4.6	9.0	15.62	0.80	2.6	261	177	179
13	15	12.26	4.6	9.0	21.26	1.10	2	358	238	232
14	20	10.38	30.1	13.7	24.12	1.75	3.3	1000	461	455

15	10	10.38	30.1	13.7	24.12	1.75	7.5	589	378	423
16	15	4.74	30.1	13.7	18.49	1.27	6.5	616	394	377
17	15	8.50	9.7	13.7	22.25	1.58	1.9	602	421	399
18	20	6.62	19.9	4.3	10.88	0.33	X	0	0	-45
19	10	6.62	19.9	4.3	10.88	0.33	2.3	133	49	54
20	15	12.26	19.9	4.3	16.51	0.45	25	102	49	67
21	15	8.50	40.3	4.3	12.75	0.36	28.7	158	54	76
22	15	8.50	25	9.0	17.50	0.89	4.9	367	229	232
23	15	8.50	25	9.0	17.50	0.89	9.5	381	239	232
24	15	8.50	25	9.0	17.50	0.89	9.8	367	230	232
Verif_1	20	14.2	45.5	27.9	27.89	2.14	3.1	1532	513	548
Verif_2	19	14.2	44.8	23.2	23.16	1.22	11.9	524	312	296
Verif_3	5	14.2	37.1	27.7	27.65	2.09	11.7	482	294	269
Verif_4	5	14.2	18.8	23.2	23.15	1.22	10.3	270	167	134

Table F.3: Results of the experimental design for $e = 2$ mm and the second version of the prototype (V2)

Test n°	h_l (cm)	$T_{cond}^{c,fs}$ (°C)	$T_{B3}^{c,fs}$ (°C)	ΔT (K)	$T_{ev}^{c,fs}$ (°C)	ΔP (kPa)	x (%)	\dot{m}_{refr} (g.h ⁻¹)	\dot{Q}_{cool} (W)	$\dot{Q}_{cool,th}$ (W)
1	15	8.50	37.5	9.0	17.50	0.89	2.3	229	170	165
2	25	8.50	37.5	9.0	17.50	0.89	1.7	220	173	148
3	20	14.13	37.5	9.0	23.13	1.22	1.8	320	237	245
4	10	14.13	37.5	9.0	23.13	1.22	2.4	309	221	215
5	5	8.50	37.5	9.0	17.50	0.89	3.7	185	123	148
6	10	2.87	37.5	9.0	11.87	0.64	3.4	136	93	85
7	20	2.87	37.5	9.0	11.87	0.64	2.4	98	49	55
8	20	10.38	43.62	9.0	19.38	0.99	3.1	130	87	111
9	10	10.38	43.62	9.0	19.38	0.99	3.7	275	190	160
10	15	4.74	43.62	9.0	13.74	0.72	3.8	7	-4	15
11	20	6.62	31.38	9.0	15.62	0.80	1.2	200	138	168
12	10	6.62	31.38	9.0	15.62	0.80	2.0	190	143	119
13	15	12.26	31.38	9.0	21.26	1.10	1.1	259	201	182
14	20	10.38	39.03	13.7	24.12	1.75	2.8	1839	433	426
15	10	10.38	39.03	13.7	24.12	1.75	2.8	750	398	409
16	15	4.74	39.03	13.7	18.49	1.27	2.6	406	305	287
17	15	8.50	32.91	13.7	22.25	1.58	1.5	979	398	411
18	20	6.62	35.97	4.3	10.88	0.33	2.1	0	-10	-21
19	10	6.62	35.97	4.3	10.88	0.33	3.0	0	-11	-4
20	15	12.26	35.97	4.3	16.51	0.45	2.1	0	-1	17
21	15	8.50	42.09	4.3	12.75	0.36	3.3	0	-15	-27
22	15	8.50	37.5	9.0	17.50	0.89	2.3	219	152	165
23	15	8.50	37.5	9.0	17.50	0.89	2.5	245	189	165
24	15	8.50	37.5	9.0	17.50	0.89	2.4	200	147	165
Verif_1	25	14.16	36.0	13.7	27.90	2.14	2.1	1991	503	553
Verif_2	6	2.87	37.5	9.0	11.87	0.64	3.8	150	95	88
Verif_3	10	4.74	37.5	9.0	13.74	0.72	3.1	161	111	113
Verif_4	12.5	6.66	37.5	9.0	15.66	0.80	2.8	211	145	139

Table F.4: Results of the experimental design for $e = 4$ mm and the second version of the prototype (V2)

Test n°	h_1 (cm)	$T_{cond}^{c,fs}$ (°C)	$T_{B3}^{c,fs}$ (°C)	ΔT (K)	$T_{ev}^{c,fs}$ (°C)	ΔP (kPa)	x (%)	\dot{m}_{refr} (g.h ⁻¹)	\dot{Q}_{cool} (W)	$\dot{Q}_{cool, th}$ (W)
1	15	8.50	37.5	9.0	17.50	0.89	2.5	312	225	225
2	25	8.50	37.5	9.0	17.50	0.89	1.8	351	261	248
3	20	14.13	37.5	9.0	23.13	1.22	1.8	409	283	286
4	10	14.13	37.5	9.0	23.13	1.22	2.5	330	247	246
5	5	8.50	37.5	9.0	17.50	0.89	3.6	230	166	178
6	10	2.87	37.5	9.0	11.87	0.64	3.6	236	172	168
7	20	2.87	37.5	9.0	11.87	0.64	2.6	285	197	197
8	20	10.38	43.62	9.0	19.38	0.99	3.1	325	250	244
9	10	10.38	43.62	9.0	19.38	0.99	3.9	300	224	218
10	15	4.74	43.62	9.0	13.74	0.72	3.8	251	186	190
11	20	6.62	31.38	9.0	15.62	0.80	1.3	342	229	236
12	10	6.62	31.38	9.0	15.62	0.80	2.1	260	187	193
13	15	12.26	31.38	9.0	21.26	1.10	1.2	350	260	257
14	20	10.38	39.03	13.7	24.12	1.75	2.6	625	447	461
15	10	10.38	39.03	13.7	24.12	1.75	3.2	550	393	387
16	15	4.74	39.03	13.7	18.49	1.27	3.2	550	379	379
17	15	8.50	32.91	13.7	22.25	1.58	1.8	550	411	403
18	20	6.62	35.97	4.3	10.88	0.33	2.1	0	-2	4
19	10	6.62	35.97	4.3	10.88	0.33	3.0	84	24	9
20	15	12.26	35.97	4.3	16.51	0.45	2.0	57	44	45
21	15	8.50	42.09	4.3	12.75	0.36	3.3	0	-5	2
22	15	12.26	31.38	9.0	21.26	1.10	1.2	365	257	257
23	15	12.26	31.38	9.0	21.26	1.10	1.3	350	257	257
24	15	12.26	31.38	9.0	21.26	1.10	1.2	350	259	257
Verif_1	25	14.16	34.0	13.7	27.90	2.14	0.8	1100	481	528
Verif_2	25	2.87	37.5	9.0	11.87	0.64	2.0	297	207	204
Verif_3	25	4.74	37.5	9.0	13.74	0.72	2.0	299	222	218
Verif_4	25	6.66	37.5	9.0	15.66	0.80	1.9	320	240	233

Table F.5: Standard error of the estimate and mean absolute error calculated for the four experimental designs realized

	Standard error of the estimate (W)	Mean Absolute Error (W)
e = 2 mm V₁	22.56	10.13
e = 4 mm V₁	37.03	16.55
e = 2 mm V₂	28.93	15.93
e = 4 mm V₂	14.73	7.99

Mean Absolute Error (MAE):

$$MAE = \frac{1}{n} \sum_{i=1}^n |\dot{Q}_{cool} - \dot{Q}_{cool,th}|$$

Standard error of the estimate:

$$\sigma_{est} = \sqrt{\frac{\sum_{i=1}^n (\dot{Q}_{cool} - \dot{Q}_{cool,th})^2}{n}}$$

APPENDIX G: Void and mass fraction obtained

Table G.1: Void and mass fraction calculated for the both version of the experimental setup (V1 and V2), for $e = 4 \text{ mm}$ and $e = 2 \text{ mm}$

e (mm)	V ₁				V ₂			
	4.0	2.0	4.0	2.0	4.0	2.0	4.0	2.0
Tests n°	x(%)	x (%)	ε (%)	ε (%)	x (%)	x (%)	ε (%)	ε (%)
1	9.7	12.6	99.99	100.00	2.5	2.3	99.94	99.94
2	X	X	X	X	1.8	1.7	99.92	99.91
3	7.8	7.5	99.98	99.99	1.8	1.8	99.89	99.89
4	10.3	9.6	99.98	99.99	2.5	2.4	99.92	99.92
5	15.7	14.9	99.99	100.00	3.6	3.7	99.96	99.96
6	13.6	21.8	99.99	100.00	3.6	3.4	99.97	99.97
7	X	X	X	X	2.6	2.4	99.96	99.96
8	14.3	15.8	99.99	100.00	3.1	3.1	99.95	99.95
9	18.2	20.3	99.99	100.00	3.9	3.7	99.96	99.96
10	18.4	31.4	99.99	100.00	3.8	3.8	99.97	99.97
11	X	X	X	X	1.3	1.2	99.90	99.89
12	2.6	3.7	99.95	99.97	2.1	2.0	99.94	99.93
13	2	2.2	99.91	99.95	1.2	1.1	99.85	99.83
14	3.3	0.8	99.94	99.86	2.6	2.8	99.92	99.92
15	7.5	6.1	99.97	99.98	3.2	2.8	99.93	99.92
16	6.5	8.0	99.98	99.98	3.2	2.6	99.95	99.94
17	1.9	1.8	99.90	99.92	1.8	1.5	99.89	99.87
18	X	X	X	X	2.1	2.1	99.95	99.95
19	2.3	50.7	99.96	100.00	3.0	3.0	99.97	99.97
20	25	X	100.00	X	2.0	2.1	99.93	99.93
21	28.7	X	100.00	X	3.3	3.3	99.97	99.97
22	4.9	12.8	99.97	99.99	ND	2.3	ND	99.94
23	9.5	12.7	99.99	99.99	ND	2.5	ND	99.94
24	9.8	13.0	99.99	99.99	ND	2.4	ND	99.94

APPENDIX H: Uncertainties on the calculation of heat fluxes at different spot of the central plate

As mentioned in the main text, the heat flux from the secondary fluid to the refrigerant at different spots is estimated by means of the Fourier's law. The experimental error can thus be calculated as mentioned in the Appendix B. The uncertainties on the temperature measurements are estimated to be 0.1 K. The uncertainties on the thermocouple position are estimated to be 0.5 mm although these ones cannot be known with accuracy due to the mounting procedure (embedded thermocouples, thermocouples placed in notches backfilled with tin, etc.). Using the equation B.2, the heat flux uncertainty is thus estimated to be of 30 % for high heat flux and more than 55 % for low heat flux. However, since the calculation of the heat flux is done using information only given by two thermocouples (vs. four thermocouples in the Chap. 2, 3 and 5), and there is a strong uncertainties on the thermocouples position, these values may not be significant. Thus, the consistency of the results is also check by checking the equality between the cooling capacity obtained by a balance at the secondary fluid side ($\dot{Q}_{cool, fs}$) and the cooling capacity obtained by summing all the heat flux calculated ($\dot{Q}_{cool, \Sigma \dot{q}}$). For this latter, it is assumed that the heat flux calculated at the measurement spot is the same for a certain area of the wall around this spot. Cooling capacities obtained for each test and by these two methods are shown in Table H.1.

Table H.1: Cooling capacity obtained by a balance at the secondary fluid (Eq. 4.1- $\dot{Q}_{cool, fs}$) and by summing all the heat fluxes calculated ($\dot{Q}_{cool, \Sigma \dot{q}}$)

Test n°	$\dot{Q}_{cool, fs}$ (W)	$\dot{Q}_{cool, \Sigma \dot{q}}$ (W)	residual (%)
1	224.59	246.17	9.61
2	260.90	297.08	13.87
3	282.53	310.83	10.02
4	246.67	241.75	-1.99
5	165.54	149.74	-9.55
6	171.89	154.36	-10.20
7	197.13	221.19	12.20
8	249.95	266.69	6.70
9	224.22	236.53	5.49
10	185.73	167.77	-9.67
11	228.99	274.33	19.80
12	187.37	163.81	-12.58
13	260.39	252.24	-3.13
14	446.58	479.92	7.46
15	392.89	425.18	8.22
16	379.39	385.50	1.61
17	410.65	435.26	5.99
1_verif	481.04	563.59	17.16
2_verif	208.17	269.44	29.43
3_verif	222.96	259.19	16.25
4_verif	240.26	270.23	12.47

Appendices

The highest discrepancy between cooling capacity obtained by a balance at the secondary fluid and the cooling capacity obtained by summing the heat fluxes calculated are estimated to be 30 %. For more than 50 % of the test realized, this discrepancy is less than 10%. The discrepancy found is thus much lower than the uncertainties calculated.

APPENDIX I: Simulation with Star CCM+ of the temperature distribution inside the central plate of the evaporator

To assess the validity of the method for the evaluation of the heat flux through the central plate, the shape of the isotherms in the plate was checked by means of a numerical simulation with Star CCM+. Different simulation were run in order to check the influence of the meshing (type and size). No significant effect of the meshing was observed (for what we were interesting on). Boundaries conditions were also changed, especially regarding the influence of the heat transfer coefficient from the wall to the ambient. Results introducing thereafter were obtained with the following boundaries conditions:

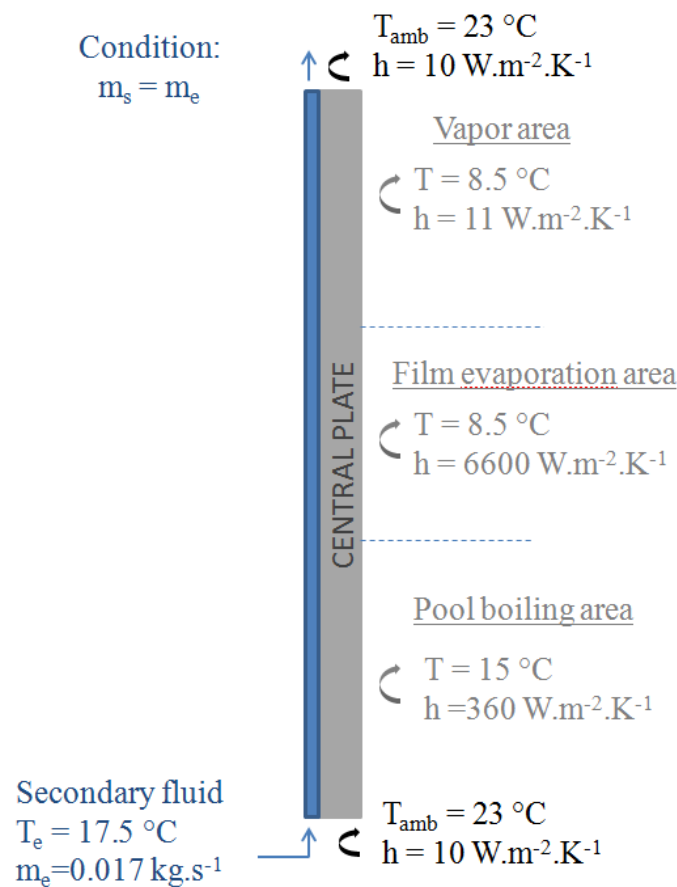


Figure I.1: Boundaries chosen for the simulation on the schematic of the central plate of the evaporator

These boundaries were chosen according to the exploitation of data collected during the test n°1. The temperature set at the pool boiling area referred to the data collected on the thermocouple situated in the bottom of the channel. Heat transfer coefficient in the liquid and vapor parts were calculated as usual, i.e. with the following relation: $Nu = hD/\lambda = 4.86$ (cf. Chap 4, section 4.4.2.). The heat transfer coefficient chosen as a boundary in the film evaporation area is an average on time and space of heat transfer coefficients estimated by thermocouples inserted inside the plate. As the simulation was first used to estimate if a 1 D inverse heat conduction method could be applied, this heat transfer coefficients was first given to $12000\text{ W.m}^{-2}\text{.K}^{-1}$. The simulation was run again with a heat transfer coefficient of $6600\text{ W.m}^{-2}\text{.K}^{-1}$ was estimated. Results obtained for the central plate and the secondary fluid are represented on Fig. I.2.

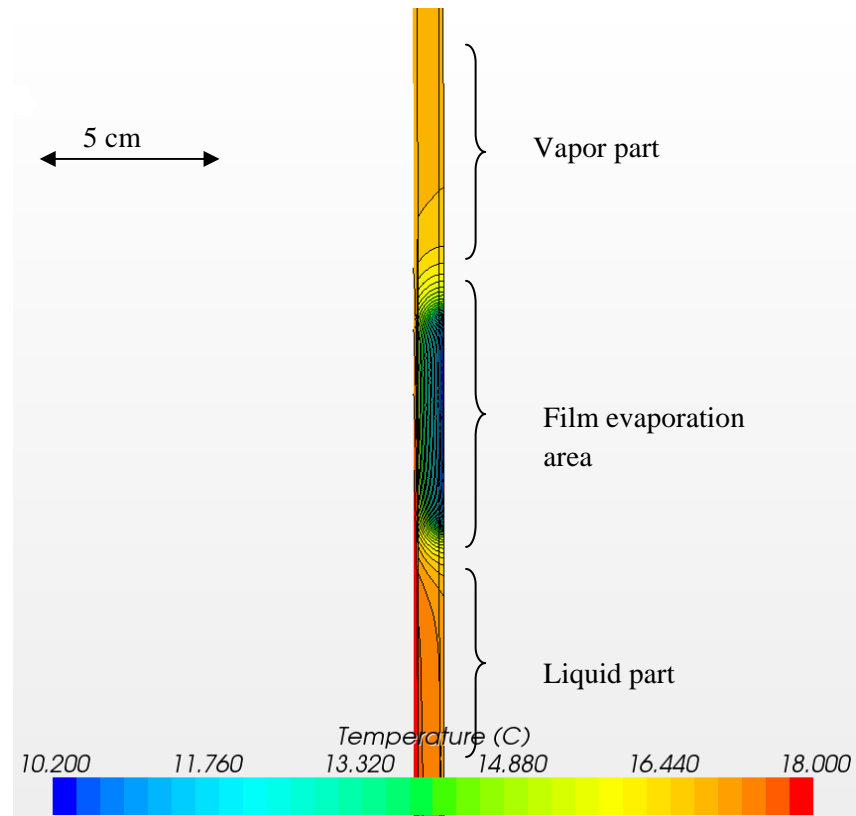


Figure I.2: Results of the Star CCM+ simulation of the temperature field for a portion of the central plate and the secondary fluid

Even though this simulation was realized in steady state condition, the results obtained are consistent with temperatures measured a posteriori by means of the thermocouples located in the plate. A discrepancy of less than 5 % between the temperatures obtained by the simulation and the experiments was found in the area of film evaporation and liquid part. In the vapor part, temperatures obtained with the simulation are much higher than those measured but:

- with the heat transfer coefficient imposed over the falling film evaporation area, the secondary fluid temperature remains at a relatively high temperature (17 °C) which is not the case during the experiments and which is not the case if a heat transfer coefficient of $12000 \text{ W}\cdot\text{m}^{-2}\cdot\text{K}^{-1}$ is set as a boundary condition in the falling film evaporation area. Such high values (and possibly even higher values) were however periodically reached during the experiments.
- the film evaporation area was estimated to be 5 cm which finally appears to be quite often underestimated: it often reaches 15 cm instead.
- simulation was realized in unfavorable conditions regarding ambient heat gains.

This discrepancy between the measured and numerical temperature is not critical in that sense that the objective of this simulation is to check if a 1 D inverse heat conduction method could be applied to evaluate the wall temperature and heat flux. As observed on Fig. I.2, there are no more than 2.5 cm above and down the film evaporation area, which remains reasonably negligible with respect to the whole height of the plate, where the isotherms are not 1 D. In addition, as shown in Fig. I.3, I.4 and I.5, isotherms are rapidly 1 D in each distinct part of the evaporator (Liquid, Film evaporation, Vapor).

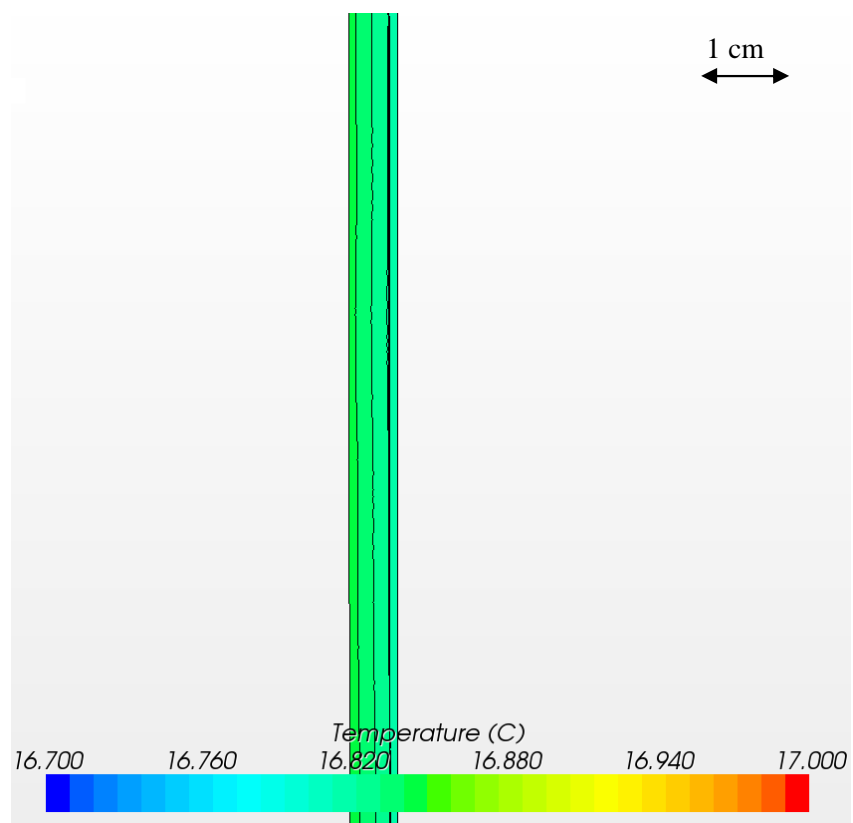


Figure I.3: Results of the Star CCM+ simulation of the temperature field in the vapor part of the central plate

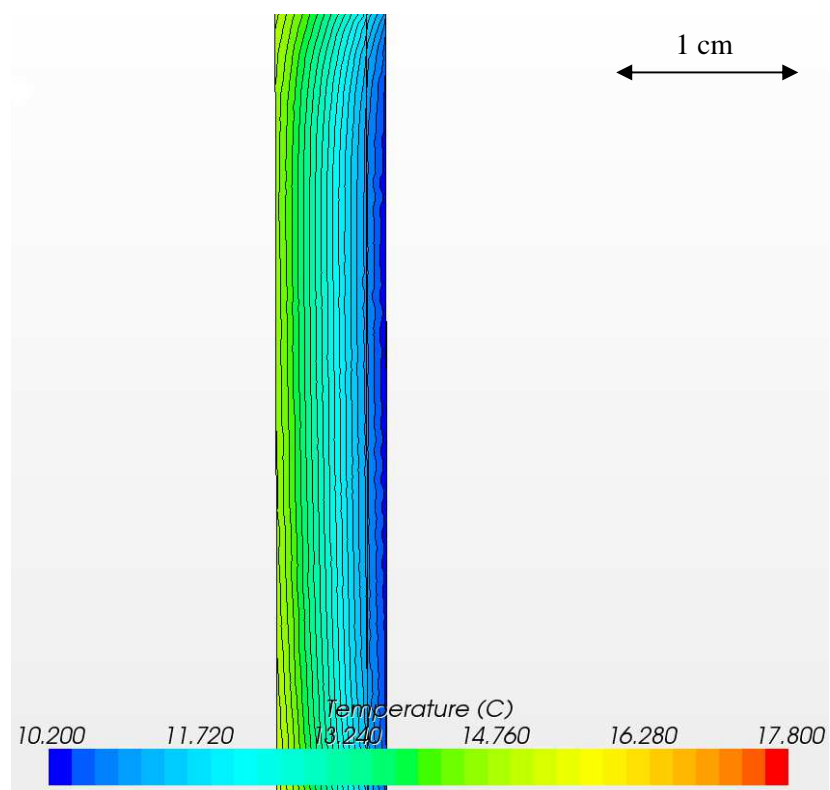


Figure I.4: Results of the Star CCM+ simulation of the temperature field in the film evaporation part of the central plate

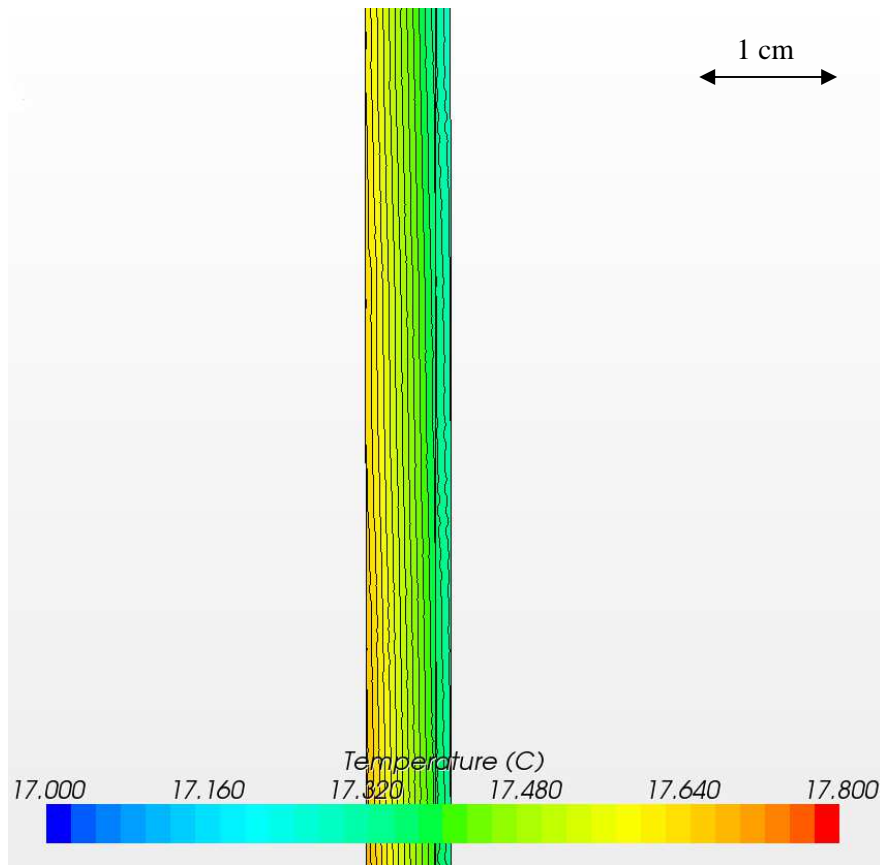


Figure I.5: Results of the Star CCM+ simulation in the liquid part of the central plate

APPENDIX J: Comparison of flow regime obtained for $e = 4$ mm and $e = 2$ mm

Tests of the experimental design with a thickness of channel of 2 mm and 4 mm were realized. Same flow regimes occurred although, as explained in the main text, some difference between phenomena occurring for a thickness of 2 mm and for a thickness of 4 mm were observed. One of this difference lies in the fact that same regime observed for the both thicknesses does not necessarily occur at the same operating conditions. Table J.1 gathers tests run and flow regime observed for the two thicknesses investigated.

Table J.1: Flow regime observed for $e = 4$ mm and $e = 2$ mm

Test n°	h_l (cm)	$T_{cond}^{c,fs}$ (°C)	$T_{B3}^{c,fs}$ (°C)	ΔT (K)	$T_{ev}^{c,fs}$ (°C)	ΔP (kPa)	\dot{Q}_{cool} (W)		Flow regime	
							e = 4 mm	e = 2 mm	e = 4 mm	e = 2 mm
1	15	8.50	37.5	9.0	17.50	0.89	225	170	R2	R2
2	25	8.50	37.5	9.0	17.50	0.89	261	173	R2	R2
3	20	14.13	37.5	9.0	23.13	1.22	283	237	R2	R2
4	10	14.13	37.5	9.0	23.13	1.22	247	221	R2	R3
5	5	8.50	37.5	9.0	17.50	0.89	166	123	R3	R3
6	10	2.87	37.5	9.0	11.87	0.64	172	93	R3	R3
7	20	2.87	37.5	9.0	11.87	0.64	197	49	R2	R2
8	20	10.38	43.62	9.0	19.38	0.99	250	87	R2	R2/R4
9	10	10.38	43.62	9.0	19.38	0.99	224	190	R3	R3
10	15	4.74	43.62	9.0	13.74	0.72	186	-4	R2	R1
11	20	6.62	31.38	9.0	15.62	0.80	229	138	R2	R2
12	10	6.62	31.38	9.0	15.62	0.80	187	143	R2	R2
13	15	12.26	31.38	9.0	21.26	1.10	260	201	R2	R2
14	20	10.38	39.03	13.7	24.12	1.75	447	433	R2	R4
15	10	10.38	39.03	13.7	24.12	1.75	393	398	R2	R4
16	15	4.74	39.03	13.7	18.49	1.27	379	305	R2	R2/R4
17	15	8.50	32.91	13.7	22.25	1.58	411	398	R2	R4
18	20	6.62	35.97	4.3	10.88	0.33	-2	-10	R1	R1
19	10	6.62	35.97	4.3	10.88	0.33	24	-11	R1	R1
20	15	12.26	35.97	4.3	16.51	0.45	44	-1	R1	R1
21	15	8.50	42.09	4.3	12.75	0.36	-5	-15	R1	R1

R1: Appearance and quick collapse of bubbles of millimeter sizes or few centimeters size located on the end of feeding tubes at the bottom of the plate.

R2: Bubbles still collapse at the inlet of the plate but from time to time a bubble of several centimeters appears about 5 cm below the free surface. Droplets are projected on the surface and a falling film is created. Evaporation then immediately takes place.

R3: No collapse of the feeding bubbles is observed. The bubbles entering the channel still grow and splashed liquid over the surface.

R4: As a bubble grows and splashed liquid on the wall, the liquid is dragged by the vapor and evacuated, forming an upward liquid flow.

R2/R4: Both regimes R2 and R4 coexist: as bubble grows and breaks, liquid is splashed on the wall above the free surface. An upward liquid flow is observed before the evaporation of the liquid film takes place.

APPENDIX K: Plot of the evolution of the cooling capacity with dimensionless numbers

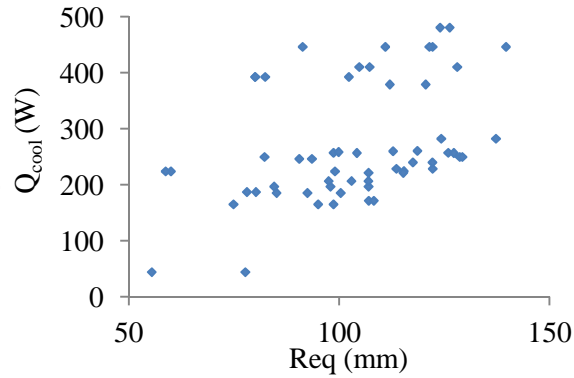


Figure K.1: Evolution of the cooling capacity achieved with the equivalent radius of the large bubble estimated

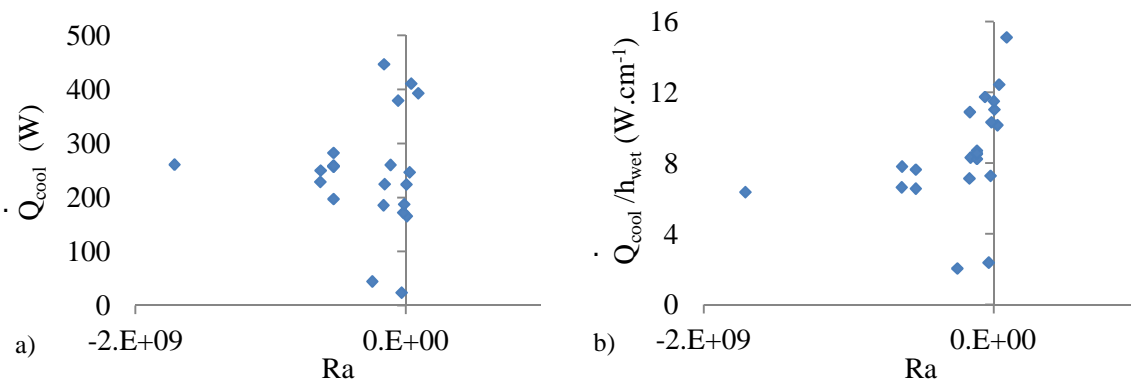


Figure K.2: Evolution of a) the cooling capacity achieved and b) the specific cooling capacity achieved with the Rayleigh Number

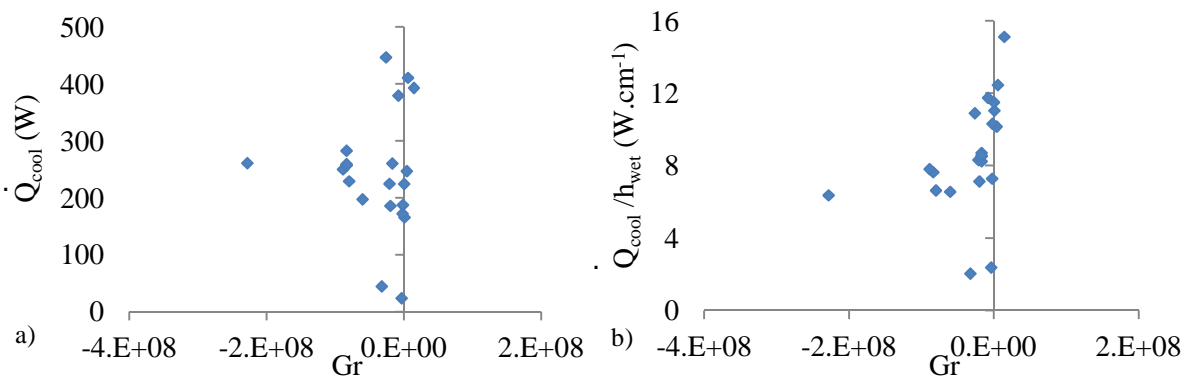


Figure K.3: Evolution of a) the cooling capacity achieved and b) the specific cooling capacity achieved with the Grashof Number

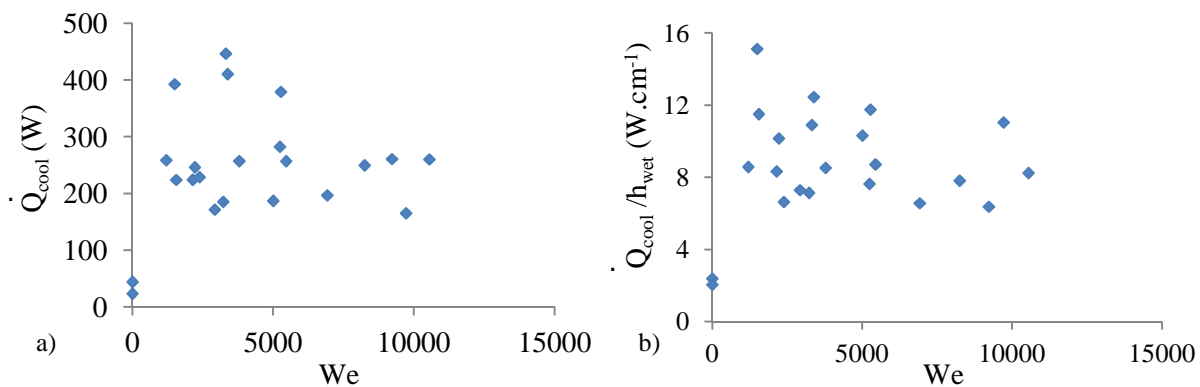


Figure K.4: Evolution of a) the cooling capacity achieved and b) the specific cooling capacity achieved with the Weber Number